MIXING IN DENSITY-STRATIFIED CONJUGATE FLOWS

Thesis by
Marco Rasi

In Partial Fulfillment of the Requirements
for the Degree of
Doctor of Philosophy

California Institute of Technology
Pasadena, California

1989

(Submitted May 15, 1989)

To Jane

Acknowledgements

I wish to express my deepest gratitude to my advisor, Professor E. John List, for his guidance and support during my graduate studies. His dedication to research and education combined with his kindness and sense of humor were always appreciated.

I would also like to thank Professor Norman H. Brooks for the many interesting conversations that we had throughout these four years. The support of Professor Fredric Raichlen during my first year at Caltech is also appreciated.

Special thanks go to my fellow students for their contributions, both personal and professional. Without the help that I received from Greg Sullivan, Regina Dugan, Talal Balaa, Imad Hannoun, Ken Wolfenbarger, Francis Ting, Kit Ng, and many others the completion of this thesis would have been impossible.

The entire staff of the W.M. Keck Laboratories helped me and solved all the problems that I was able to think of. Excellent library assistance was provided by Rayma Harrison and Gunilla Hastrup. Technical support by Joe Fontana, Rich Eastvedt and Hai Vu made the construction of laboratory equipment an easy and rewarding experience. Administrative problems were never problems due to the cheerful help of Joan Mathews, Evelina Cui, Elaine Granger, and Sandy Brooks.

The constant help that I received from my wife, Jane, could hardly be overstated. I also want to thank my parents for being supportive of all my educational achievements, even when they involved a change of continent, and Professors Franco Sassoli and Valerio Milano for initiating my interest in the field of hydraulics.

The support of the California Institute of Technology and the Charles Lee Powell Foundation during my graduate years are deeply appreciated.

Abstract

Two-layer stratified shear flows have been studied in the laboratory using combined laser-induced fluorescence and laser-Doppler velocimetry. Use of this high-resolution, non-intrusive instrumentation has enabled new insight on the entraining characteristics of supercritical two-layer flows and the phenomenon known as an internal hydraulic jump.

In the experiments, salt water was discharged at a steady flowrate from a rectangular slot located at the bottom of the upstream end of a horizontal channel containing fresh water. The flow of the dense bottom layer was controlled at the downstream end of the channel by either a free overfall or a broad-crested weir. The transition between the wall-jet-like flow near the source and the subcritical downstream counterflow took place through an internal hydraulic jump, characterized by a steep interfacial slope and a local recirculating flow region.

A one-dimensional theory based on the assumptions of uniformity of velocity and density distributions downstream of the mixing region was discussed and extended to predict the overall internal flow geometry and the dilution attained by the source fluid across the mixing region. The analysis, which applies to the general case of a mixing channel of finite depth and length, was carried out in three stages. First, the flow at the upstream end of the channel was considered, and a conservation of flow force in the total channel depth across the jump was hypothesized. Second, the gradually-varied counterflow, governed by boundary shear and interfacial momentum transfer, as well as by the critical flow condition at the channel end, was studied by applying the momentum principle to both layers. Finally, the upstream and downstream equations were combined to obtain hydraulic solutions, in a way that clearly establishes that the overall problem can only be solved if the importance of the interplay between source and control is recognized.

An extensive series of experiments confirmed the general predictions of the one-dimensional theory. Four predicted mixing modes (free internal hydraulic jump, flooded jump, upstream-controlled instability, and downstream-controlled instability) were all observed in the experiments. The dependence of the entrainment rate, both on the depth of the ambient water and on the control establishing the critical flow at the end of the channel, has been documented with comprehensive experimental data.

The non-intrusive laser-based instrumentation used has enabled a detailed experimental description of the density and velocity distributions at several locations in the flow field and has pointed out some inaccuracies in the one-dimensional approach. A procedure to overcome these inaccuracies has been proposed.

The ideas developed and the experimental results obtained from this work can be readily extended to further the understanding of many of the two-layer stratified shear flows of interest to engineers and geophysicists.

Contents

List of Figures

List of Tables

Nomenclature

A	momentum flux in the lower layer
A'	momentum flux in the lower layer (one-dimensional theory)
b	channel width
B	momentum flux in the upper layer
$B = b/h_0$	dimensionless channel width
B'	momentum flux in the upper layer (one-dimensional theory)
c	speed of long internal waves
C	hydrostatic pressure force term
C'	hydrostatic pressure force (one-dimensional theory)
c_0	salt concentration at the source
c_1	correction factor for the velocity distribution (Eq. 5.21)
$c(y)$	salt concentration at depth y
d	total depth of flow in the mixing channel
d_1	depth of the lower layer
d_2	depth of the upper layer
e	specific energy of the flow (Eq. 2.16)
f_b	bottom friction factor (page 22)
f_i	interfacial friction factor (page 22)
f_{wl}	wall friction factor in the lower layer (page 22)
f_{wu}	wall friction factor in the upper layer (page 22)
F	boundary shear force along the mixing region

F_b	bottom shear force along the entraining region
F_s	boundary shear force in the region $L_e < x < 2\,L_j$
F_t	total boundary shear force between sections 0 and 1
F_w	wall shear force along the entraining region
$\mathbf{F_0}$	discharge densimetric Froude number (page 30)
$\mathbf{F_1}$	densimetric Froude number of the lower layer (Eq. 1.2)
$\mathbf{F_2}$	densimetric Froude number of the upper layer (Eq. 1.2)
$\mathbf{F}_{free-surface}$	free surface Froude number (Eq. 2.1)
$\mathbf{F_j}$	densimetric Froude number at section j
FF_0	flow force at section 0 (Eq. 5.7)
FF_1	flow force at section 1 (Eq. 5.7)
g	gravity acceleration
$g' = g\Delta\rho/\rho$	reduced gravity acceleration
g'_0	reduced gravity at the source
g'_1	reduced gravity after the jump region
h	depth of the lower layer
$H = d/h_0$	dimensionless ambient water depth
h_A	lower layer depth just upstream of the broad-crested weir
h_c	depth of the lower layer at critical flow
h_j	lower layer depth just upstream of the roller region
h_w	height of the broad-crested weir
h_0	discharge inlet height
h_1	depth of the lower layer after the jump region
h_{1v}	height of zero-velocity line after the jump
h_2	depth of the upper layer

l	channel length
L_j	length of the jump region
L_j'	length of the jump region in upstream-controlled unstable flows
L_j''	length of the jump region in downstream-controlled unstable flows
q_f	rate of freshwater inflow into the experimental channel
q_l	flowrate per unit width in the lower layer
q_s	withdrawal flowrate of mixed fluid from the experimental channel
q_{salt}	salt flux per unit width of channel
q_u	flowrate per unit width in the upper layer
q_0	discharge flowrate per unit width of channel
q_1	flowrate in the lower layer after the jump region
q_2	flowrate in the upper layer
Q_f	rate of freshwater inflow into the experimental channel
Q_s	withdrawal flowrate of mixed fluid from the experimental channel
Q_0	discharge flowrate into the experimental channel
$r = h/h_0$	dimensionless depth of the lower layer in the subcritical counterflow
$r_A = h_A/h_0$	dimensionless depth of the lower layer upstream of the weir
$r_c = h_c/h_0$	dimensionless critical depth of the lower layer
r_{c1}	dimensionless lower critical depth
r_{c2}	dimensionless upper critical depth
$r_w = h_w/h_0$	dimensionless weir height
$r_1 = h_1/h_0$	dimensionless depth of the lower layer after the jump
r_{1d}	dimensionless depth after the jump as predicted by Eq. 2.23
r_{1u}	dimensionless depth after the jump as predicted by Eq. 2.22
$\mathbf{R_i}$	gradient Richardson number (page 174)

$\mathbf{R_{ih}}$	bulk Richardson number in terms of centerline parameters (Eq.6.1)
$\mathbf{R_{i0}}$	bulk Richardson number
$S = q_1/q_0$	dilution attained by the source fluid across the mixing region
u	horizontal fluid velocity
U	characteristic velocity of the lower layer
u_c	centerline velocity
u_{max}	maximum horizontal velocity
u_1	lower layer convective velocity
u_2	upper layer convective velocity
W	weight of empty gravity flask
W_f	weight of gravity flask full of fresh water
W_s	weight of gravity flask full of salt water
x	longitudinal distance from the source or from the control section
x_j	distance between source and roller region
y	vertical coordinate
y_{max}	depth where the horizontal velocity is a maximum
y_0	depth of zero-velocity line
$y_{0.1}$	depth at which the horizontal velocity is $0.1\,u_{max}$
$y_{50\%}$	depth at which the density difference is 50% of the total density difference between the two layers
z	horizontal coordinate perpendicular to the channel walls

Greek symbols

$\alpha = f_i/f_b$	ratio between interfacial and bottom friction factors
β	variable entrainment coefficient for buoyant jet (Eq 6.1)
β_0	constant entrainment coefficient for non-buoyant jet (Eq. 6.1)

δ	stagnation rise over the source (Eq. 2.2)
δ^*	displacement thickness of boundary layer (Eq. 5.1)
ΔFF_{01}	flow force loss between sections 0 and 1 (Eq.5.7)
$\Delta\rho = \rho - \rho_a$	density difference between the two layers
$\eta = x/h_0$	dimensionless horizontal distance from downstream critical section
θ	momentum thickness of boundary layer (Eq. 5.2)
θ_b	slope of the channel bottom
θ_i	slope of the interface
μ	dynamic viscosity of water
ν	kinematic viscosity of water
ρ	fluid density
ρ_a	ambient fluid density
ρ_0	source fluid density
ρ_1	lower layer density
ρ_2	upper layer density
τ_b	bottom shear stress (page 22)
τ_i	interfacial shear stress (page 22)
τ_{wl}	wall shear stress in the lower layer (page 22)
τ_{wu}	wall shear stress in the upper layer (page 22)

Subscripts

a	referring to the ambient fluid
b	referring to the channel bottom
i	referring to the interface
j	referring to a cross-section just preceding the roller region
l	referring to the lower layer

u	referring to the upper layer
w	referring to the channel walls
0	referring to flow conditions at the source
1	referring to a cross-section just downstream of the jump region

Chapter 1

Introduction

1.1 The research project

Internal hydraulic jumps are encountered in many flow systems of interest to engineers, environmental scientists and geophysicists. They occur, in general, in all flows where a supercritical-subcritical transition is present.

As an example, consider a two-dimensional vertical submerged turbulent buoyant jet, discharging in a shallow fluid layer of uniform density. The buoyant jet region is followed by a surface impingement region, which in turn is followed by a spreading layer. If the flow is supercritical in the impingement region, and subcritical in the spreading stratified counterflow region, the formation of an internal hydraulic jump can take place. The importance of such a jump is apparent if one realizes that the mixing in this region can substantially increase the dilution already attained in the jet region. The phenomenon may also be exploited where pollutant discharges require premixing to comply with environmental regulations, before their release into a lake, river or ocean. Mixing of dense and buoyant discharges may be attained in a channel connected to the receiving natural water body. The prediction of the performance of such mixing channels requires an understanding of the dynamics of density currents, and, more specifically, of the transition from supercritical to subcritical two-layer flows. While maximum dilution of the pollutant discharge is desired in the case of

mixing channels, there are situations in which the designer of an outfall wants to limit dilution to the smallest amount possible. This is often the case for power station cooling ponds, where the cooling water is drawn from a reservoir. Because of the temperature difference between the water in the pond and the water discharged from the power station back into the pond, the discharge will spread and form a warm layer at the surface of the reservoir. Since maximum heat transfer from the warm surface layer to the atmosphere is desired before the cooling water is reused, radiation and evaporation are optimized when the surface layer is as warm and as thin as possible. Such layering will occur if the mixing between the ambient water and the discharged water is minimal. Again, an understanding of the dynamics of two-layer density flows is necessary. In particular, the outfall designer needs to know the conditions for the formation of a flooded internal hydraulic jump, which is characterized by extremely low mixing.

Two-layer gravity currents can also form internal jumps in large scale natural phenomena, such as atmospheric fronts and ocean currents. Jumps occurring in nature have been observed in Föhn winds and katabatic flows in Antarctica (Schweitzer, 1953, Ball, 1956, 1957, 1959). Meteorological measurements were taken by Lied (1964), who walked through a standing katabatic jump. The account of his exciting experience is worth reading. Jumps in the atmosphere have also been observed by Clarke, Smith, and Reid (1981) and others. Farmer and Denton (1985) detected internal hydraulic jumps in Canadian fjords using acoustic imaging.

Not only hydraulic and environmental, but also mechanical and chemical engineers can encounter internal hydraulic jumps, which occur for example in the interaction of fire plumes with ceilings, and in the design of air conditioning systems and jet mixing devices for tanks or combustion chambers.

The examples illustrated above all point to the need for a sound understand-

ing of the hydraulics and turbulent mixing characteristics of flow systems involving internal hydraulic jumps.

Although the present investigation is restricted to the case of a two-dimensional mixing channel, the results are considered sufficiently general to be capable of being applied to all problems involving internal hydraulic jumps. It is recognized, however, that there may be important extensions to be made for problems whose geometry is significantly different from that of a mixing channel.

On the other hand, focusing attention on a very specific case allows key issues to be addressed in a sufficiently simple way, both theoretically and experimentally. In particular, the importance of the role played by the downstream control and by the ambient water depth in determining the mechanics of the flow can be fully emphasized.

The present investigation therefore studies flows that occur when a dense fluid is discharged on the bottom of a rectangular mixing channel. The channel is horizontal and connected to a receiving body containing a finite depth of water with uniform density. A fluid with density greater than the ambient density is discharged, with a steady flowrate, from a rectangular slot located at the bottom of the upstream end of the channel. The flow of the dense bottom layer is controlled at the downstream end of the channel by either a free overfall or a broad-crested weir. Discharge and ambient fluids are miscible and their relative density difference is small.

1.2 Two-layer flows: general considerations

The flow of a layer of dense fluid under a layer of lighter fluid is now considered. If both layers occupy a semi-infinite space, there is only one characteristic length scale in the flow, which is the length of the waves at the interface. The amplitude of these waves decreases with distance from the interface.

On the other hand, if both layers are sufficiently shallow for the fluid velocities to be approximately uniform over the depth of each layer, it can be shown (Schijf and Schönfeld, 1953) that the speed at which long internal waves propagate is

$$c = \frac{u_1 h_2 + u_2 h_1}{h_1 + h_2} \pm \sqrt{\frac{g' h_1 h_2}{h_1 + h_2} - \frac{h_1 h_2}{(h_1 + h_2)^2}(u_1 - u_2)^2}\,, \tag{1.1}$$

where h_1 and h_2 are depths of the two layers, u_1 and u_2 are their velocities, $g' = g(\rho_1 - \rho_2)/\rho_2$, with ρ_1 and ρ_2 being the densities of the two layers.

The dispersion relation 1.1 has been derived under the condition

$$\Delta\rho = \rho_1 - \rho_2 \ll \rho_2.$$

It can be rearranged to show that $c = 0$ when

$$\mathbf{F_1}^2 + \mathbf{F_2}^2 = 1, \tag{1.2}$$

where $\mathbf{F_1} = u_1/\sqrt{g'h_1}$ and $\mathbf{F_2} = u_2/\sqrt{g'h_2}$ are called the densimetric Froude numbers of the two layers. When Equation 1.2 is satisfied, the two-layer flow is said to be critical.

Suppose now that only the lower layer, layer 1, is flowing. If $\mathbf{F_1}^2 + \mathbf{F_2}^2 = \mathbf{F_1}^2 < 1$ the flow is called subcritical, and interfacial disturbances can propagate upstream, since the speed of internal waves, c, is larger than the convective velocity of the moving layer, u_1. This implies that, in close analogy with open channel flow, subcritical two-layer flows are controlled from downstream. On the other hand, if $\mathbf{F_1}^2 + \mathbf{F_2}^2 > 1$, the flow is called supercritical, the convective velocity u_1 is larger than the speed of the internal waves c, and all interfacial disturbances are swept downstream. For this reason supercritical flows are upstream-controlled flows.

When both layers are in motion, the situation is conceptually similar, provided that a moving reference system is considered, with respect to which the second layer is at rest.

As for the case of open channel flow, the concepts of control sections and hydraulic jumps are central to the understanding of the dynamics of two-layer stratified flows. Any feature which causes a transition from a subcritical to a supercritical flow is called a control, since long interfacial waves can travel both upstream and downstream of the feature, thus influencing both the upstream and the downstream flows. At the control section Equation 1.2 is satisfied and the flow is critical.

Experimental evidence also shows that transitions from supercritical to subcritical flows can occur. These are abrupt transitions that take the form of shock waves, called hydraulic jumps, which are characterized by significant turbulence and energy dissipation.

Since this investigation is mainly concerned with the phenomenon of the hydraulic jump, only flows which are supercritical at the discharge will be taken into consideration.

1.3 Outline and scope of work

The complexity of internal flows has induced previous investigators to make various simplifying assumptions. In the study of flows in mixing channels one of the most appealing theoretical analyses is based on the assumption of uniform velocity and density distributions in the two layers (Baddour, 1987). However, few experimental data are available to support such a one-dimensional theory. For this reason an extensive series of laboratory experiments was carried out, so as to remedy this deficiency.

Ninety-nine different flow conditions have been obtained by varying ambient water depth, discharge densimetric Froude number, and downstream control height. This series of experiments was characterized by flow visualization by means of blue dye

mixed with the dense lower layer, and it will be referred to as 'visual observations' or 'blue-dye experiments' in the following pages. The visual observations fundamentally support the general results of the above-mentioned one-dimensional theory. Some discrepancies, though, exist between the observed and the predicted dilutions attained in the mixing region for a certain range of discharge, control and ambient parameters.

In order to investigate the causes of such discrepancies, more detailed experiments were performed by means of laser-Doppler velocimetry (LDV) and a laser-induced fluorescence technique (LIF). These non-intrusive, high resolution techniques allowed the determination of complete velocity and density distributions at chosen cross-sections in the channel. The complexity of these 'laser-based experiments' was such that only a limited number of them could be performed. However, they were sufficient to point out clearly the limits of the one-dimensional approach, and to explain the discrepancies found between the theory and the visual observations.

A critical review of the present theoretical understanding of flow in mixing channels is given in Chapter 2, together with some proposed extensions. A description of the apparatus and procedures employed in the experimental investigation may be found in Chapter 3. The visual observations are presented and discussed in Chapter 4, while Chapter 5 deals with the laser-based experiments. The main results of this investigation are summarized in Chapter 6.

Chapter 2

Theoretical analysis and historical background

The goal of this chapter is to describe in some detail the present understanding of the behavior of mixing channels. The work of previous investigators is discussed, and a few extensions are introduced.

The discussion is subdivided into five parts. Section 2.1 describes in general, qualitative terms the types of flow that can occur in a mixing channel. This description is useful to define some concepts and terminology that will be used later and to give a physical intuition of the key features of the flows under investigation. Section 2.2 deals with the 'upstream problem' and the flow near the upstream end of the channel. The 'downstream problem' is considered in Section 2.3. Here the flow near the source is taken as known, and attention is focused on the downstream part of the channel. Section 2.4 combines the ideas developed in the two previous sections in order to find solutions satisfying both upstream and downstream conditions. The results found are summarized in Section 2.5.

2.1 General features of flow in mixing channels

Observations show that four substantially different flow configurations can occur in a mixing channel. These are illustrated in Figures 2.1, 2.2, 2.3 and 2.4.

The flow in Figure 2.1, which will be called a *free internal hydraulic jump*, is

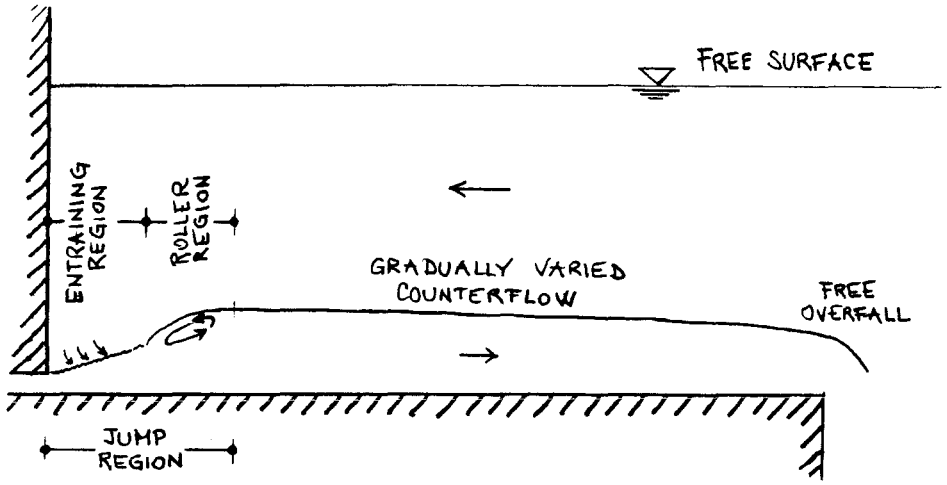

Figure 2.1: Sketch of free internal hydraulic jump.

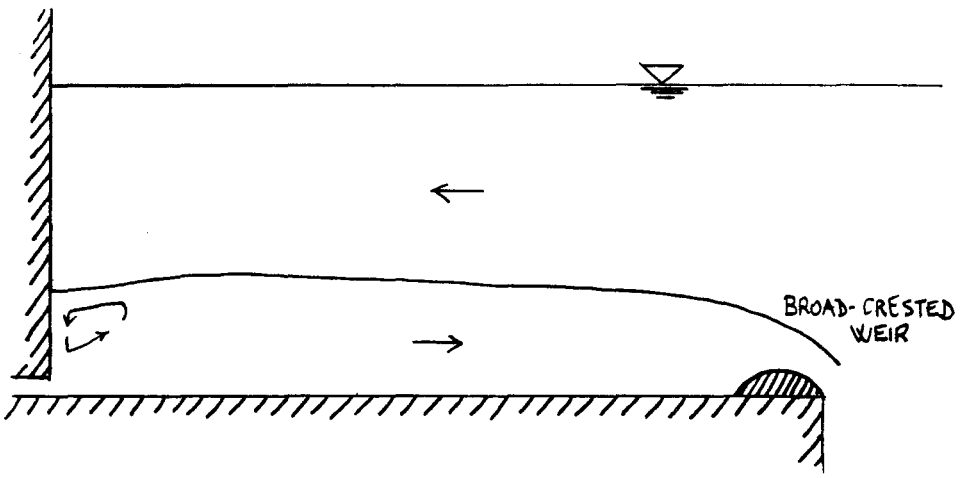

Figure 2.2: Sketch of flooded internal hydraulic jump.

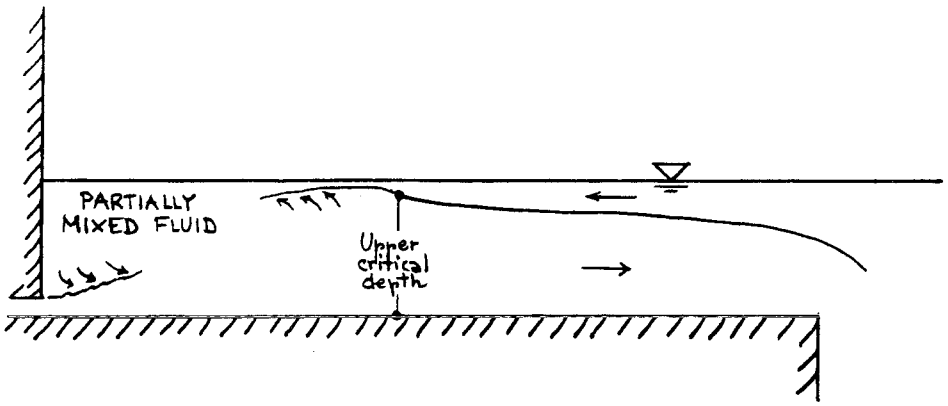

Figure 2.3: Sketch of upstream-controlled unstable flow.

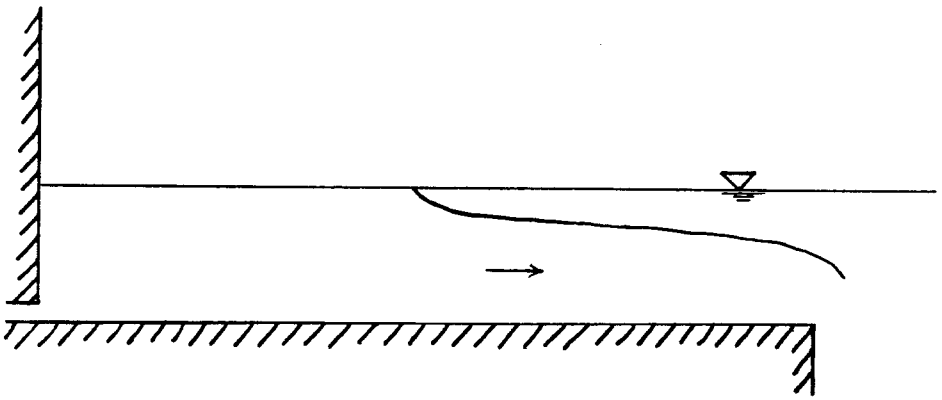

Figure 2.4: Sketch of downstream-controlled unstable flow.

characterized by a supercritical, wall-jet-like region near the source, and a subcritical gradually-varied counterflow region terminating with a critical section at the downstream end of the channel. Between these two regions is a roller region, which has an interfacial slope noticeably steeper, and an interfacial shear markedly lower, than the initial jet-like region.

The free internal hydraulic jump is in many respects similar to the well-known open channel hydraulic jump. There is, though, an important difference: entrainment of ambient fluid occurs in the supercritical region preceding the roller of the free internal hydraulic jump. This causes a change in the density, as well as in the flowrate, of the dense bottom layer. Furthermore, the amount of such entrainment depends not only on the discharge conditions, but also on the position and length of the roller region, which in turn are influenced by the downstream control of the flow. In other words, unlike the open channel jump, the internal jump does not have unique conjugate states. Different downstream states, with different flowrates and densities, are possible for a given set of source conditions. The actually occurring downstream state can be determined only if the interaction of the downstream control with the source conditions is taken into account.

If the downstream control acts in such a way as to raise the depth of the dense layer in the counterflow region, the roller tends to move upstream, and this reduces the extent of the supercritical entraining region. In the limit, the roller region will reach the source, and entrainment will be reduced to a negligible amount. If the downstream depth is further raised by the control, the jump will be drowned, and the flow in the mixing channel will appear as sketched in Figure 2.2. Such a flow is characterized by a permanent presence of denser fluid over the source, and will be referred to as a *flooded internal hydraulic jump.*

The flows illustrated in Figures 2.3 and 2.4 are a result of the interaction of the

dense layer with the free surface of the channel. They will be called unstable, since they are characterized by recirculation of dense fluid flowing back towards the source.

The flow sketched in Figure 2.3, which, for reasons that will be explained later, will be referred to as an *upstream-controlled unstable flow*, exhibits a very thin layer of ambient water flowing towards the source, with only occasional touching of the free surface by the dense layer.

In the flow sketched in Figure 2.4, called a *downstream-controlled unstable flow*, entrainment of ambient water towards the mixing zone is completely blocked, and the entire depth over the source is occupied by the discharged dense fluid.

All four flows have been observed in the laboratory and will be discussed in the following chapters in more detail.

2.2 The upstream problem

The hydraulic jump phenomenon in regular open channels is well known. Early comprehensive studies were conducted by Backhmeteff and Matze (1936) and by Rouse, Siao and Nagaratnam (1959), and they represent, together with an abundant number of related discussions, the basis of our present understanding.

However, the situation in two-layer systems is more complex and, although the problem of relating the flow conditions across a jump in two-layer stratified flows has been approached in many fundamentally different ways, the understanding is still incomplete. The goal of this work is to resolve these deficiencies.

The assumption of immiscibility of the fluids forming the two layers has been the basis of many investigations. For example, Yih and Guha (1955) derived momentum equations for the two layers and showed the existence of several solutions. Hayakawa (1970) refined the analysis relating to the physical interpretation of the solutions.

Many other studies concerned with general aspects of two-layer flow systems were founded on this assumption of negligible entrainment across the interface. Among them, Long (1953, 1954) and Mehrotra and Kelly (1973) studied the behavior of the flow in the neighborhood of obstructions, where friction losses could be neglected. Chu and Baddour (1977) pointed out that over the short distance of a jump, the energy losses in the contracting layer were likely to be an order of magnitude less than in the expanding layer. Neglecting such losses and assuming constancy of flow force for the system of both layers, the authors obtained a particularly simple conservation relation. A comparison between the immiscible theories developed by Yih and Guha (1955) and by Chu and Baddour (1977) was presented by Wood and Simpson (1984). It was shown that the two theories gave similar results as long as the shear on the interface was below a certain value. Beyond this value, both theories broke down, since the mixing could no longer be ignored.

The simplicity of these immiscible theories makes them appealing, and they have been applied to different flow systems, e.g., buoyant discharges (Jirka and Harleman, 1979). On the other hand, the very assumption that these theories are founded on is rarely encountered in actual flow systems. In most applications, and certainly in the problem of the mixing channel, entrainment of one fluid into the other does occur, and it represents one of the most interesting aspects of the problem.

The following discussion will therefore focus only on the investigations that explicitly allow for entrainment and mixing. The 'school of thought' initiated by Wilkinson (1970) will be the object of the next section. The one-dimensional approximation previously mentioned will then be discussed and finally the inadequacy of buoyant jet theories in the study of the mixing channel problem will be pointed out.

2.2.1 General upstream equations

Consider the flow situation indicated in Figure 2.5. The goal of this section is to relate the flow conditions at sections 0 and 1. Section 0 coincides with the rectangular jet opening, while section 1 is taken at a position immediately downstream of the jump region.

Arguments in favor of a hydrostatic pressure distribution at both sections can be found in Wilkinson (1970).

Bottom and wall friction are neglected between the two sections, an approximation which is justified by the fact that in the jump region the flow is rapidly varied; it is therefore unlikely to be strongly affected by boundary shear stresses. Such an approximation is usually made in open channel rapidly-varied flow, and its extension to two-layer flows is generally accepted (Wilkinson and Wood, 1971; Wright, 1986; Baddour, 1987). The importance of boundary friction in the jump region will be reanalyzed in Chapter 5.

The Boussinesq approximation of small density difference effects on flow inertia is made ($\Delta\rho = \rho - \rho_a \ll \rho$); this is true for most environmental applications (Turner, 1973). Furthermore, it is assumed that the distance between the free surface and the channel bottom is constant and equal to d, except for a small stagnation rise at the discharge section. This is equivalent to restricting the analysis to flows in which the free surface Froude number, defined as

$$\mathbf{F}_{free-surface} = \frac{q_0/h_0}{\sqrt{gd}} , \tag{2.1}$$

is much smaller than 1 (Jirka and Harleman, 1979). In Equation 2.1, q_0 is the discharge flowrate and h_0 is the discharge height.

Finally, the velocity and the density are assumed to be uniform at the discharge, and equal to q_0/h_0 and ρ_0 respectively.

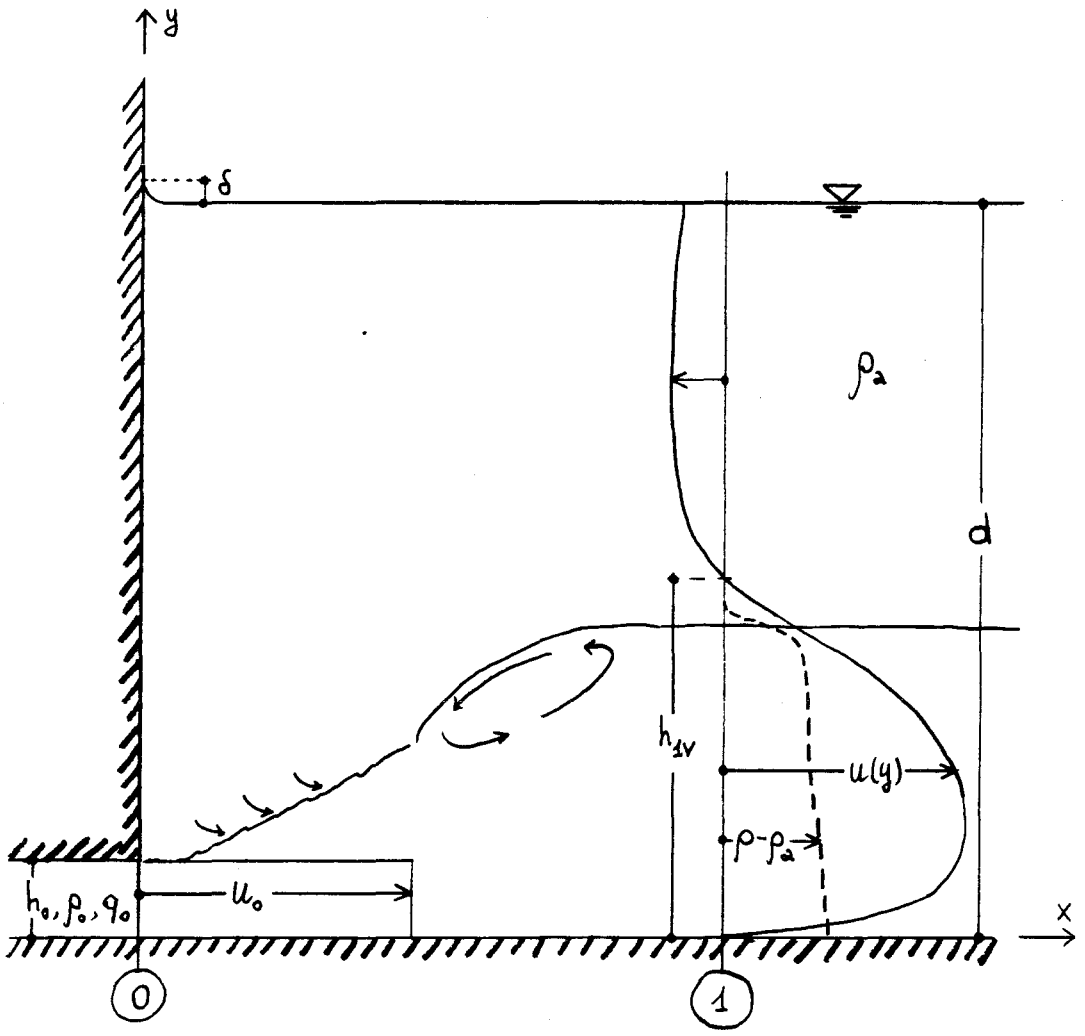

Figure 2.5: Upstream problem. General definition sketch.

If momentum fluxes and pressure forces are balanced over the entire water depth at sections 0 and 1 (neglecting turbulent transport), the following equation is obtained:

$$\frac{q_0^2}{h_0} + \frac{1}{2}g_0' h_0^2 + \frac{1}{2}g(d+\delta)^2 = \int_0^d u^2 dy + \int_0^d \int_y^d g' dy dy + \frac{1}{2}gd^2, \tag{2.2}$$

where

$u(y)$ = horizontal component of fluid velocity at section 1

$g'(y) = g(\rho - \rho_a)/\rho_a$, reduced gravity at section 1

$\rho(y)$ = fluid density at section 1

ρ_a = ambient fluid density

$g_0' = g(\rho_0 - \rho_a)/\rho_a$

δ = stagnation rise at section 0.

If the height h_{1v} of the zero-velocity line at section 1 is introduced, Equation 2.2 can be rewritten as

$$\frac{q_0^2}{h_0} + \frac{1}{2}g_0' h_0^2 + gd\delta = \int_0^{h_{1v}} u^2 dy + \int_{h_{1v}}^d u^2 dy + \int_0^d \int_y^d g' dy dy, \tag{2.3}$$

in which the term of order δ^2 has been neglected.

Equation 2.3 is the result of the analysis formulated by Wilkinson (1970) and Wilkinson and Wood (1971) and extended by Bewick (1974) and others. It was adopted also by Wright (1986), in a form very similar to that presented here.

Fluid continuity implies

$$\int_0^{h_{1v}} u dy = q_0 - \int_{h_{1v}}^d u dy, \tag{2.4}$$

and conservation of flux of density difference yields

$$\int_0^d u g' dy = q_0 g_0'. \tag{2.5}$$

Equations 2.3, 2.4 and 2.5 relate the flow conditions at sections 0 and 1, but, as was already discussed in Section 2.1, an infinity of conditions at section 1 are possible for each condition at section 0. In other words, Equations 2.3, 2.4 and 2.5 define *possible* states downstream of the jump, but the determination of the *actual* downstream state requires that the downstream control be taken into consideration.

Besides, not even the possible flow conditions can be determined from Equations 2.3, 2.4 and 2.5 in a straightforward way. This is due to the fact that the shapes of the velocity and density profiles are not known a priori, so that the integrals in the equations cannot be expressed in a simple way in terms of characteristic velocities and densities. To be sure, it is possible to eliminate the integrals by introducing appropriate correction factors (Wilkinson, 1970; Stefan and Hayakawa, 1971; Wilkinson and Wood, 1971; Wright, 1986). While it is recognized that this may be convenient for purposes of presentation and discussion, it does not represent a step forward in the theoretical analysis, since the numerical value of such factors and their dependence on the discharge conditions and downstream control are unknown.

2.2.2 The one-dimensional approximation

In order to overcome the difficulties encountered in the previous section, an additional approximation will be introduced. The velocity and density profiles will be assumed to be uniform over the depth of the flowing layer, as well as in the counterflowing upper layer.

This situation is sketched in Figure 2.6. The fluid velocity is equal to q_1/h_1 in the lower layer and to $-(q_1 - q_0)/(d - h_1)$ in the upper layer. The depth of the dense lower layer after the jump is denoted by h_1, while $(q_1 - q_0)$ is the amount of ambient fluid entrained into the lower layer in the jump region.

It is easily shown that in this one-dimensional framework Equations 2.5 and 2.3

reduce respectively to

$$q_1 g'_1 = q_0 g'_0, \tag{2.6}$$

and

$$\frac{q_0^2}{h_0} + \frac{1}{2} g'_0 h_0^2 + \frac{1}{2} \frac{(q_1 - q_0)^2 d}{(d - h_1)^2} = \frac{q_1^2}{h_1} + \frac{(q_1 - q_0)^2}{d - h_1} + \frac{1}{2} g'_1 h_1^2, \tag{2.7}$$

while continuity of mass has been implicitly used in stating that the amount of the counterflow is $(q_1 - q_0)$.

It should be noticed that in deriving Equation 2.7 the free surface stagnation rise δ has been taken equal to

$$\frac{(q_1 - q_0)^2}{2g(d - h_1)^2}$$

(Baddour and Abbink, 1983).

The simplicity of Equations 2.6 and 2.7 allows them to be solved, together with downstream equations that will be discussed later, to obtain hydraulic solutions for the mixing channel problem.

Discussion of the merits and limits of this one-dimensional approach is deferred to Chapters 4 and 5.

2.2.3 Shortcomings of buoyant jet analyses

The simplicity of the analysis presented in the preceding sections makes such an analysis appealing despite the fact that it provides only predictions regarding the flow downstream of the jump region.

A completely different approach, one that provides predictions of the flow evolution throughout the whole mixing region, has been taken by many investigtors (e.g., Jirka, 1982; Chu and Baddour, 1984; Rajaratnam and Subramanyan, 1985). It is the

buoyant jet or mixing layer approach, in which entrainment rates and pressure distributions in the mixing region are specified, and suitable similarity assumptions to describe velocity and density distributions are made.

Wright (1986) eloquently points out the shortcomings of this type of analysis. All integral analyses are based on boundary layer approximations, which include the assumption of lack of coupling between upstream and downstream conditions through the pressure gradient. The resulting equations do not admit the possibility of a recirculation in the flowfield. But inspection of Figure 2.5 clearly shows that the ambient fluid entrained by the dense layer must come from downstream, so that boundary layer approximations are acceptable only if the ambient fluid is very deep, which is not usually the case in many environmental applications. It will be shown that the effect of the counterflow, which is neglected in buoyant jet theories, is very important in determining the behavior of mixing channels.

Furthermore, buoyant jet and mixing layer analyses presume that the mixing process is entirely controlled by upstream conditions. This is conceptually questionable. If the flow downstream of the jump is subcritical, it will be influenced by downstream controls, since disturbances can travel upstream from the controls to the jump, and modify the characteristics of the jump itself. It is for this reason that investigators who claim that the boundary conditions in the far-field do not influence the discharge region (e.g., Jirka and Harleman, 1979) are believed to be at fault.

Some merits of the buoyant jet theories are recognized. They provide flow descriptions throughout the entraining region, and they explicitly describe the importance of buoyancy in reducing entrainment. On the other hand, they are believed to be inadequate to study the problem of the mixing channel, because of their inability to cope with downstream controls and counterflows, which are essential elements of the dynamics of flows involving internal hydraulic jumps.

2.3 The downstream problem

Wilkinson (1970) first recognized the importance of the role played by the downstream control on the global turbulent mixing properties of a buoyant discharge. He analyzed the interaction of various types of tailwater control with internal hydraulic jumps in a deep channel.

After this pioneering work, many other investigators explicitly included some form of downstream control on the flow. Wilkinson and Wood (1971) used a broad-crested weir at the channel end. Koh (1971) studied the case in which the downstream flow is controlled by friction (if only friction is controlling the downstream flow, though, no steady-state solution is possible and the depth of the flowing layer will keep on increasing). Stefan and Hayakawa (1971) and Stefan (1972) included the effect of a limited ambient depth on the mixing characteristics of surface buoyant jets. Baddour and Abbink (1983) adopted a channel contraction as downstream control device, while Wright (1986) and Baddour (1987) considered a free overfall.

From a slightly different perspective, several investigations have also been conducted with an unsteady gravity current advancing along a channel (e.g., Wilkinson, 1970; Wright, 1986). The implied assumption was that the flow field near the source could be considered steady while the layer was spreading away from the source region.

An exhaustive list of all the types of controls found in the literature is not intended here. Suffice it to say that, although the details will differ from case to case, the general concepts involved can be illustrated using any one of such controls.

Since a prototype mixing channel is likely to be influenced by boundary friction, bottom, wall and interfacial shear stresses have been included in the present analysis. The way they influence the development of the gradually-varied counter-

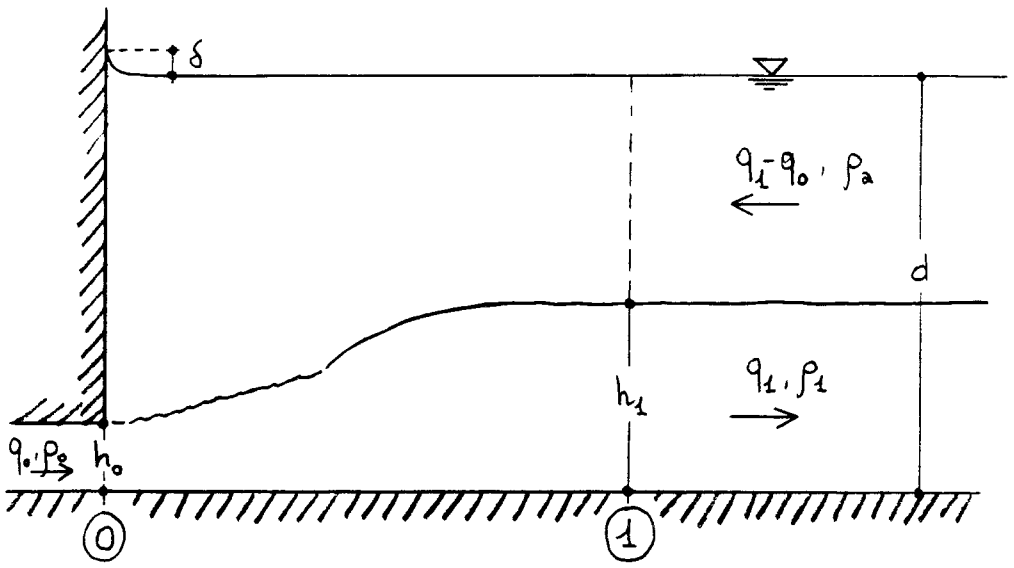

Figure 2.6: Upstream problem. One-dimensional approximation.

flow is discussed in the next section. The successive section deals with the critical flow condition at the channel end. A free overfall and a broad-crested weir have been chosen in this study because they are easy to handle in the laboratory and they are considered to be the controls that most clearly point out the interplay of source and control factors.

2.3.1 Gradually-varied counterflow

The gradually-varied two-layer counterflow sketched in Figure 2.7 is now studied with the following assumptions:

- the density difference between the two layers is small;
- velocity and density profiles are uniform;
- the slopes of bottom, free surface, and interface are small;
- the pressure is hydrostatic;

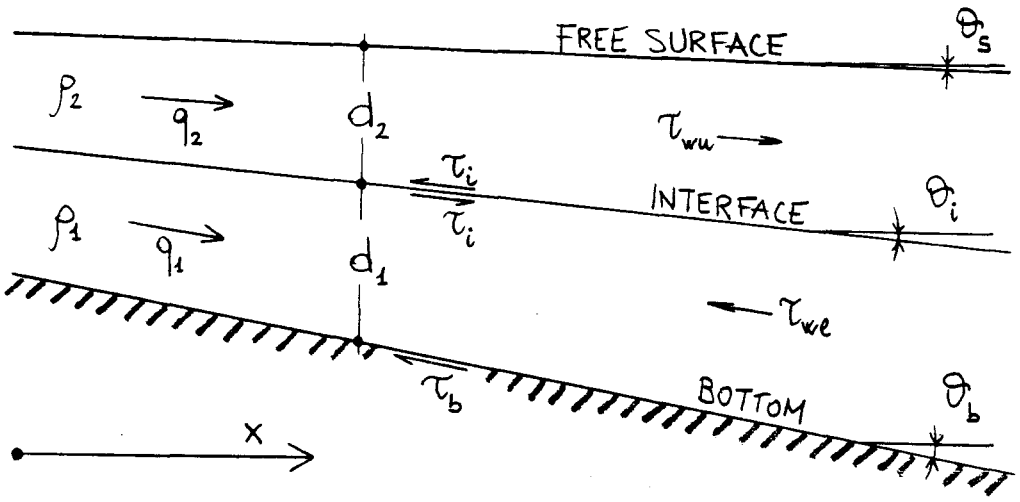

Figure 2.7: Gradually-varied counterflow. Definition sketch.

- mixing across the interface is negligible. This assumption is fully justified for the case of subcritical flow. Both theoretical arguments and experimental evidence support the idea of interfacial stability for subcritical two-layer flows. For a recent discussion on the subject, see Wright (1986);

- flow conditions are steady;

- bed, wall and interfacial shear stresses are proportional to the square of the shearing velocity;

- there is no shear at the free surface, and surface tension is negligible.

Application of the momentum principle to the lower layer results in

$$\frac{\rho_1 q_1^2}{d_1^2}\frac{dd_1}{dx} = \rho_2 g[\frac{dd_2}{dx}d_1+\frac{dd_1}{dx}d_2]+\rho_1 g d_1\frac{dd_1}{dx}+\tau_i+\tau_b+2\tau_{wl}\frac{d_1}{b}+\rho_2 d_2 g\theta_i-(\rho_1 d_1+\rho_2 d_2)g\theta_b, \tag{2.8}$$

where the meaning of the symbols is as shown in Figure 2.7 and

$$b = channel\ width$$

$$\tau_b = \frac{1}{8} f_b \rho_1 \frac{q_1}{d_1} |\frac{q_1}{d_1}|,\ bottom\ shear\ stress$$

$$\tau_i = \frac{1}{8} f_i \frac{\rho_1 + \rho_2}{2} (\frac{q_1}{d_1} - \frac{q_2}{d_2}) |\frac{q_1}{d_1} - \frac{q_2}{d_2}|,\ interfacial\ shear\ stress$$

$$\tau_{wl} = \frac{1}{8} f_{wl}\, \rho_1 \frac{q_1}{d_1} |\frac{q_1}{d_1}|,\ wall\ shear\ stress\ in\ the\ lower\ layer.$$

Also, let

$$\tau_{wu} = \frac{1}{8} f_{wu}\, \rho_2 \frac{q_2}{d_2} |\frac{q_2}{d_2}|,\ wall\ shear\ stress\ in\ the\ upper\ layer,$$

where f_b, f_i, f_{wl} and f_{wu} are friction factors at the bottom, interface, wall in lower layer, and wall in upper layer respectively. They will be discussed in detail at a later stage. Similarly, applying the momentum principle to the upper layer,

$$\rho_2 \frac{q_2^2}{d_2^2} \frac{dd_2}{dx} = \rho_2 g \frac{dd_2}{dx} d_2 - \tau_i + 2\tau_{wu} \frac{d_2}{b} - \rho_2 d_2 g \theta_i. \tag{2.9}$$

Equations 2.8 and 2.9 represent an extension of the equations given by Schijf and Schönfeld (1953), the extension consisting in the inclusion of wall shear in the analysis.

In the mixing channel which is the object of the present investigation, the bottom is horizontal, i.e., $\theta_b = 0$. This implies that $\theta_i = -dd_1/dx$. Also, $q_2 = -(q_1 - q_0)$. Equations 2.8 and 2.9 take then the form

$$\frac{q_1^2}{g d_1^3} \frac{dd_1}{dx} = \frac{\rho_2}{\rho_1} \frac{dd_2}{dx} + \frac{dd_1}{dx} + \frac{1}{8} f_b \frac{q_1^2}{g d_1^3} + \frac{1}{8} \frac{f_i}{g d_1} \frac{\rho_1 + \rho_2}{2\rho_1} (\frac{q_1}{d_1} + \frac{q_1 - q_0}{d_2})^2 + \frac{1}{4} \frac{f_{wl}}{gb} \frac{q_1^2}{d_1^2}, \tag{2.10}$$

$$\frac{(q_1-q_0)^2}{gd_2^3}\frac{dd_2}{dx}=\frac{dd_1}{dx}+\frac{dd_2}{dx}-\frac{1}{8}\frac{f_i}{gd_2}\frac{\rho_1+\rho_2}{2\rho_2}(\frac{q_1}{d_1}+\frac{q_1-q_0}{d_2})^2-\frac{1}{4}\frac{f_{wu}}{gb}\frac{(q_1-q_0)^2}{d_2^2}. \quad (2.11)$$

Equations 2.10 and 2.11 coincide with the equations given by Baddour (1987) if the wall shear is neglected. Wall shear has been included in this analysis to facilitate comparison between theory and experimental data, since wall shear is unlikely to be negligible in the usually narrow laboratory channels.

If it is further assumed that the total depth is constant, $d_1 + d_2 = d$, and, for convenience, d_1 is replaced by h and the x axis is taken pointing to the left ($x = 0$ at the downstream end of the channel). Equations 2.10 and 2.11 can then be combined to yield

$$(1-\mathbf{F_1}^2-\mathbf{F_2}^2)\frac{dh}{dx}=\frac{1}{8}(f_b+2f_{wl}\frac{h}{b})\mathbf{F_1}^2+\frac{f_i}{8g_1'}(\frac{q_1}{h}+\frac{q_1-q_0}{d-h})^2(\frac{1}{h}+\frac{1}{d-h})+\frac{f_{wu}}{8g_1'}\frac{2}{b}\frac{(q_1-q_0)^2}{(d-h)^2}, \quad (2.12)$$

in which

$\mathbf{F_1} = q_1/\sqrt{g_1'h^3}$, densimetric Froude number in the lower layer,

$\mathbf{F_2} = (q_1 - q_0)/\sqrt{g_1'(d-h)^3}$, densimetric Froude number in the upper layer,

$g_1' = g(\rho_1 - \rho_a)/\rho_a$,

$\rho_a \equiv \rho_2$, ambient fluid density.

If the flow characteristics at the end of the channel are known (see following discussion on controls), Equation 2.12 can be integrated to determine the flow conditions at all points in the gradually-varied counterflow region.

It is stressed once again, though, that the values of q_1 and ρ_1 to use in Equation 2.12 are unknown a priori, and they can be determined only when the interaction of the upstream and downstream equations is brought into the analysis.

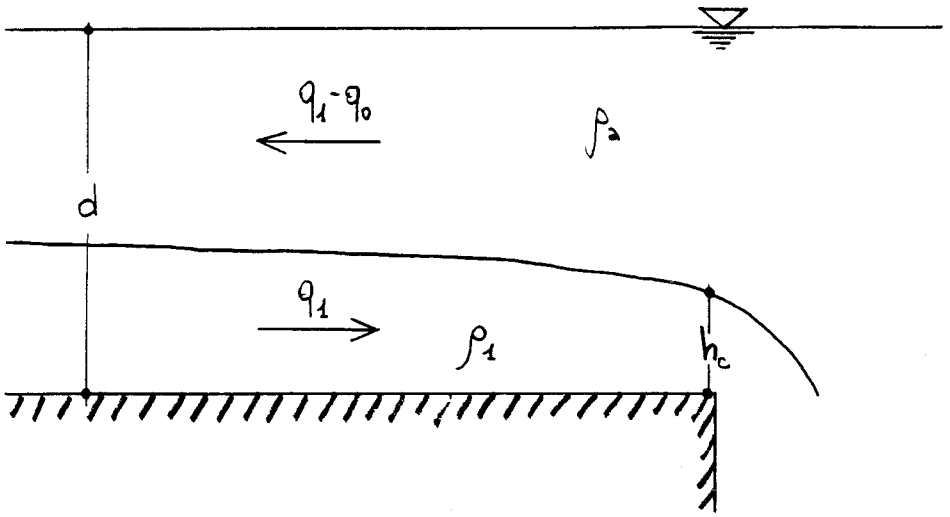

Figure 2.8: Free overfall.

2.3.2 Critical flow at the downstream control section

It has been previously stated that in order to start integration of Equation 2.12 it is necessary to know the depth of the lower layer at the downstream end of the mixing channel.

Such depth is obtained in a straightforward manner if the channel ends with a free overfall, as sketched in Figure 2.8. The critical flow condition at the control section, Equation 1.2, requires that the sum of the squares of the densimetric Froude numbers in the lower and upper layer be equal to one:

$$\mathbf{F_1}^2 + \mathbf{F_2}^2 = 1, \tag{2.13}$$

i.e.

$$\frac{q_1^2}{g_1' h_c^3} + \frac{(q_1 - q_0)^2}{g_1'(d - h_c)^3} = 1. \tag{2.14}$$

Equation 2.13 can also be obtained setting $dh/dx = \infty$ in Equation 2.12

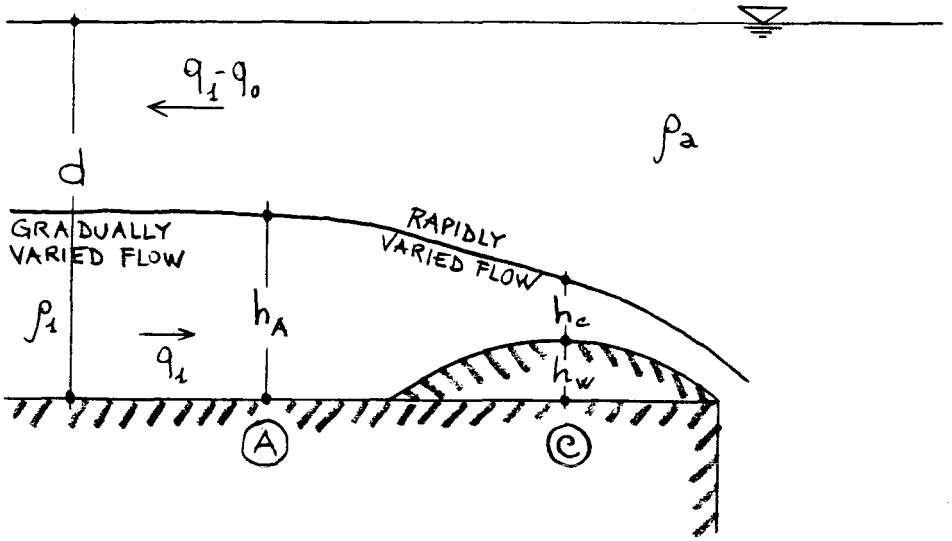

Figure 2.9: Broad-crested weir.

(Harleman, 1960). It should be mentioned that the criticality of the flow over the brink of the overfall is predicted by a one-dimensional analysis. However, near the brink the flow is highly curvilinear, and the approximations of the one-dimensional theory break down. Critical depth actually occurs some distance upstream of the brink (Wilkinson, 1970). This can be neglected in the analysis presented here, since such distance is very small when compared to the length of the channel.

If q_1 and g_1' are known, Equation 2.14 can be solved to find the required depth h_c (of the three roots, only the smaller of the two positive roots is relevant in this case).

The situation is more complex if the channel ends with a broad-crested weir, as shown in Figure 2.9. In this case the critical flow condition over the weir is

$$\frac{q_1^2}{g_1' h_c^3} + \frac{(q_1 - q_0)^2}{g_1'(d - h_c - h_w)^3} = 1, \tag{2.15}$$

where h_w is the weir height.

This is obtained by minimizing the specific energy of the flow

$$e = h + \frac{q_1^2}{2g_1' h^2} - \frac{(q_1 - q_0)^2}{2g_1'(d - h - h_w)^2}\,, \tag{2.16}$$

with respect to h, the depth of the lower layer over the weir.

The depth of flow over the weir cannot be used to start integration of Equation 2.12, since the channel is not horizontal between sections A and C (Figure 2.9). It will be hypothesized that energy is conserved in the rapidly-varied flow between these two sections. Taking Equation 2.16 into consideration, this results in

$$h_A + \frac{q_1^2}{2g_1' h_A^2} - \frac{(q_1 - q_0)^2}{2g_1'(d - h_A)^2} = h_w + h_c + \frac{q_1^2}{2g_1' h_c^2} - \frac{(q_1 - q_0)^2}{2g_1'(d - h_c - h_w)^2}\,. \tag{2.17}$$

The depth h_A can be used to start the integration of Equation 2.12, and the distance between section A and the end of the channel is negligible if compared with the length of the channel.

2.4 Combining the upstream and downstream problems to obtain hydraulic solutions

2.4.1 Proposed analytical model

Equations 2.6, 2.7, 2.12 and 2.14 represent the one-dimensional analytical model that will be discussed in this section. Such a system of equations coincides with the one proposed by Baddour (1987), with the exception of the modifications introduced in Equation 2.12 to include wall shear in the analysis.

If the source conditions q_0, g_0' and h_0 are given, and the ambient depth d and channel characteristics (length, width, and friction factors) are specified, the four equations can be solved to determine all the other parameters that characterize the flow sketched in Figure 2.10, i.e., q_1, g_1', h_1 and h_c.

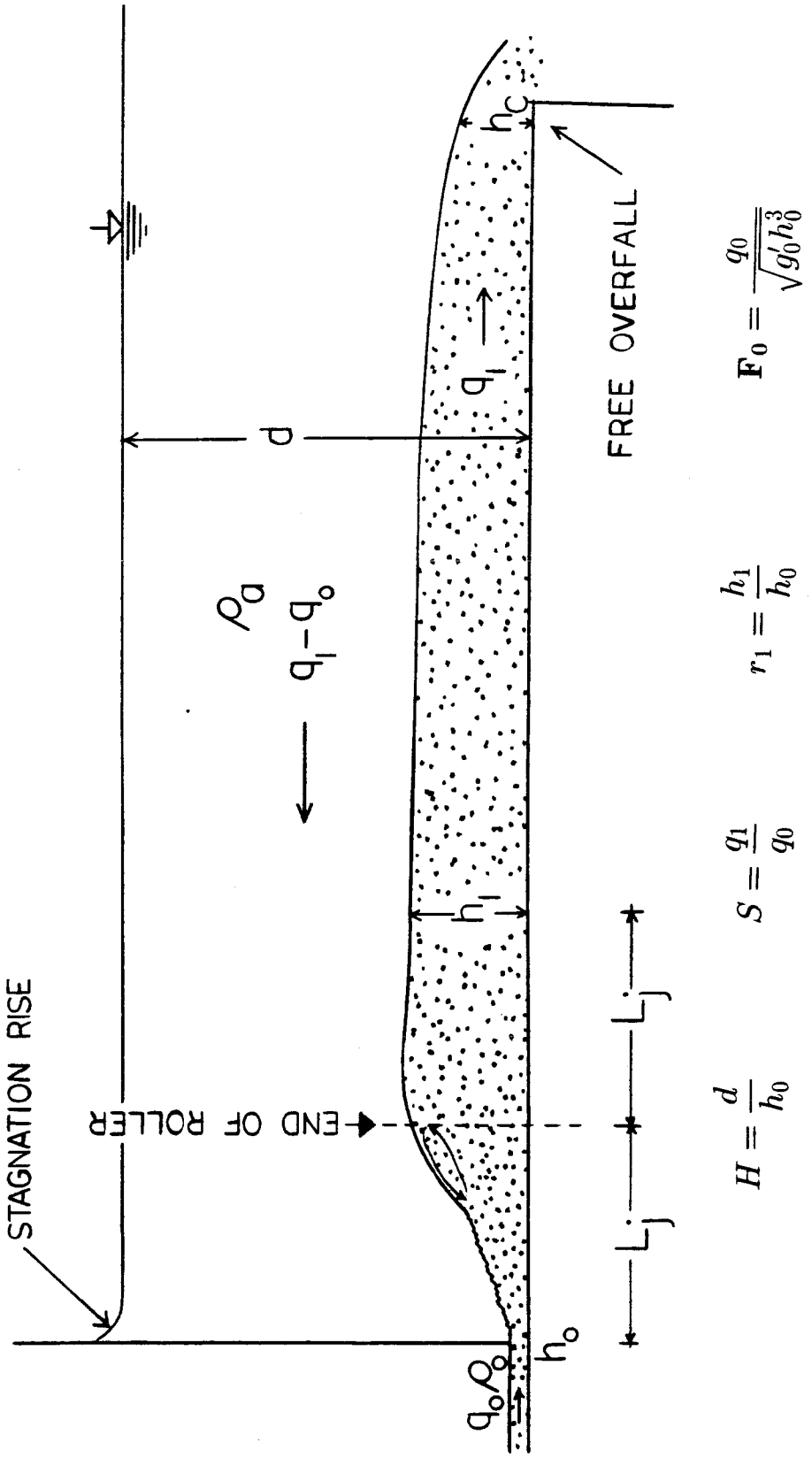

Figure 2.10: The one-dimensional problem.

If a broad-crested weir controls the downstream end of the channel (Figure 2.9) Eq. 2.14 has to be replaced by Equations 2.15 and 2.17. For a given height h_w of the weir, 2.6, 2.7, 2.12, 2.15 and 2.17 allow the determination of q_1, g_1', h_1, h_c and h_A.

In order to eliminate solutions which are physically meaningless, a group of constraints has to be associated with the above-mentioned equations.

The lower layer cannot be deeper than the total flow depth, so that it must be

$$0 \leq h_1 \leq d. \tag{2.18}$$

The flowrate in the lower layer cannot decrease across the jump, i.e.,

$$q_1 \geq q_0. \tag{2.19}$$

The specific energy cannot increase across the jump. This can be expressed as (Baddour and Abbink, 1983)

$$h_0 + \frac{(q_0/h_0)^2}{2g_0'} - [h_1 + \frac{(q_1/h_1)^2}{2g_1'} - \frac{(q_1 - q_0)^2}{2g_1'(d-h_1)^2}] \geq 0. \tag{2.20}$$

Finally, the two-layer flow downstream of the jump is subcritical, and this implies that the sum of the squares of the densimetric Froude numbers of the two layers is less than one (Harleman, 1960), i.e.,

$$\frac{q_1^2}{g_1' h_1^3} + \frac{(q_1 - q_0)^2}{g_1'(d-h_1)^3} \leq 1. \tag{2.21}$$

2.4.2 Non-dimensional governing equations

It is convenient to rewrite the equations and the constraints of the proposed analytical model in terms of non-dimensional variables. The discharge flowrate q_0 and the height of the source h_0 are used to normalize the other variables. Equation 2.6 is used to eliminate g_1' from all the other equations.

The following system of equations is obtained for the case of a free overfall as downstream control.

- Flow force conservation across the jump:

$$2S\mathbf{F_0}^2[\frac{S^2}{r_1}+(\frac{S-1}{H-r_1})^2(\frac{H}{2}-r_1)-1]=S-r_1^2\,; \tag{2.22}$$

- Gradually varied counterflow:

$$\frac{dr}{d\eta}=\frac{S\mathbf{F_0}^2[(f_b+\frac{2r}{B}f_{wl})\frac{S^2}{r^3}+f_i(\frac{S}{r}+\frac{S-1}{H-r})^2(\frac{1}{r}+\frac{1}{H-r})+\frac{2f_{wu}}{B}(\frac{S-1}{H-r})^2]}{8\{1-S\mathbf{F_0}^2[\frac{S^2}{r^3}+\frac{(S-1)^2}{(H-r)^3}]\}}\,; \tag{2.23}$$

- Critical flow at the free overfall:

$$S\mathbf{F_0}^2[\frac{S^2}{r_c^3}+\frac{(S-1)^2}{(H-r_c)^3}]=1\,; \tag{2.24}$$

- Constraints:

$$0\le r_1\le H, \tag{2.25}$$

$$S\ge 1, \tag{2.26}$$

$$S\mathbf{F_0}^2[\frac{S^2}{r_1^3}+\frac{(S-1)^2}{(H-r_1)^3}]-1\le 0, \tag{2.27}$$

$$1+\frac{\mathbf{F_0}^2}{2}-r_1-\frac{S\mathbf{F_0}^2}{2}[\frac{S^2}{r_1^2}+\frac{(S-1)^2}{(H-r_1)^2}]\ge 0, \tag{2.28}$$

where the dimensionless variables not yet defined have the following meaning:

$r(x)=h(x)/h_0$, lower layer depth

$r_1=h_1/h_0$, lower layer depth after the jump

$r_c=h_c/h_0$, lower layer critical depth

$S=q_1/q_0$, dilution attained in the jump region

$H=d/h_0$, ambient water depth

$B = b/h_0$, channel width

$\eta = x/h_0$, horizontal distance from channel downstream end

$\mathbf{F_0} = q_0/\sqrt{g_0' h_0^3}$, discharge densimetric Froude number.

The same system of equations and constraints applies to the case of broad-crested weir control, except for Equation 2.24, which has to be replaced by

- Critical flow over the weir:

$$S\mathbf{F_0}^2[\frac{S^2}{r_c^3} + \frac{(S-1)^2}{(H-r_c-r_w)^3}] = 1 \; ; \tag{2.29}$$

- Energy conservation in rapidly-varied flow preceding the weir:

$$r_A + \frac{S\mathbf{F_0}^2}{2}[\frac{S^2}{r_A^2} - \frac{(S-1)^2}{(H-r_A)^2}] = r_c + r_w + \frac{S\mathbf{F_0}^2}{2}[\frac{S^2}{r_c^2} - \frac{(S-1)^2}{(H-r_c-r_w)^2}] \tag{2.30}$$

in which $r_w = h_w/h_0$ and $r_A = h_A/h_0$.

2.4.3 Properties of governing equations

The presented system of equations is non-linear. Thus, it is instructive to analyze the equations separately, before combining them to describe the overall flow.

Equation 2.22 describes the dependence of the jump properties on the discharge densimetric Froude number $\mathbf{F_0}$, for a given value of H. It states flow force conservation across the jump, without taking into account in any way the downstream control condition (friction factors or weir height do not appear in the equation). For every value of S and fixed H and $\mathbf{F_0}$, Equation 2.22 can be solved for r_1. Of the three roots, only one is real and satisfies constraints 2.25 and 2.27. A convenient way of presenting the solutions of 2.22 is to plot r_1 versus S for given H and $\mathbf{F_0}$. Such plots can be found in Baddour and Abbink (1983) and in Baddour (1987) for $H = 15$. Figures 2.11 and 2.12 show the cases $H = 26.6$ and $H = 15.3$. More of these curves

are presented later, when theory and visual observations are compared (Sections 4.2.3 and 4.3.3). An interesting discussion of limiting cases for Equation 2.22 can be found in Baddour and Abbink (1983). They show that

- there exists an upper bound value, S_m^*, of the dilution that can be achieved in a confined flow,

$$S_m^* \simeq \frac{2}{3} H^{\frac{4}{9}}, \tag{2.31}$$

  which corresponds to a conjugate depth

$$r_m^* \simeq \frac{2}{3} H^{\frac{8}{9}}, \tag{2.32}$$

- in unconfined flow ($H \rightarrow \infty$), the maximum dilution achievable is

$$S_m = \frac{2}{3} \mathbf{F_0}^{\frac{2}{3}} (1 + \frac{1}{2\mathbf{F_0}^2}), \tag{2.33}$$

  which corresponds to a conjugate depth

$$r_m = \frac{1}{3} \mathbf{F_0}^{-\frac{2}{3}} (1 + 2\mathbf{F_0}^2); \tag{2.34}$$

- the confined flows behave essentially as the unconfined flow provided that $\mathbf{F_0}$ is less than

$$\mathbf{F_0}^* \simeq H^{\frac{2}{3}}. \tag{2.35}$$

It is also interesting to notice that if the dilution S is set equal to 1, Equation 2.22 reduces to

$$r_1 = \frac{h_1}{h_0} = \frac{1}{2}(\sqrt{1 + 8\mathbf{F_0}^2} - 1), \tag{2.36}$$

which is a classical result for immiscible jumps (Yih and Guha, 1955).

Equation 2.23 is the differential equation describing the gradually-varied counterflow region. If a value of S is assumed, and all friction factors are specified, Equation 2.23 can be integrated starting from the channel downstream end, $\eta = 0$, where r

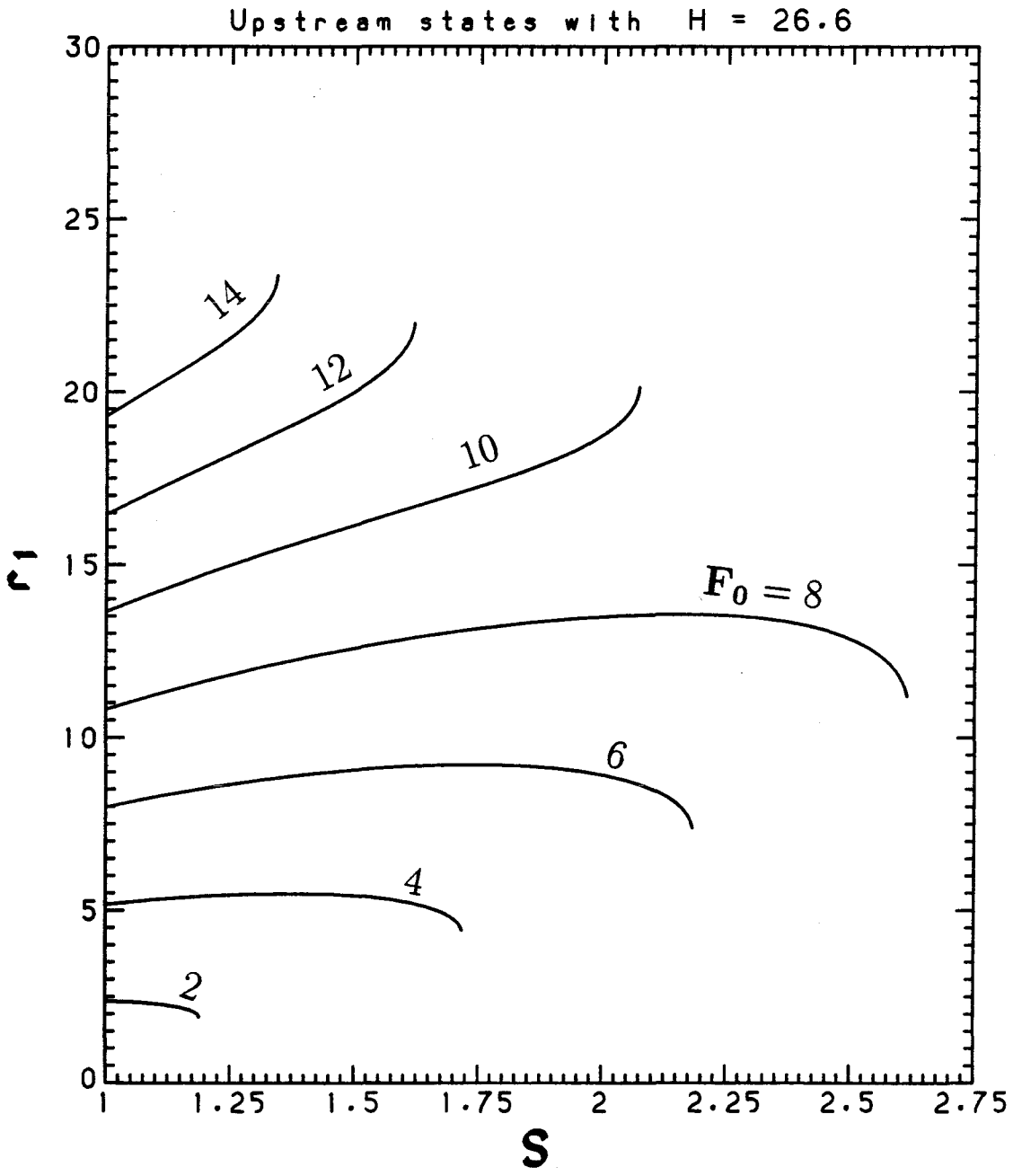

Figure 2.11: Possible upstream states with H = 26.6.

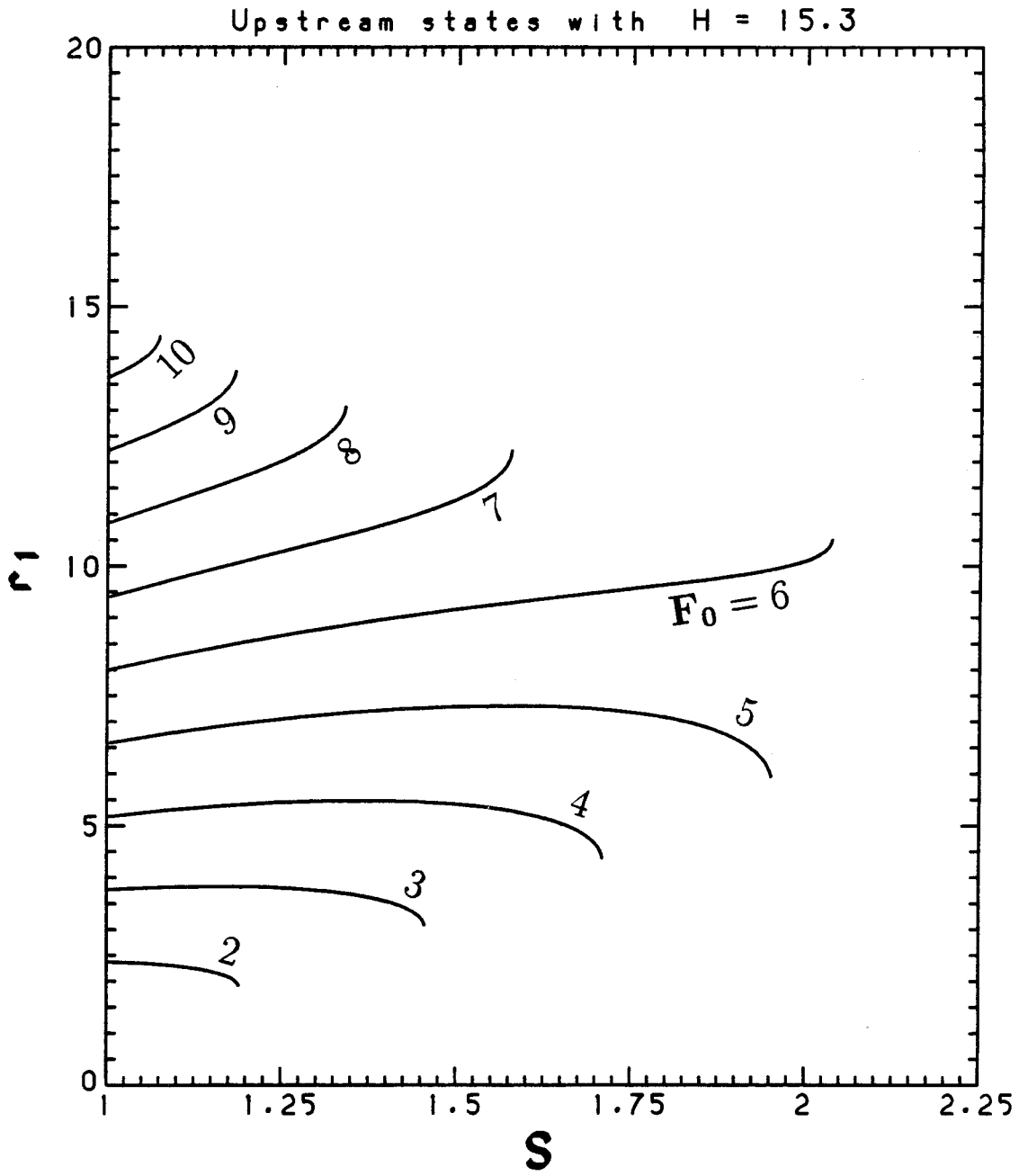

Figure 2.12: Possible upstream states with H = 15.3.

is equal to the critical value r_c (with free overfall) or equal to r_A (with broad-crested weir).

The choice of the friction factors is a delicate point that requires additional consideration. The discussion of this is deferred to Chapter 4. Interfacial profiles obtained integrating 2.23 are also found in Chapter 4, where theory and visual observations are compared. If the wall friction factors f_{wl} and f_{wu} are set equal to zero, Equation 2.23 coincides with the equation given by Baddour (1987), and some additional examples of the resulting interfacial profiles are plotted in his article.

Equation 2.24 can be regarded as a particular case of Equation 2.29, with $r_w = 0$, therefore only Equation 2.29 will be discusssed. Equation 2.29 states the criticality of the two-layer flow over the weir. For given H, r_w and $\mathbf{F_0}$, a value of S can be assumed, and Equation 2.29 can be solved for r_c. For each S, two critical depths, r_{c1} and r_{c2} ($r_{c1} < r_{c2}$), are found, as shown in Figure 2.13 for $\mathbf{F_0} = 9$. The lower critical depth is the relevant one at $\eta = 0$. The significance of the upper critical depth will be mentioned later. Note that if $S = 1$, i.e. if no entrainment occurs in the jump region, 2.29 reduces to

$$r_c = \mathbf{F_0}^{\frac{2}{3}}. \tag{2.37}$$

Finally, Equation 2.30 can be solved for r_A after r_c has been obtained from Equation 2.29. Only the root $r_A \geq r_w + r_c$ is of interest here. Note that if $r_w = 0$, Equation 2.30 gives $r_A = r_c$, which confirms that the free overfall can be regarded as a broad-crested weir with zero height.

2.4.4 Interaction of source and control. Hydraulic solutions.

It is now shown how the system of equations can be used to determine the flow behavior.

Suppose that a channel of length l is given for which H, B and all the friction

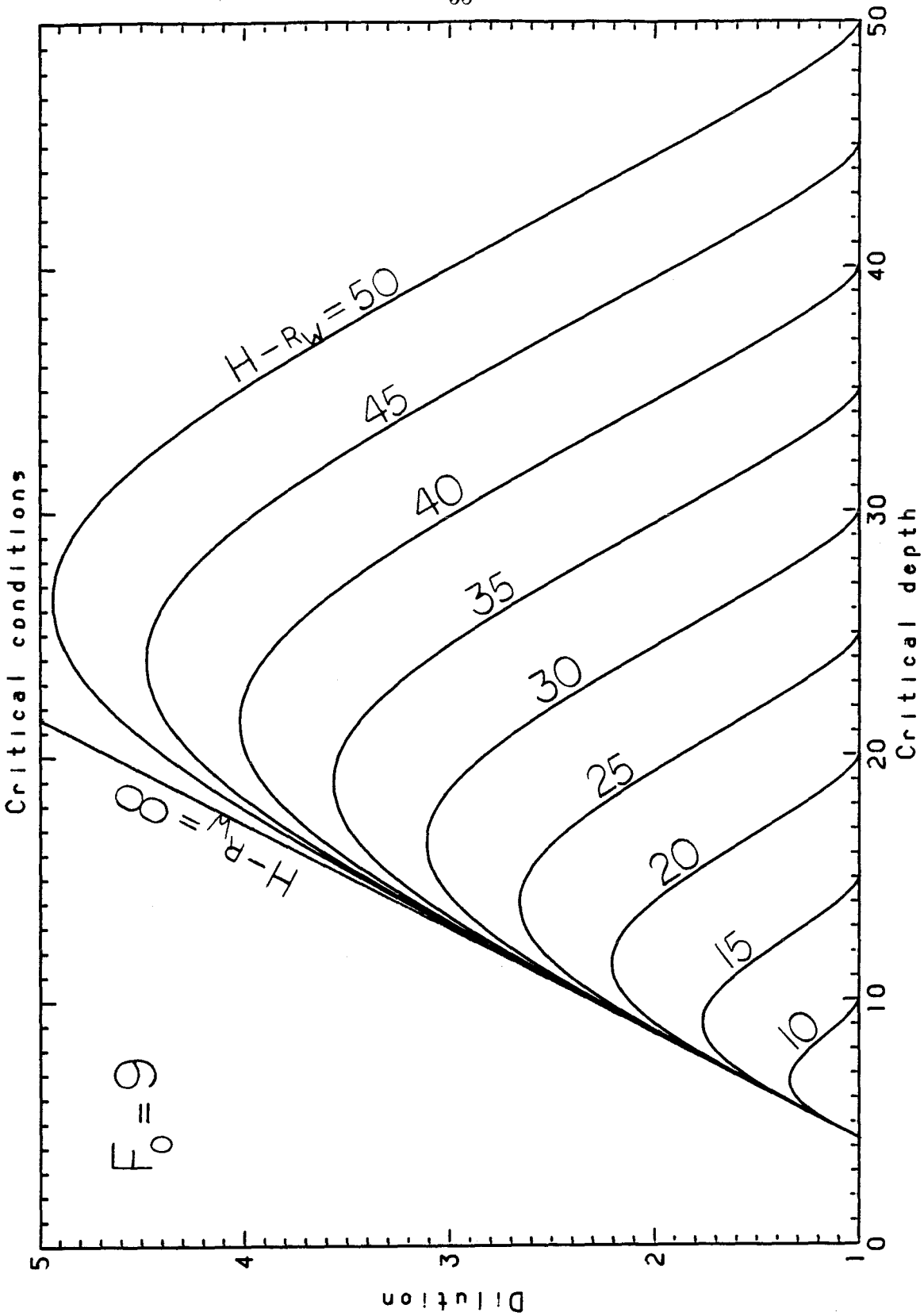

Figure 2.13: Example of critical conditions at the end of the channel.

factors, f_b, f_{wu}, f_{wl} and f_i, are known (constancy of these factors along the channel is assumed). Suppose that a free overfall acts as control at the downstream end (the extension to the case of the weir is straightforward and will be mentioned later). Suppose also that the discharge densimetric Froude number $\mathbf{F_0}$ is specified. Finally, suppose that L_j, the length of the jump region (distance between sections 0 and 1 in Figure 2.6), is known. Under these circumstances, the system of governing equations can be numerically integrated to obtain the downstream parameters r_1 and S.

The method is illustrated in Figure 2.14. (The parameters used for this example were $\mathbf{F_0} = 8.88$, $H = 26.6$, $B = 14.535$, $f_b = f_{wl} = f_{wu} = 0.037$, $\alpha = f_i/f_b = 1.3$, $L_j/h_0 = 54.874$, $l/h_0 = 721.5$.) The curve $r_c = r_c(S)$ was obtained solving Equation 2.24 as already discussed. The curve $r_{1u} = r_{1u}(S)$ of the possible upstream states was obtained solving Equation 2.22.

For every value of r_c, Equation 2.23 was integrated from ($\eta = 0$, $r = r_c$) to ($\eta = L_j/h_0$, $r = r_{1d}$). The curve of the possible downstream states $r_{1d} = r_{1d}(S)$ was therefore obtained. A Runge-Kutta scheme was employed to perform the integration.

It can be seen that only one point is both a possible upstream state and a possible downstream state. Such a point represents the unique hydraulic solution sought. The depth ratio across the jump, r_1, and the dilution attained in the mixing region, S, can be read off the graph. Now that S is known, it is possible to go back to Equation 2.23 and draw the entire interfacial profile in the gradually varied counterflow region.

In the example discussed above, a solution was found which satisfied both mixing zone and gradually-varied counterflow equations. This characterizes the occurrence of a free internal hydraulic jump, and the flow appears like the one sketched in Figure 2.1. But a perfect matching of the upstream and downstream equations is not always possible. The three flows described next illustrate this fact.

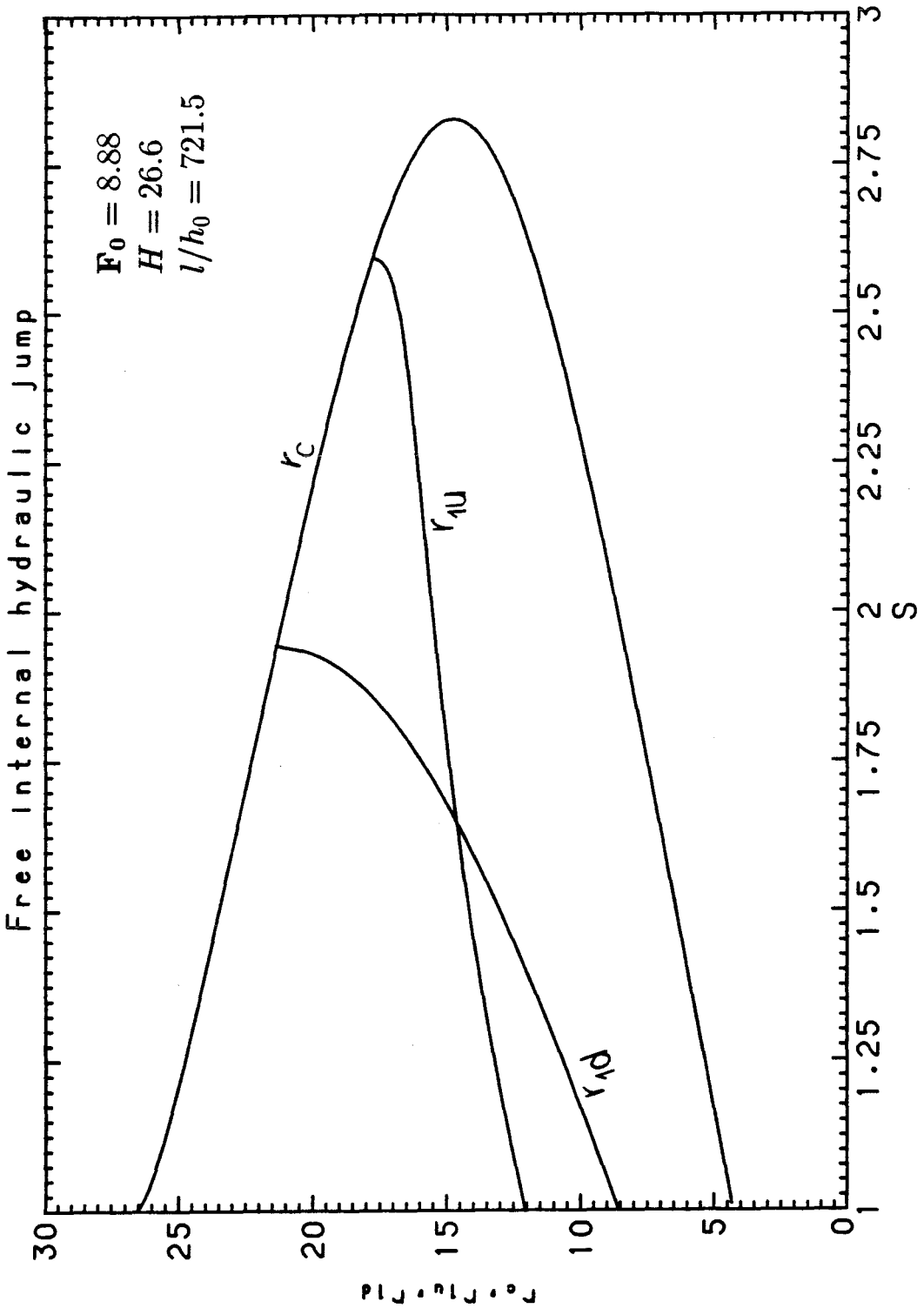

Figure 2.14: Example of a free internal hydraulic jump in the (S, r_1) plane.

Consider the same channel of the previous example, but suppose that now the discharge densimetric Froude number $\mathbf{F_0}$ is reduced to a smaller value ($\mathbf{F_0} = 3.21$ is considered as an example). Numerical solution of the governing equations yields the curves plotted in Figure 2.15. It can be seen that the depth r_{1d} expected at the end of the jump region from gradually-varied profiles is always higher than the conjugate depth of the mixing zone r_{1u}. A flooded internal hydraulic jump is expected to occur, with negligible entrainment of ambient fluid.

It is easy to realize that in order to drown a free jump such as the one described in Figure 2.14, two different routes can be taken. One way is by lowering the $r_{1u} = r_{1u}(S)$ curve, and this was just done by reducing $\mathbf{F_0}$. The other way is by raising the $r_{1d} = r_{1d}(S)$ curve, and this can obviously be done by introducing a weir at the channel end (the resulting flow, if the weir is tall enough to flood the source, is the flow shown in Figure 2.2).

The third possible type of flow is now analyzed. Consider, once again, the channel of the two previous examples. Suppose, however, that the discharge densimetric Froude number $\mathbf{F_0}$ is larger than previously assumed ($\mathbf{F_0} = 13.68$ is used in this example). In this case the numerical solution of the governing equations gives the curves plotted in Figure 2.16. A situation just the opposite of the case of the flooded jump is occurring: the depth r_{1u} expected from the mixing region analysis is always higher than the depth r_{1d} expected from the gradually-varied counterflow profiles.

It is argued by Baddour (1987) that, under such circumstances, what is referred to as an upstream-controlled unstable flow will take place. The transition from the unstable type of mixing zone sketched in Figure 2.3 and the gradually-varied counterflow is likely to occur through a critical section, with the critical depth corresponding to the upper critical depth r_{c2} mentioned before (Baddour, 1987; Jirka and Harleman, 1979; Righter, 1970). If this is the case, the nondimensional depth after the

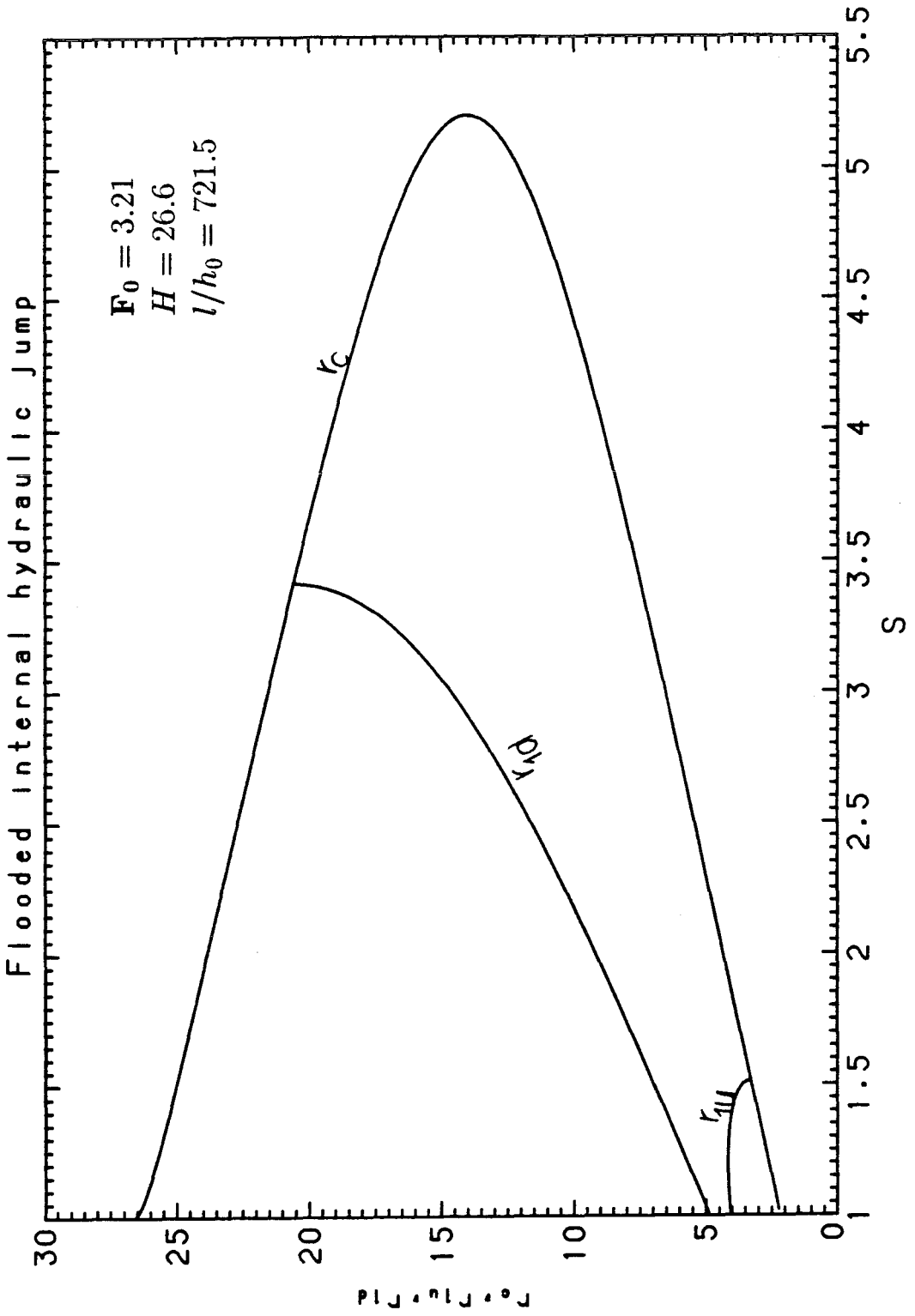

Figure 2.15: Example of a flooded internal hydraulic jump in the (S, r_1) plane.

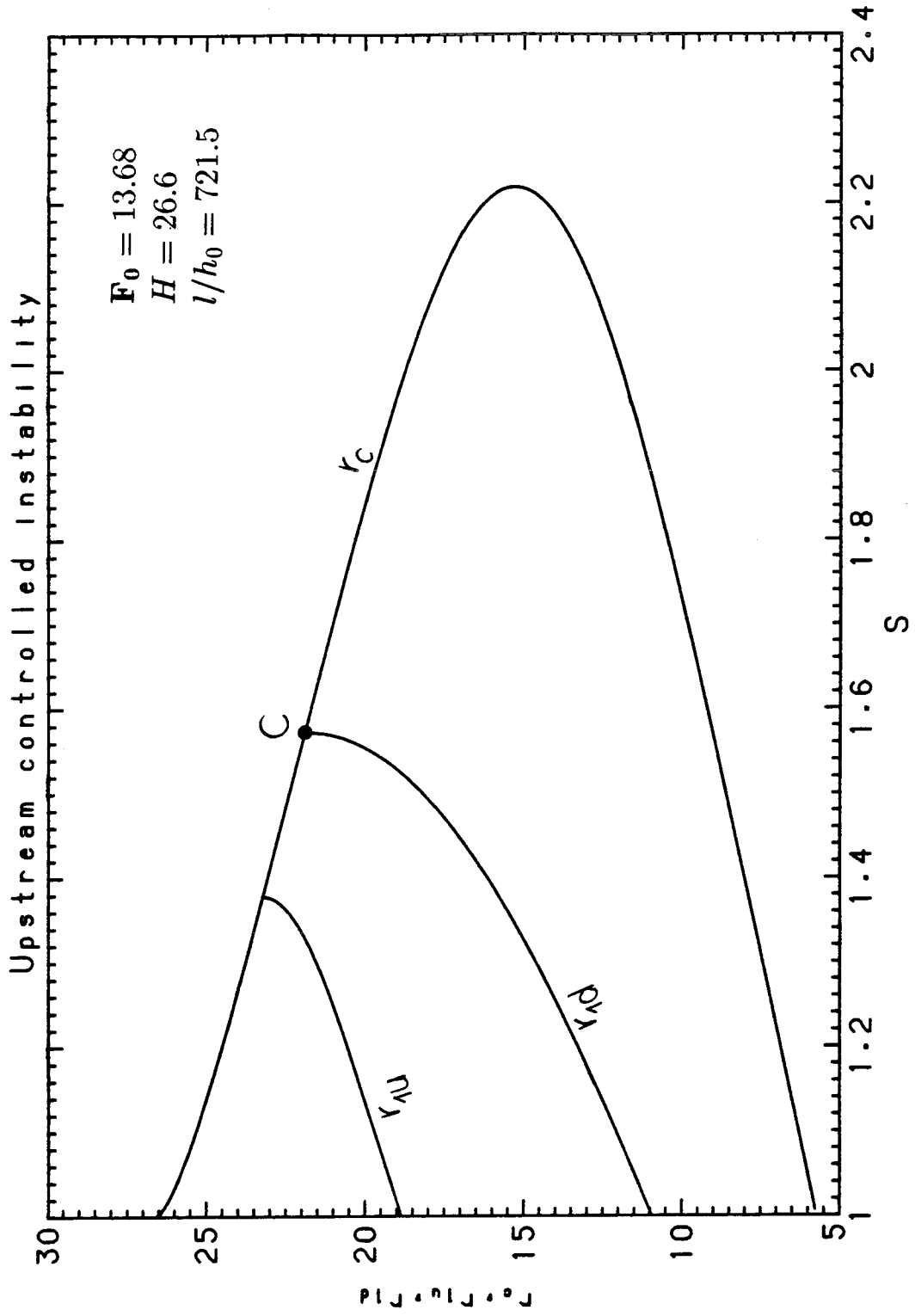

Figure 2.16: Example of an upstream-controlled unstable flow in the (S, r_1) plane.

jump, r_1, and the dilution, S, can be read off the graph from the critical point C.

The last type of flow that can take effect in a mixing channel is called a downstream-controlled unstable flow. Suppose that the discharge densimetric Froude number $\mathbf{F_0}$ is so large that the entire depth of the two-layer flow, d, is completely occupied by source fluid in some region near the source. This situation is sketched in Figure 2.4. Since the entrainment of ambient fluid into the mixing region is blocked, the dilution S is equal to one. Then, the critical depth over the overfall is immediately found using Equation 2.37, and Equation 2.23 can be directly integrated.

If the hypothesized downstream-controlled instability does indeed occur, it will be found that the interfacial profile obtained by integrating 2.23 will attain the free surface before the source region is reached. For instance, consider the same channel used in the previous examples, but suppose that the discharge densimetric Froude number is very large (e.g., $\mathbf{F_0} = 60$). The interfacial profile obtained integrating Equation 2.23 with $S = 1$ is shown in Figure 2.17. It can be seen that the free surface is reached by the interface at $\eta \simeq 270$, well before the upstream end of the channel (at $\eta = l/h_0 = 721.5$) is reached. The flow structure is entirely governed in this case by the downstream control and the shear stresses in the channel, and this justifies the name of downstream-controlled instability.

Several comments on the previous discussion are in order.

First of all, it is stressed that the described methodology is general. It can be applied to different channels and with discharge conditions different from the ones used in the examples. The examples were used only for clarity of presentation.

If the downstream control is a broad-crested weir instead of a free overfall, Equations 2.29 and 2.30 are to be used in place of Equation 2.24. However, the discussion of the way in which upstream and downstream equations interact still holds, and the same four types of flow can be predicted.

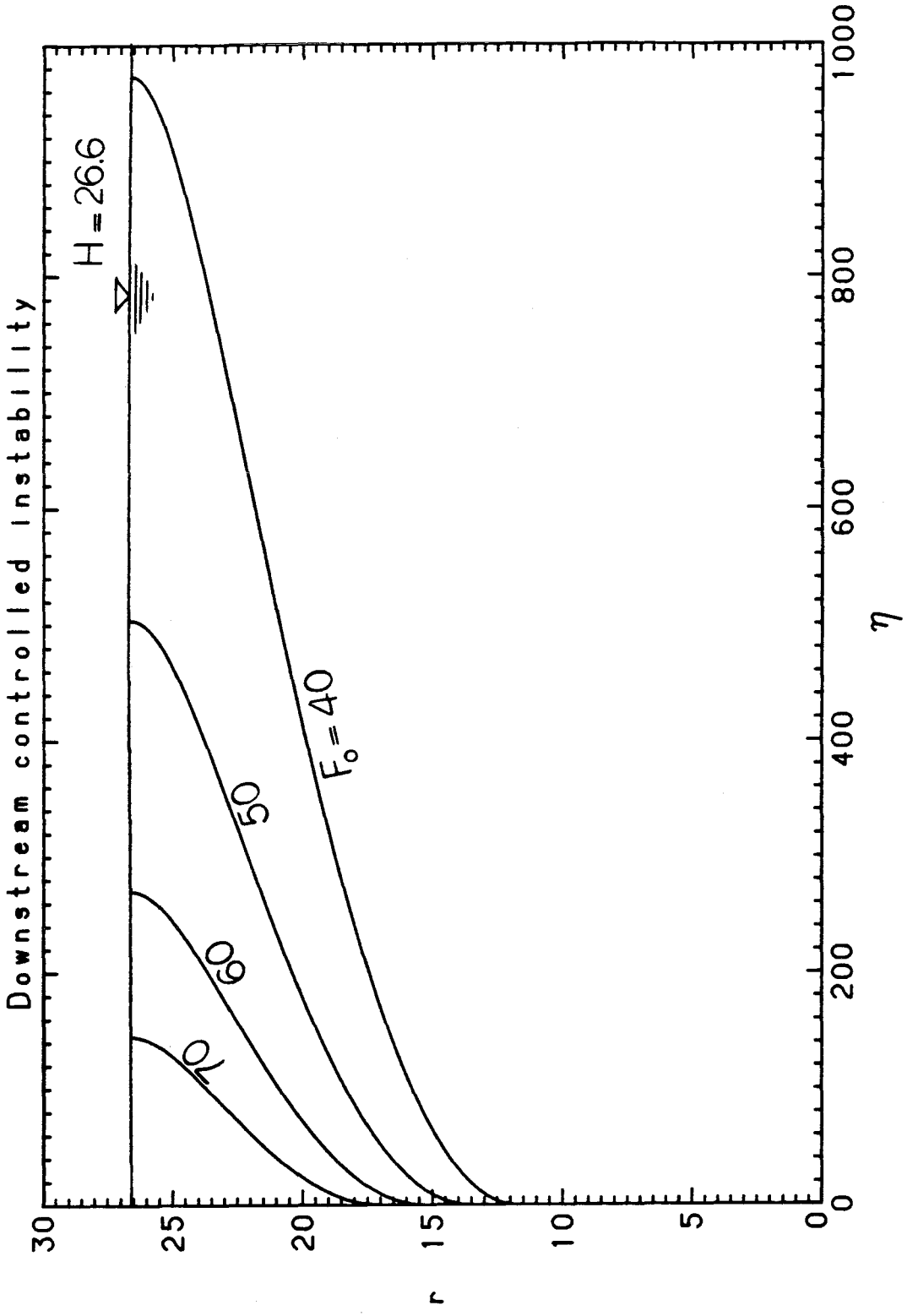

Figure 2.17: Interfacial profiles with downstream-controlled unstable flows.

Finally, it is pointed out that the knowledge of the length of the jump region, L_j, was assumed. In general, however, such length is not known a priori. The momentum equation, Equation 2.22, related the conjugate states across the jump, without providing any information about the details of the development of the flow in the entraining region and in the roller region. A sensitivity analysis was conducted to see whether the length of the jump region affected the flow in an important way. As it should be expected, the dependence of the solutions on L_j was found to be very weak, since the slope of the interfacial profile in the gradually-varied counterflow is very small far away from the downstream control. This implies that an error in the choice of L_j only slightly shifts the $r_{1d} = r_{1d}(S)$ curves. The sensitivity of the solutions to the length of the jump region is indeed so limited that previous investigators (e.g. Baddour, 1987) assumed $L_j = 0$, i.e., the matching of the upstream and downstream flows was assumed to take place at the source. An improvement to this approximation, involving an empirical relation between L_j and $\mathbf{F_0}$, is discussed in Chapter 4, and a way to accurately predict L_j is discussed in Chapter 6.

2.5 Concluding remarks

Given a rectangular horizontal mixing channel of specified characteristics (depth, length, width, friction factors and downstream control), for each set of discharge conditions (flowrate, discharge depth and density) a method is available to

- predict the qualitative flow characteristics; in particular, predict which one of the four possible mixing modes will occur (free or flooded internal hydraulic jump, upstream- or downstream-controlled instability);
- predict the dilution that will take place in the dense lower layer, and draw the interface between the two layers along the whole subcritical flow region.

The weaknesses of the method are basically two:

- it is a one-dimensional approximation, and, as such, it will be acceptable as long as the cross-sectional variability of velocity and density in the subcritical flow region is limited (this point will be discussed at length in Chapter 5);
- it does not describe the details of the development of the mixing region (buoyant jet theories, however, have been shown to be unsuitable to study this type of problem).

On the other hand, the method represents the best available tool to study mixing channels, since

- it fully recognizes the importance of the interaction between the source and the downstream control in determining the flow structure;
- it explicitly accounts for the effect of the limited depth of the channel, and the resulting counterflow;
- it includes in the analysis boundary friction, which is likely to be an important factor in prototype applications;
- it is relatively simple to use, and it can be applied, with small modifications, with every type of downstream control.

The validity of the predictions will be tested in a laboratory flume. Such tests will be the object of the following chapters.

Chapter 3

Experimental setup and procedure

3.1 The flume

All the experiments were performed in the flume shown schematically in Figure 3.1, which was built in the laboratory specifically for this investigation. From the salt water inlet to the free overfall, it is approximately 5 m long, 67 cm deep and 10 cm wide and it extends for an additional 1.7 m length if the salt water inlet and the chambers after the free overfall are included. These chambers consist of a rectangular box, $50 \times 85 \times 10$ cm, used to collect the mixed fluid from the dense lower layer, and a reservoir, $80 \times 67 \times 60$ cm, used to establish and maintain a constant depth of ambient fluid in the flume.

The test channel is constructed from 1/2 inch Lucite sheeting and was built inside a 60 cm wide steel-framed old flume, which provided the table on which the Lucite channel rests. Precision rails run the whole length of the steel flume, so that instrument carriages can be freely moved along the channel. Supports with adjustable screws were placed between the bottom of the Lucite channel and the bed of the old flume. This enabled the test channel to be made horizontal with great precision.

The test channel bottom and side walls were found initially to exhibit slight but measurable non-uniformities. These were caused by variations in the thickness of the Lucite, as well as by deflections of the side walls under the hydrostatic water pressure.

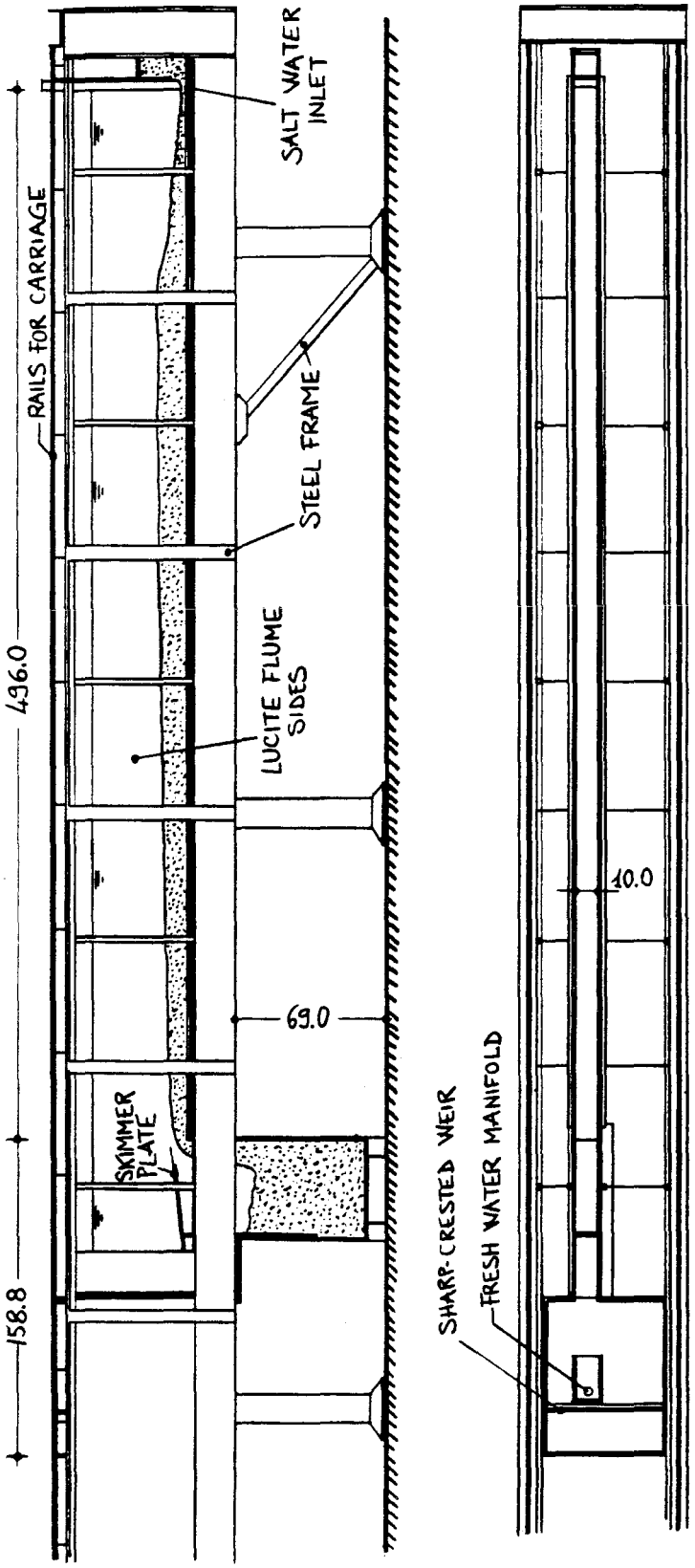

Figure 3.1: Sketch of the experimental flume (dimensions in cm).

This problem was partially corrected with the above-mentioned adjustable supports and a number of lateral struts tightened against the supporting flume, leaving very small departures from ideal uniform conditions. The bottom elevation varied along the channel by less than 1.5 mm and the width variations were everywhere below 2% of the entire channel width.

The salt water inlet consisted of an adjustable gate with a rounded entrance (see Figure 3.2). The radius of curvature of the gate was approximately 4 cm, and, so far as could be detected, no contraction of the flow occurred beyond the gate.

Only one discharge depth, $h_0 = 0.688$ cm, was used in the experiments, as it was found more convenient to vary flowrates and density differences rather than move the gate up and down when a change in discharge conditions was desired. (This also made the comparison between experimental data and theory easier, since all the lengths in the non-dimensional equations have been normalized using h_0.)

A detail of the downstream end of the test channel is shown in Figure 3.3. As mentioned before, broad-crested weirs of different heights were used ($h_w = 4.90$, 3.65, 2.34, 0.99 and 0.00 cm, the last one being the limiting case of the free overfall).

A skimmer plate with a sharp end in the front, also made from Lucite, could be set in any desired position by translating and rotating the plate itself or by moving the adjustable gate up and down. The plate was then temporarily sealed by spreading grease on its sides and then pressing the channel walls against it by tightening the lateral struts. This method, while preventing leaks completely, allowed frequent and easy changes in the plate's position. The flowrate withdrawn from the bottom of the vertical box could be varied continuously, so that any desired flowrate could be withdrawn under the skimmer plate.

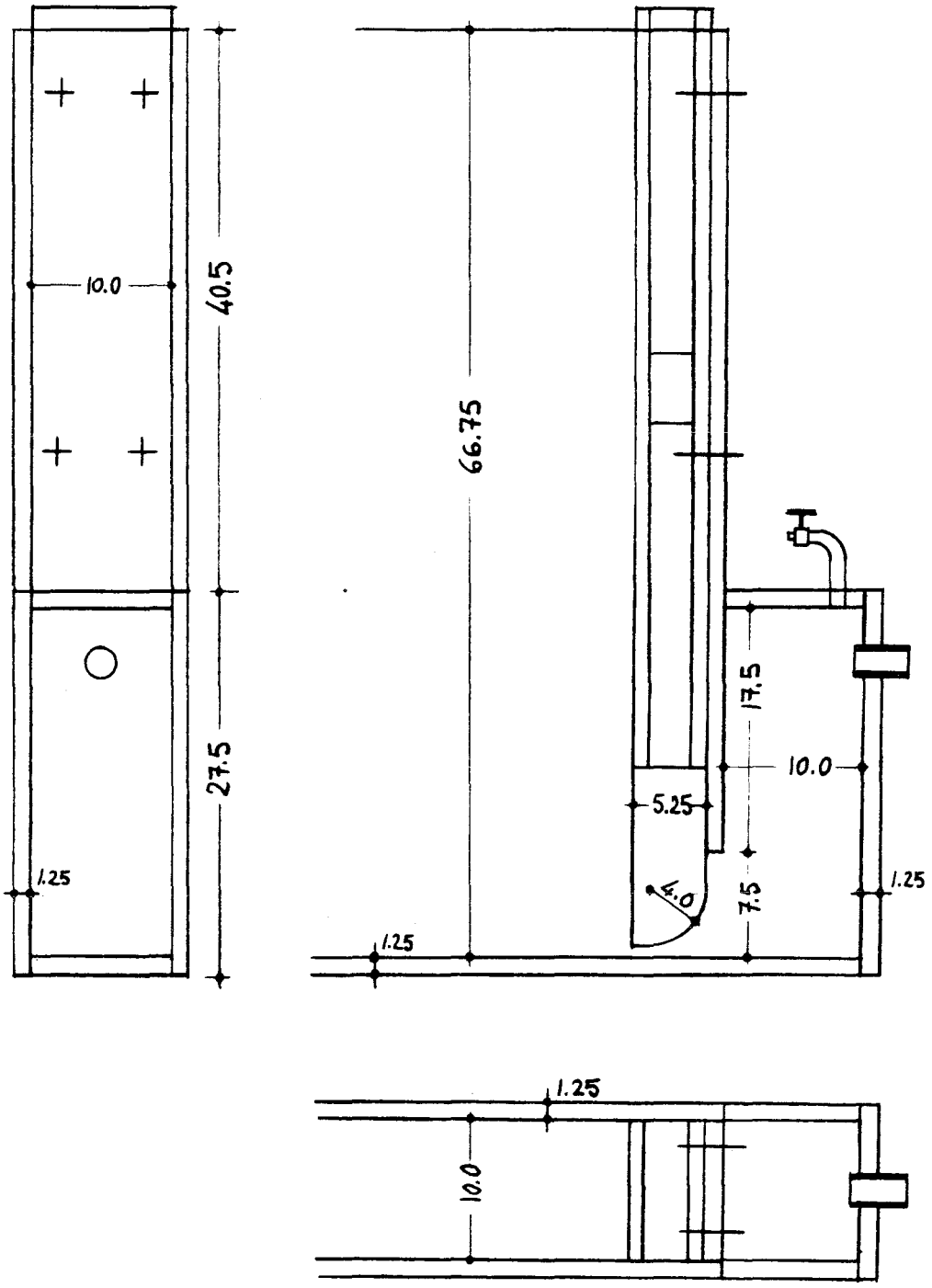

Figure 3.2: Salt water inlet (dimensions in cm).

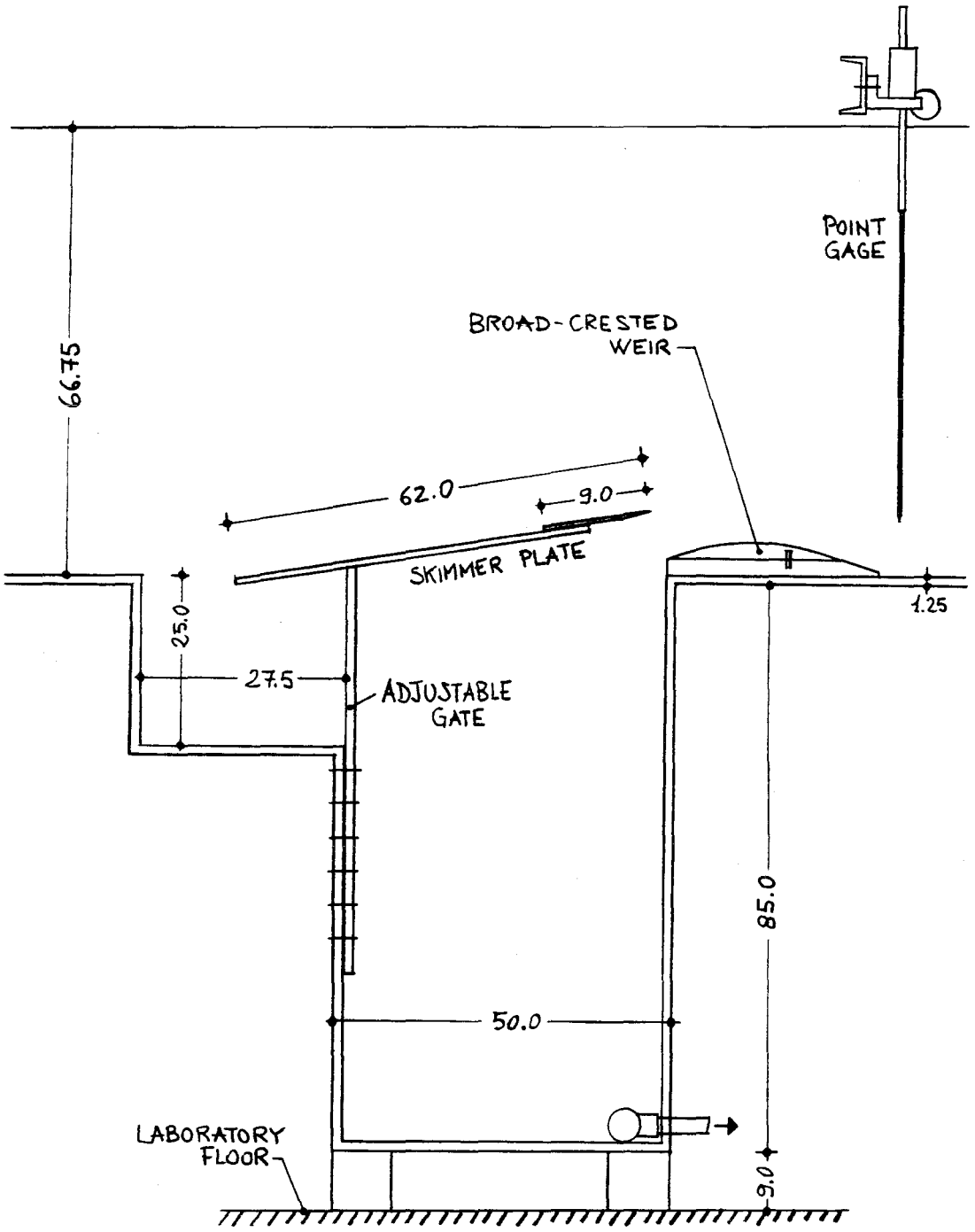

Figure 3.3: Downstream end of the test channel

3.2 Flow generation apparatus

The general flow system is sketched in Figure 3.4. The fresh water supply system comprised a mixing tank with capacity of about $2\,m^3$, which could be filled with filtered laboratory water. If necessary, ethyl alcohol could be added in the desired amount and mixed by injecting air into the tank bottom (addition of alcohol was necessary in the laser experiments, as explained later). The fresh water was then pumped up to a constant head tank located near the laboratory ceiling. Then it passed through a valve and a flowmeter, and entered the flume through a PVC manifold, specifically designed to minimize any disturbance to the test channel flow. For clarity of presentation, the rate of fresh water inflow will be denoted by Q_f.

The salt water system was similar to the fresh water supply. A mixing tank with a capacity of about $1\,m^3$ was used to dissolve the desired amount of salt. The salt water was then filtered and pumped up to a constant head tank from which it descended to the flume, passing through a valve (which could be adjusted to obtain the desired discharge flowrate Q_0), a flowmeter, a rectangular region behind the discharge gate, and finally through the inlet previously described.

Water could leave the flume in two ways. First, excess water would fall down a sharp-crested weir, thus ensuring constancy of ambient water depth in the flume. The height of the weir could be easily modified; water depths of $52.7, 22.7, 18.3, 13.4$ and 10.5 cm were used in the experiments.

Second, a mixture of salt and fresh water was withdrawn from the box below the skimmer plate. The mixture, whose flowrate Q_s could be continuously varied by means of a valve, passed through a flowmeter and then through a PVC pipe, which ended in the laboratory pit, approximately 3.5 m below the level of the flume bottom.

For any chosen values of Q_0 and Q_s, the supply of a fresh water at a flowrate

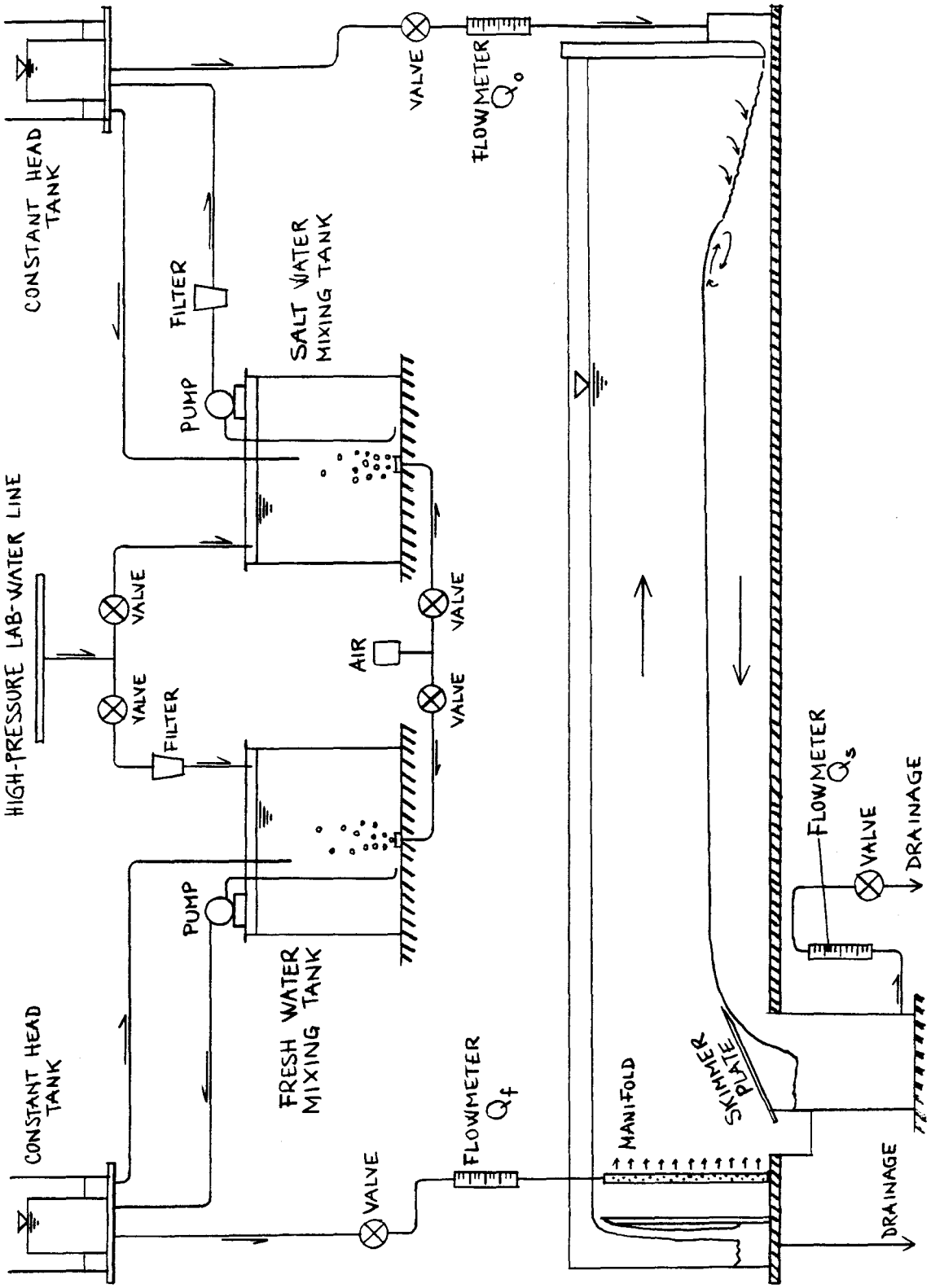

Figure 3.4: General flow generation system.

$Q_f > Q_s - Q_0$ ensured the establishment of a steady flow in the channel. Steady flow could be maintained until either one of the mixing tanks was empty. This posed an upper limit on the duration of the experiments.

Three calibrated precision bore flowrates were used to measure the salt water discharge flowrate, Q_0, the fresh water flowrate, Q_f, and the withdrawn mixed water flowrate, Q_s (see Figure 3.4). The calibration curves for flowmeters Q_0 and Q_s are shown in Figures 3.5 and 3.6 respectively.

More details of the system operation will be given in the description of the experimental procedure.

3.3 Measurement techniques

3.3.1 General considerations

Several techniques were employed to gain information on the flows generated in the experimental flume.

Flow visualization, by premixing of blue dye with the salt water, enabled much insight to be gained by simple observations. Additional qualitative data were obtained from photographs of many flows.

A point gage, mounted on a small carriage that could be moved on rails along the whole flume, was used to measure visually both layer thicknesses and ambient water depths. A very thin rod (diameter $\approx$ 2 mm) was used to minimize flow disturbance by the gage.

Laser-Doppler velocimetry and a laser-induced fluorescence technique were employed for detailed, non-intrusive measurements of the flow velocity and density distributions. The next two sections are devoted to a description of the experimental apparatus used for these laser-based techniques.

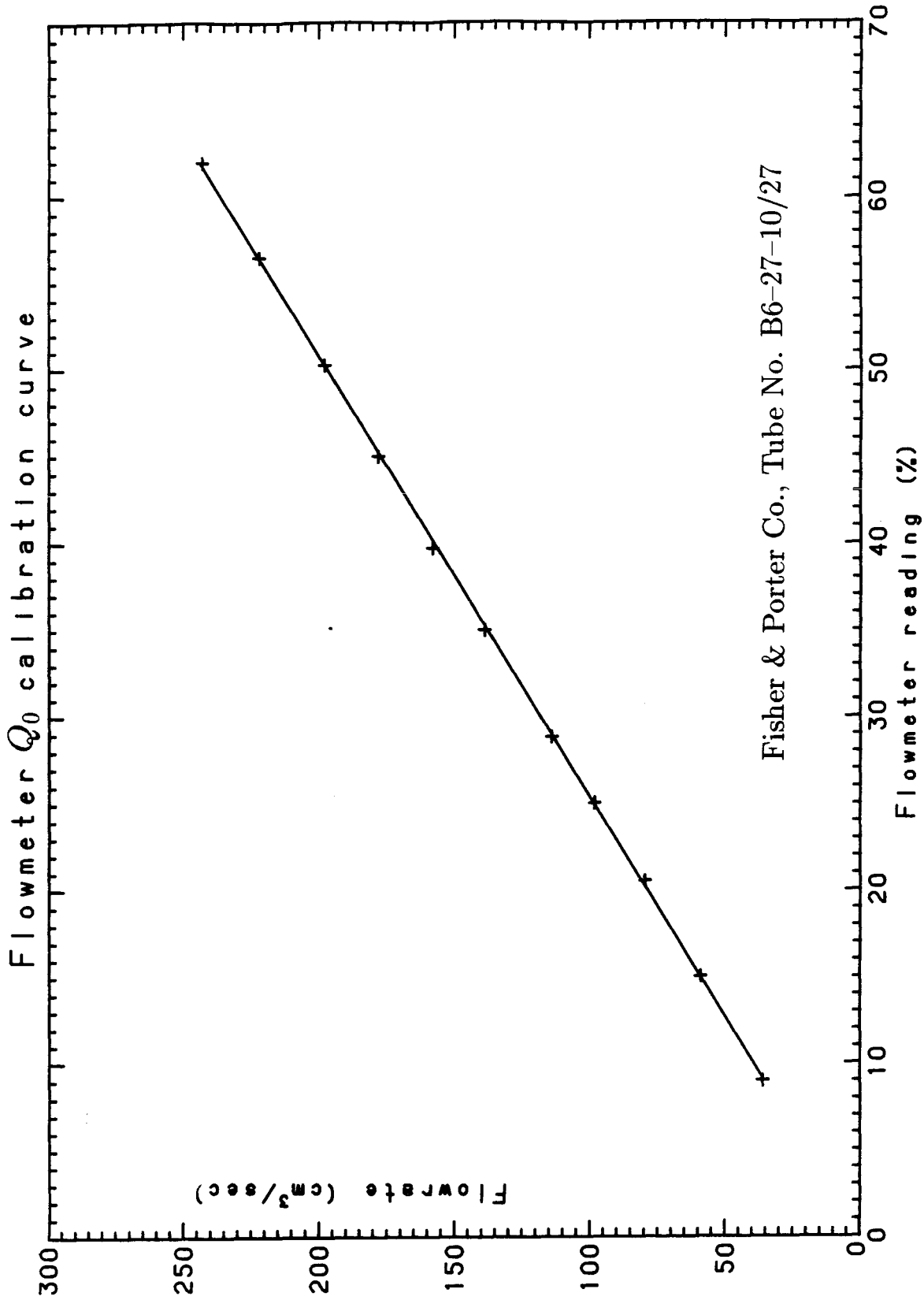

Figure 3.5: Calibration curve for flowmeter Q_0.

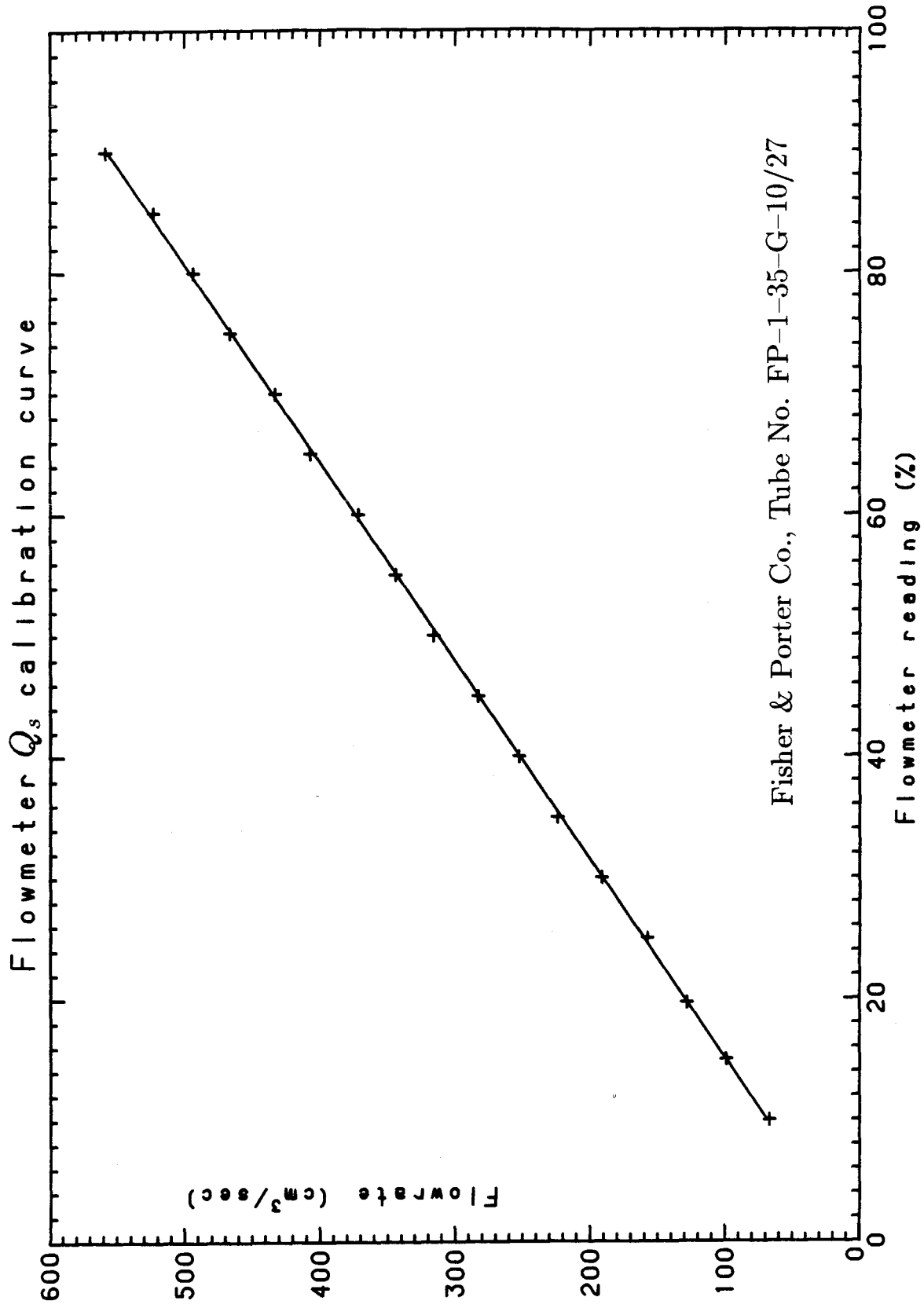

Figure 3.6: Calibration curve for flowmeter Q_s.

3.3.2 Laser-Doppler velocimeter system

A laser-Doppler velocimeter was used to measure the horizontal velocity component along the channel. The emitting and receiving optics for the LDV were mounted on an instrument carriage, built in the laboratory for this purpose. Sketches describing the carriage are presented in Figures 3.7 to 3.10. The carriage consists of two main frames, constructed from $3 \times 3 \times \frac{3}{16}$ *in* square aluminum tubing. The 'movable' frame, on which the optics are bolted, can be vertically translated so as to allow the laser beam to span the entire vertical extent of the flume. The 'fixed' frame, supported by roller bearings, can move on rails along the whole flume in the longitudinal direction.

The two frames are connected by means of three precision travel, linear stages (manufactured by DEADAL, Inc.), and can slide with respect to each other. The displacement is controlled by two large threaded rods mounted on worm gear screw jacks (manufactured by Linear Industries, Inc.).

The LDV uses a 7 mW He-Ne laser (Hughes model 3227H-PC), which emits monochromatic linearly polarized light with a wavelength of 6328 $\mathring{A}$. The light of the laser beam has a Gaussian distribution normal to the beam axis and the $1/e^2$ beam diameter is 0.80 mm. A reference beam system is used.

The general optical layout is sketched in Figure 3.11 and the details of the emitting optics are shown in Figure 3.12. The laser beam is split (90%–10%) using a prism and the two resulting beams are directed by a mirror and a 400 mm focal length converging achromatic doublet to intersect in the middle plane of the flume. A 1^0 wedge prism is used to make the reference beam parallel to the scattering beam.

In order to discriminate the flow direction, the frequencies of the laser beams are shifted by approximately 86.55 KHz using two 40 MHz Bragg cells (Coherent

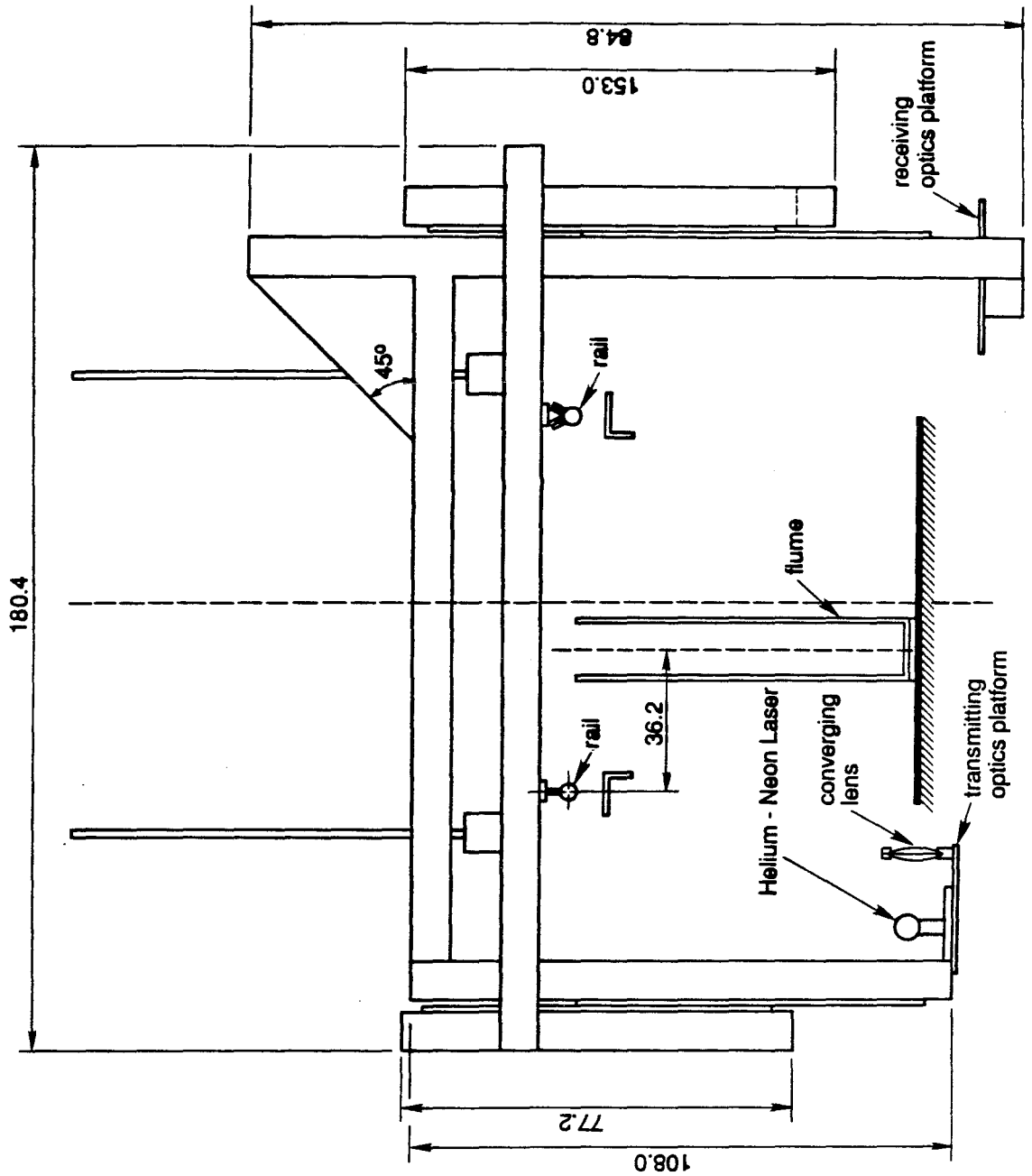

Figure 3.7: Instrument carriage. Elevation (dimensions in cm).

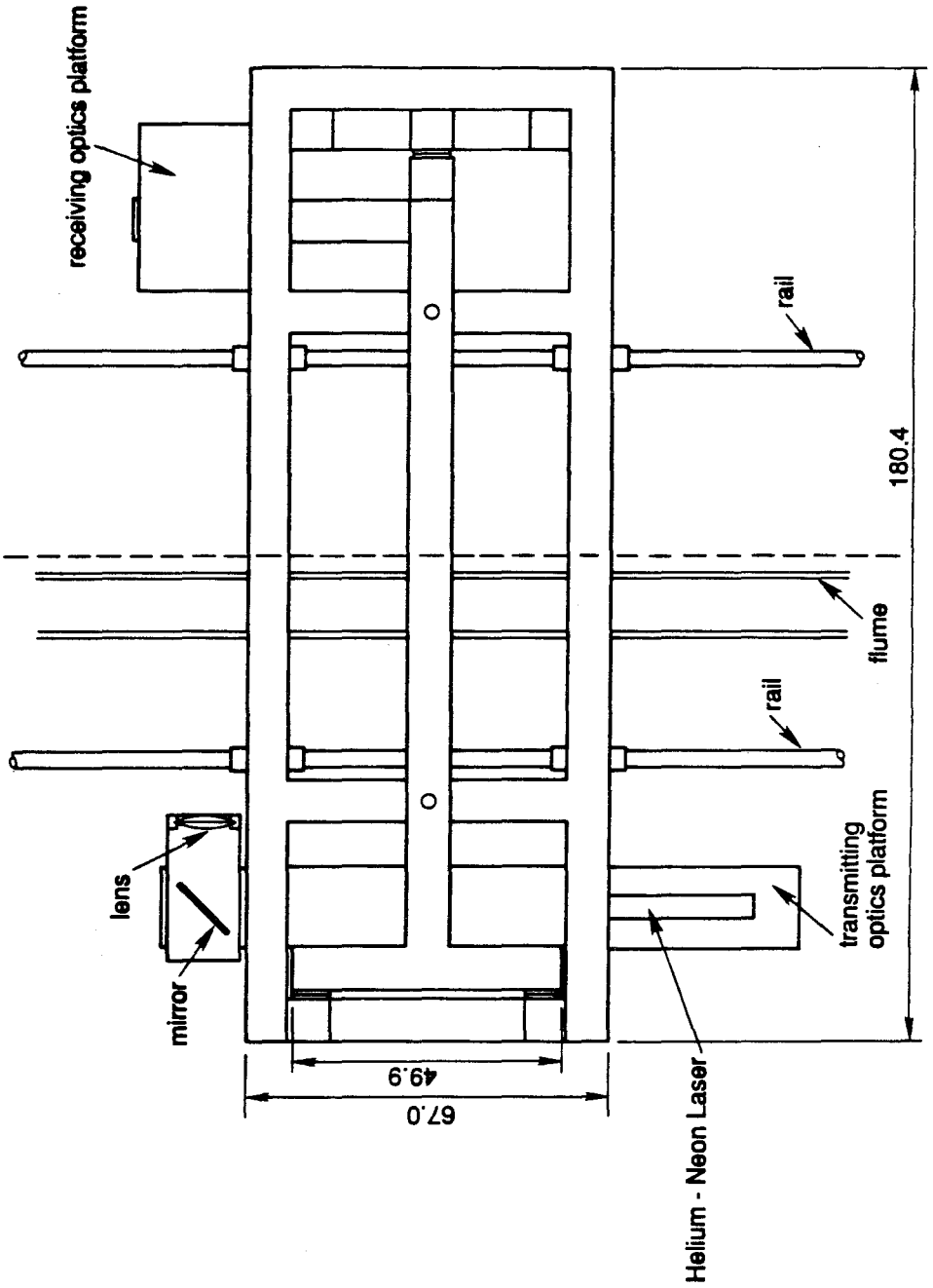

Figure 3.8: Instrument carriage. Plan view.

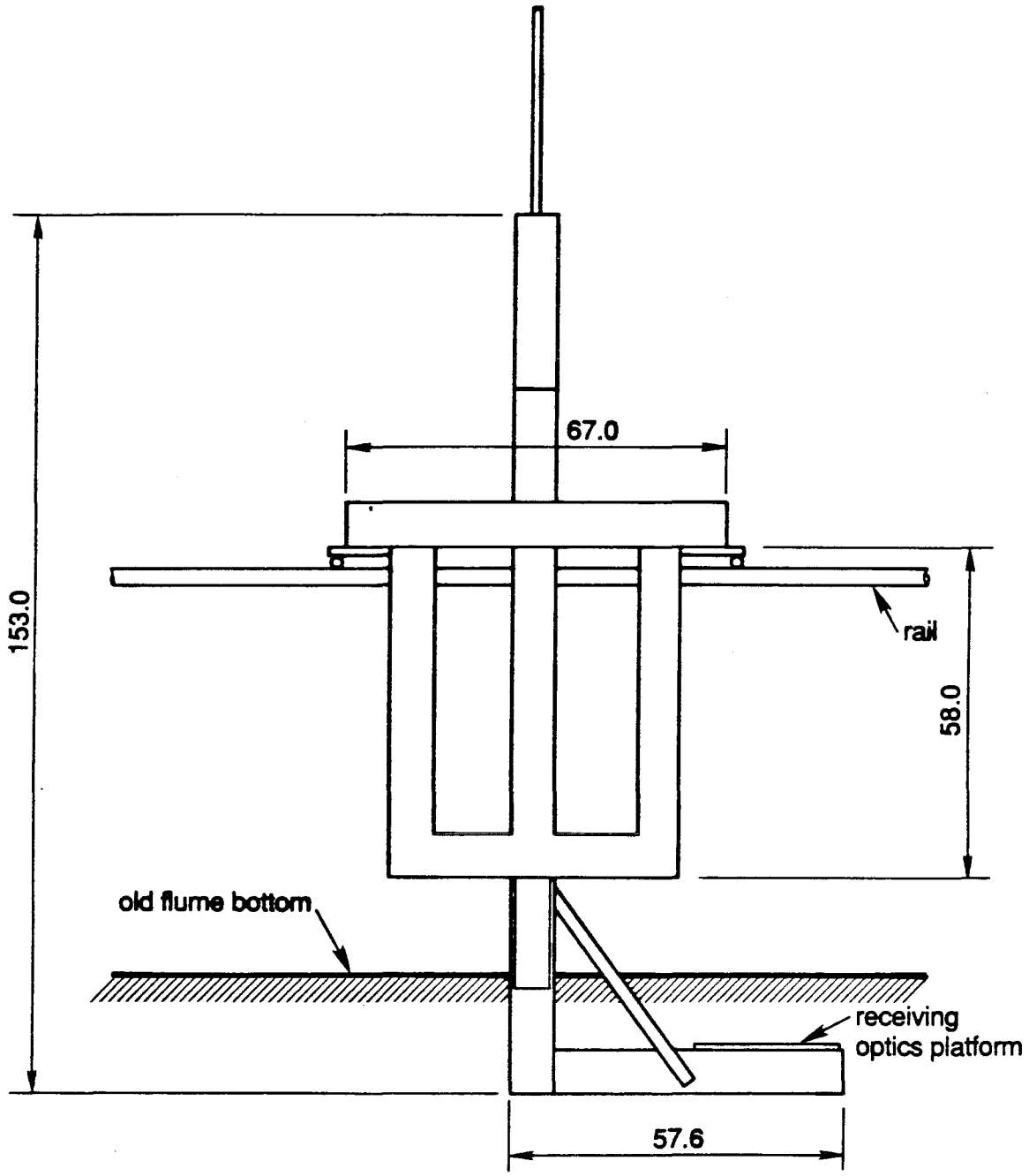

Figure 3.9: Instrument carriage. Side view.

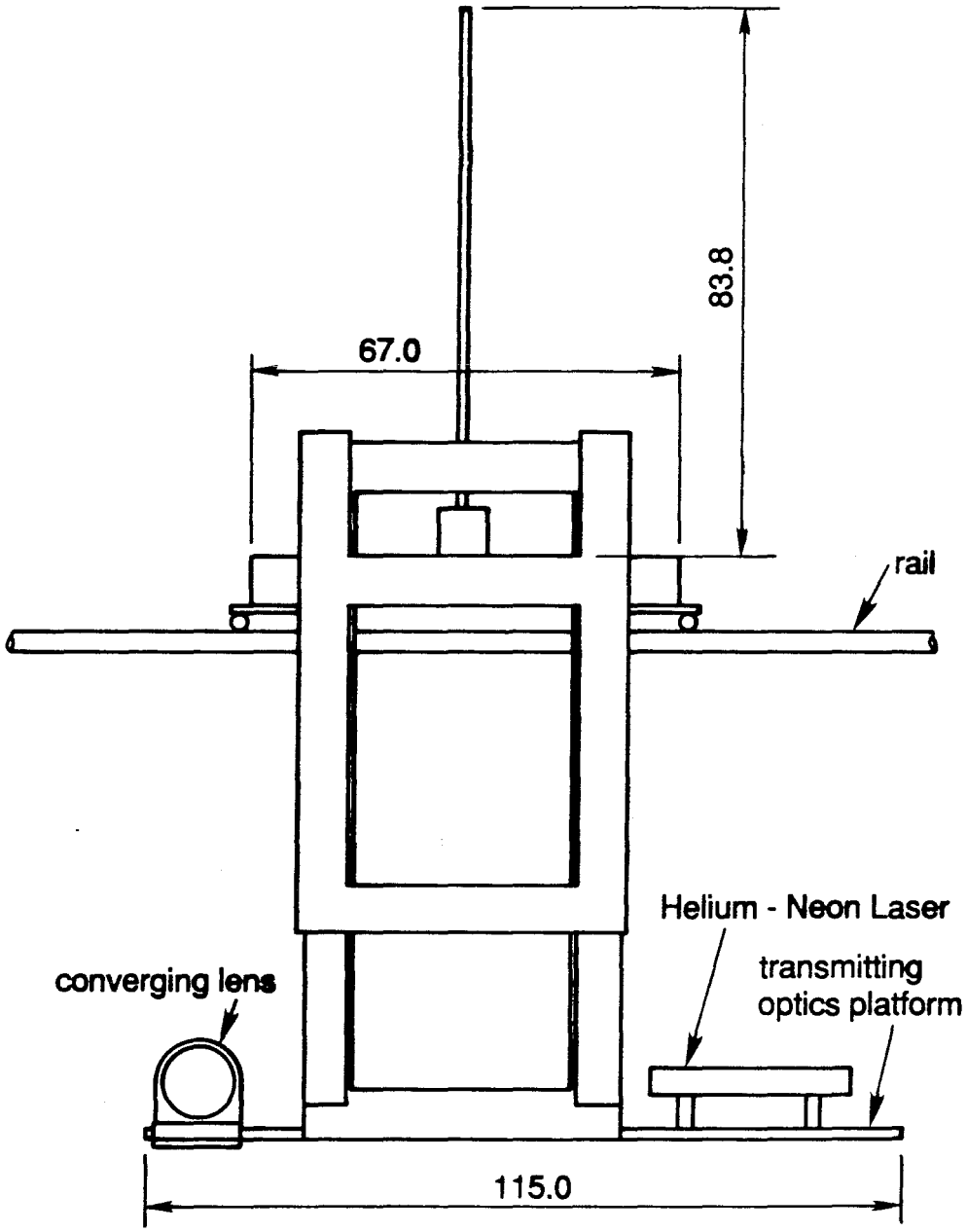

Figure 3.10: Instrument carriage. Side view.

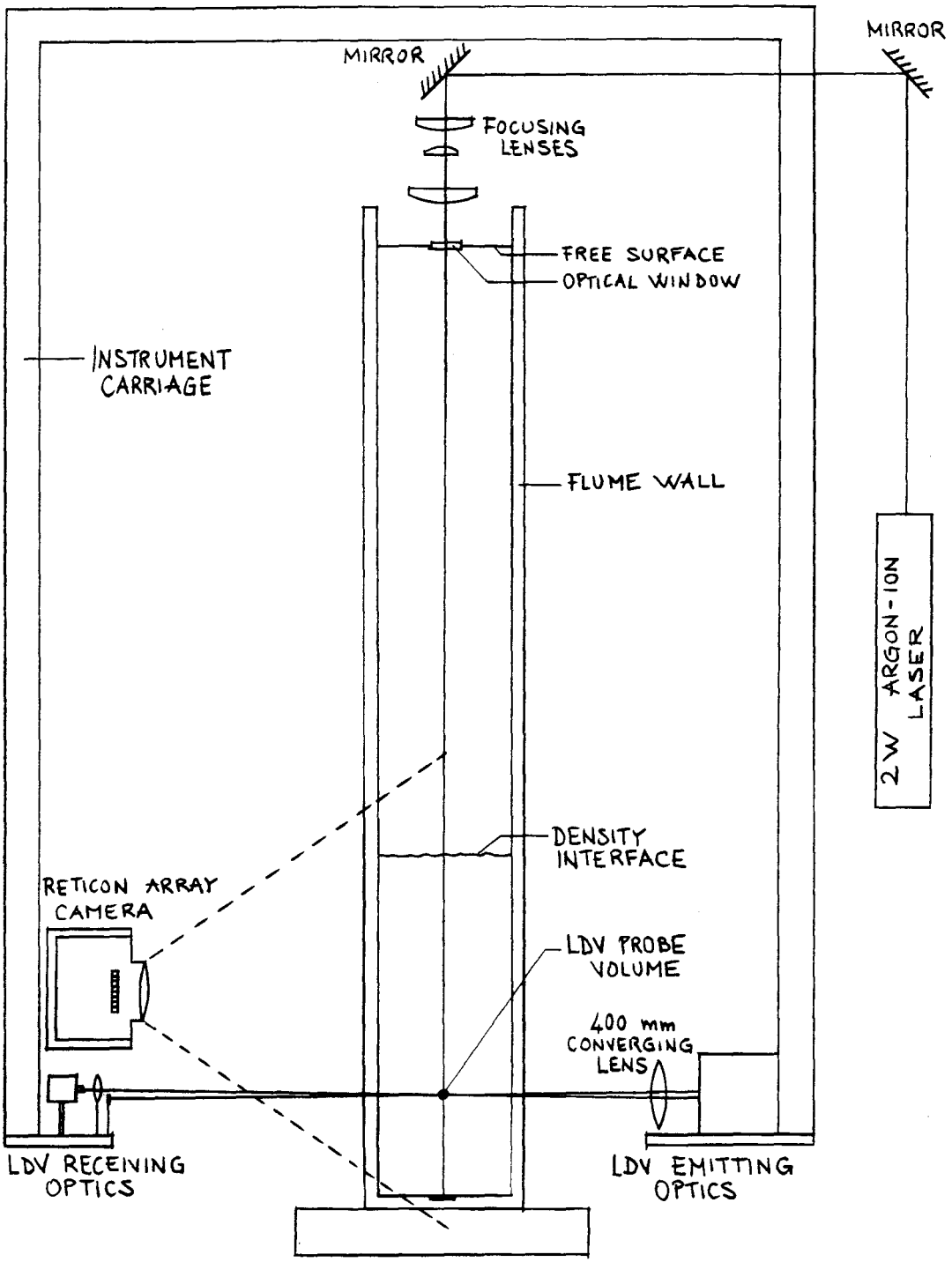

Figure 3.11: General optical layout.

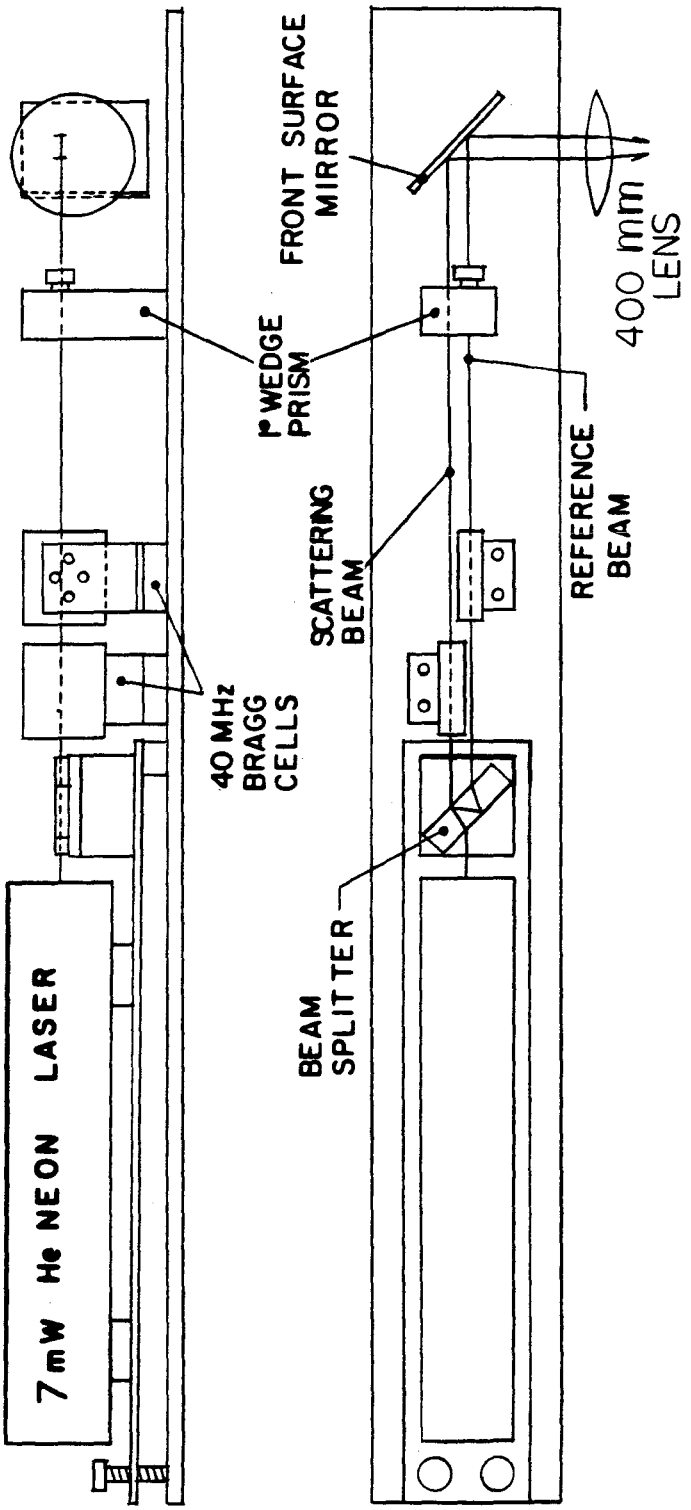

Figure 3.12: LDV emitting optics.

model 305). The amplifiers used to drive the Bragg cells are model 300L RF broad-band power amplifiers manufactured by Electronic Navigation Industries, Inc.. The Doppler shift obtained is 724.5 Hz/(cm/s).

Other details of the optical setup can be found in Papanicolaou (1984), although some important changes have been introduced to adapt the LDV system to the new flume. More specifically, the emitting and receiving optics are closer to one another than they were in the tank used by Papanicolaou (1984), the converging lens has a smaller focal length and the vertical component of velocity has not been measured in this study.

The angle formed by the two beams in air has been accurately measured to be $\theta_{air} = 2.636^0$. The approximately ellipsoidal focal volume is estimated to have minor and major diameters of ≈ 0.1 mm and ≈ 4.3 mm, respectively.

The reference beam and the light scattered by the particles in the water are focused onto a fast response silicon photodiode (EG&G type DT-25) using a 125 mm converging lens as shown in Figure 3.13. The amount of particles present in the laboratory water supply system was adequate for velocity measurements. No addition of seed particles was necessary. The laboratory water was filtered using commercial filters (Sears) that trapped large particles present in the water supply. Detailed characteristics of the particles present in the laboratory water supply are discussed in Papanicolaou (1984).

The preamplified signal output of the laser-Doppler receiving photodiode is fed to a laboratory-built signal processor. The signal processor is of the counter type and includes electronic circuitry for the detection of Doppler bursts. A schematic of the signal processor and of the data acquisition system is shown in Figure 3.14. The raw signal from the photodiode is amplified and band-pass filtered (Kron-Hite model 3202 filter) at 76 and 96 KHz. The filtered signal is then fed to two parallel

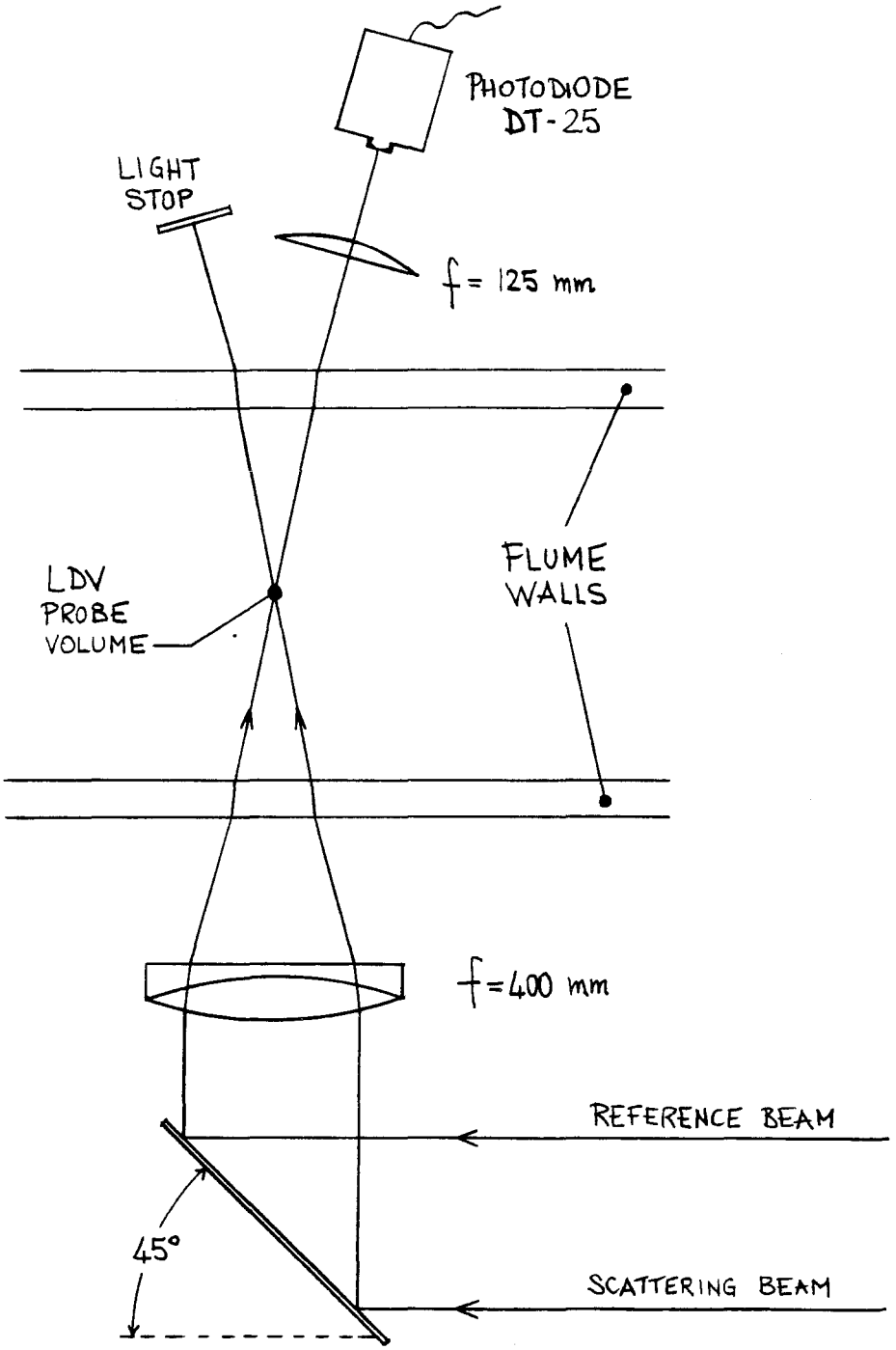

Figure 3.13: LDV optics. Plan view.

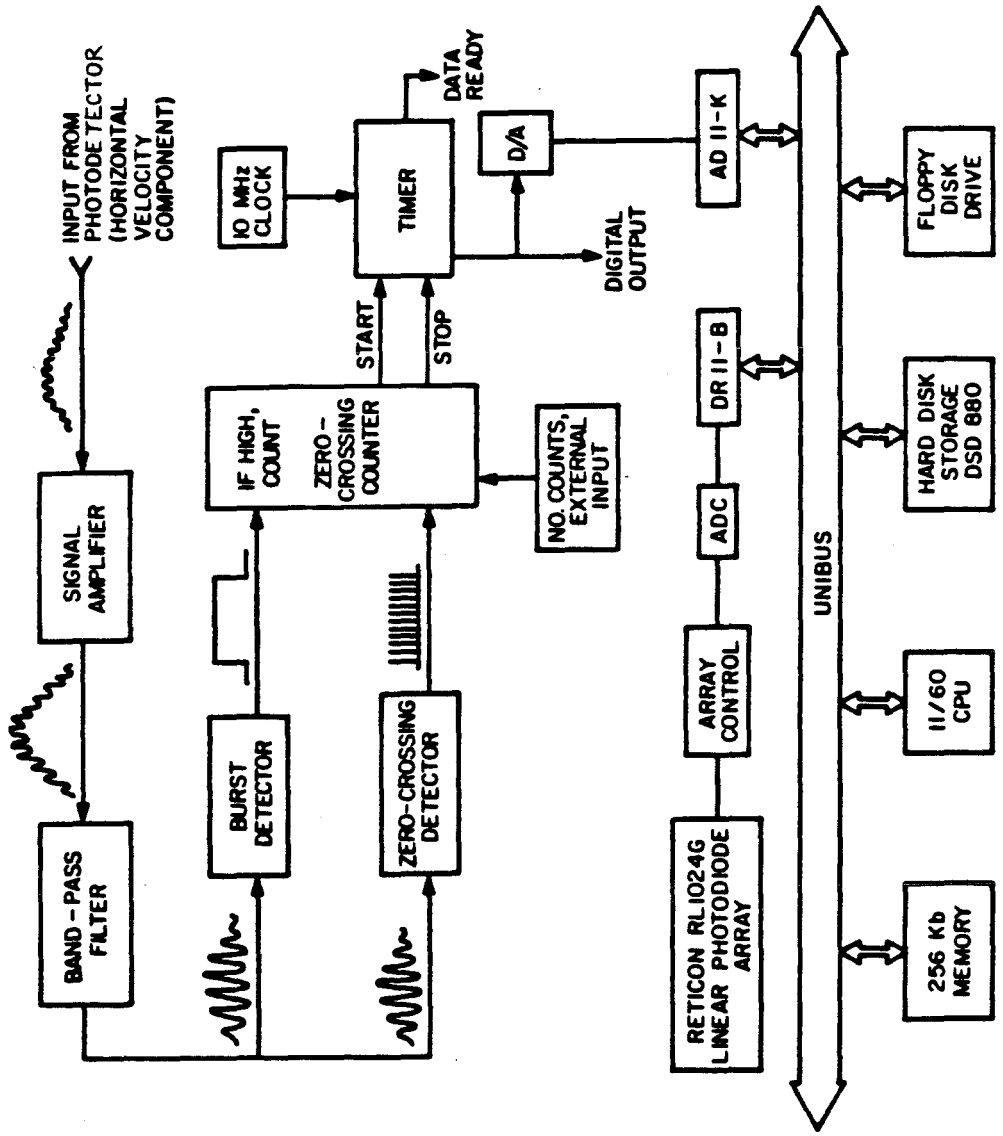

Figure 3.14: Schematic of signal processor and data acquisition system.

circuits: the first circuit is a zero crossing counter, while the other parallel circuit is a validation circuit that reinitializes the counting if the signal falls below a certain preset threshold. This ensures that the only signals considered are those due to particles passing in the central region of the probe volume. Details of the signal processor can be found in Gartrell (1979). The signal processor was calibrated before and after every experiment by using a sinusoidal signal generator with known input frequencies f_i that covered the range of the expected frequency output of the photodiode during the course of an experiment. The corresponding analog output of the processor, V_i, was recorded by the computer. From the (f_i,V_i) pairs a least square fit of the form $f_a = A/V + B$ was determined, where f_a is the estimated frequency output of the photodiode, V the analog output of the processor, and A and B are constants. Such a fit proved to be very accurate and the correlation coefficient was always above 0.999. After determining the constants A and B, f_a (and hence the Doppler shift $f_d = f_a - 86.55$) can be calculated. The velocity is then obtained from f_d using simple formulas (e.g. Drain, 1980; Durst, et al., 1976).

3.3.3 Laser-induced fluorescence system

A laser-induced fluorescence (LIF) technique was employed to measure density profiles at chosen cross-sections in the channel. The technique is based on the property of Rhodamine 6G dye to fluoresce at wavelengths of about 570 nm when exposed to an intense light with a wavelength of 514 nm. Within a certain range of dye concentrations, the intensity of the emitted light is proportional to the concentration of the dye. This light can therefore be used to carry information about dye concentrations from the flowfield to outside light-collecting devices. This non-intrusive method for measuring concentrations has been recently employed with success by several investigators (e.g. Papantoniou, 1986; Hannoun, 1987), and details about it can be found

in Liu et al. (1977).

A 2W argon-ion laser (Spectra Physics model 265) is used to generate the 514 nm (green) beam. As sketched in Figure 3.11, the beam is directed vertically downward in the desired position along the flume by a series of coated front surface mirrors. The last mirror is mounted on the instrument carriage, together with an optical minirail which supports three plano-convex lenses (focal lengths 100, 20 and 800 mm from top to bottom). This group of lenses provides flexibility in the beam focusing procedure: a nearly uniform beam, with waist size estimated to be below 0.25 mm, can always be obtained in the test section, regardless of the location of the test section itself along the channel.

The beam enters the water through a partially immersed 1/2 in thick Lucite optical window and, after traversing the test section, is stopped by the flume bottom, which is coated with flat black paint at the point of beam incidence.

The fluorescent portion of the laser beam is imaged onto an array of 1024 photodiodes (EG&G Reticon model RL1024G). The array is encased in an LC300A camera (EG&G) which is mounted on a rigid surveying tripod. The photodiodes, which are 26 μm wide, are located in a single column with a center-to-center spacing of 25 μm. An orange filter, placed in front of the array, filters out the original 514 nm light, as well as part of the background noise. A 50 mm f1.8 Nikon lens is used to focus the fluoresced light onto the array.

The imaged laser beam is contained in the middle plane of the channel, and the camera is located 39–49 cm away from the beam, depending on the experiment considered, thus giving a magnification ratio of 6.8–8.8 and a spatial resolution of 0.16–0.22 mm.

The array is scanned by a sample and hold circuit controlled by a clock, which switches from diode to diode at intervals with adjustable period T. After the last

diode is scanned, there is an adjustable blanking period before the first diode of the successive scan is sampled. T is supplied by a pulse generator and it was equal to approximately 45 μs in all the laser-based experiments.

The frequency at which data are available from each pixel is given by 1/(NT), where N equals the number of array diodes (1024) plus the blanking period clock cycles (equal to 64 in these experiments). This gives a data output rate of $\approx$ 20 Hz per pixel. However, because of the large amount of data generated and the limited disk storage volume, only every fourth array scan was digitized, giving then a frequency of about 5 Hz per pixel.

Details about the electronic circuitry associated with the camera can be found in the Reticon LC300A manual (1981), while a description of how to use the camera is given in Hannoun (1986). The analog output of the camera has an amplitude of zero to 1.0 Volt. Dark noise is typically less than 2% of such output. The analog output is digitized using a custom built A/D converter (for details, see Papantoniou, 1986) and then fed to a PDP 11/60 computer through a direct memory access (DMA) interface, as sketched in Figure 3.14.

A description of the data acquisition system is given in Section 3.6.

3.4 Matching the index of refraction

It is a known fact that index of refraction fluctuations within density stratified fluids can create problems with laser-based measurements. A discussion of this subject can be found in Hannoun (1987). However, the indices of refraction of two mixing liquids can be matched while maintaining a significant density difference (up to $\approx$ 2%) by using ethyl alcohol and common salt as solutes for the upper and lower layer respectively. 95% ethyl alcohol and Culinox 999 food grade salt were employed in

this investigation.

A hand refractometer (American Optics model AO 10419) was used to match the refractive indices of the fluids contained in the two mixing tanks. The fresh water mixing tank, as well as the constant head tank, had wooden lids to minimize alcohol evaporation.

Other details on the method of matching the index of refraction using salt and alcohol can be found in Hannoun (1987).

3.5 Procedure in visual observations

The steps followed in a typical blue-dye experiment are now described.

First of all, the parameters of the experiment were chosen; specifically, the discharge densimetric Froude number, $\mathbf{F_0}$, the ambient water depth, d, and the broad-crested weir height, h_w, if such weir was present. The appropriate weirs were then positioned.

After filling the mixing tanks, an amount of salt was dissolved in the salt water mixing tank, together with a few grams of blue dye (Kriegrocine Brilliant Blue, produced by Special-T). The salinity attained was typically about 1%. The highest and lowest values used in all the experiments were 2.05% and 0.55%.

To ensure a completely homogeneous solution, an air-bubble plume that stirred and mixed the fluid in the tank was left on overnight. Checks revealed that the solution obtained was indeed homogeneous. Another advantage resulted from having the fluids in the mixing tanks for several hours. The water from the laboratory supply system was often considerably colder than the room temperature. Had the fluids not spent a long time warming up in the tanks before an experiment, some temperature increase would have taken place in the flume during the experiment, possibly causing

undesirable density changes.

In the next step the density difference between the two fluids was measured. Two 25 ml gravity flasks (manufactured by Thomas, Inc.) were filled first with the salt water solution and weighed on a precision scale. Then they were filled with water from the fresh water tank, and weighed again.

If we let W, W_s and W_f be the weights of the empty flasks, of the flasks filled with salt water and of the flasks filled with fresh water, the density difference was obtained from

$$(\frac{\Delta\rho}{\rho})_0 = \frac{W_s - W_f}{W_f - W}.$$

Two flasks rather than one were used to avert the risk of undetected errors. The two independent measurements served as checks for one another.

The discharge flowrate per unit width of channel, q_0, was then chosen so as to obtain the desired discharge densimetric Froude number

$$\mathbf{F_0} = \frac{q_0}{\sqrt{g(\frac{\Delta\rho}{\rho})_0 h_0^3}},$$

where h_0 = height of salt water inlet.

The discharge flowrates used spanned the range $q_0 = 6.9 - 20.9\, cm^2/s$ (more details on the experimental parameters can be found in the next chapter).

The preparatory phase was completed by filling the flume with fresh water. The temperature of the water in the flume and in the tanks was measured and compared with the laboratory room temperature.

The valve regulating the salt water influx was then opened to produce a steady discharge flowrate per unit width of channel, q_0. After a brief period in which an unsteady gravity current traveled along the flume bottom, the valve located downstream of the skimmer plate (see Figure 3.4) was gradually opened until a flowrate q_s was attained for which *all* the blue fluid was withdrawn under the skimmer plate

itself.

The third and last valve, which regulates the fresh water inflow into the flume, was then opened to yield a flowrate q_f large enough for a small amount of fresh water to be continuously spilling over the sharp-crested weir at the downstream end of the experimental facility. After a few minutes, a visually steady flow was established along the whole channel. Five minutes after the attainment of the visual steadiness, the procedure was started for the measurement of the flowrate q_1 in the blue layer at the downstream end of the channel.

The procedure is best illustrated referring to the sketch in Figure 3.15 and to the following photographs. Consider a given flowrate of (blue) dense water q_1 flowing over the downstream control, be it a weir or a free overfall. If $q_s > q_1$, all the blue fluid, as well as some of the clear ambient fluid, will flow under the skimmer plate, and an interfacial profile of type 1 (Figure 3.15) will occur (see also Figures 3.16 and 3.17). On the other hand, if $q_s < q_1$, part of the blue fluid will necessarily flow over the plate (profile 3, and Figures 3.18 and 3.19). Between these two situations is the case $q_s = q_1$, in which the interfacial profile is touching the skimmer plate, and neither does clear fluid go below it, nor does blue fluid go above it (profile 2). It is interesting to notice that the only change between Figures 3.17 and 3.19 has been a decrease in q_s amounting to less than $1.2\,cm^2/s$. Still, it is quite clear that $q_s > q_1$ in the former picture, while $q_s < q_1$ in the latter.

Great care was taken to make sure that the position of the skimmer plate and the withdrawal rate q_s did not affect the flow in the channel upstream of the critical control section. Theoretical considerations suggest that perturbations in the supercritical region downstream of the critical section (such as, for example, a change in q_s) cannot travel upstream. Experimental verification was obtained by measuring the visual thickness of the blue layer in the subcritical gradually-varied counterflow:

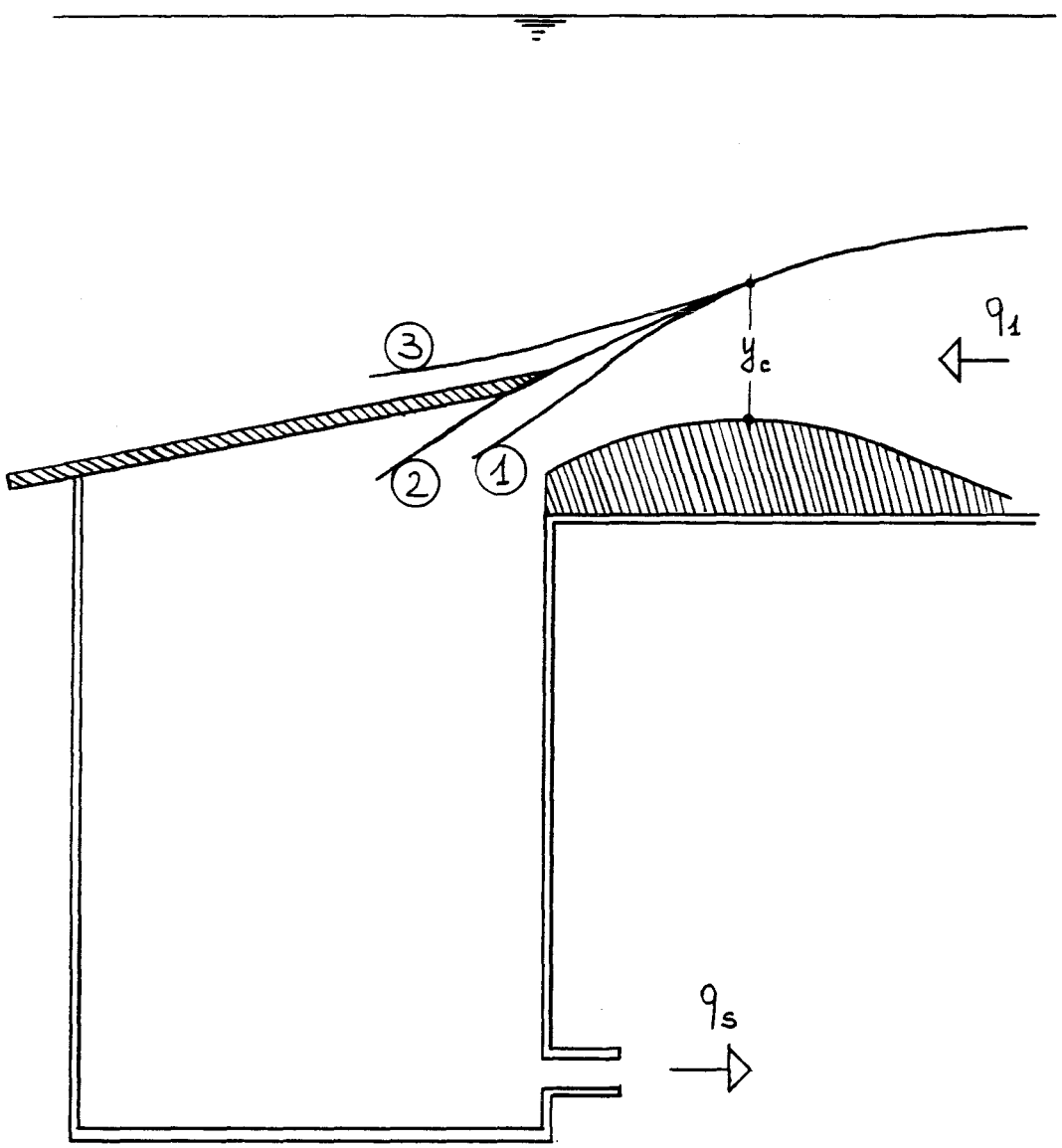

Figure 3.15: Three types of interfacial profiles.

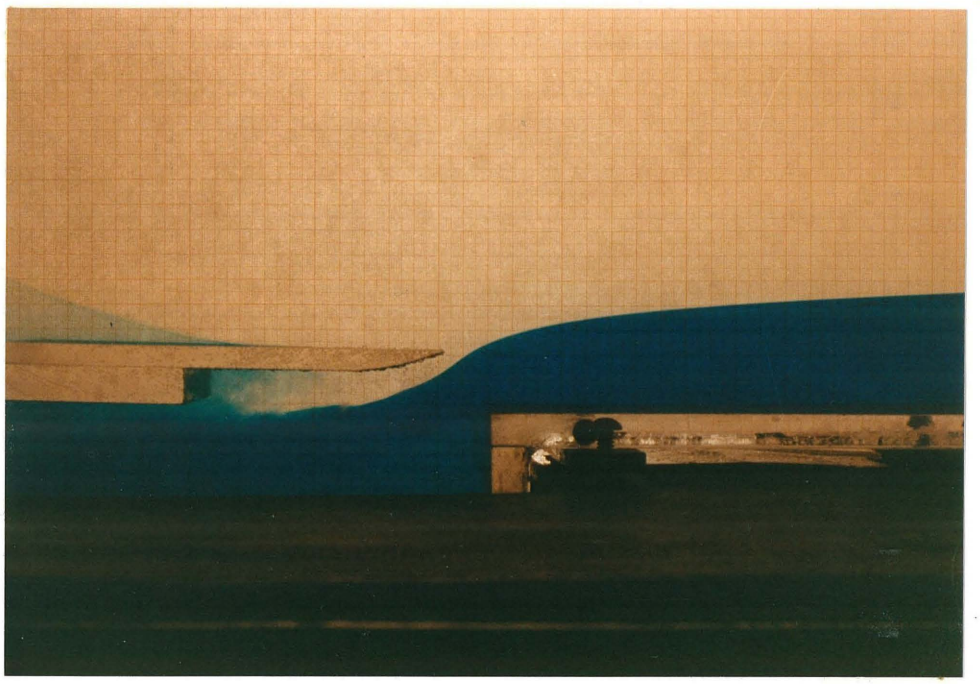

Figure 3.16: Free overfall, $q_s > q_1$.

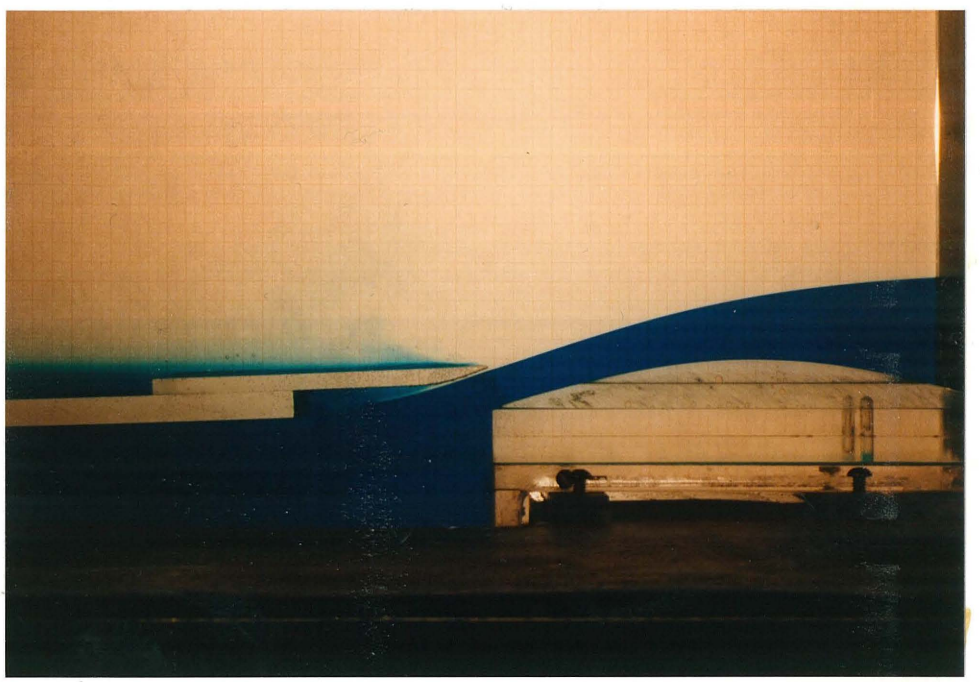

Figure 3.17: Broad-crested weir, $q_s > q_1$.

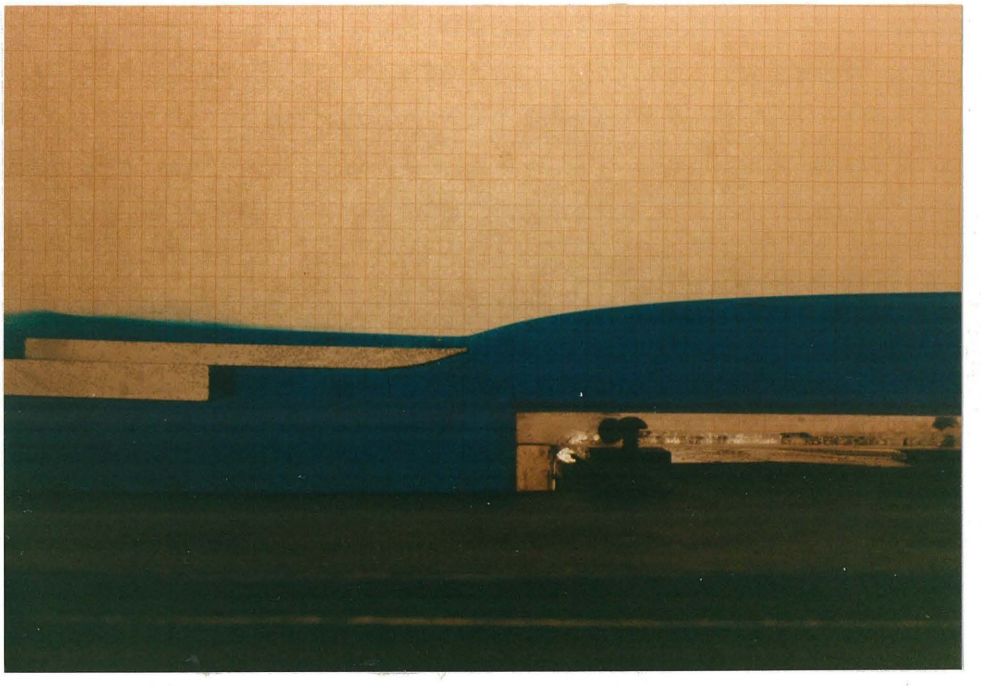

Figure 3.18: Free overfall, $q_s < q_1$.

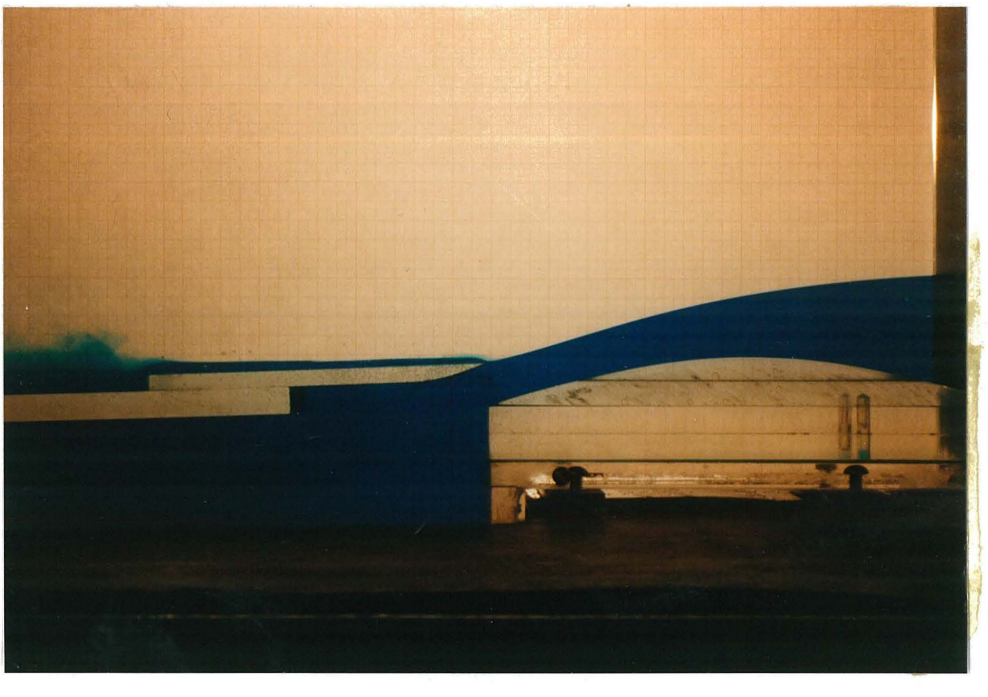

Figure 3.19: Broad-crested weir, $q_s < q_1$.

changes in q_s of the order of 300%, as well as dramatic changes in the position of the skimmer plate, did not produce any measurable variation in the thickness of the subcritical layer.

At any rate, the skimmer plate at this point was positioned in such a way that it was approximately tangent to the interfacial profile when $q_s \approx q_1$. This plate position adjustment could not be performed without perturbing the flow in the channel; additional time was then allowed for reestablishment of a steady flow.

The actual measurement of q_1 was then initiated. By careful successive adjustments of the valve regulating q_s, the minimum of the q_s values exceeding q_1 and the maximum of the q_s values below q_1 were determined. These two values were usually very close to each other (the difference between them was typically about 2% of the total q_1, and in no experiment was it more than 5%). The arithmetic mean of the two values was taken to represent the measured flowrate q_1, and divided by q_0 to obtain the dilution S.

The type of overall flow structure was then classified. In particular, it was observed whether the source was flooded with blue fluid or a free jump was present, and whether the blue layer reached the free surface.

The length of the jump region, L_j, was defined as the distance from the source to the downstream-most point of the roller exhibiting blue fluid moving backwards. For upstream-controlled unstable flows, where the limits of the roller were difficult to define visually, the length of the jump region, L_j', was taken as the distance from the source to the point at which the fresh water layer was the thinnest, i.e., the blue layer was the closest to the free surface. Finally, in the case of downstream-controlled unstable flows, L_j'' was taken as the distance from the source to the point where the blocked clear layer initiated. These definitions of the length of the jump region may seem somewhat arbitrary and unnecessary. Their usefulness will become clear

later. For the time being, suffice it to say that these lengths were easily and quickly measured, and their measurement was repeatable and fairly accurate (within $\approx 10\%$).

The most time consuming phase of the visual observations consisted in the measurement of blue layer thicknesses along the gradually-varied counterflow region. The point gage previously described was employed, but the reading of the layer depth was not completely straightforward.

Despite the subcriticality of the flow, the essentially flat interface had occasional ripples and cusps, and superimposed on those interfacial waves, with an amplitude very limited in many cases, but as large as ≈ 4 cm (crest to trough) under some experimental conditions and at certain locations along the channel. In other words, the interface, although well defined and visible, was continuously moving up and down, with several frequencies of oscillation.

To cope with these problems, the following procedure was adopted for all experiments. The highest point attained by the interface over a period of approximately ten times the period of the longest waves present was recorded first. The lowest point over the successive ten periods was recorded next. The arithmetic mean of the two readings was taken to characterize the visual thickness of the blue dense layer at that cross-section. The layer thickness measurements were performed, together with a few measurements of total ambient depth, until the salt water mixing tank was empty. This allowed typically a dozen data points to be obtained. It will be shown in Chapter 4 that this was usually sufficient to characterize fairly well the shape of the interfacial profile in the entire subcritical counterflow region.

The steady flow time available for measurements varied from experiment to experiment, depending on the discharge flowrate, and it was usually in the range between 1.5 and 3 hours.

To summarize, the visual observations (or 'blue-dye experiments') were simple

experiments which could be performed in one day and which allowed determination of the bulk characteristics of the flow: the overall flow structure was classified, the dilution in the mixing region measured, the length of the jump region, the depth of the two layers and the slope of the interface in the gradually-varied counterflow obtained.

The experimental results are presented in the next chapter, along with a comparison with the predictions of the one-dimensional theory.

3.6 Procedure in laser-based experiments

The procedure followed in a typical laser-based experiment is now described. The different tasks are listed in chronological order, as they were performed in the laboratory. This is done in an attempt to describe the experiment as faithfully as possible, in all its complexity. The simultaneous treatment of operations related to both LDV and LIF should not generate confusion.

First, a decision was made regarding the flow conditions to study. The discharge densimetric Froude number, $\mathbf{F_0}$, was chosen, and the instrument carriage was placed at the desired position along the channel.

After cleaning the flume walls and all the optical surfaces, the LIF beam was focused by adjusting the three-lens system described before, as well as the mirrors, when necessary.

A position for the Reticon array camera was chosen so as to maximize the spatial resolution for the given experimental conditions (the bulk characteristics of the flow to expect were fairly well known from the previous blue-dye experiments).

The salt water mixing tank was filled with water from the laboratory supply, and a small amount of anhydrous granular sodium sulfite (Na_2SO_3) was added to

dechlorinate the water. Dechlorination of the tank water was a precaution taken to avert the risk of the chlorine oxidizing the Rhodamine 6G dye. Salt was then added in the desired amount, and the mixing air-bubble plume was started.

The fresh water mixing tank, on the other hand, was filled with a solution of water and ethyl alcohol. The amount of alcohol used (typically 2–3% by weight) was such that the fluid in this tank had approximately the same index of refraction as the fluid in the salt water tank. Mixing was achieved again by means of an air-bubble plume. Mixing was continued for several hours for the reasons explained before. This also eliminated the problem of a temperature increase occurring in the fresh water tank upon introduction of the alcohol.

Calibration of the LDV signal processor was then performed following the modalities previously described.

Before the completion of the mixing phase, a known amount of Rhodamine 6G dye was added to the salt water tank. Typically, a dye concentration between 0.75×10^{-7} and 1.0×10^{-7} molar was attained.

The indices of refraction of the fluids in the two tanks were then measured and matched exactly by means of a rather tedious trial-and-error procedure involving small additions of water, alcohol or salt. The matching was considered satisfactory when the two indices were identical within the precision of the refractometer used. This resulted in a complete elimination of any visible beam wobbling during the experiments.

The density difference between the two fluids was then measured, using the same procedure discussed in the previous paragraph. The discharge flowrate q_0 necessary to attain the desired $\mathbf{F_0}$ was then determined.

Both lasers and all electrical units such as amplifiers, Bragg cell exciters, photodiode and Reticon power supply were turned on, and the filling of the channel with

the less dense fluid was initiated.

A series of calibration operations (sketched in Figure 3.20) then followed, in which several Lucite boxes were employed. The boxes had a 3×3 in square base and a height that varied between 3 and 20 in.

A short box, approximately as tall as the expected depth of the dense lower layer in the experiment to be performed, was filled with the salt water solution and inserted in the LIF beam path, inside the flume. The image of the fluorescent portion of the beam was then focused onto the Reticon array by carefully positioning the 50 mm converging lens in front of the camera. This was possible because the intensity of the light hitting the pixels on the array could be visualized on an oscilloscope.

The magnification ratio was then determined accurately. The number of pixels with output above a threshold, multiplied by the distance between pixels, was divided into the known height of the Lucite box. This method resulted in a much more accurate and reliable measurement than a simple measurement of the distance between the camera and the flume middle plane.

The actual calibration of the LIF system was then performed, to account for the effects of lens aberrations, variable beam width, imperfections and distortions in the Lucite, slight misalignments of the optics, etc..

A box taller than the field of view of the Reticon array, filled with the salt water solution, was at this point put in place of the previous short box. A data collection program was run and each pixel was sampled, typically 512 times over approximately 100 seconds, and its output was time-averaged. The necessary transfer function for the array, to be used later for data processing, was thus obtained.

It should be mentioned that all the Lucite boxes contained a magnetic stir-bar, which was used to implement mixing of the fluid inside the box itself, in order to prevent photo-bleaching and thermal blooming of the fluorescent dye (for a discussion

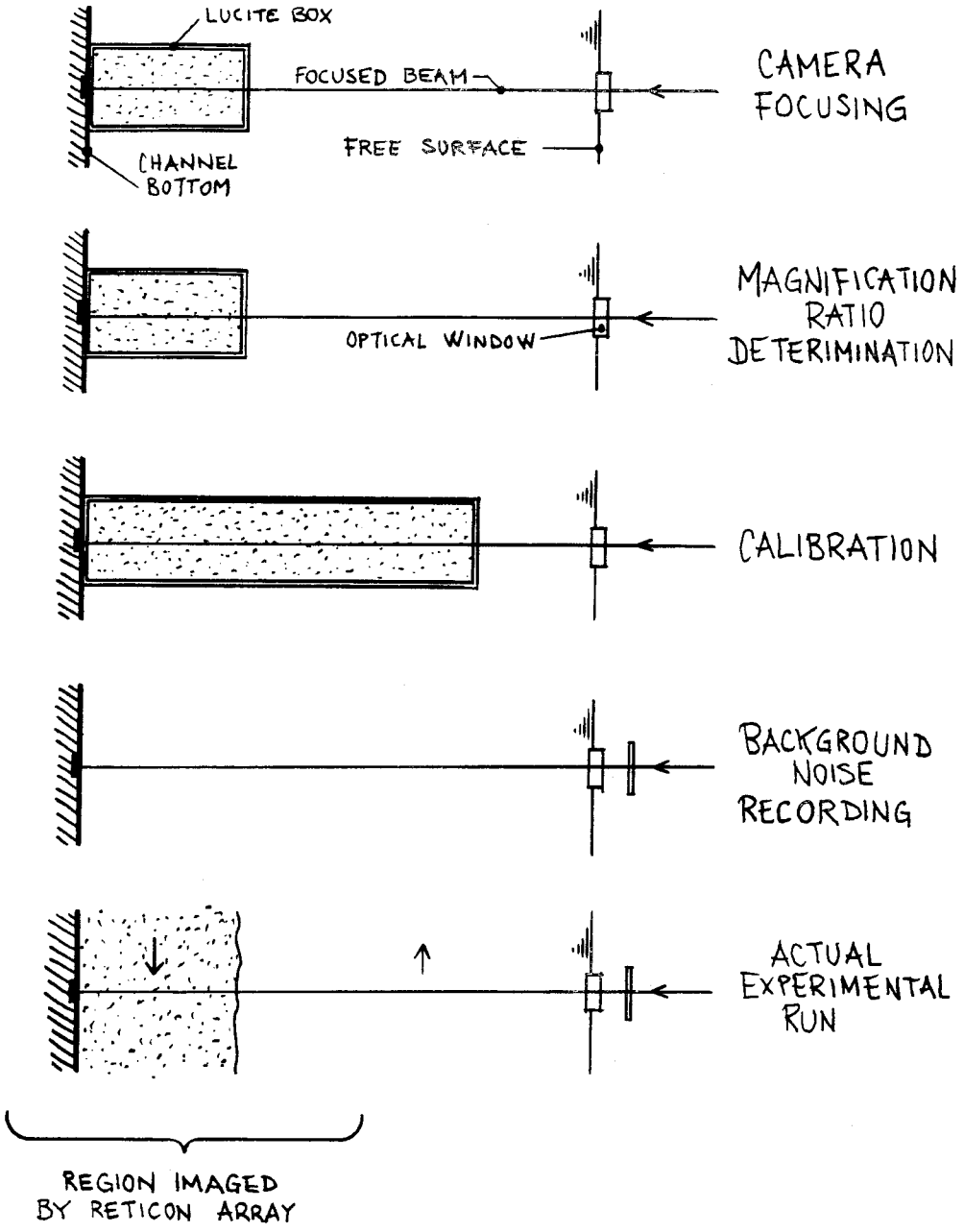

Figure 3.20: Sequence of LIF operations.

on these phenomena, see Koochesfahani, 1984).

As the last LIF test before the actual run, the data collection and averaging program was run after removing all boxes from the flume, that is to say with only the less dense ambient solution in the cross-section. This enabled background noise to be determined.

The quality of the LDV signal was checked, and the output frequencies from the Bragg cell exciters were measured. Their difference, which was measured again after each experiment, was the frequency shift between the reference and the scattering beams.

Finally the flow was initiated and the desired steady-state conditions were attained in the way described in the previous section.

Despite the lengthy preparations just described, the actual LIF data-taking lasted only a few minutes.

In a typical experiment, 1024 array scans were recorded. In other words, 1024 'instantaneous' dye concentration profiles, each one comprising 1024 data points, were obtained. The scanning of each profile took about 50 ms, with a blanking period of 150 ms before the next profile was recorded. This resulted in a total LIF recording time of about 200 seconds.

The analog output of the camera was digitized using a custom made analog-to-digital converter (Papantoniou, 1986) and then fed to a PDP 11/60 computer through a DMA interface.

The data were recorded on a DSD 880 Winchester disk, as sketched in Figure 3.14. The data acquisition program was based on an assembly language subroutine that maximized the efficiency of the process. Details of the data acquisition system are given in Papantoniou (1986).

The LDV system was then employed to characterize the velocity field. A total

Chapter 4

Visual observations

4.1 Introduction

This chapter describes the results of experiments in which the development of the dense flowing layer was observed visually. The purpose was to gain insight into the bulk characteristics of the flows occurring in mixing channels.

In these experiments a wide range of discharge and downstream parameters was covered, and the four mixing modes defined and discussed from a theoretical standpoint in Chapter 2 were all observed. Some of the flow structures obtained in the experimental channel are shown in Figures 4.1 to 4.8.

Free internal hydraulic jumps observed in a deep channel ($H = 76.6$) are presented in Figures 4.1 and 4.2. In the experiments shown in these figures, the downstream control was a free overfall, and the discharge densimetric Froude number was $\mathbf{F_0} = 9.72$. The wall-jet-like entraining region is clearly visible near the source. A roller region follows where the dense (blue) fluid could be seen to move backwards, towards the source, near the interface. This roller buffered the high velocity salt water from the ambient fresh water, causing a much reduced shear between the two layers. The beginning of the two-layer stratified flow in the gradually-varied counterflow region is visible in Figure 4.1.

A flooded internal hydraulic jump is shown in Figures 4.3 and 4.4. The only

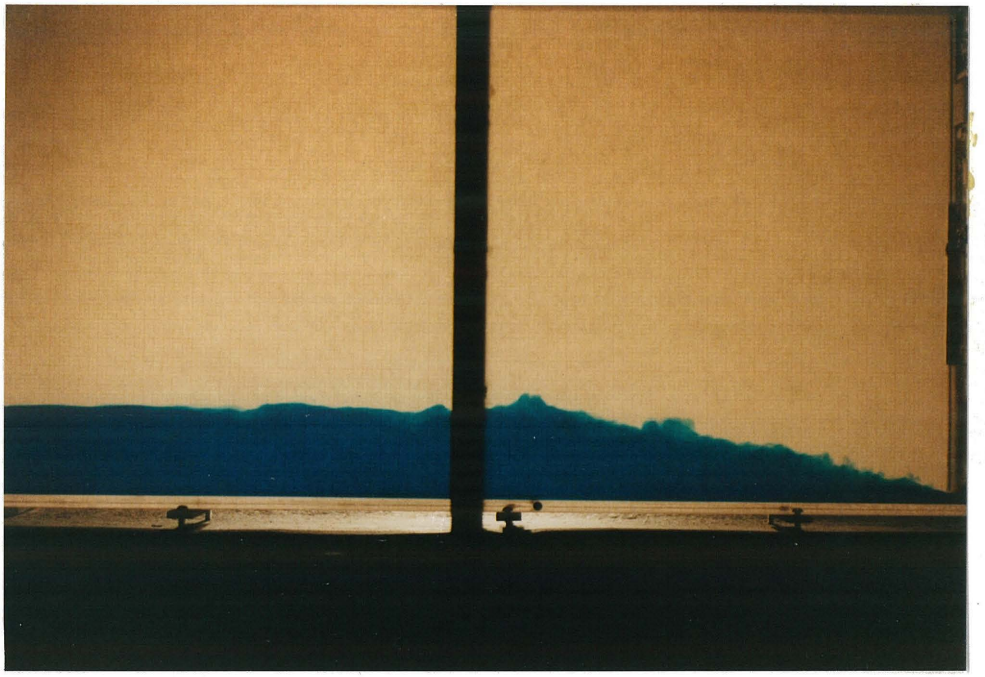

Figure 4.1: Free internal hydraulic jump. Approximately 100 cm of channel.

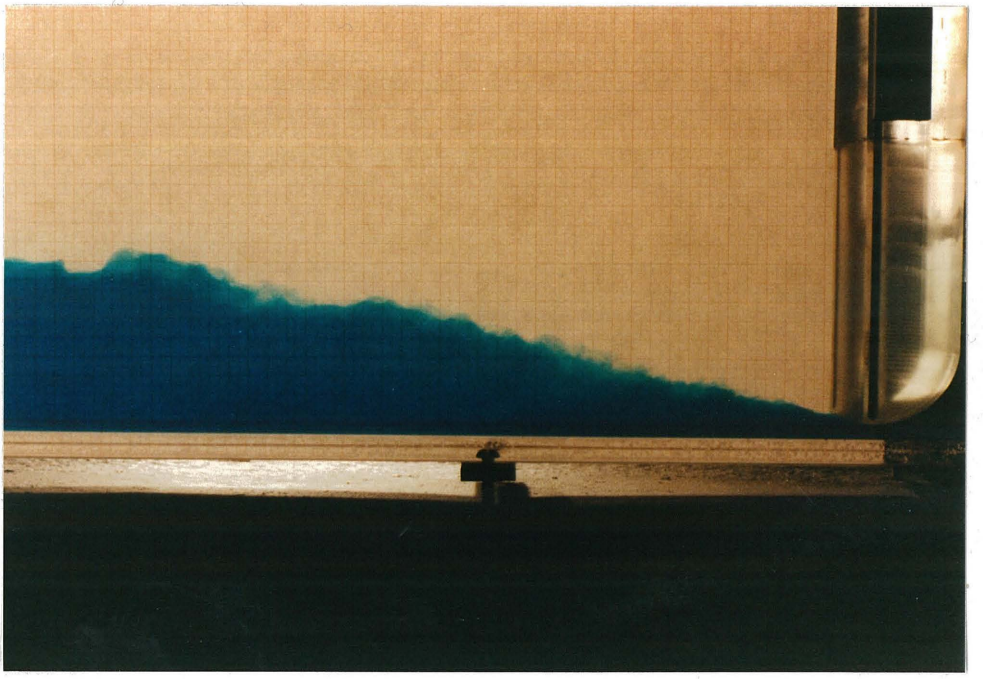

Figure 4.2: Free internal hydraulic jump. Approximately 50 cm of channel.

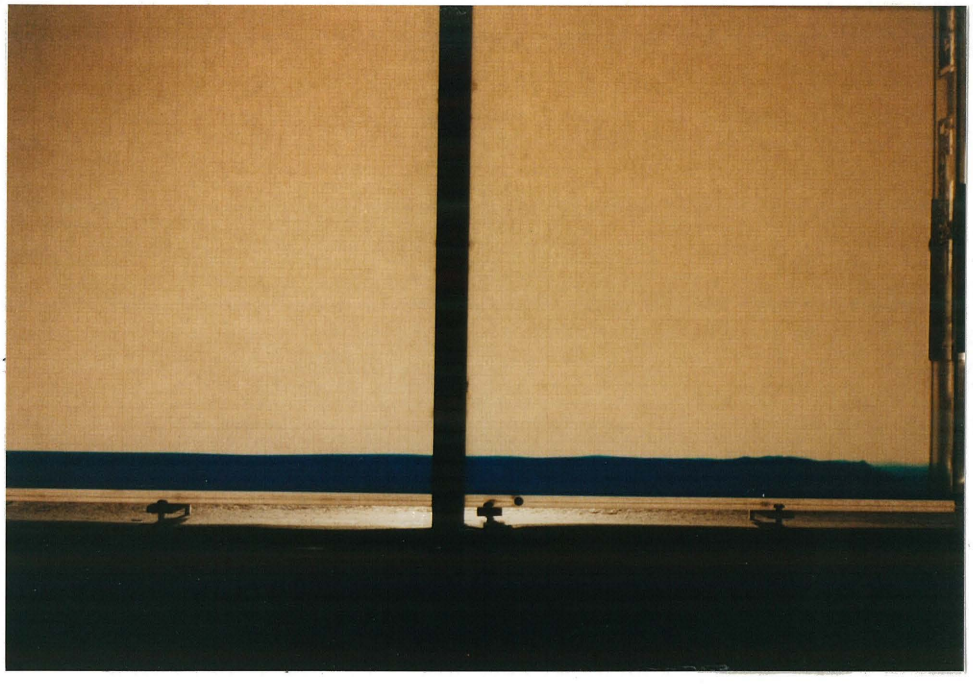

Figure 4.3: Flooded internal hydraulic jump. Approximately 100 cm of channel.

Figure 4.4: Flooded internal hydraulic jump. Approximately 50 cm of channel.

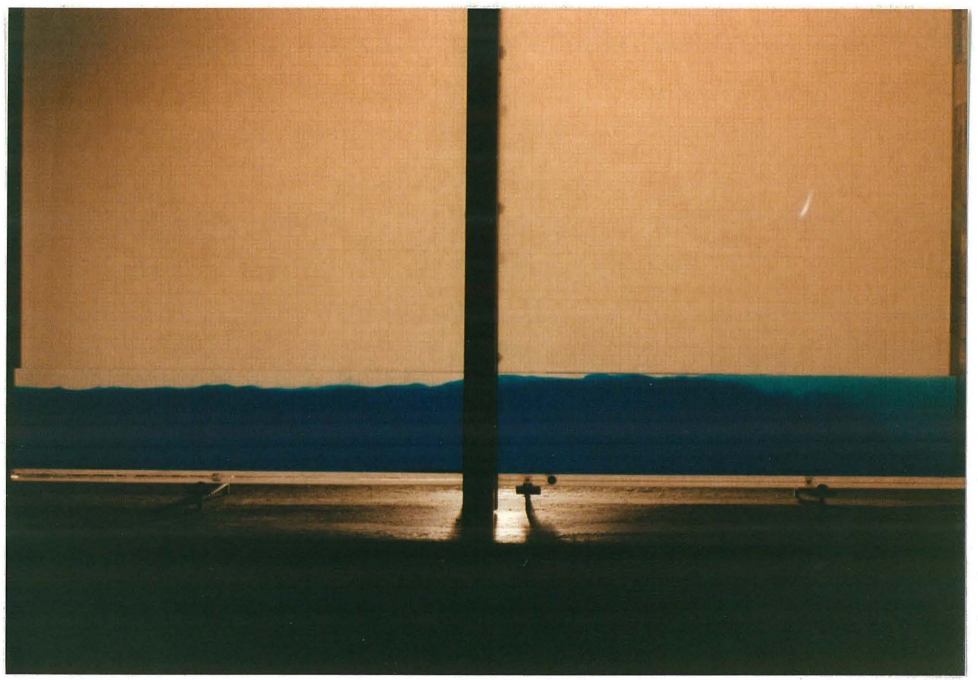

Figure 4.5: Upstream-controlled unstable flow. Approximately 100 cm of channel.

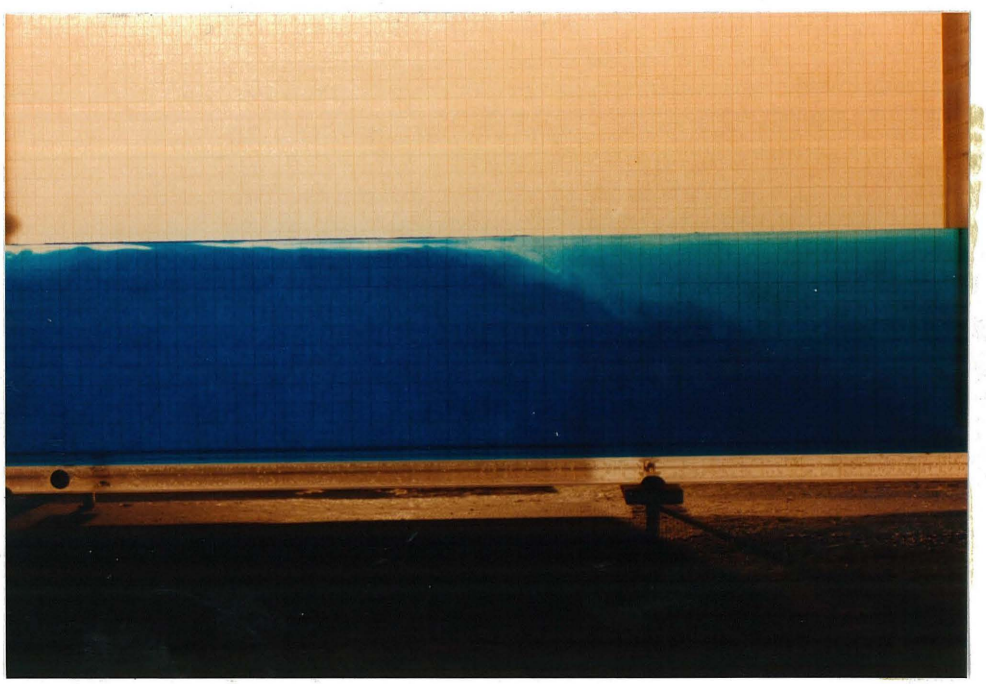

Figure 4.6: Upstream-controlled unstable flow. Approximately 50 cm of channel.

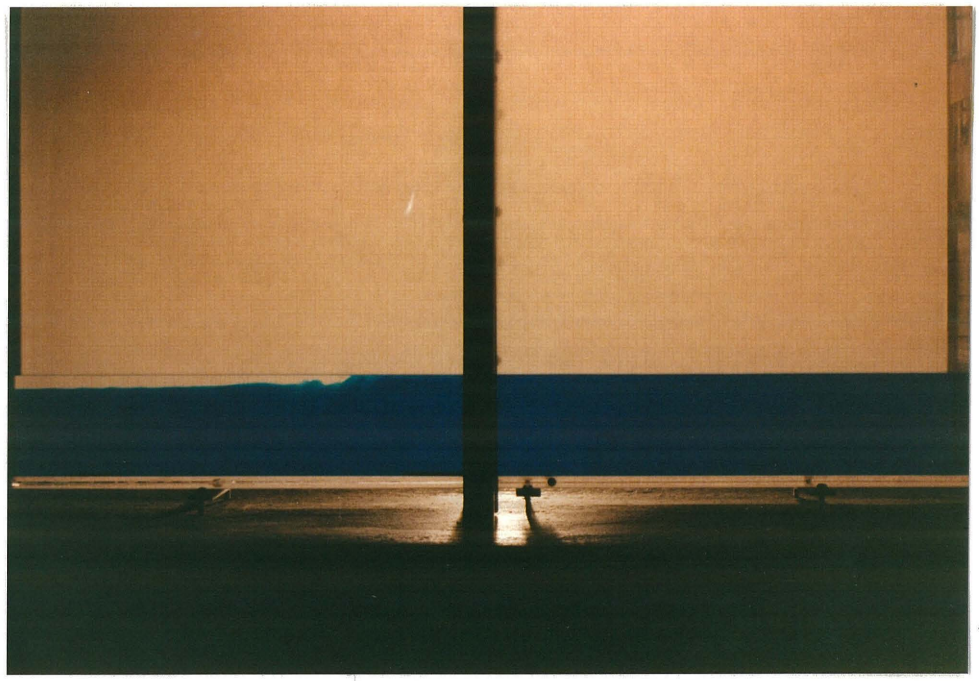

Figure 4.7: Downstream-controlled unstable flow. Approximately 100 cm of channel.

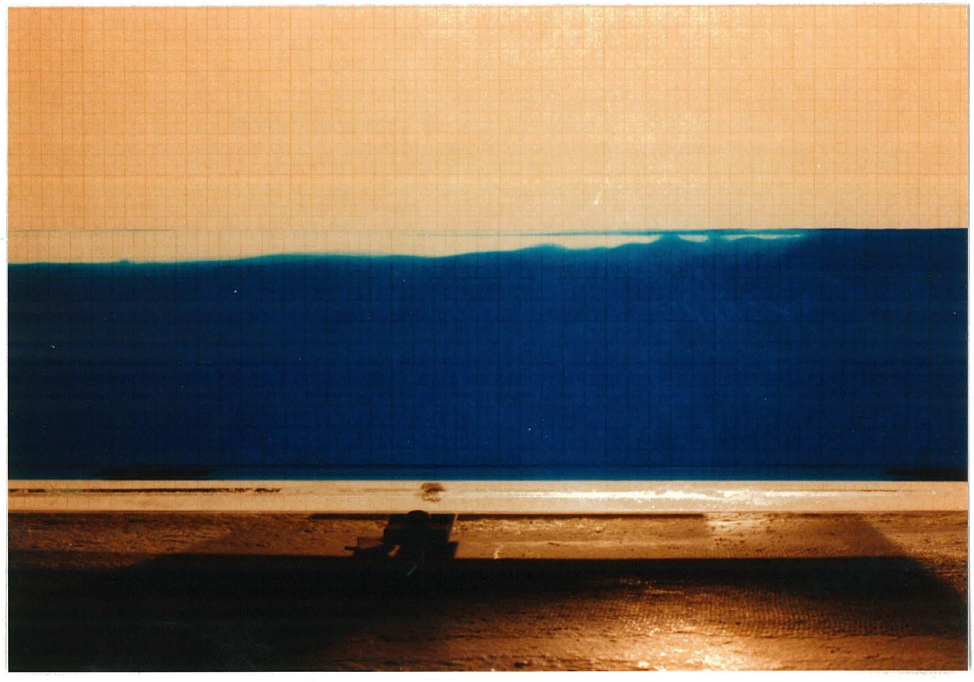

Figure 4.8: Downstream-controlled unstable flow. Detail of the transition from one-layer to two-layer flow.

change in experimental parameters between the previously seen free jump and this flooded jump consisted in a reduction of $\mathbf{F_0}$ from 9.72 to 3.56. A permanent 'cloud' of blue fluid is visible over the source. Entrainment of ambient fluid is negligible in this type of flow.

In order to observe unstable flow conditions in the range of $\mathbf{F_0}$ attainable in the laboratory it was necessary to reduce the ambient water depth. For the flows shown in Figures 4.5 to 4.8 the nondimensional ambient water depth H was equal to 15.3 and the flow was controlled by a free overfall at the downstream end of the channel.

An upstream-controlled unstable flow ($\mathbf{F_0} = 11.33$) is shown in Figures 4.5 and 4.6. The blue layer was clearly interacting with the free surface. A very thin layer of ambient water, which can be seen near the free surface, was moving towards the source and entraining salt water. This gave rise to a recirculation of salt water, which was responsible for the presence of mixed fluid in the source region.

A downstream-controlled unstable flow is presented in Figures 4.7 and 4.8. This was obtained, under the same conditions as the previously shown upstream-controlled instability, by increasing $\mathbf{F_0}$ from 11.33 to 15.28. It can be seen that the entire water depth is occupied by unmixed source fluid. An arrested fresh water wedge is visible at the beginning of the two-layer stratified region. No measurable dilution of the source fluid was present under these conditions.

The presentation of the visual observations ('blue-dye experiments') is subdivided into three parts. Section 4.2 deals with the experiments performed with a free overfall at the downstream end of the channel. The main focus of these experiments was the role played by the ambient water depth in the channel. A description of the experiments in which the downstream control was a broad-crested weir is given in Section 4.3. The effect of the weir height on the flow structure and properties was the main object of this portion of the investigation.

Finally, a brief discussion and a summary of the most significant experimental results can be found in Section 4.4.

4.2 Free overfall experiments

Fifty nine different experiments were performed in this series. Table 4.1 summarizes the experimental conditions and some of the experimental results. The discharge densimetric Froude number, $\mathbf{F_0}$, was varied between approximately 3 and 15. This was done by varying both the discharge flowrate q_0 and the initial density difference $(\Delta\rho/\rho)_0$, while maintaining a constant discharge depth h_0. Five different non-dimensional ambient water depths H were used. They varied between 76.6 ('deep channel') and 15.3. The table reports the type of flow observed, the dilution S measured, the length of the jump region, and two salt water layer thicknesses, h_1 and h_1'. It also reports the flowrate at the downstream end of the channel, q_1, measured as discussed in the previous chapter, from which the dilution S was computed. The depth h_1 is defined as the visual thickness of the dense lower layer at a distance from the source equal to twice the length of the jump region. The depth h_1' is defined as the visual thickness of the same layer in the subcritical gradually-varied counterflow, at the location along the channel where the interface was most nearly horizontal, i.e., had minimum slope. Only h_1 will be used in the following discussion, since the two depths are basically equivalent (h_1' is always a little lower than h_1, as should be expected) and h_1 was easier to measure and was consequently determined in more experiments. The depth h_1 will be considered to be 'the depth after the jump'. However, this concept, which has been used by many investigators, and which is a necessary element of the theoretical analysis, unfortunately does not correspond to a well-defined experimental entity.

Table 4.1: Summary of parameters for free overfall experiments.

Exp. #	F_o	H	S	h_1 (cm)	L_j (cm)	$(\Delta\rho/\rho)_o$ (%)	q_o (cm^2/s)	q_1 (cm^2/s)	d (cm)	h_1' (cm)	Flow type
F0	3.209	76.5	1.021	3.52	12	2.054	8.22	8.39	52.66	3.13	FL
F1	4.138	76.6	1.026	-	-	2.054	10.33	10.60	52.71	-	
F2	4.851	76.7	1.060	4.81	11	1.204	9.53	10.10	52.79	4.19	FL
F3	4.860	76.6	1.090	-	-	2.054	12.45	13.57	52.71	-	
F4	5.655	76.6	1.229	-	-	1.148	10.83	13.31	52.71	-	
F5	6.443	76.6	1.309	6.24	27	0.754	10.00	13.09	52.68	5.62	FR
F6	6.444	76.6	1.319	-	-	1.148	12.34	16.28	52.73	-	
F7	7.253	76.6	1.422	-	-	1.148	13.89	19.75	52.71	-	
F8	8.059	76.6	1.491	7.56	34	1.033	14.64	21.83	52.69	7.11	FR
F9	9.688	76.6	1.692	9.23	46	0.982	17.16	29.03	52.72	8.57	FR
F10	10.496	76.5	1.849	-	-	1.148	20.10	37.17	52.66	-	
F11	11.301	76.6	1.942	11.10	60	0.882	18.97	36.85	52.69	10.37	FR
F12	12.876	76.6	2.154	12.35	72	0.765	20.13	43.35	52.68	12.20	FR
F13	3.209	33.0	0.983	4.06	10	1.435	6.87	6.75	22.71	-	FL
F14	4.857	33.0	1.050	4.88	11	1.435	10.40	10.92	22.70	4.21	FL
F15	5.652	33.0	1.252	-	-	1.339	11.69	14.64	22.69	-	
F16	6.440	33.0	1.387	6.21	25	1.339	13.32	18.48	22.72	5.51	FR
F17	8.060	33.1	1.530	7.60	38	1.183	15.67	23.98	22.75	7.02	FR
F18	9.692	33.1	1.694	9.42	44	0.987	17.21	29.15	22.75	8.97	FR
F19	11.298	33.0	1.832	11.36	60	0.972	19.91	36.47	22.68	10.39	FR
F20	12.878	33.0	1.881	12.29	75	0.752	19.96	37.54	22.67	11.69	FR
F21	3.209	26.6	1.016	3.79	12	1.629	7.32	7.44	18.29	3.43	FL
F22	4.860	26.5	1.055	5.00	14	1.010	8.73	9.21	18.23	4.40	FL
F23	5.651	26.6	1.190	-	-	1.358	11.77	14.01	18.29	-	
F24	6.443	26.6	1.363	6.36	23	1.358	13.42	18.29	18.33	5.65	FR

Table 4.1 (Cont.)

Exp. #	F_o	H	S	h_1 (cm)	L_j (cm)	$(\Delta\rho/\rho)_o$ (%)	q_o (cm^2/s)	q_1 (cm^2/s)	d (cm)	h_1' (cm)	Flow type
F25	7.254	26.6	1.394	-	-	1.358	15.11	21.07	18.29	-	
F26	8.059	26.6	1.504	7.67	35	1.099	15.10	22.71	18.31	6.99	FR
F27	8.875	26.6	1.594	-	-	1.099	16.63	26.50	18.33	-	
F28	9.688	26.6	1.623	9.53	44	1.026	17.54	28.46	18.32	8.65	FR
F29	10.495	26.7	1.671	-	-	1.026	19.00	31.74	18.35	-	
F30	11.299	26.6	1.659	10.51	60	0.744	17.42	28.90	18.32	-	FR
F31	12.882	26.6	1.637	11.95	65	0.735	19.74	32.31	18.33	-	FR
F32	13.682	26.6	1.608	12.66	68*	0.702	20.49	32.94	18.30	-	UI
F33	14.489	26.6	1.557	13.02	66*	0.600	20.06	31.23	18.28	11.99	UI
F34	3.208	19.5	1.020	3.95	11	1.734	7.55	7.70	13.45	3.56	FL
F35	4.860	19.5	1.062	4.88	13	1.031	8.82	9.37	13.45	4.35	FL
F36	5.652	19.5	1.167	-	-	1.289	11.47	13.38	13.42	-	
F37	6.441	19.5	1.289	6.06	26	1.289	13.07	16.85	13.40	5.41	FR
F38	7.251	19.5	1.340	-	-	1.042	13.23	17.73	13.39	-	FR
F39	8.062	19.5	1.364	7.78	33	1.042	14.71	20.07	13.39	6.93	FR
F40	8.875	19.5	1.426	-	-	1.289	18.01	25.68	13.39	-	FR
F41	9.691	19.4	1.413	8.95	47	1.075	17.96	25.37	13.38	8.23	FR
F42	10.495	19.4	1.392	-	50	1.075	19.45	27.07	13.38	-	FR
F43	11.296	19.5	1.335	9.79	50*	0.930	19.47	26.00	13.39	8.88	UI
F44	12.088	19.5	1.297	-	-	0.653	17.46	22.65	13.41	-	
F45	12.880	19.5	1.270	10.38	44*	0.810	20.72	26.31	13.41	-	UI
F46	13.681	19.5	1.239	-	-	0.653	19.76	24.48	13.40	-	
F47	14.490	19.5	1.209	10.55	45*	0.650	20.88	25.24	13.42	9.31	UI
F48	3.209	15.3	1.001	3.79	11	1.737	7.56	7.57	10.50	3.33	FL
F49	4.857	15.3	1.063	4.97	16	1.123	9.20	9.78	10.51	4.34	FL

Table 4.1 (Cont.)

Exp. #	F_o	H	S	h_1 (cm)	L_j (cm)	$(\Delta\rho/\rho)_o$ (%)	q_o (cm^2/s)	q_1 (cm^2/s)	d (cm)	h_1' (cm)	Flow type
F50	5.651	15.3	1.164	-	-	1.234	11.22	13.06	10.54	-	
F51	6.442	15.3	1.204	6.10	23	1.234	12.79	15.40	10.55	5.36	FR
F52	7.253	15.3	1.227	-	-	1.234	14.40	17.67	10.56	-	
F53	8.059	15.2	1.234	7.32	29	1.118	15.23	18.80	10.48	6.39	FR
F54	8.879	15.3	1.221	-	-	1.234	17.63	21.52	10.56	-	
F55	9.689	15.3	1.175	8.26	36*	1.047	17.72	20.82	10.50	7.16	UI
F56	11.296	15.2	1.139	8.85	33*	1.116	21.33	24.29	10.47	7.32	UI
F57	12.878	15.3	1.075	8.49	50**	0.717	19.49	20.95	10.51	7.65	UI
F58	14.489	15.3	1.017	8.68	55**	0.597	20.01	20.35	10.50	7.92	DI

* L_j' was measured instead of L_j
** L_j'' was measured instead of L_j

FL = flooded internal hydraulic jump
FR = free internal hydraulic jump
UI = upstream controlled instability
DI = downstream controlled instability

For all experiments in this table, h_o = 0.688 cm

The interface typically reaches its highest point within the roller region, collapses to a slightly lower point immediately downstream of the roller and then starts sloping down because of friction (e.g., see Figure 4.1). The 'depth after the jump' then depends on the specific position chosen 'after the jump' to measure it. The choice made for the definition of h_1 in this investigation was dictated by the desire to have a uniquely-defined, easy-to-measure quantity. However, the ambiguity associated with the concept of a 'depth after the jump' should be kept in mind, especially in situations of upstream-controlled instabilities, where the slope of the interface after the jump region is considerable.

To complement these 59 experiments, many additional flows were generated for the purpose of observing the transition between the four different types of flow.

A clear transition between flooded jumps and free jumps was not observed. Between the situation where the source was definitely flooded, with a permanent and large cloud of dense (blue) fluid over the source and negligible ambient water entrainment, and the free jump situation, characterized by a visible wall-jet-like entraining region near the salt water inlet, there existed a full range of intermediate situations. Flows were observed in which the 'blue cloud' over the source was small in size and light in color, indicating some mixing. At larger $\mathbf{F_0}$, flows were observed in which the cloud was intermittently entrained and reformed. In other words, the transition between flooded and free jumps was not sharp, and a number of 'partially flooded' jumps were observed.

In a similar way, the transition from free internal hydraulic jumps to upstream-controlled unstable flows was poorly defined. The onset of instability has been defined to occur when the lower dense layer interacts with the free surface, with recirculation of lower fluid towards the source. But in many flows a thin layer of fresh water passed above the salt water with only occasional touching of the free surface by the

salt water. Furthermore, the salt water eddies which attained the free surface were clearly three-dimensional, and they were more often located near the center of the channel than near the walls, so that at times the salt water did attain the surface near the center of the channel, but fresh water layers flowing towards the source still existed near the walls.

The experimental results are presented in the next section. A comparison between the one-dimensional theory and the experimental results, presented in Section 4.2.3, will conclude the description of this series of experiments with a free overfall as the dowstream control.

4.2.1 Results

The data presented in Table 4.1 can be used to derive functional relationships that describe the experimental findings. The most interesting of these relates the measured dilution S to the discharge densimetric Froude number $\mathbf{F_0}$. In Figure 4.9 five curves, distinguished by five different plotting symbols, are presented for the five different dimensionless ambient water depths H used in the experiments.

At very low $\mathbf{F_0}$, flooded jumps are present and dilutions are very limited for all water depths H. A transitional region appears to be located at about $\mathbf{F_0} = 4 - 5$, where S begins to grow more or less linearly with $\mathbf{F_0}$, until the effect of the limited ambient water depth is apparent.

For increasing $\mathbf{F_0}$, if the ambient water depth is limited, more and more of the lower (blue) fluid is recirculated towards the source, resulting in decreasing values of S. This can be observed in the curves for $H = 15.3$, $H = 19.5$ and $H = 26.6$.

For $H = 15.3$ and $\mathbf{F_0} = 14.49$, which was the only downstream-controlled unstable flow observed in this series of experiments, the dilution has dropped to approximately one, indicating negligible entrainment of ambient fluid.

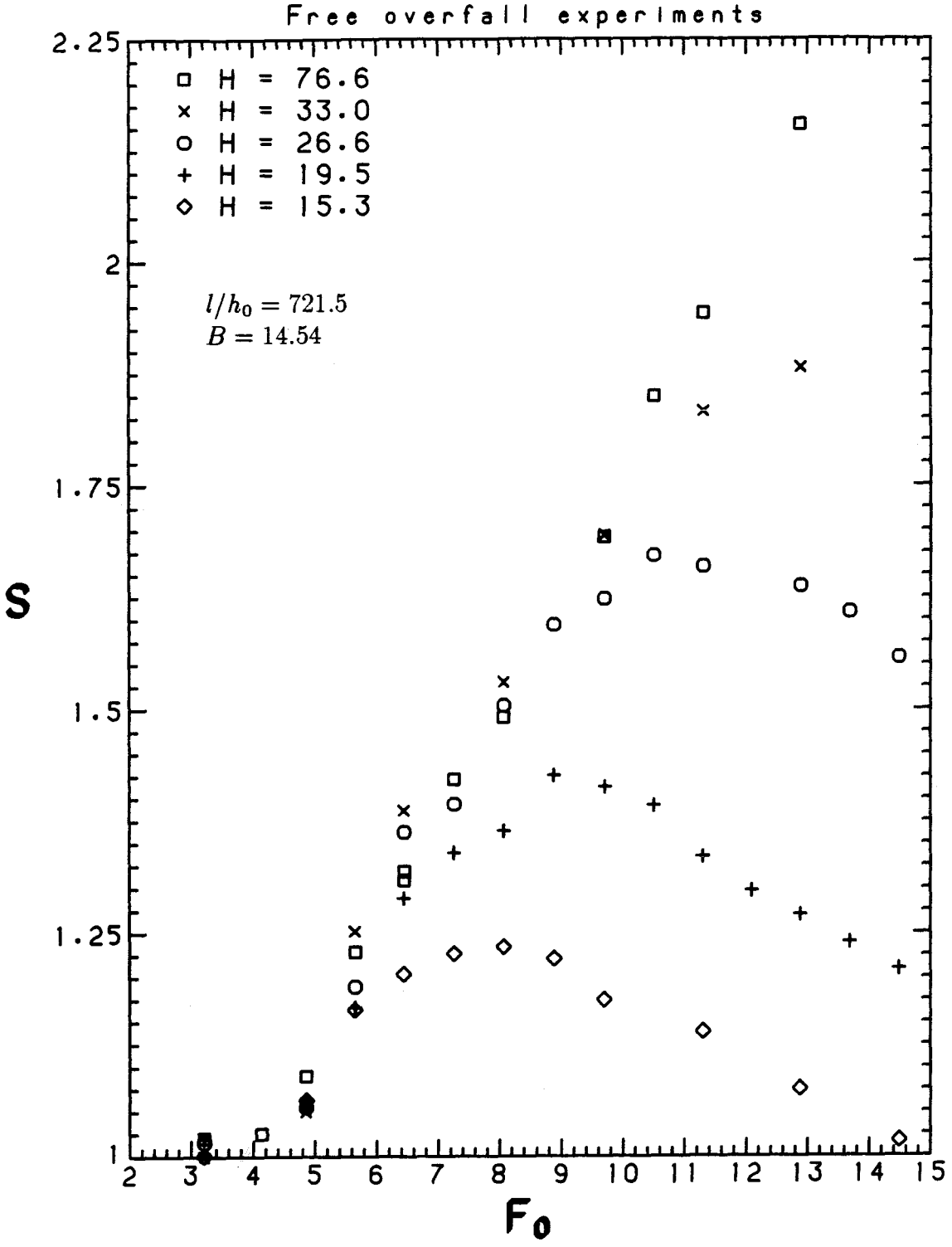

Figure 4.9: Measured dilution versus discharge densimetric Froude number.

The smoothness of the curves described by the experimental points is an indirect validation of the method used to measure S.

Experiments F5 and F6 (see Table 4.1) have the same discharge densimetric Froude number and the same ambient water depth. They were performed as a test of the reproducibility of the flow and of the repeatability of the dilution measurements. It can be seen that the two experimental points are indeed very close.

The same data are presented in a different perspective in Figure 4.10. The dependence of S on the water depth H is highlighted, with $\mathbf{F_0}$ as a parameter.

It can be generally concluded that an increase in the ambient water depth (keeping other variables constant) results in an increase in the entrainment rate (actually, the experimental points for $\mathbf{F_0} = 6.44$, 8.06 and 9.69 seem to indicate that S decreases as H passes from 33.0 to 76.6. However, such a decrease is very small, and it is very difficult to explain from a theoretical standpoint. It might therefore be caused by experimental error in the measurement of S). However, if the ambient water is deep at the outset, a further increase of H does not have any effect. It is understood that the concept of 'deep' ambient water is relative to the range of densimetric Froude numbers considered. For example, at $\mathbf{F_0} = 3.21$, $H = 15.3$ is already deep, while at $\mathbf{F_0} = 12.88$, $H = 15.3$ is definitely shallow and an increase in depth produces a dramatic increase in S.

The nondimensional depth of the lower layer after the jump region, r_1, versus the discharge densimetric Froude number, $\mathbf{F_0}$, is shown in Figure 4.11. The points representative of unstable flow conditions have been excluded from this plot, because of the ambiguity in the definition of a 'depth after the jump' in those flows.

The experimental points appear to be more or less on a straight line, and r_1 seems to be very little dependent on H.

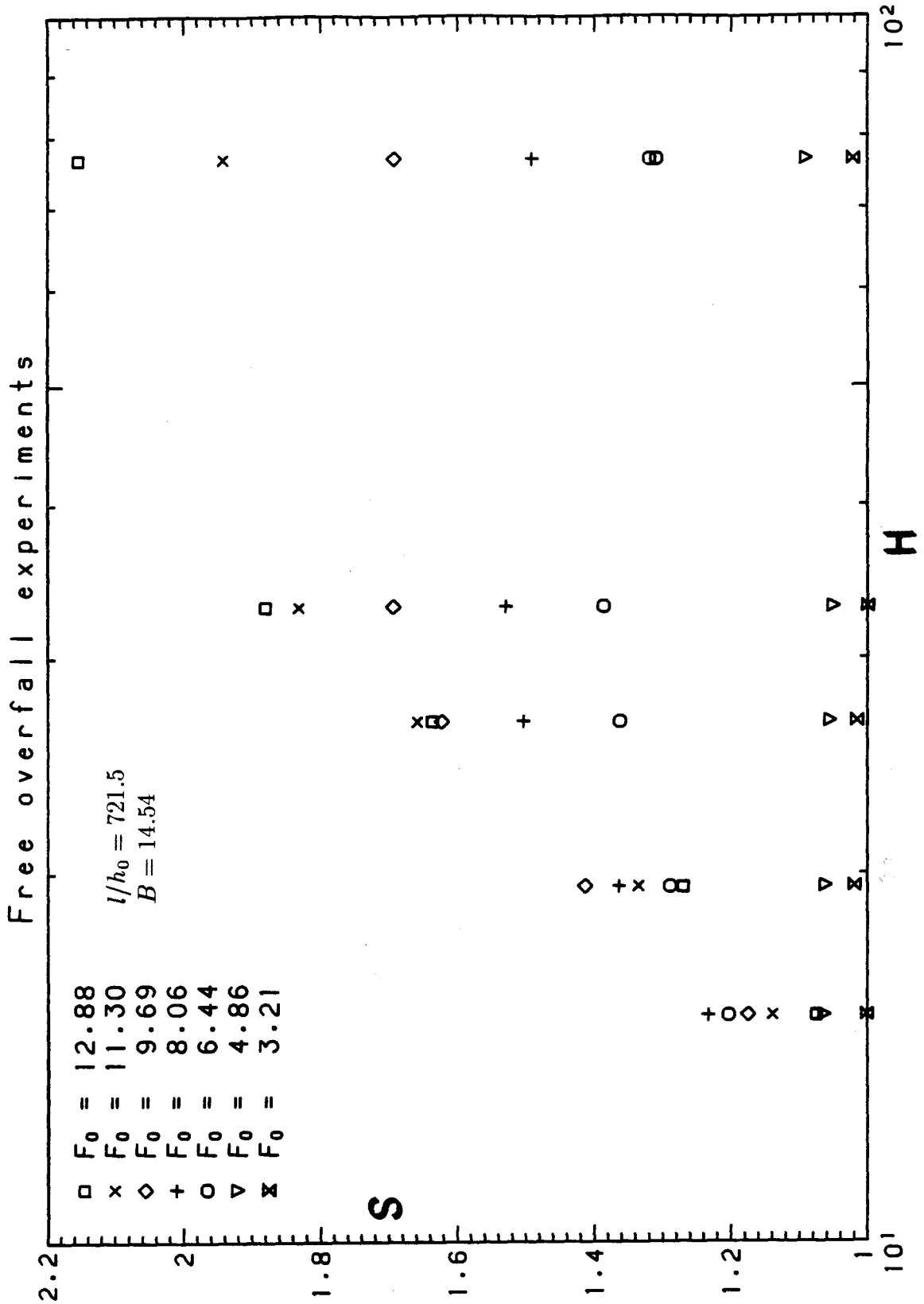

Figure 4.10: Measured dilution versus dimensionless ambient water depth.

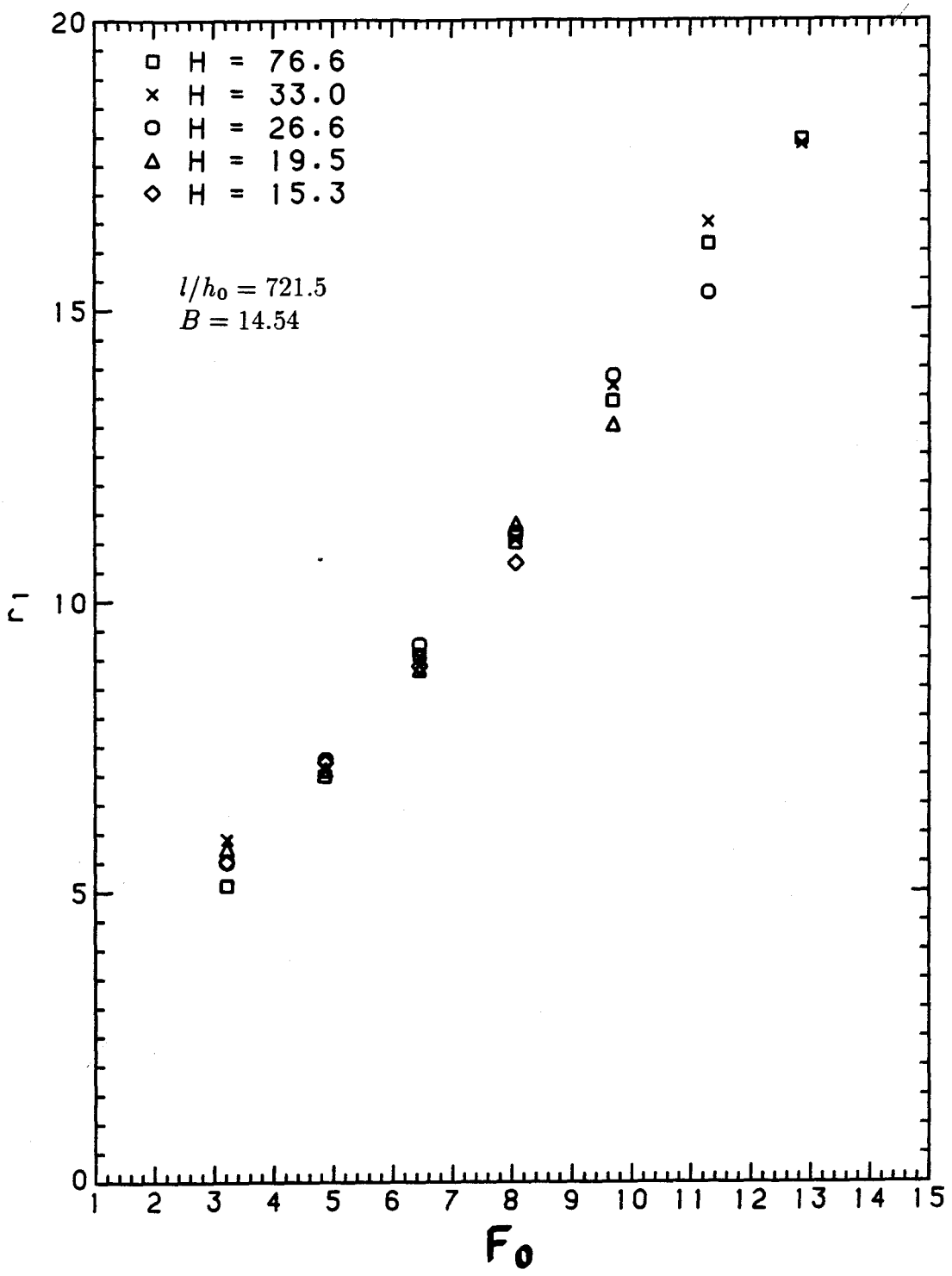

Figure 4.11: Depth of lower layer versus discharge densimetric Froude number.

Another interesting way of looking at the data is presented in Figure 4.12. It is often quoted in the literature (e.g., Wright, 1986) that the effect of the limited depth is negligible when the thickness of the flowing layer is less than a certain fraction of the total depth. In Figure 4.12 the ratio of the measured dilution, S, to the dilution measured in deep ambient water (with the same value of $\mathbf{F_0}$), $S_{76.6}$, is plotted in terms of h_1/d, the ratio of the salt water layer thickness to the ambient water depth.

It can be seen that in this series of experiments the presence of a limited depth is apparent only for values of h_1/d larger than ≈ 0.45.

The significance of the data is discussed further in Section 4.4.

4.2.2 Determination of the channel parameters

In this section the theory developed in Chapter 2 is applied to predict the characteristics of the flows occurring in the experimental channel. This will allow an assessment of the validity of the theory and, possibly, will allow more insight to be gained into the significance of the experimental results.

In order to integrate Equations 2.22, 2.23 and 2.24, with the constraints 2.25–2.28, in the way discussed in Section 2.4.4, it is necessary to determine the value of many parameters contained in those equations.

The length and width of the channel are known: b=10 cm and l=496.4 cm. But the friction factors f_b, f_{wl}, f_{wu} and f_i are not known a priori, and their determination involves several approximations that need some discussion.

The bottom friction factor f_b can be determined from the Moody curve for smooth channels. The Reynolds number used is based on the hydraulic radius of the lower layer, and it is given by

$$\mathbf{R_e} = 4\,\frac{q_1}{\nu}\,\frac{b}{2b + 2h_1'}\,, \tag{4.1}$$

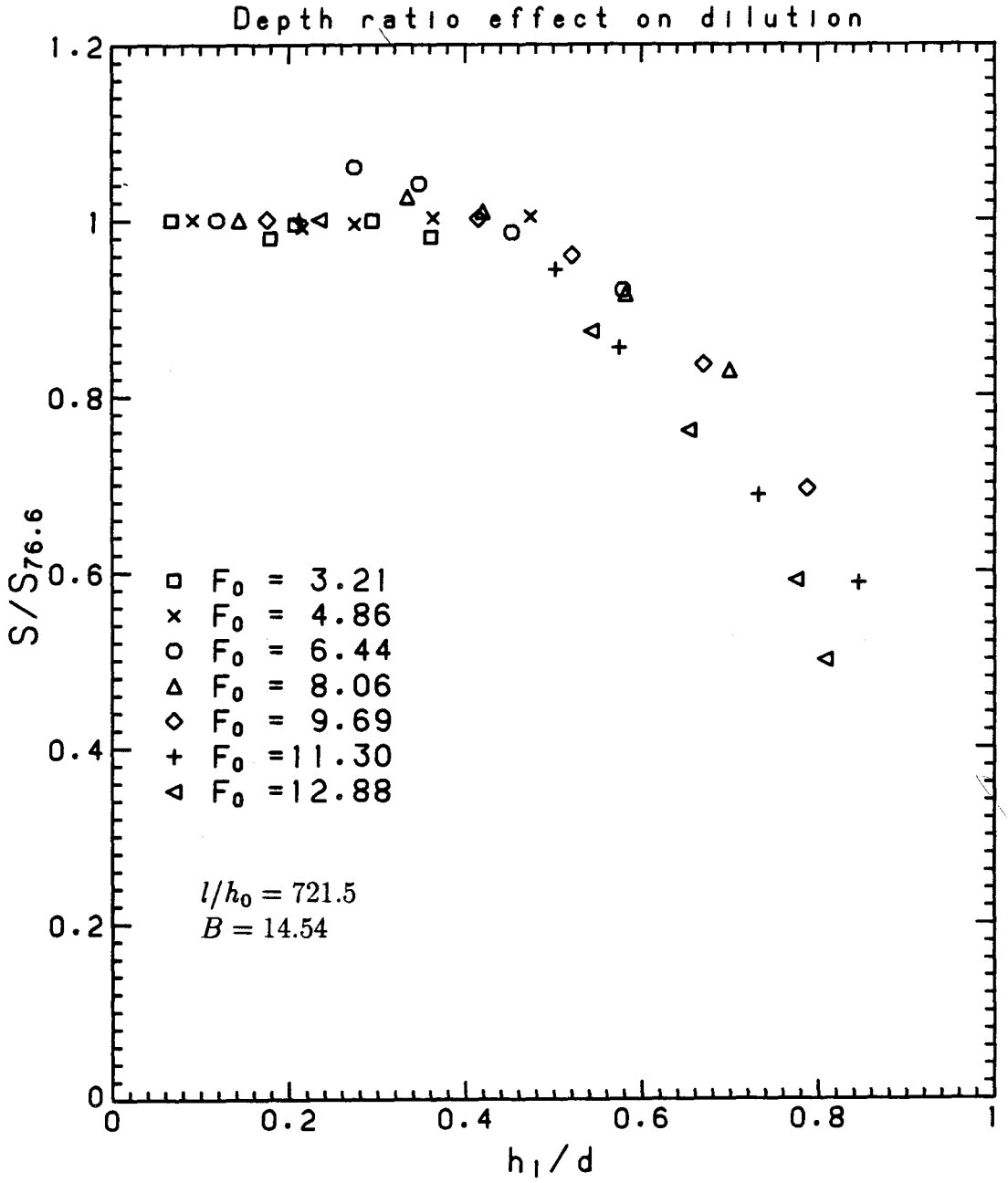

Figure 4.12: Depth ratio effect on dilution.

where all the symbols are as previously defined.

Strictly speaking, f_b will vary along the channel, since the layer thickness does. However, the approximation of constant friction factors in the gradually-varied counterflow will be introduced. Using the Moody diagram with values of $\mathbf{R_e}$ obtained from Equation 4.1, with the values of the variables taken from the experiments, leads to f_b in the range 0.016–0.058 for the experiments performed. As an additional simplifying assumption, the wall friction factors in the two layers, f_{wl} and f_{wu}, will be taken to be equal to the bottom friction factor.

A more difficult task is that of finding appropriate friction factors f_i which simulate momentum transfer at the interface along the entire gradually-varied counterflow. Known data on interfacial resistance are not very conclusive as yet. According to investigations by Lofquist (1960), Abraham and Eysink (1971), Keulegan (1981), and Arita and Jirka (1987), f_i is expected to depend mainly on Reynolds and densimetric Froude numbers, or on a combination of both. Dermissis and Partheniades (1984) suggested a dependence of f_i also on the density difference between the two fluids. However, these considerations lead to a degree of complexity undesirable in the present context. What is sought here is an average, bulk value of f_i to introduce into Equation 2.23, in the same spirit of the approximations introduced by Jirka and Harleman (1979) and Baddour (1987). A function giving f_i in terms of $\mathbf{R_e}$ and $\mathbf{F}$, and maybe $\Delta\rho/\rho$, could be used only in an iteration scheme, since the values of the Reynolds and Froude numbers are not known prior to the solution of the system of governing equations.

Determination of average friction factors representative of the resistance to the flow in the experimental channel was possible because of the availability of measured interfacial profiles. The procedure followed is illustrated in Figures 4.13, 4.14 and 4.15. For each experiment, f_b was obtained as discussed before from the Moody

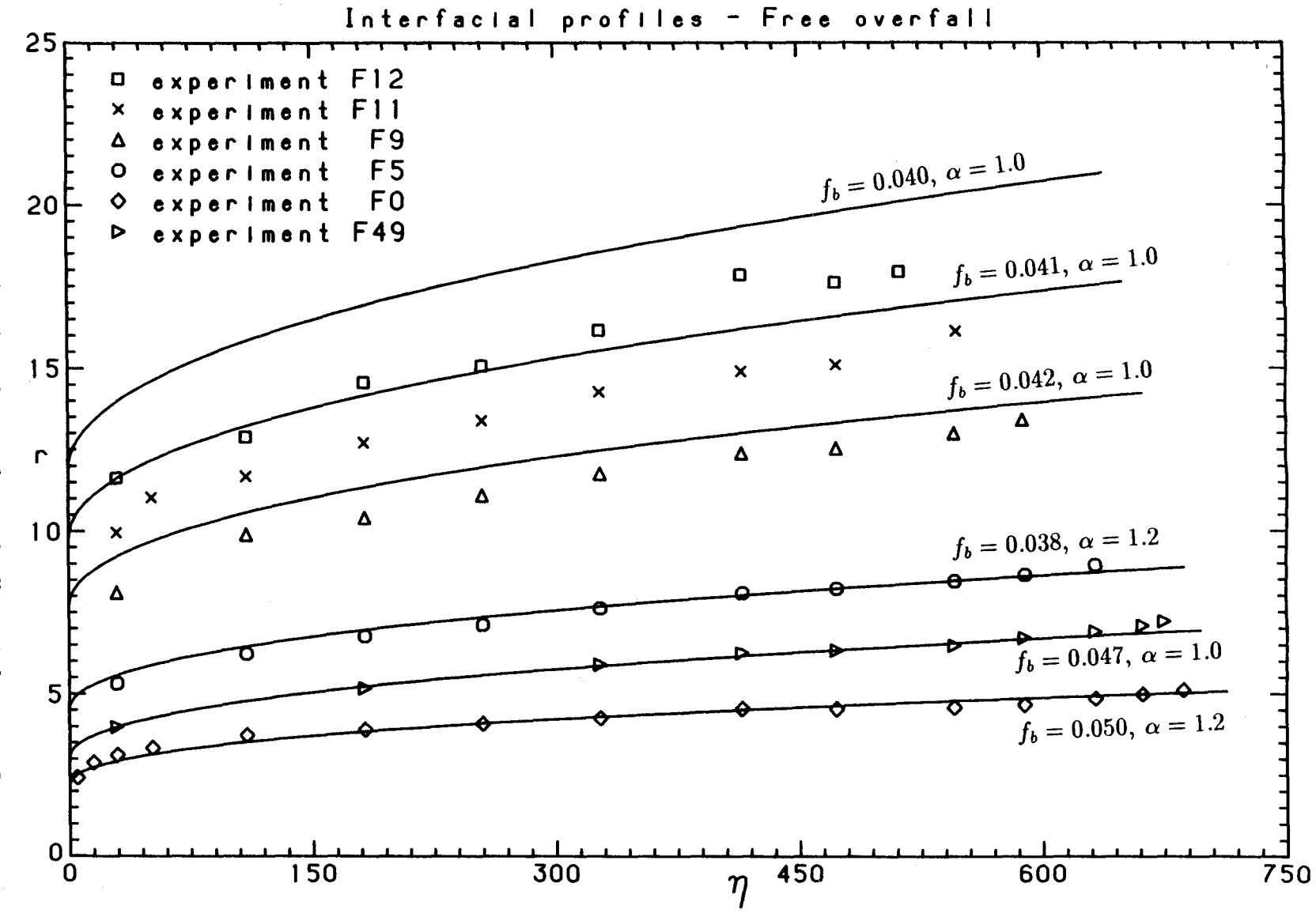

Figure 4.13: Interfacial profiles in the gradually-varied counterflow.

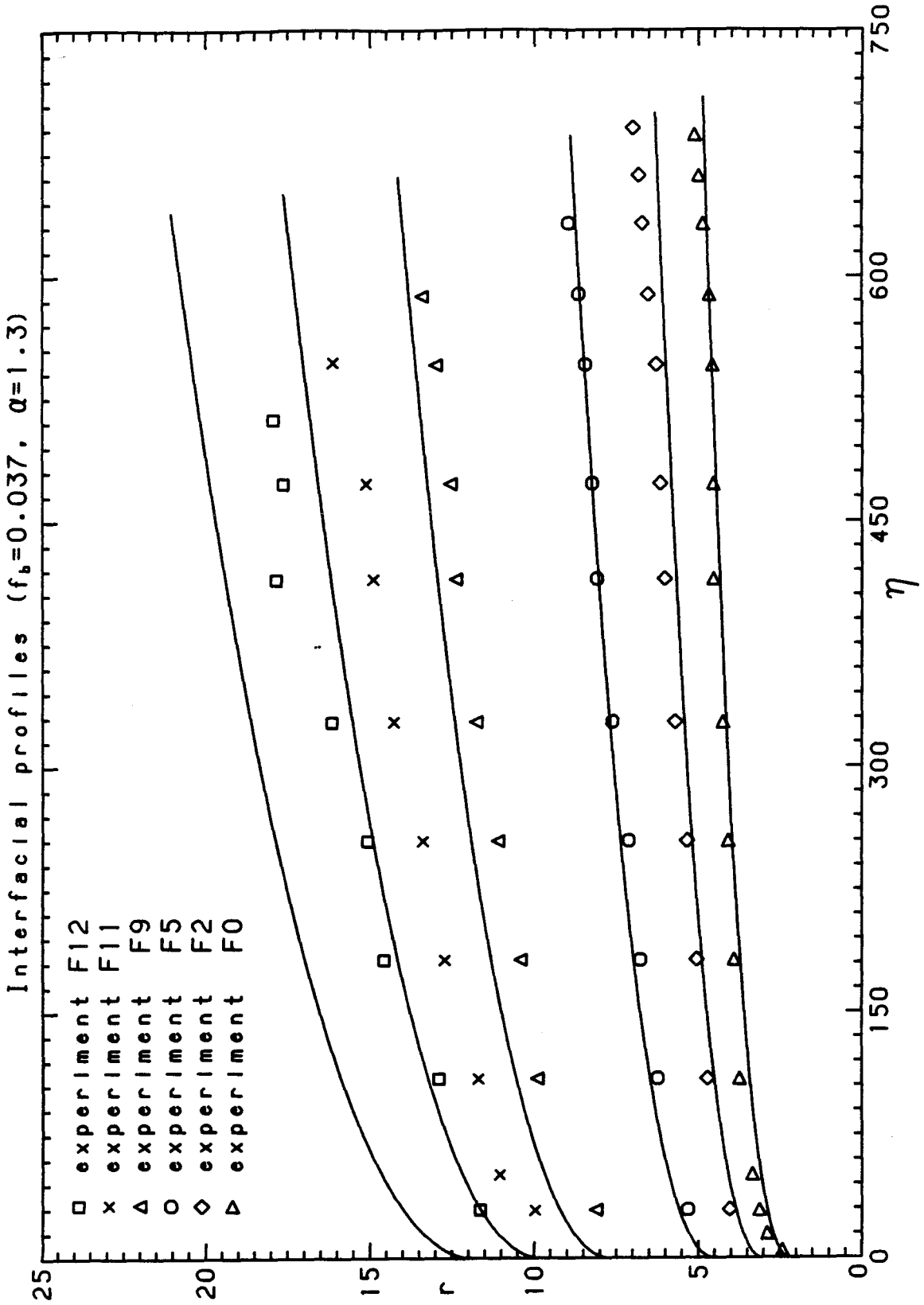

Figure 4.14: Interfacial profiles in the gradually-varied counterflow.

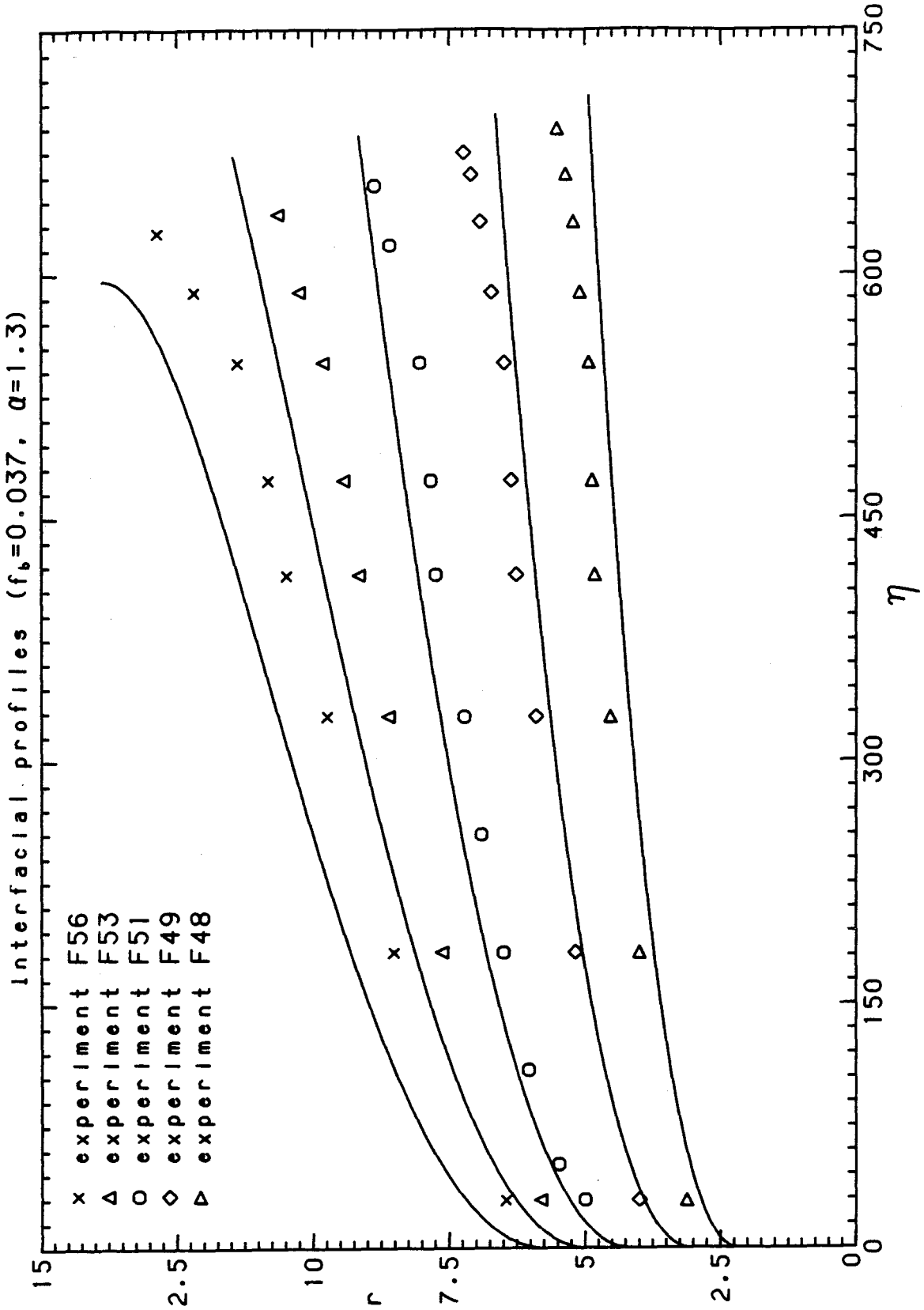

Figure 4.15: Interfacial profiles in the gradually-varied counterflow.

diagram, and Equations 2.23 and 2.24 were integrated, with S as obtained from the experiments and with several different trial values of $\alpha = f_i/f_b$. For each experiment the value of α giving the best fit between the integrated curve and the experimental points was obtained. This led to values of α in the range 1.0–2.6.

The fit obtained following this procedure is shown in Figure 4.13 for six experiments. In this figure, the nondimensional thickness of the dense layer, $r = h/h_0$, is plotted against the nondimensional distance from the free overfall, $\eta = x/h_0$. A good agreement is obtained between predicted and measured interfacial profiles. The small disagreement in the upper part of the graph is attributed to two factors. First, the actual critical section is very likely to occur somewhat upstream of the overfall brink, in analogy with what is observed in open channel flow (this fact has already been discussed in some detail in Chapter 2). The approximation of criticality at $\eta = 0$ is then expected to give theoretical profiles which are shifted towards the left in Figure 4.13 with respect to the actual measured profiles. Second, it should not be forgotten that the experimental points are defined by the *visual* thickness of the lower layer. It will be shown in Chapter 5 that the visual interface is in general lower than the zero-velocity line. Further dicussion of this matter is deferred to Chapter 5.

Sensitivity analyses were performed to assess the importance of the values of f_b and α in determining the shape of the integrated interfacial profiles. It was found that Equation 2.23 was affected very little by changes in the friction factors used, so much so that if $f_b = 0.037$ and $\alpha = 1.3$ were used in every case, the agreement between predicted and measured profiles remained fair (some examples are shown in Figures 4.14 and 4.15).

It will be recalled (Section 2.4.4) that a choice of the length of the jump region, L_j, had to be made to find the hydraulic solutions by matching the upstream and

downstream equations. It will also be recalled that the solutions were minimally sensitive to the choice made for L_j, since the chosen value was only used to determine the position where integration of Equation 2.23 had to be arrested.

Measured values of L_j are shown in Figure 4.16 for all of the free overfall experiments. The filled symbols represent unstable flows. As a crude, first order approximation, it can be stated that L_j grows linearly with $\mathbf{F_0}$ (the statement would be much more precise if the unstable flows were excluded, but an input value for L_j is desired for all experimental conditions). The equation of the least-square fit line,

$$\frac{L_j}{h_0} = -10.2 + 7.3\,\mathbf{F_0}\ , \tag{4.2}$$

will be used to obtain an approximate location of the point at which to arrest integration of Equation 2.23 and determine the value of the layer thickness r_{1d}.

In summary, the parameters which will be used to integrate the governing equations have been chosen to be $f_b = 0.037$, $\alpha = f_i/f_b = 1.3$ and L_j as given by Equation 4.2. This choice, which had to be made for a comparison between theory and experiments to be possible, resulted from a series of rather crude approximations. Nevertheless the values chosen have been shown to be reasonable when considered in conjunction with the experimental data, and they can be regarded as best-fit or 'calibration' values.

4.2.3 Comparison between theory and experiments

The one-dimensional theory presented in Chapter 2 is now tested against the experimental findings of the free overfall experiments.

The technique of solving the upstream and downstream problems separately, and then matching them to find the hydraulic solution satisfying all the governing equations (see Section 2.4.4) was repeatedly applied to find many plots on the (S, r_1)

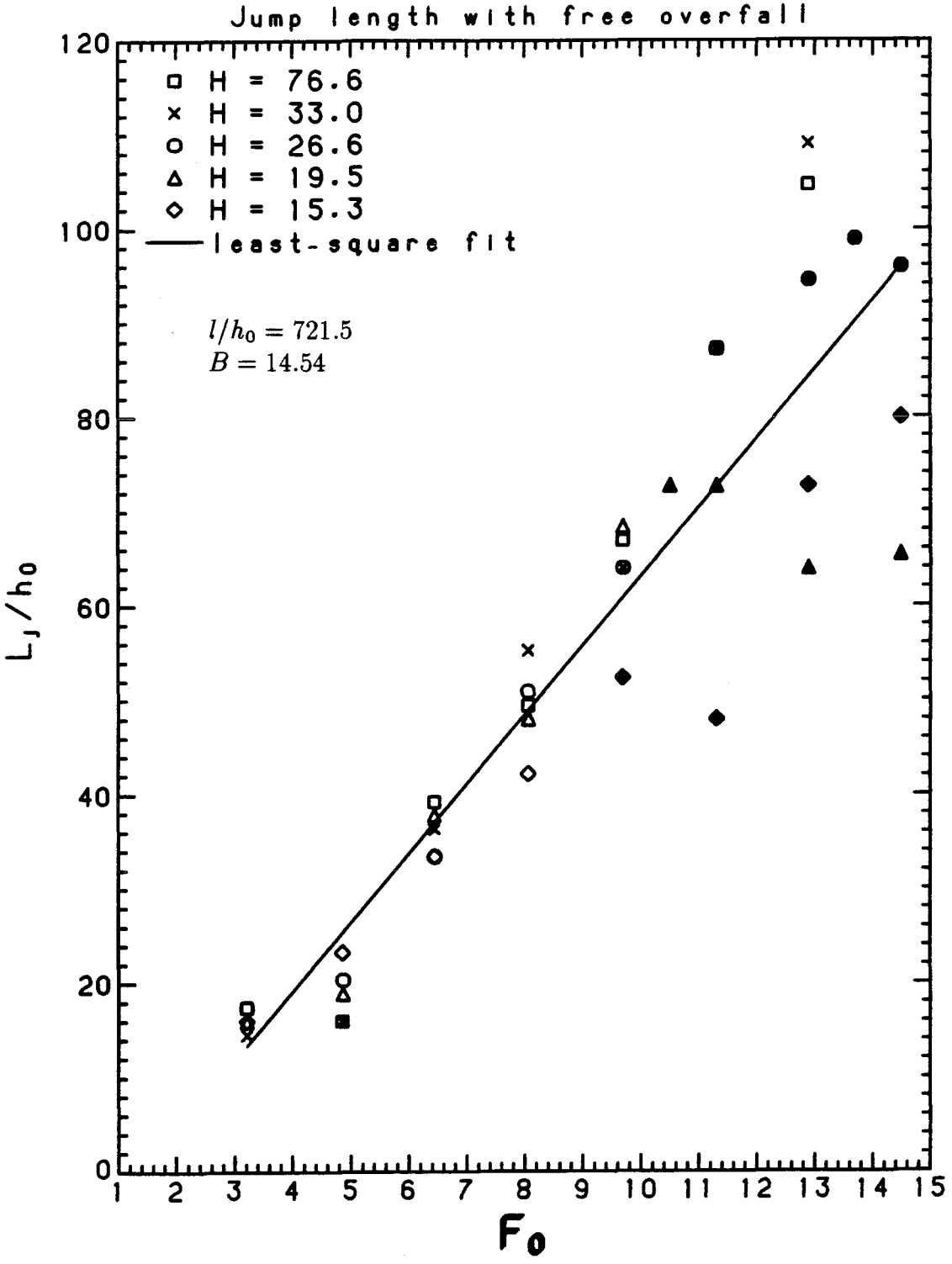

Figure 4.16: Nondimensional jump length vs. discharge densimetric Froude number.

plane, such as the ones shown in Figures 2.14, 2.15 and 2.16. This allowed the determination of theoretical predictions for the dilution S and for the lower layer thickness r_1, under several different flow conditions. The predicted points are presented, together with experimental data, in Figures 4.17 and 4.18. Only three ambient water depths H are presented in Figure 4.17, in order to maintain good legibility.

Considering all of the approximations that have been necessary to obtain the theoretical curves, the agreement between theory and experiments is remarkable in the cases $H = 26.6$ and $H = 15.3$.

The assumption of uniform velocity and density profiles, which is at the base of the one-dimensional theory, appears to be satisfactory. Not only does the one-dimensional theory correctly predict the general behavior of the hydraulic solutions, but it even affords a fairly precise determination of the dilution S resulting from a given discharge densimetric Froude number $\mathbf{F_0}$ in a given ambient water depth H.

The agreement is not as satisfactory for the case of 'deep' ambient water, $H = 76.6$, especially at large values of $\mathbf{F_0}$. The general shape of the curve agrees with the experimental data, but the entrainment rates predicted are up to 30% larger than the measured values.

A similar behavior can be observed in Figure 4.18, where the dimensionless flow depth $r_1 = h_1/h_0$ is plotted versus $\mathbf{F_0}$ (the experimental points are the same as presented in Figure 4.11). It can be seen that the one-dimensional theory predicts values of r_1 exceeding those actually observed, especially at high values of $\mathbf{F_0}$.

A plausible explanation for the discrepancy between theory and experiments can be derived from an observation of the graph in Figure 4.19. This figure shows the upstream predicted depth curve, $r_{1u} = r_{1u}(S)$, and the downstream predicted depth curve, $r_{1d} = r_{1d}(S)$, which intersect at the point (S, r_1). The actually measured point obtained from the experiment is also shown for comparison (this graph refers to

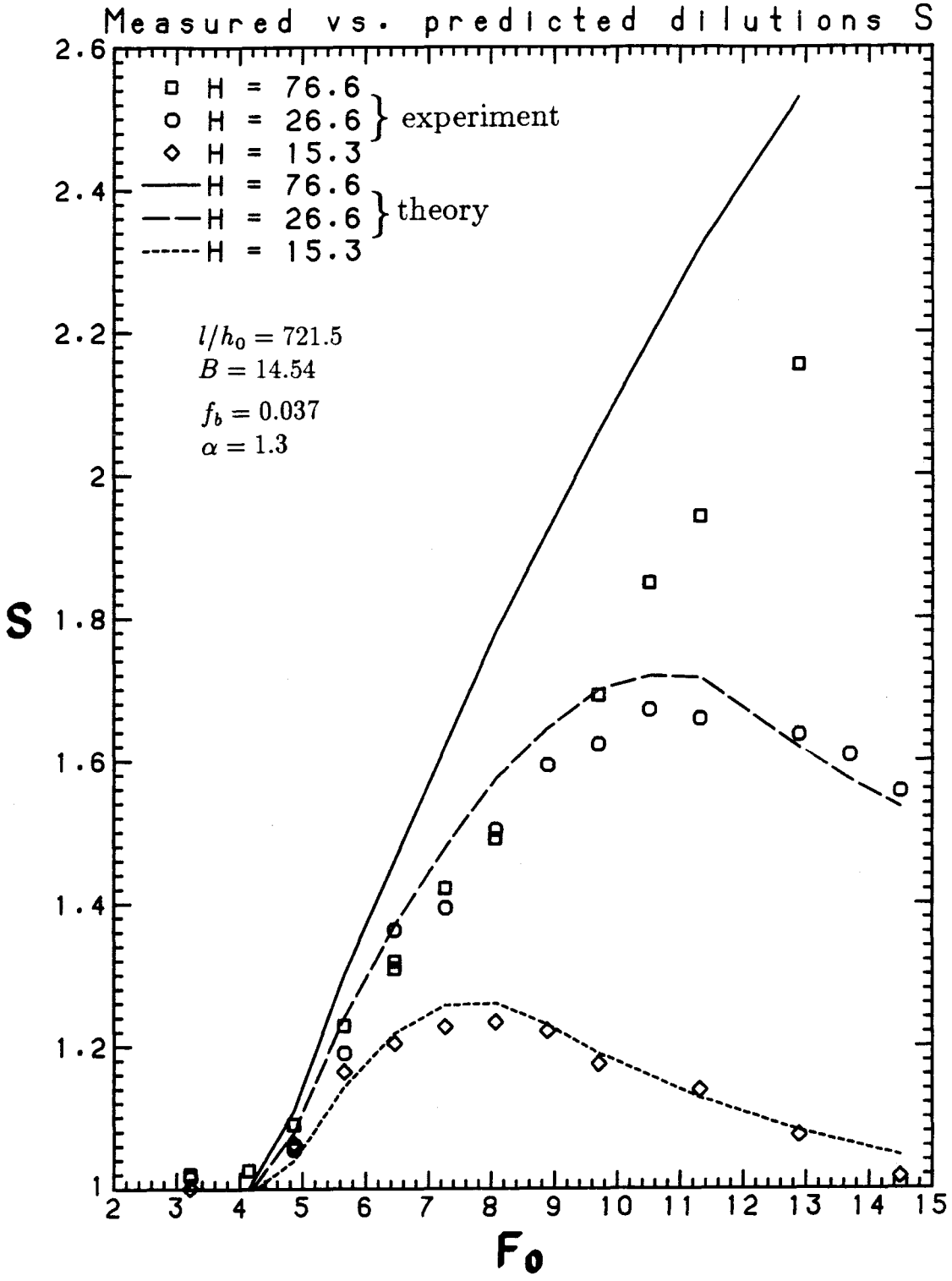

Figure 4.17: Comparison between theory and experiments.

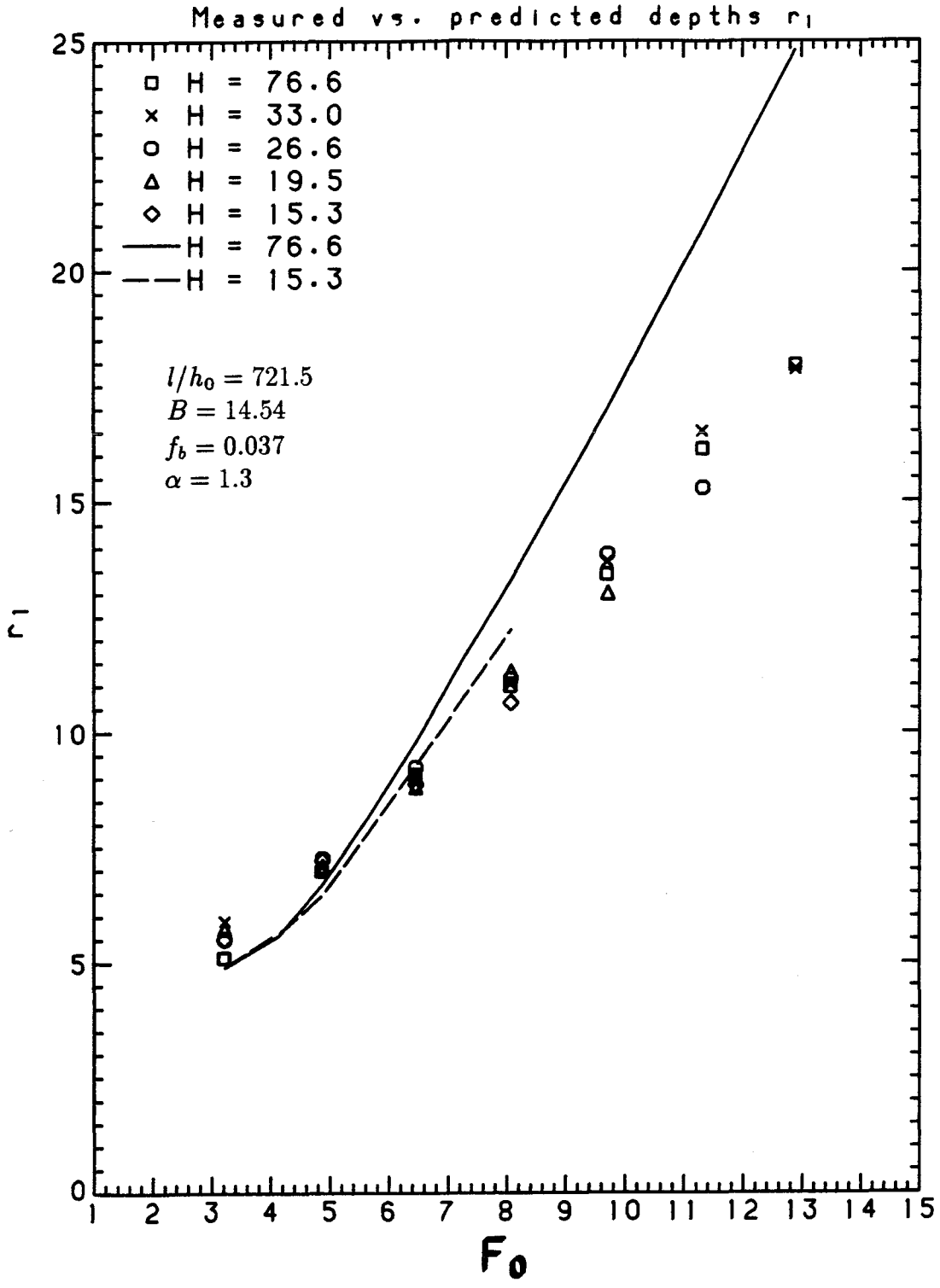

Figure 4.18: Comparison between theory and experiments

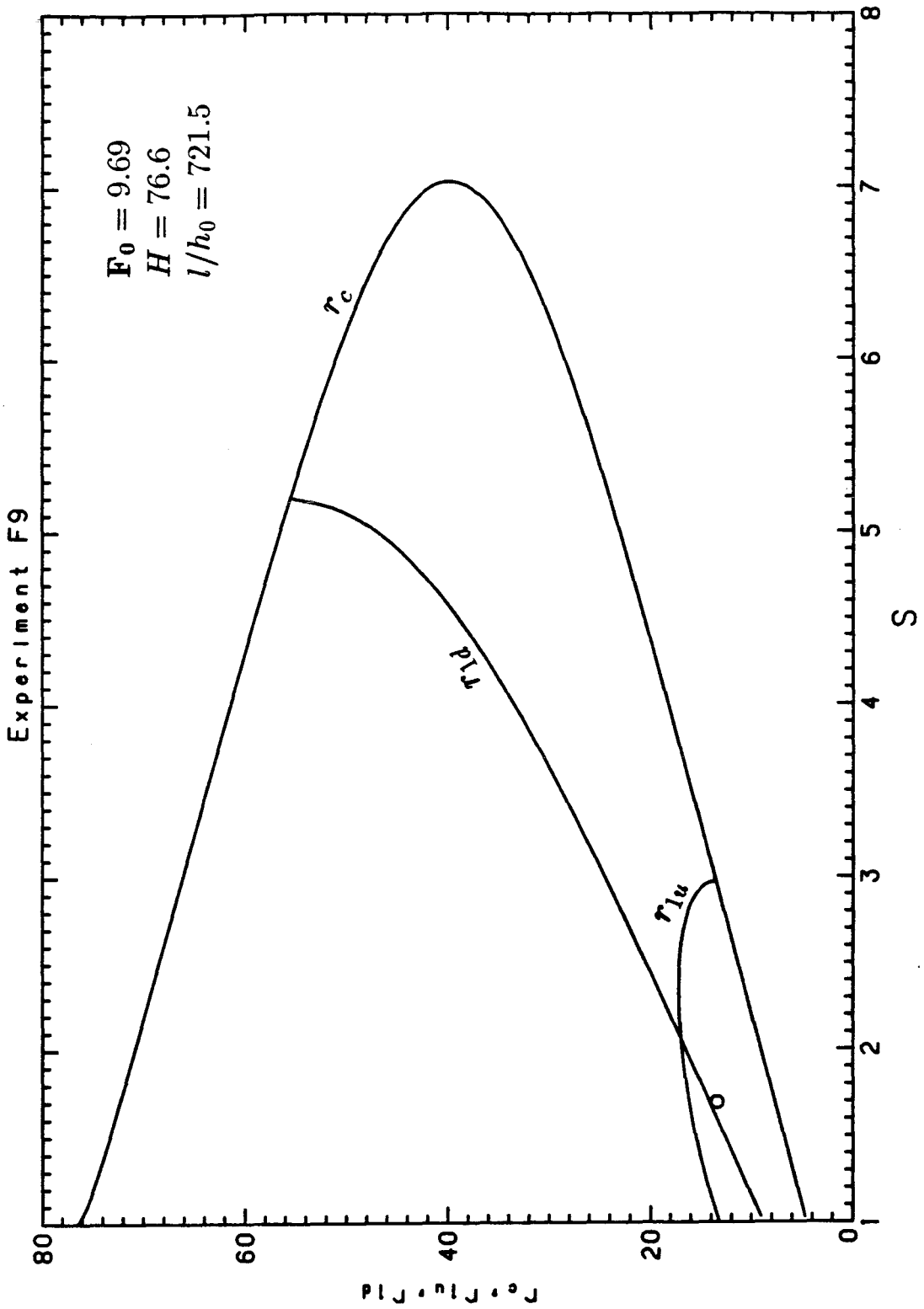

Figure 4.19: Example of comparison between theory and experiment in the (S, r_1) plane.

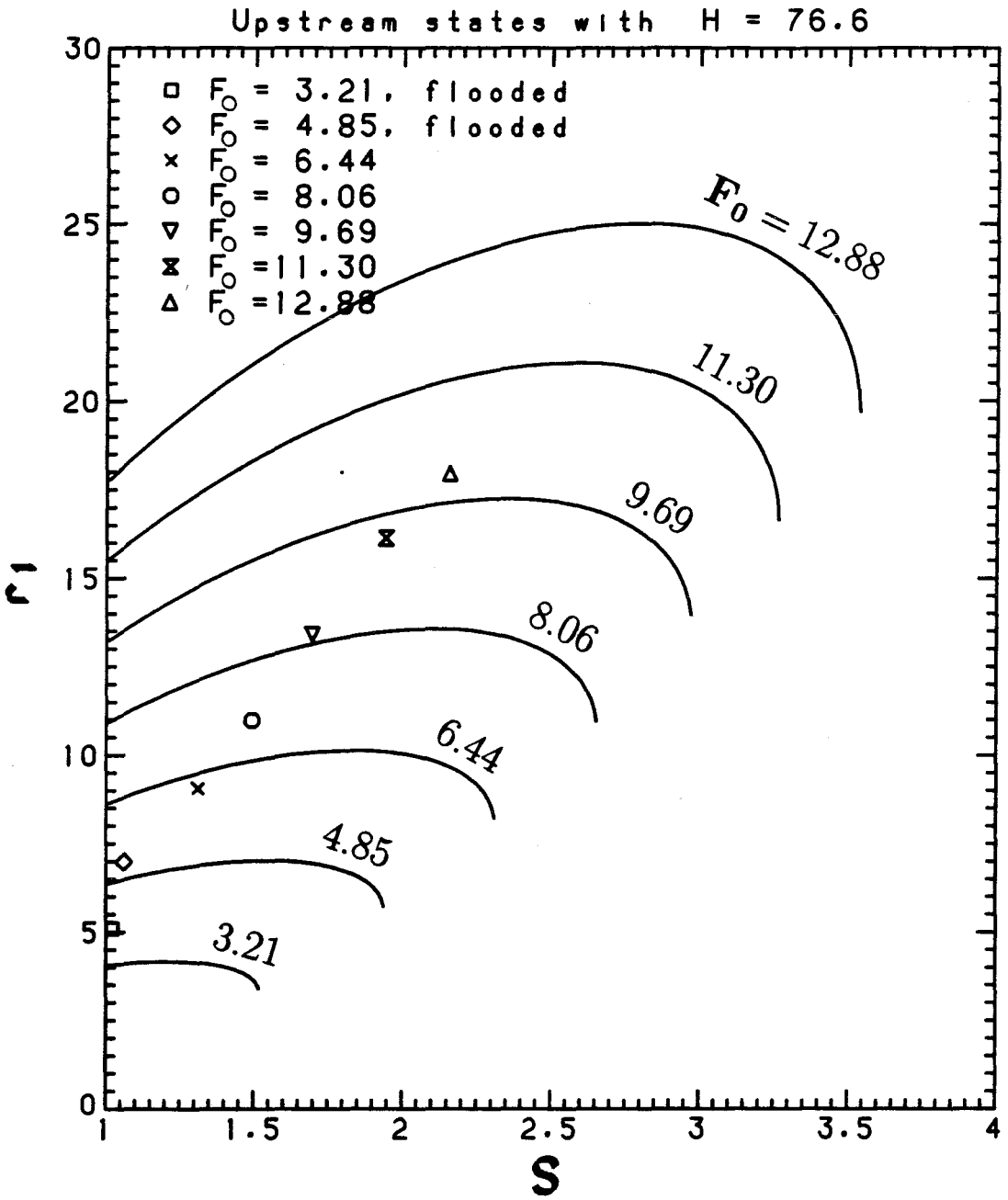

Figure 4.20: Comparison between predicted and measured upstream states.

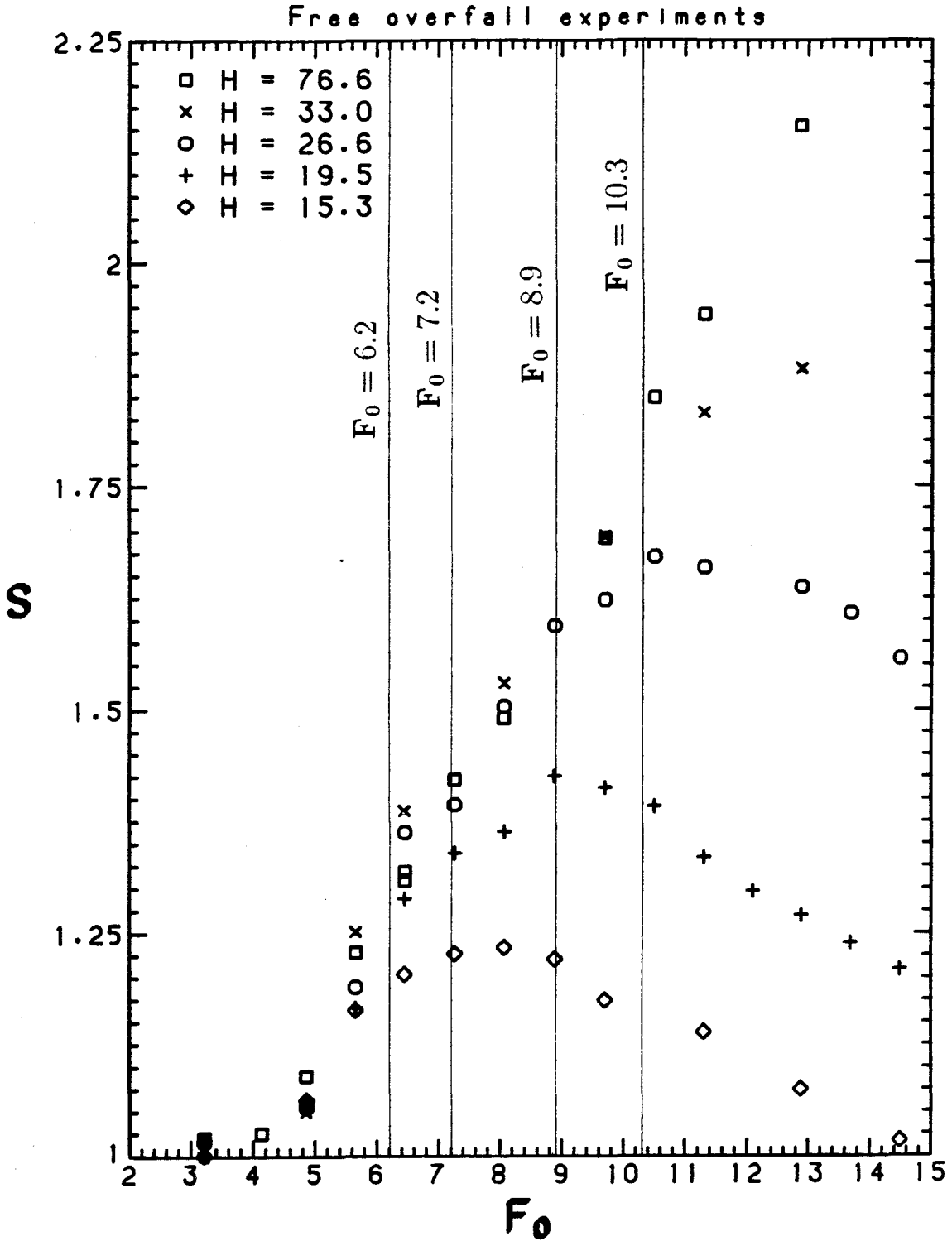

Figure 4.21: Predictions of Eq. 2.35 vs. experimental points.

$H = 76.6$ and $\mathbf{F_0} = 9.69$, i.e., to the conditions of experiment F9, but the situation observed here is typical of all the experiments with $H = 76.6$ and $\mathbf{F_0} > 7$). It can be observed that the experimental point falls very nearly on the curve $r_{1d} = r_{1d}(S)$, but is below the curve $r_{1u} = r_{1u}(S)$. This suggests that the error observed results from an inaccuracy in Equation 2.22, which defines the upstream flow, rather than from problems related to Equations 2.23 and 2.24, which define the downstream conditions. In other words, the upstream curve obtained by solving Equation 2.22 predicts a depth of the dense layer subsequent to the jump larger that what one actually observes. This analysis appears to be confirmed by the data in Figure 4.20. At large $\mathbf{F_0}$, the sets of possible upstream states (solid curves, obtained by solving Equiation 2.22) are all above the observed points. The conservation of flow force, as stated by Equation 2.22, appears to fail at large values of H and $\mathbf{F_0}$. This may result from several factors.

First, it is possible that in the experimental channel the loss of flow force due to boundary shear in the jump region is not negligibly small.

Second, it will be recalled that Equation 2.22 was based on the assumption of a uniform velocity profile. If the velocity profile is not uniform, a correction factor may have to be introduced into the equation. This could well result in increasing the computed flow force downstream of the jump.

Third, the assumption of a horizontal free surface may not be justified over the entraining region, where a non-hydrostatic pressure field in the ambient water is likely to occur (see Miller and Comings, 1957).

Further discussion of this issue is presented in Chapter 5, where new insight is gained from the detailed velocity and density measurements.

To conclude, it is remarkable to notice how well the data presented in Figure 4.9 agree with Equation 2.35, which predicted the value of $\mathbf{F_0}$ where the effect of the

flow confinement would become apparent. For $H = 76.6$, 33.0, 26.6, 19.5 and 15.3, Equation 2.35 predicts that the curve $S = S(\mathbf{F_0})$ will depart from the approximately linear behavior of the case $H = \infty$ at $\mathbf{F_0} = 18.0$, 10.3, 8.9, 7.2 and 6.2, respectively. Figure 4.21 indicates that, as expected, for $H = 76.6$ ('deep' ambient water) the effect of confinement is not felt in the range of $\mathbf{F_0}$ used in the experiments, since $\mathbf{F_0}$ was always below the value 18.0. However, in the other cases departure from the deep water curve takes place at values of $\mathbf{F_0}$ very close to those predicted.

4.3 Broad-crested weir experiments

Fifty-three experiments represent the data base for this series. Table 4.2 summarizes the experimental conditions and some of the experimental results.

The discharge densimetric Froude number, $\mathbf{F_0}$, was varied between approximately 3 and 15. This was done by varying both the discharge flowrate, q_0, and the initial density difference, $(\Delta\rho/\rho)_0$, while maintaining a constant discharge depth, h_0. Weirs with five different heights were employed at the downstream end of the channel, including the case of zero height ('free overfall'). These resulted in five different nondimensional weir heights, r_w, which varied between 0.000 and 7.122. The ambient water depth was held constant, with $H = 76.6$ ('deep' ambient water), in order to distinguish between the effects of weir height and limited ambient depth on the characteristics of the flow.

Table 4.2 reports the type of flow observed, the measured dilution S, the length of the jump region and the two previously defined salt water layer thicknesses, h_1 and h_1', as well as the measured flowrate in the lower layer at the end of the channel, q_1.

Table 4.2. Summary of parameters for broad-crested weir experiments.

Exp. #	F_o	r_w	S	h_1 (cm)	L_j (cm)	$(\Delta\rho/\rho)_o$ (%)	q_o (cm²/s)	q_1 (cm²/s)	d (cm)	h_1' (cm)	Flow type
W0	3.209	0.000	1.021	3.52	12	2.054	8.22	8.39	52.66	3.13	FL
W1	4.138	0.000	1.026	-	-	2.054	10.33	10.60	52.71	-	
W2	4.851	0.000	1.060	4.81	11	1.204	9.53	10.10	52.79	4.19	FL
W3	4.860	0.000	1.090	-	-	2.054	12.45	13.57	52.71	-	
W4	5.655	0.000	1.229	-	-	1.148	10.83	13.31	52.71	-	
W5	6.443	0.000	1.309	6.24	27	0.754	10.00	13.09	52.68	5.62	FR
W6	6.444	0.000	1.319	-	-	1.148	12.34	16.28	52.73	-	
W7	7.253	0.000	1.422	-	-	1.148	13.89	19.75	52.71	-	
W8	8.059	0.000	1.491	7.56	34	1.033	14.64	21.83	52.69	7.11	FR
W9	9.688	0.000	1.692	9.23	46	0.982	17.16	29.03	52.72	8.57	FR
W10	10.496	0.000	1.849	-	-	1.148	20.10	37.17	52.66	-	
W11	11.301	0.000	1.942	11.10	60	0.882	18.97	36.85	52.69	10.37	FR
W12	12.876	0.000	2.154	12.35	72	0.765	20.13	43.35	52.68	12.20	FR
W13	3.209	1.439	1.018	-	-	1.737	7.56	7.70	52.72	-	
W14	4.860	1.439	1.051	4.77	28	1.239	9.67	10.16	52.68	4.52	FL
W15	5.650	1.439	1.100	-	-	1.737	13.31	14.64	52.68	-	
W16	6.443	1.439	1.145	5.89	26	1.048	11.79	13.50	52.67	5.49	FR
W17	7.246	1.439	1.327	-	-	1.737	17.07	22.65	52.72	-	
W18	8.062	1.439	1.369	7.36	36	1.239	16.04	22.40	52.69	7.01	FR
W19	9.067	1.439	1.565	-	-	1.737	21.36	33.44	52.72	-	
W20	9.690	1.439	1.568	9.29	44	1.079	17.99	28.21	52.71	8.45	FR
W21	10.493	1.439	1.700	-	-	0.811	16.89	28.71	52.70	-	
W22	11.296	1.439	1.795	10.75	58	1.048	20.67	37.10	52.64	9.91	FR
W23	11.299	1.439	1.803	10.82	55	0.901	19.17	34.58	52.70	10.37	FR
W24	12.879	1.439	1.927	12.14	65	0.811	20.73	39.94	52.70	11.89	FR
W25	4.860	3.401	0.995	5.95	21	1.247	9.70	9.65	52.72	5.70	FL
W26	6.442	3.401	1.026	6.59	26	1.106	12.11	12.43	52.69	6.34	FL
W27	8.059	3.401	1.093	7.61	32	1.005	14.44	15.78	52.72	7.26	FL
W28	8.875	3.401	1.222	-	-	0.790	14.10	17.23	52.73	-	
W29	9.689	3.401	1.364	9.26	45	1.113	18.27	24.92	52.72	8.85	FR

Table 4.2 (Cont.)

Exp. #	F_o	r_w	S	h_1 (cm)	L_j (cm)	$(\Delta\rho/\rho)_o$ (%)	q_o (cm /s)	q_1	d (cm)	h_1' (cm)	Flow type
W30	10.493	3.401	1.495	-	-	0.790	16.67	24.92	52.78	-	
W31	11.299	3.401	1.590	10.87	54	0.969	19.88	31.61	52.72	10.49	FR
W32	12.092	3.401	1.715	11.64	56	0.790	19.21	32.94	52.75	-	FR
W33	12.876	3.401	1.778	12.48	65	0.759	20.05	36.65	52.75	-	FR
W34	4.859	5.305	1.005	6.93	26	1.601	10.99	11.04	52.69	6.82	FL
W35	6.444	5.305	1.024	7.57	30	0.937	11.15	11.42	52.72	7.47	FL
W36	8.063	5.305	1.063	8.34	35	0.937	13.95	14.83	52.71	8.09	FL
W37	9.692	5.305	1.138	9.26	37	1.082	18.02	20.51	52.73	8.94	FL
W38	10.492	5.305	1.199	-	-	0.718	15.89	19.06	52.75	-	
W39	11.300	5.305	1.332	10.73	48	0.934	19.52	26.00	52.74	10.55	FR
W40	12.090	5.305	1.458	-	-	0.718	18.31	26.69	52.71	-	
W41	12.875	5.305	1.571	12.51	60	0.738	19.77	31.05	52.70	12.60	FR
W42	13.681	5.305	1.699	-	-	0.718	20.72	35.21	52.75	-	
W43	14.491	5.305	1.764	13.98	72	0.598	20.03	35.34	52.69	13.29	FR
W44	4.856	7.122	1.010	8.25	34	1.075	9.00	9.09	52.72	8.19	FL
W45	6.442	7.122	0.999	8.89	33	1.052	11.81	11.80	52.69	8.76	FL
W46	8.062	7.122	1.031	9.40	42	1.075	14.94	15.40	52.71	9.35	FL
W47	9.693	7.122	1.090	10.38	39	1.064	17.87	19.47	52.69	10.10	FL
W48	11.298	7.122	1.124	10.95	45	0.842	18.53	20.82	52.69	10.76	FL
W49	12.877	7.122	1.195	12.30	48	0.701	19.27	23.03	52.67	12.02	FL
W50	13.682	7.122	1.327	-	-	0.549	18.12	24.04	52.72	-	
W51	14.488	7.122	1.418	14.13	67	0.587	19.84	28.14	52.75	13.65	FR
W52	15.291	7.122	1.599	-	-	0.549	20.25	32.37	52.69	-	

FL = flooded internal hydraulic jump
FR = free internal hydraulic jump

For all the experiments in this table, h_o = 0.688 cm

As for the case of the free overfall experiments, a clear transition between flooded jumps and free jumps was not observed. Unstable flows were not present in this series, as should be expected with a deep ambient water layer.

The presentation of the results of these experiments will be very similar to the presentation of the results of the free overfall series. A few graphs will be used to summarize the experimental data. A determination of the channel parameters will then lead to a comparison between the predictions of the one-dimensional theory and the measurements in the laboratory.

4.3.1 Results

The data contained in Table 4.2 can be described graphically in ways that facilitate the interpretation of the experimental findings.

The most interesting functional relationship involves the measured dilutions S and the discharge densimetric Froude numbers $\mathbf{F_0}$. Five different plotting symbols have been employed in Figure 4.22 for the five different weir heights r_w used in the experiments. It can be seen that for all values of r_w, S is equal to one and is independent of $\mathbf{F_0}$ at low values of $\mathbf{F_0}$ (flooded jumps), while S is more or less linearly increasing with $\mathbf{F_0}$ at high values of $\mathbf{F_0}$ (free jumps). However, the value of $\mathbf{F_0}$ at which S starts increasing is strongly dependent on r_w: for large values of r_w, the jumps remain flooded, with $S \simeq 1$, until $\mathbf{F_0}$ becomes quite large. For example, if $r_w = 7.122$ (which represents the highest weir used in this investigation) the entrainment of ambient fluid remains negligible for all values of $\mathbf{F_0} < 8$. On the other hand, if the weir is low, the entrainment rates at $\mathbf{F_0} \approx 8$ are considerable.

Experiments W22 and W23 (see Table 4.2) have the same discharge densimetric Froude number and the same weir height. They were performed as a test of the reproducibility of the flow and of the repeatability of the dilution measurement. It

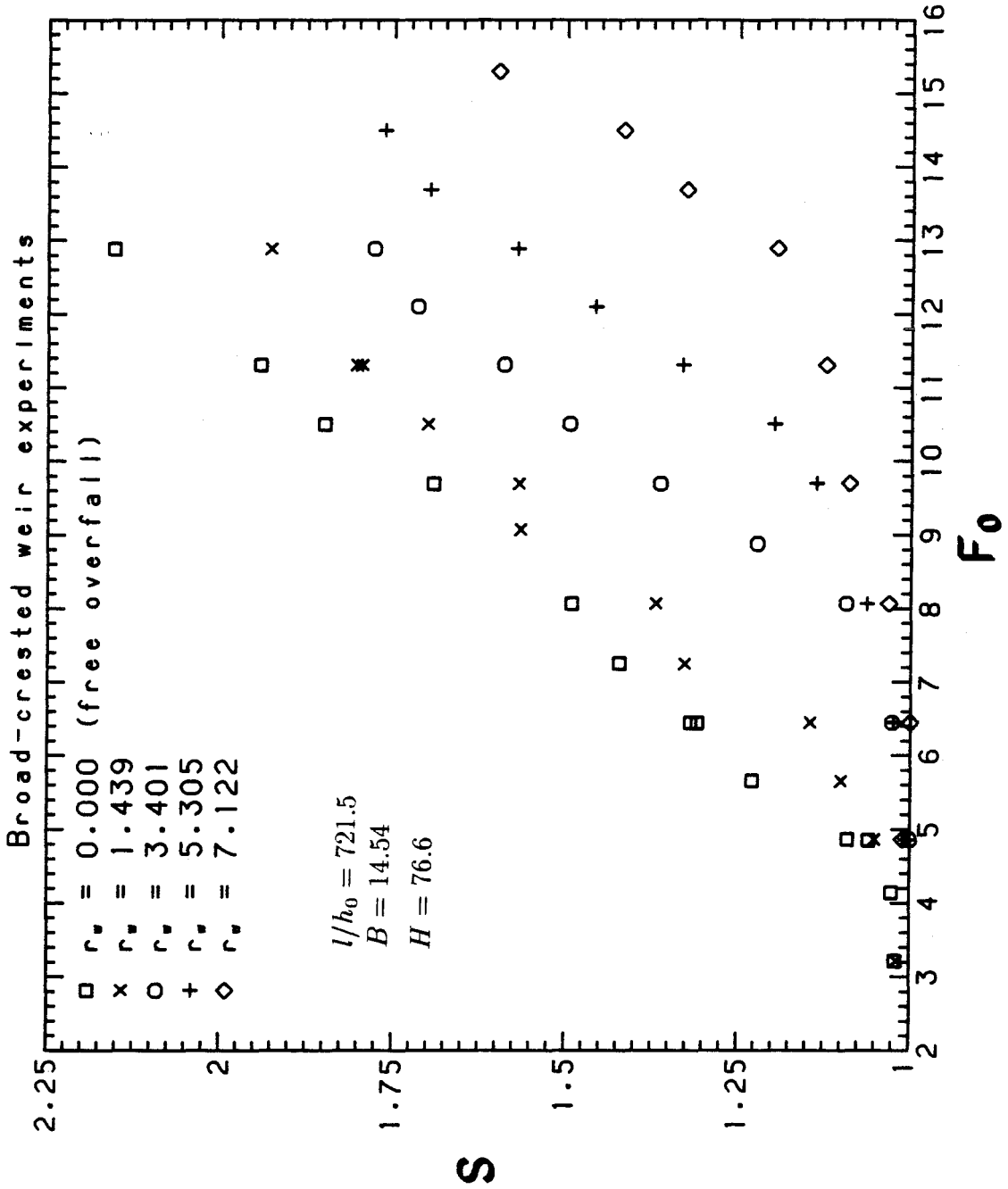

Figure 4.22: Measured dilution versus discharge densimetric Froude number.

can be seen from Figure 4.20 that the two experimental points are indeed very close.

The same data are presented in a different perspective in Figure 4.23. The dependence of S on r_w is highlighted, with $\mathbf{F_0}$ as a parameter. It can be observed how an increase in r_w causes a reduction in S, for any given $\mathbf{F_0}$. At very low values of $\mathbf{F_0}$, however, the jump is flooded even with $r_w = 0$, so that no substantial change in dilution results from an increase in r_w.

The nondimensional depth of the lower layer after the jump region, r_1, is shown as a function of the discharge densimetric Froude number in Figure 4.24. The same data are presented in Figure 4.25, but here r_1 is plotted against the nondimensional weir height, r_w. The filled symbols represent flooded internal hydraulic jump conditions. An interesting observation emerges from these two figures. While for flooded jumps an increase in r_w results in an increase in r_1, in the case of free internal hydraulic jumps r_1 is approximately constant for a fixed $\mathbf{F_0}$, and notably independent of r_w. In other words, the increase in thickness of the lower layer caused by an increase in weir height is offset by a decrease due to the reduced entrainment in the mixing region. The net result is an unchanged lower layer thickness. Although somewhat counterintuitive, this should not be considered at all surprising. It had been argued by Wilkinson and Wood (1971) that an increase in weir height could have even resulted in a decrease in the depth of flow upstream of the weir, although experimental evidence had not been provided.

Further discussion of the significance of the data is presented in Section 4.4.

4.3.2 Determination of the channel parameters

In order to integrate Equations 2.22, 2.23, 2.29 and 2.30, along with constraints 2.25–2.28, in the way discussed in Section 2.4.4, it is necessary to choose values for the parameters contained in those equations. Since this is done with the

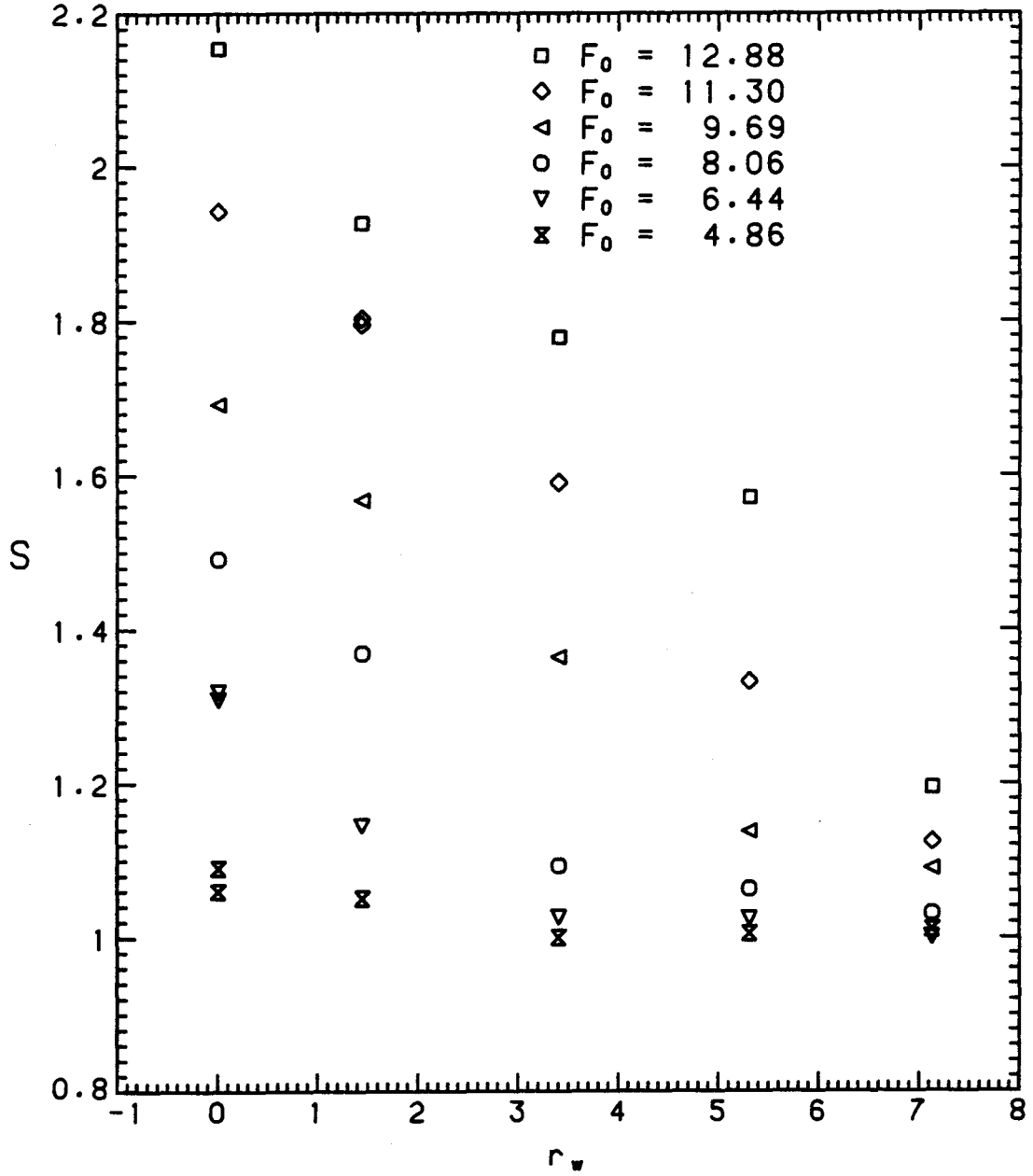

Figure 4.23: Measured dilution versus dimensionless weir height.

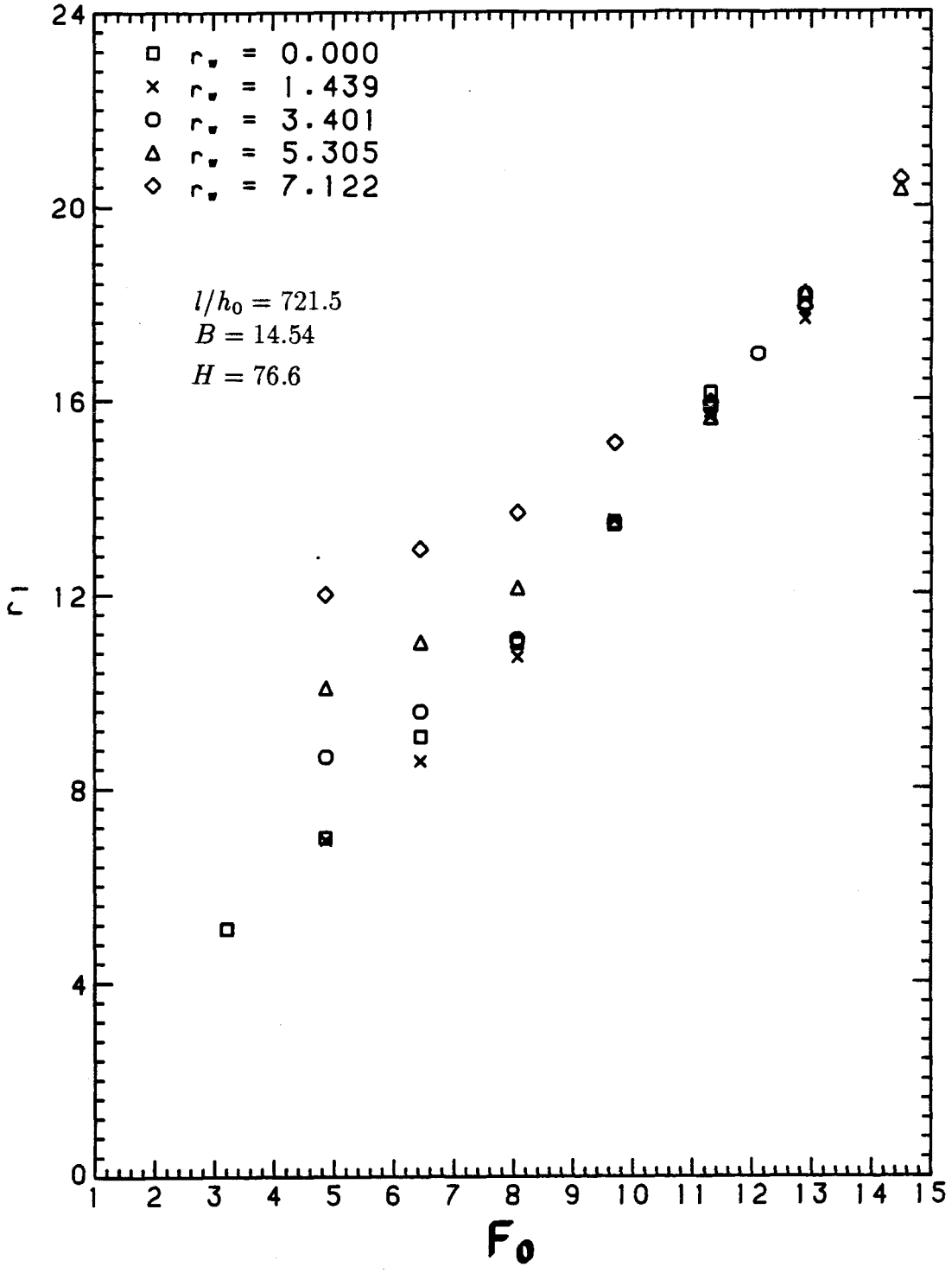

Figure 4.24: Depth of lower layer versus discharge densimetric Froude number.

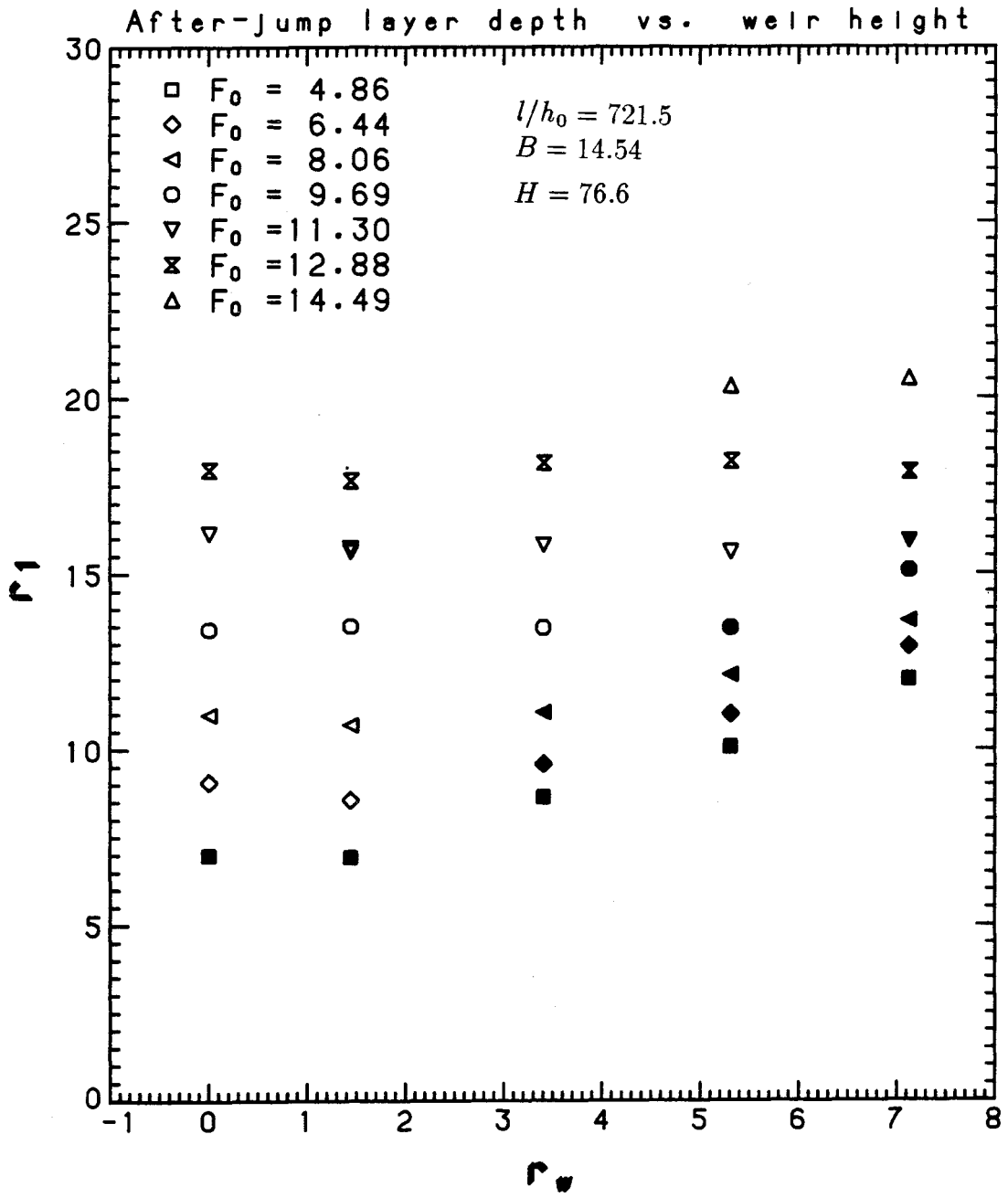

Figure 4.25: Depth of lower layer versus weir height.

intent of comparing the predictions of the one-dimensional theory discussed in Chapter 2 with the experimental results of the broad-crested weir experiments, values of the parameters representative of the channel used in those experiments are sought.

The same criteria discussed in Section 4.2.2 are adopted here. The value of the bottom friction factor f_b, as determined from the Moody curve for smooth channels using the Reynolds number based on the hydraulic radius of the lower layer (Equation 4.1), was found to be in the range between 0.017 and 0.064 for this series of experiments.

The values of $\alpha = f_i/f_b$ were then determined which afforded the best fit between the predicted interfacial profiles (obtained integrating Equation 2.23) and measured profiles. Examples are shown in Figure 4.26. Possible explanations for the limited discrepancies in the upper portion of the plot are as previously discussed (Section 4.2.2). The best-fit values of α were found to be in the range 0.9–2.0.

Sensitivity analyses revealed a weak dependence of the integrated profiles on the values of f_b and α, provided that they were chosen within the above-mentioned ranges. Use of the values $f_b = 0.037$ and $\alpha = 1.3$ in every case resulted in predicted profiles in good agreement with the measured profiles (see Figure 4.27). These values were therefore chosen to model the bulk characteristics of boundary and interfacial shear.

It will be recalled (Section 2.4.4) that a choice of the length of the jump region, L_j, was necessary to find the hydraulic solutions given by matching of upstream and downstream equations. It will also be recalled that the solutions were very insensitive to the choice made for L_j, since the chosen value was only used to determine the position where integration of Equation 2.23 had to be arrested. Measured values of L_j are shown in Figure 4.28 for all the broad-crested weir experiments. As a first order approximation, it can be stated that L_j grows linearly with $\mathbf{F_0}$. The equation

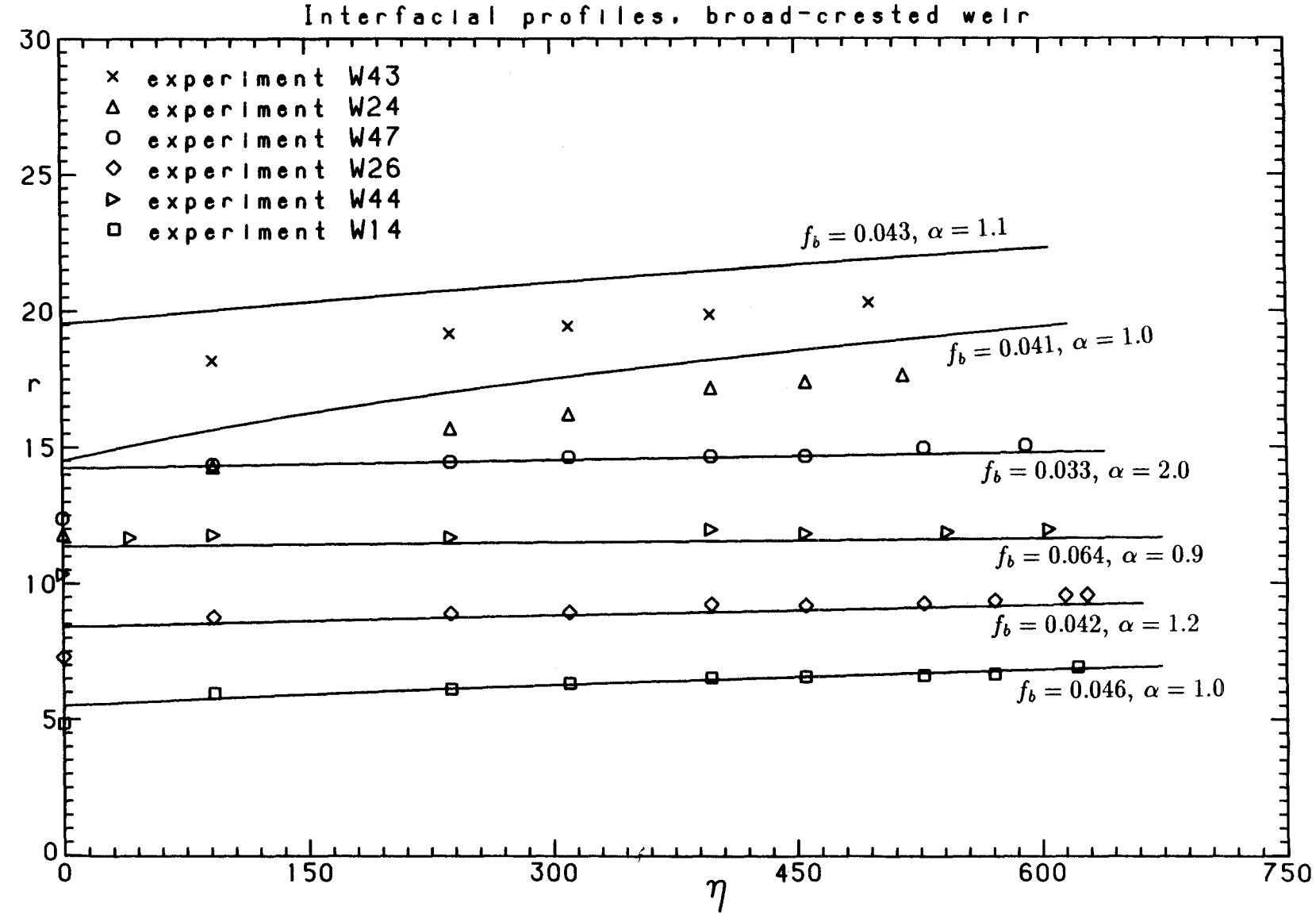

Figure 4.26: Interfacial profiles in the gradually-varied counterflow.

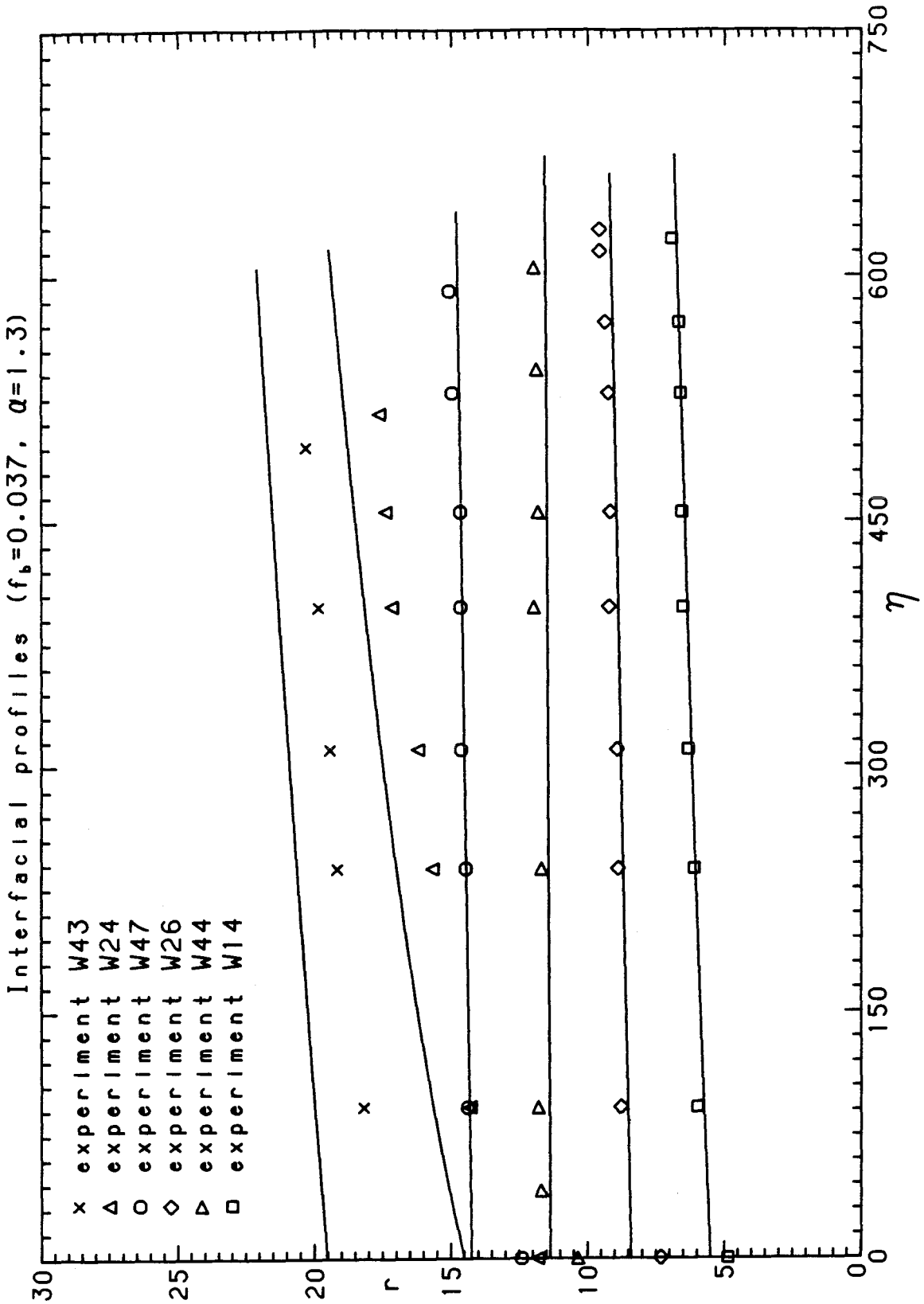

Figure 4.27: Interfacial profiles in the gradually-varied counterflow.

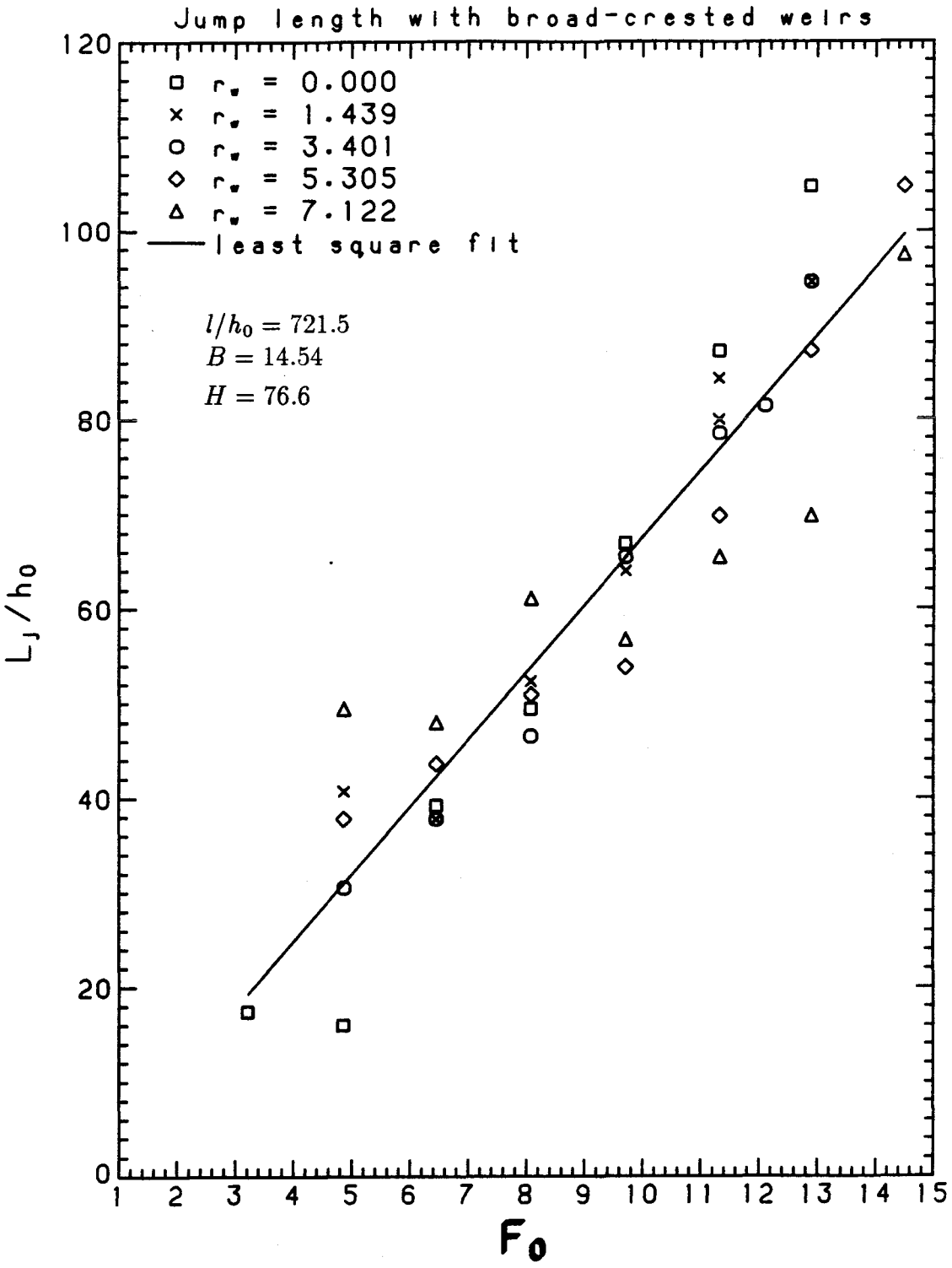

Figure 4.28: Nondimensional jump length vs. discharge densimetric Froude number.

of the least-square fit line,

$$\frac{L_j}{h_0} = -3.6 + 7.1\,\mathbf{F_0}, \tag{4.3}$$

will be used to obtain an approximate location of the point at which to arrest integration of Equation 2.23 and determine the value of the layer thickness r_{1d}.

It is interesting to notice that in both Equations 4.2 and 4.3 $L_j/h_0 \sim 7\,\mathbf{F_0}$. Stefan and Hayakawa (1972) found that for buoyant surface jets a first approximation of their experimental data was $L_j/h_0 \sim 10\,\mathbf{F_0}$. The lower values of L_j found in the present investigation might be caused by the presence of a solid boundary in contact with the fast-flowing layer.

4.3.3 Comparison between theory and experiments

The one-dimensional theory presented in Chapter 2 is now tested against the experimental findings of the broad-crested weir experiments.

The technique discussed in Section 2.4.4 has been repeatedly applied to find many plots such as the ones shown in Figures 2.14, 2.15 and 2.16. It has therefore been possible to determine several predicted values of the dilution S and of the nondimensional lower layer thickness r_1, corresponding to many different flow conditions.

The predicted points thus obtained are presented, together with experimental data, in Figure 4.29. Only three broad-crested weir heights r_w are presented in Figure 4.29, in order to maintain good legibility.

It can be noticed that the agreement between predicted and measured dilutions is rather poor. While the theory correctly predicts the general behaviour of the curves $S = S(\mathbf{F_0})$ for given values of r_w, the predictions are quantitatively incorrect. While the predicted value of $\mathbf{F_0}$ above which dilutions start to increase with $\mathbf{F_0}$ is more or less correct, for larger values of $\mathbf{F_0}$ the predicted dilutions are much larger than the dilutions measured in the laboratory channel.

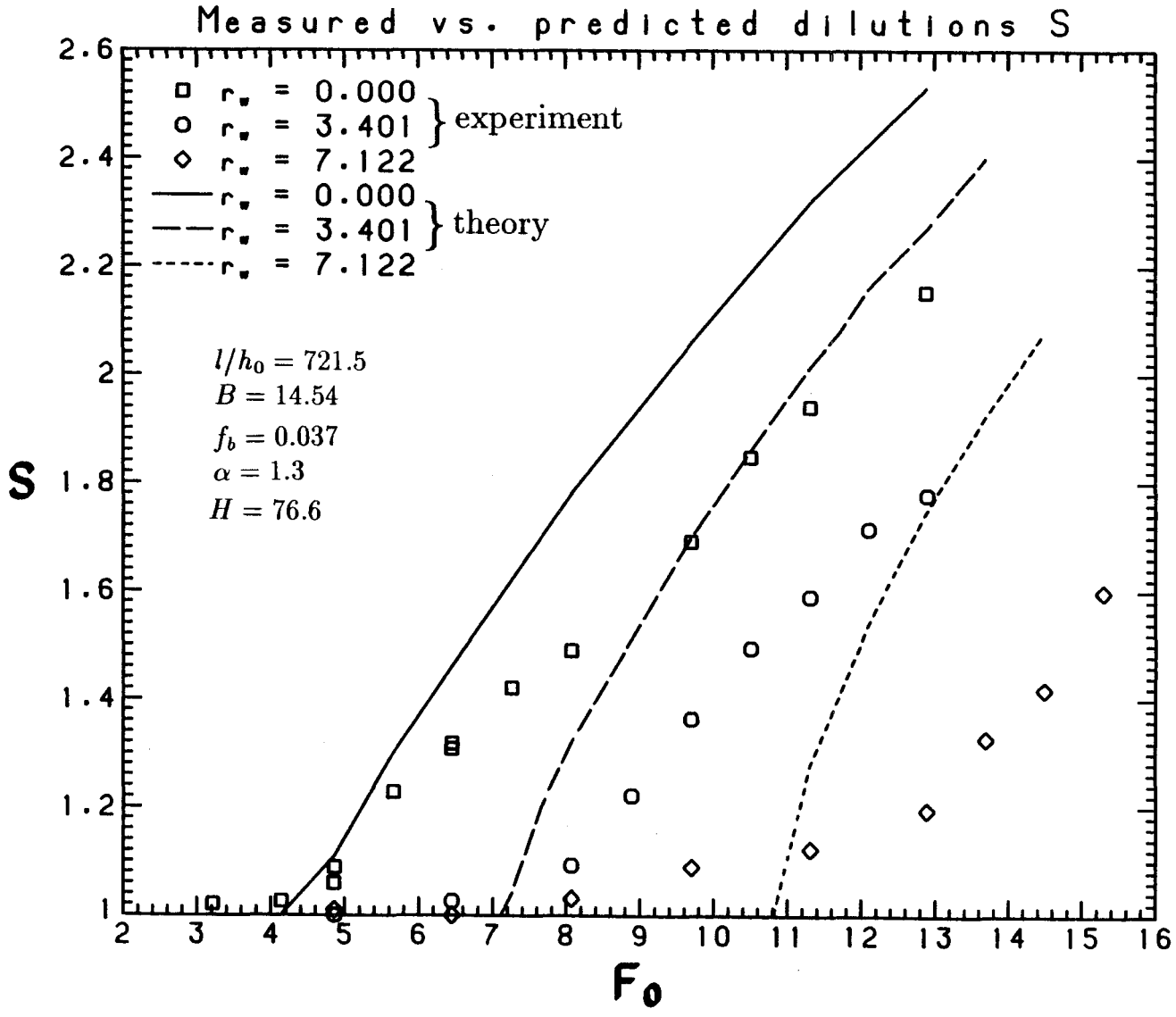

Figure 4.29: Comparison between theory and experiments.

Inspection of Figure 4.30 sheds some light on the causes of this disagreement. This figure shows both the experimental point obtained from experiment W51 (see Table 4.2 for details on the flow conditions) and the theoretical curves $r_{1u} = r_{1u}(S)$ and $r_{1d} = r_{1d}(S)$ that were used to predict the dilution S (the predicted point being the intersection of the two curves, as previously explained). This particular experiment has been chosen to illustrate the following ideas for two reasons. The first is that the disagreement between theory and experiment was a maximum under these flow conditions. The second is that the type of situation shown in Figure 4.30 is typical of all the large Froude number experiments.

Two basic ideas emerge from Figure 4.30. First, it is clear that while the downstream curve $r_{1d} = r_{1d}(S)$ passes through the experimental point, the upstream curve $r_{1u} = r_{1u}(S)$ is higher than it should be to give a correct prediction. In other words, it appears that Equation 2.22, and not Equations 2.29, 2.30 and 2.23, is responsible for the incorrect prediction. This argument agrees with what was found examining the free overfall experiments. Also Figure 4.31 confirms the fact that the roots r_1 of Equation 2.22 for given values of S and $\mathbf{F_0}$ (solid curves) are larger than the measured values of r_1 (the filled symbols should not be compared with the curves, since they represent flooded jumps). Explanations for the inaccuracy of Equation 2.22 have been discussed in Section 4.2.3 and will be discussed further in Chapter 5.

The second fact that emerges from observation of Figure 4.30 is that the upstream and downstream curves have a very similar slope near the point of intersection. This implies that a small error that shifts either curve up or down by a small amount will result in a relatively large error in the predicted value of S. In this sense, the system of equations governing the mechanics of a mixing channel appears to be very 'rigid'. The inaccuracy of Equation 2.22 is 'amplified' and, although small, it causes the large errors in the predicted values of S which have been observed in Figure 4.29.

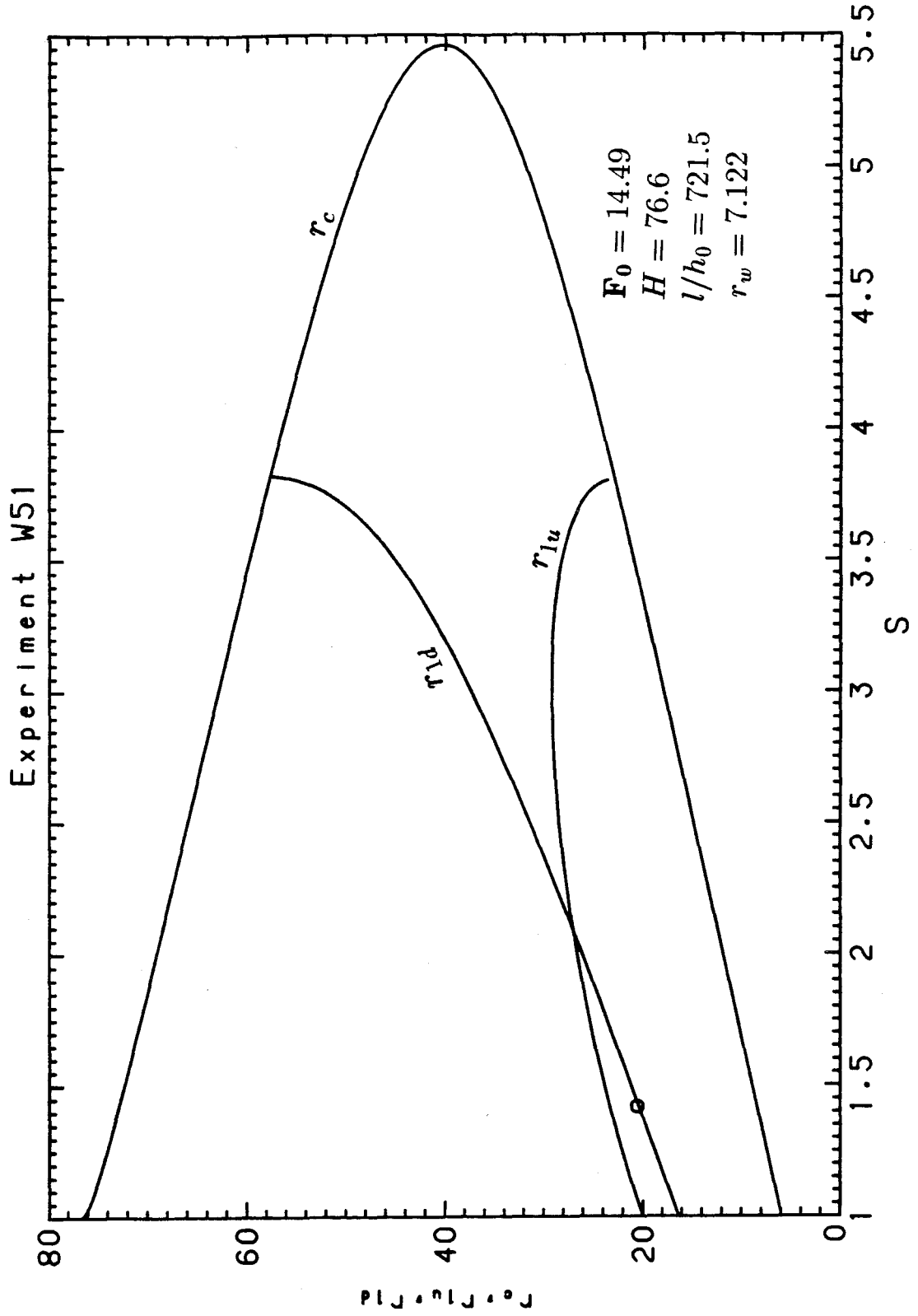

Figure 4.30: Example of comparison between theory and experiment in the (S, r_1) plane.

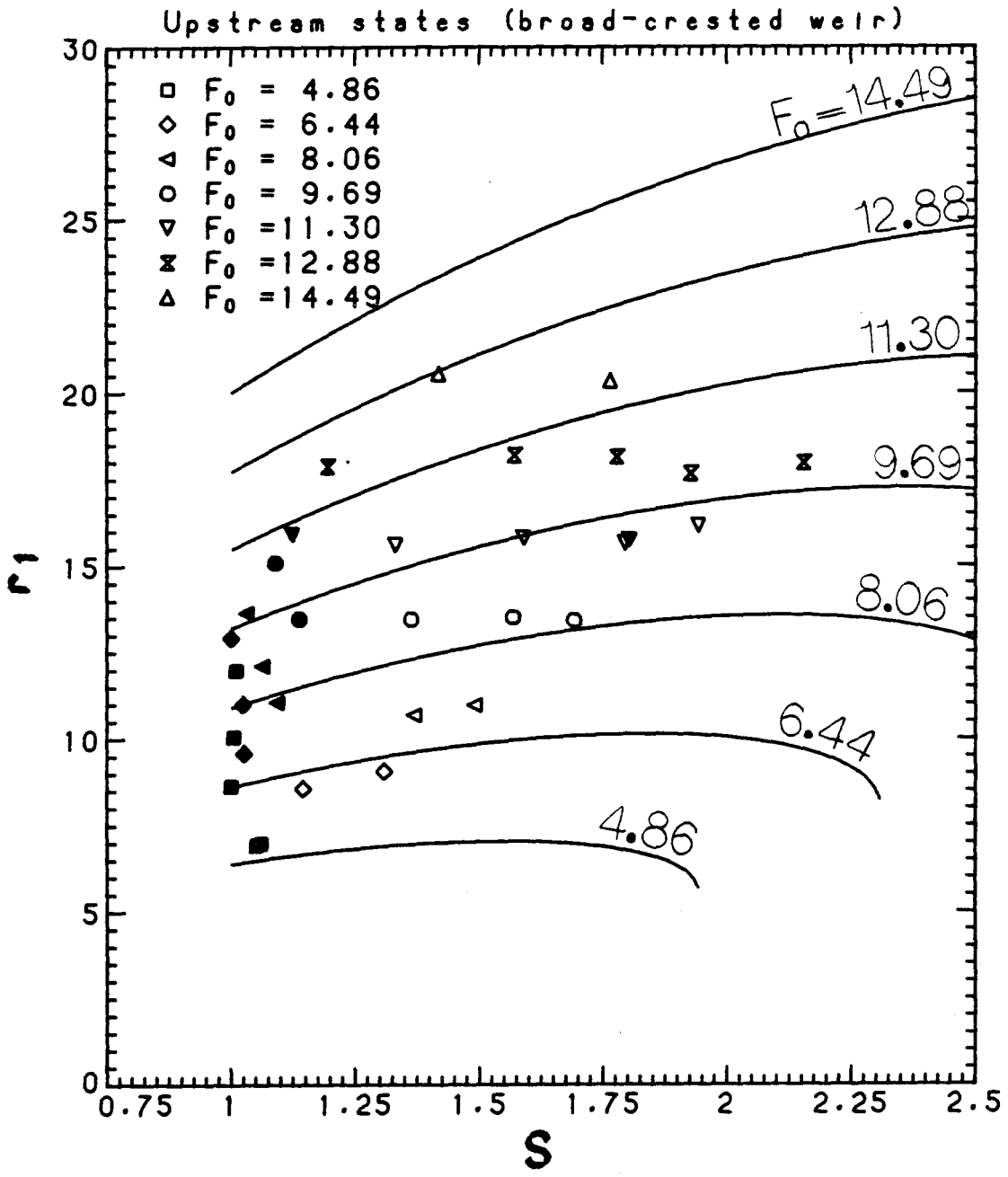

Figure 4.31: Comparison between predicted and measured upstream states.

4.4 Summary and discussion

The experiments in which the lower dense layer was visually observed clearly pointed to the importance of both the downstream control and the ambient depth in determining the characteristics of flows in mixing channels.

The four different mixing modes have been obtained in the experimental channel and investigated. It has been shown that flooded internal hydraulic jumps and downstream-controlled unstable flows are characterized by negligible entrainment, while free internal hydraulic jumps and upstream-controlled unstable flows afford variable entrainment rates, which depend not only on the discharge conditions, but also on the downstream control and on the ambient depth.

The effect of the limited depth and of the resulting counterflow in the determination of dilutions was so pronounced in the experiments that buoyant jet theories that ignore this effect should be viewed with circumspection. Situations in which the ambient depth is so large that it can be regarded as infinite, while easy to envision from an abstract standpoint, are difficult to encounter in practice.

Similarly, the height of the broad-crested weir has been shown to influence the flow characteristics so strongly that any theory not explicitly including a downstream control is bound to be unsuccessful even in predicting the basic features of the flow.

In agreement with the classical work of Wilkinson and Wood (1971), increases in the height of the weir have been found to cause an upstream migration of the roller region towards the source. This caused a reduction in the length of the entraining region and a consequent reduction in the dilution of the discharged fluid. The depth of the lower layer, on the other hand, appeared to be insensitive to changes in the downstream control in the range of laboratory conditions investigated, at least until flooding of the source took place.

The experimental results support the idea, first formulated by Baddour and Abbink (1983), that for a fixed ambient depth an 'optimum' value of the discharge densimetric Froude number, which corresponds to a maximum dilution, exists. Previous investigators (e.g., Stefan and Hayakawa, 1972) had suggested the occurrence of a constant dilution when the discharge densimetric Froude number was allowed to increase indefinitely. The present experimental investigation has clearly shown the existence of an 'optimum' value of the Froude number. An increase in $\mathbf{F_0}$ beyond this resulted in a reduction of turbulent mixing, which appeared to be caused by the recirculation of source fluid, typical of upstream-controlled unstable flow conditions. Further increase in the Froude number eventually eliminated mixing completely, with the onset of a downstream-controlled instability.

The one-dimensional theory discussed in Chapter 2 has been shown to be capable of predicting the essential features of the flow in a stratified mixing channel. This is an argument in favor of the idea that turbulent mixing in this type of flow is more a function of the bulk characteristics of the flow than it is a function of the turbulent structure of the flow, although it is recognized that there probably is a complex interaction between the two (see Chapter 6).

The characterization of the flow only in terms of assumed uniform profiles, although adequate for qualitative predictions, has been shown to result in predicted dilutions which are too high in a certain range of experimental parameters (deep channel and high discharge densimetric Froude number).

Analysis of the separate upstream and downstream problems pointed out that the inaccurate predictions could be attributed to the inadequacy of the hypothesis of flow force conservation across the jump region, at least as stated, in a one-dimensional setting, by Equation 2.22. It is to clarify this aspect, as well as to gain new insight into the inner structure of the flows studied, that the detailed laser-based experiments

described in the next chapter were performed.

Chapter 5

Laser-based experiments

5.1 Introduction

This chapter is devoted to the presentation and the discussion of the results of the laser-based experiments. These experiments were performed to study the details of the flow structure in the experimental channel, and more specifically to obtain density and velocity profiles at designated cross-sections in the flow field. The use of LIF and LDV in measuring such profiles was previously described in Chapter 3.

Five laser-based experiments were performed, each one comprising the measurement of a mean density profile, several 'instantaneous' density profiles, and a velocity profile. The experimental parameters are summarized in Table 5.1.

All the experiments were characterized by 'deep' ambient water (H=76.6) and a free overfall at the downstream end of the channel. The flow conditions for three of the blue-dye experiments described in Chapter 4 (F5, F9 and F11) were closely reproduced, in order to facilitate comparisons.

In experiments 'F5, x = 55.9 cm', 'F9, x = 92.0 cm' and 'F11, x = 120.0 cm' (upstream experiments), the longitudinal position along the channel, x, was approximately $2L_j$ downstream of the discharge inlet, where L_j is the length of the jump region measured in the corresponding blue-dye experiment.

On the other hand, in experiments 'F9, x = 323.6 cm' and 'F11, x = 323.6 cm'

Name of experiment (and distance from discharge inlet)	q_o (cm^2/s)	$(\Delta\rho/\rho)_o$	h_o (cm)	F_o
F5, x= 55.9 cm	10.26	0.00794	0.688	6.44
F9, x= 92.0 cm	16.79	0.00940	0.688	9.69
F9, x=323.6 cm	16.73	0.00934	0.688	9.69
F11, x=120.0 cm	18.80	0.00866	0.688	11.30
F11, x=323.6 cm	18.93	0.00878	0.688	11.30

Table 5.1: Summary of parameters for laser-based experiments.

(downstream experiments), the profiles were measured at a location further downstream, near the center of the subcritical gradually-varied counterflow region.

The measured density profiles are presented in Section 5.2, while the velocity profiles are given in Section 5.3. The accuracy of the data is discussed in Section 5.4, together with a series of 'continuity checks'. In Section 5.5 the correction factors mentioned in Section 2.2.1 are computed, the boundary shear along the jump region is estimated, and flow force balance across the jump region is discussed. This will lead to an explanation for the discrepancy that was encountered when one-dimensional theory and visual observations were compared.

5.2 Density profiles

An 'instantaneous' density profile measured in experiment 'F5, x = 55.9 cm' is shown in Figure 5.1. While each instantaneous profile was recorded in approximately 45 ms, the time-averaged profile was obtained averaging over a period of about 200

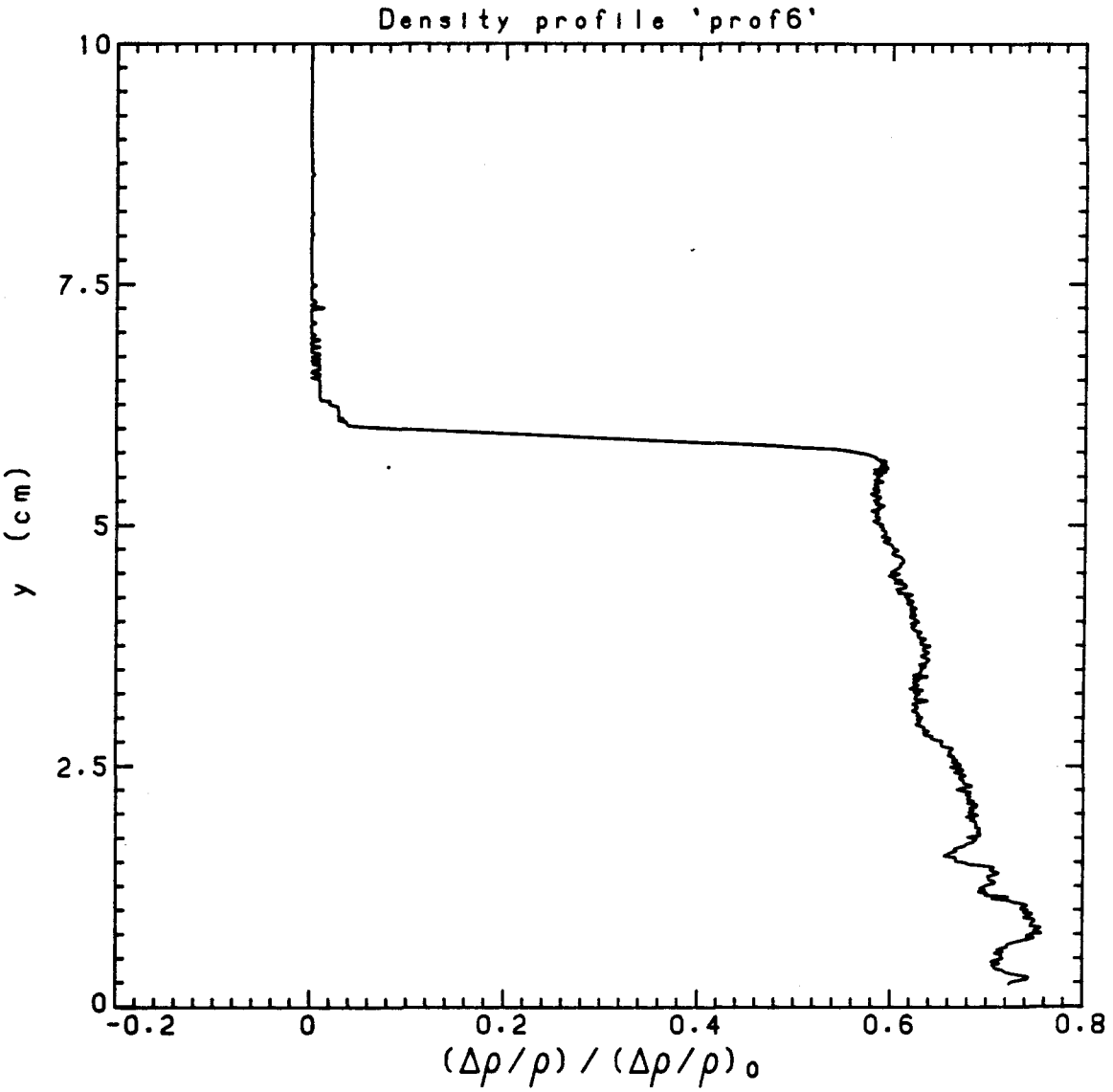

Figure 5.1: Instantaneous density profile for experiment 'F5, x = 55.9 cm'.

seconds, since only every fourth scan of the array of 1024 photodiodes was recorded. The average of 1440 instantaneous density profiles is shown in Figure 5.2.

It can be observed that the interface between the salt water and the fresh water is very sharp in the instantaneous profile (Fig. 5.1). The apparently thicker interface that appears in the average profile (Fig. 5.2) is an artifact of averaging the vertical displacement of the interface due to interfacial waves.

Analogous considerations apply to the density profiles measured in the other four experiments. For example, Figures 5.3 and 5.4 show, respectively, one of the instantaneous profiles and the average profile obtained in experiment 'F9, x = 92.0 cm'.

The average profiles are not as smooth as one would expect after averaging over more than 1000 instantaneous profiles, and the cause of this is not fully understood, although it is suspected that some non-random noise could be associated with the A/D converter. However, the amplitude of this 'noise' is very small, and its effect on the integrals that will be computed in Sections 5.4 and 5.5 is certainly negligible if compared with other sources of error, as discussed later.

The time-averaged density profiles for experiments 'F9, x = 323.6 cm', 'F11, x = 120.0 cm' and 'F11, x = 323.6 cm' are presented, respectively, in Figures 5.5, 5.6, and 5.7.

The five time-averaged profiles are plotted on the same graph in Figure 5.8. It is interesting to compare the position of the density interface with the position of the visual interface measured in the corresponding blue-dye experiment. If the depth of the density interface, $y_{50\%}$, is defined as the depth at which the density difference is 50% of the total density difference between the two layers, then Table 5.2 shows that the depth of the visual interface coincides with the depth of the density interface so defined. The small differences are attributed to two factors: the experimental conditions in the laser-based experiments were not exactly identical to the experimental

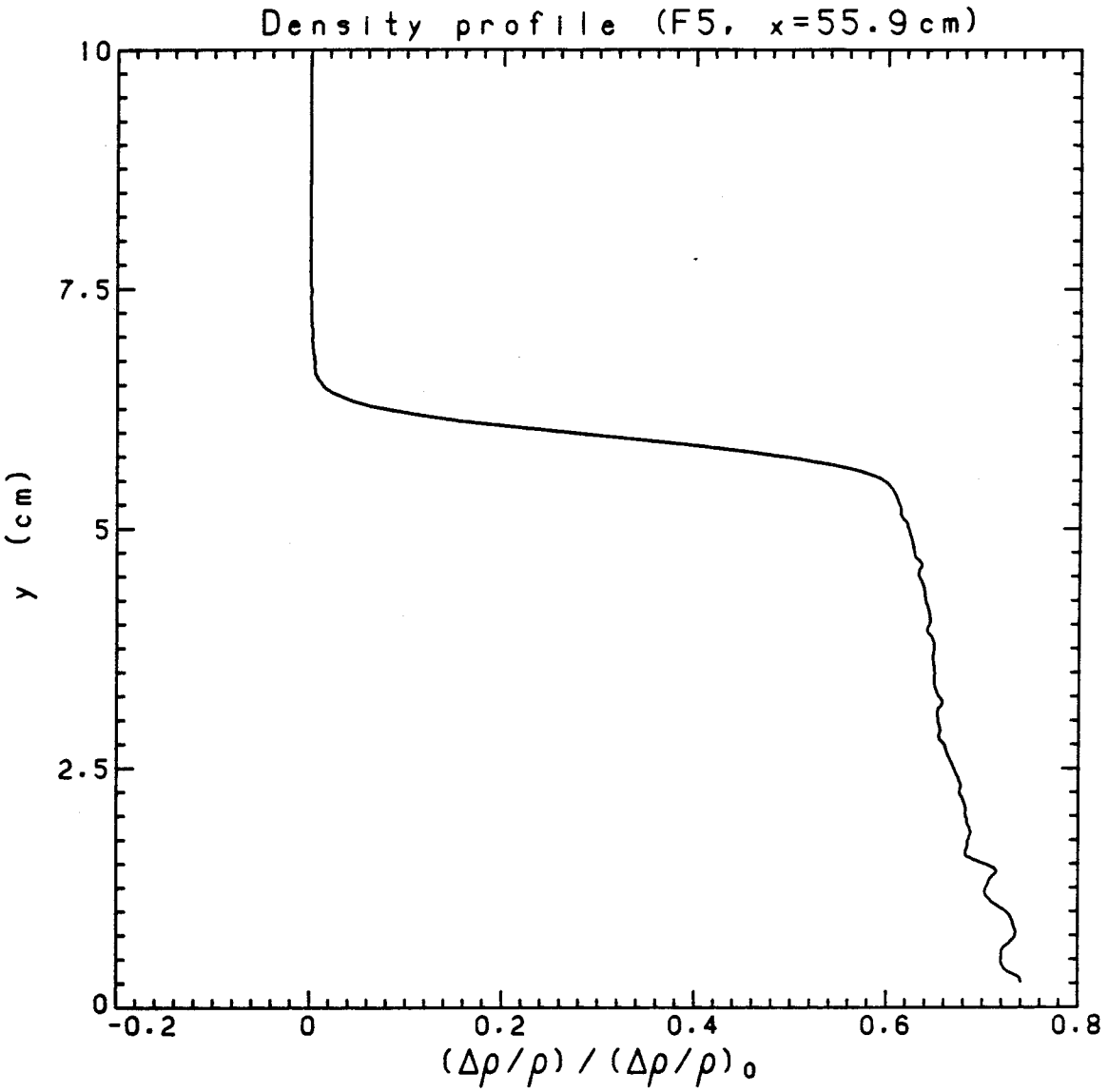

Figure 5.2: Average density profile.

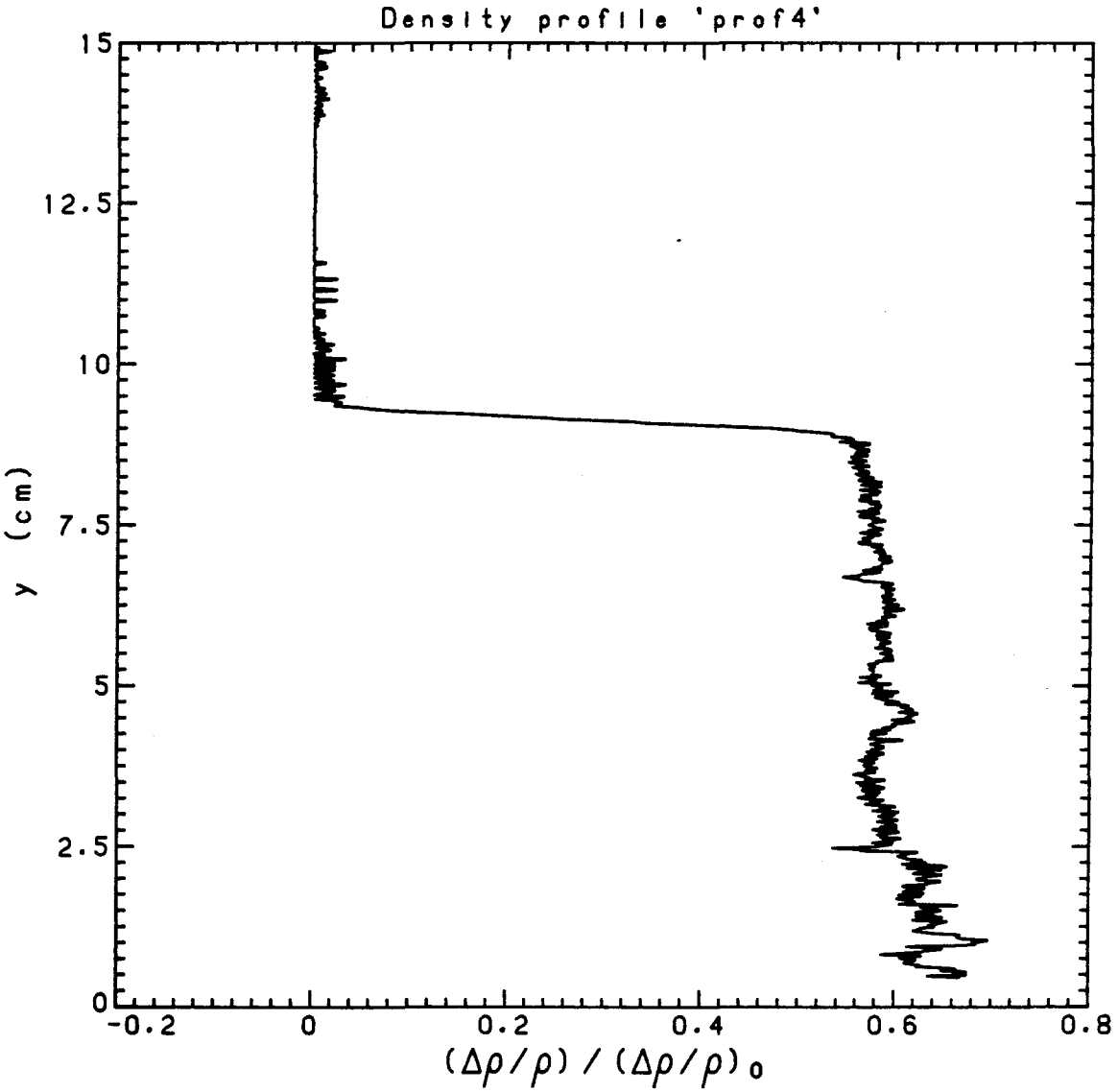

Figure 5.3: Instantaneous density profile for experiment 'F9, x = 92.0 cm'.

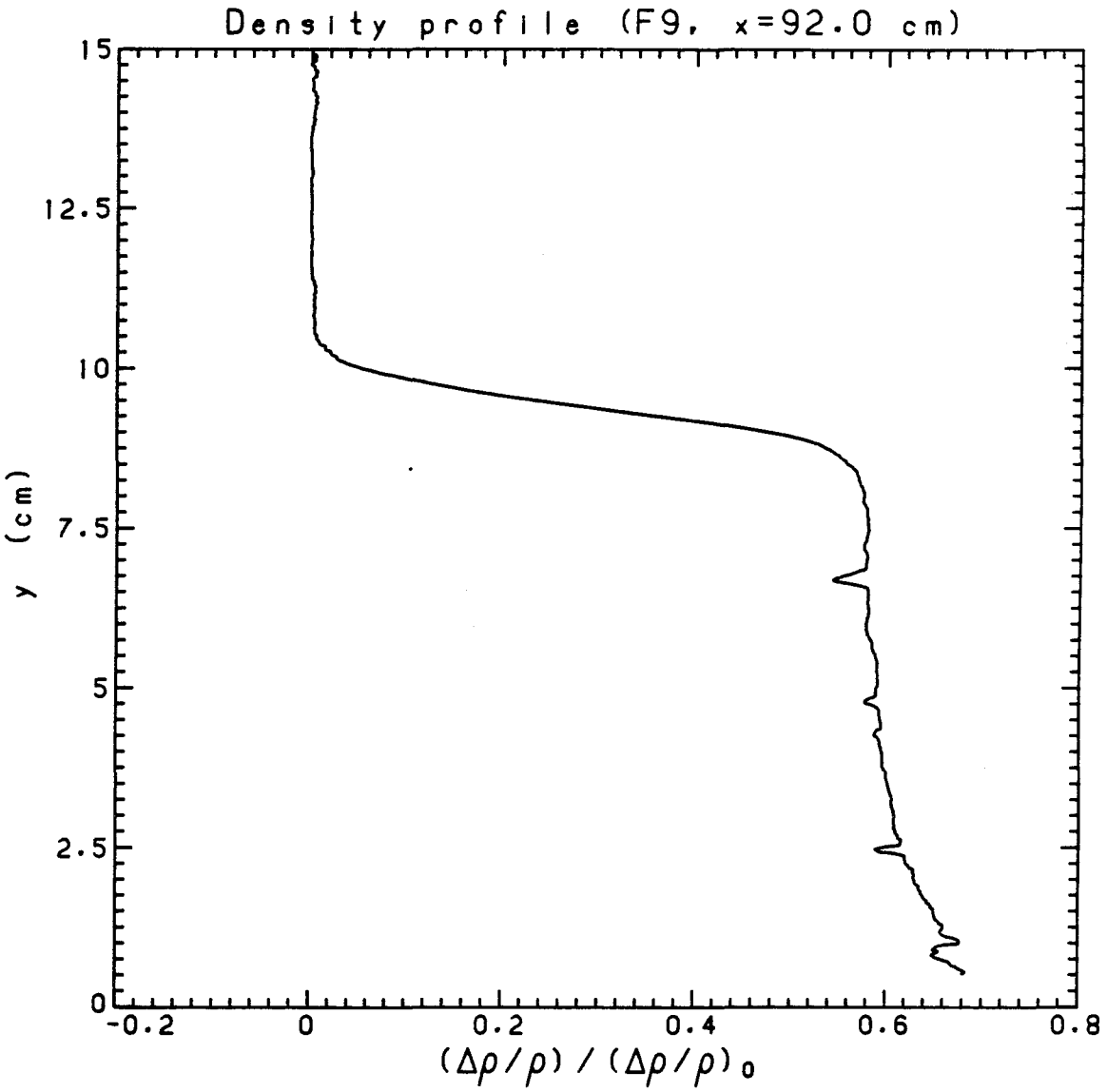

Figure 5.4: Average density profile.

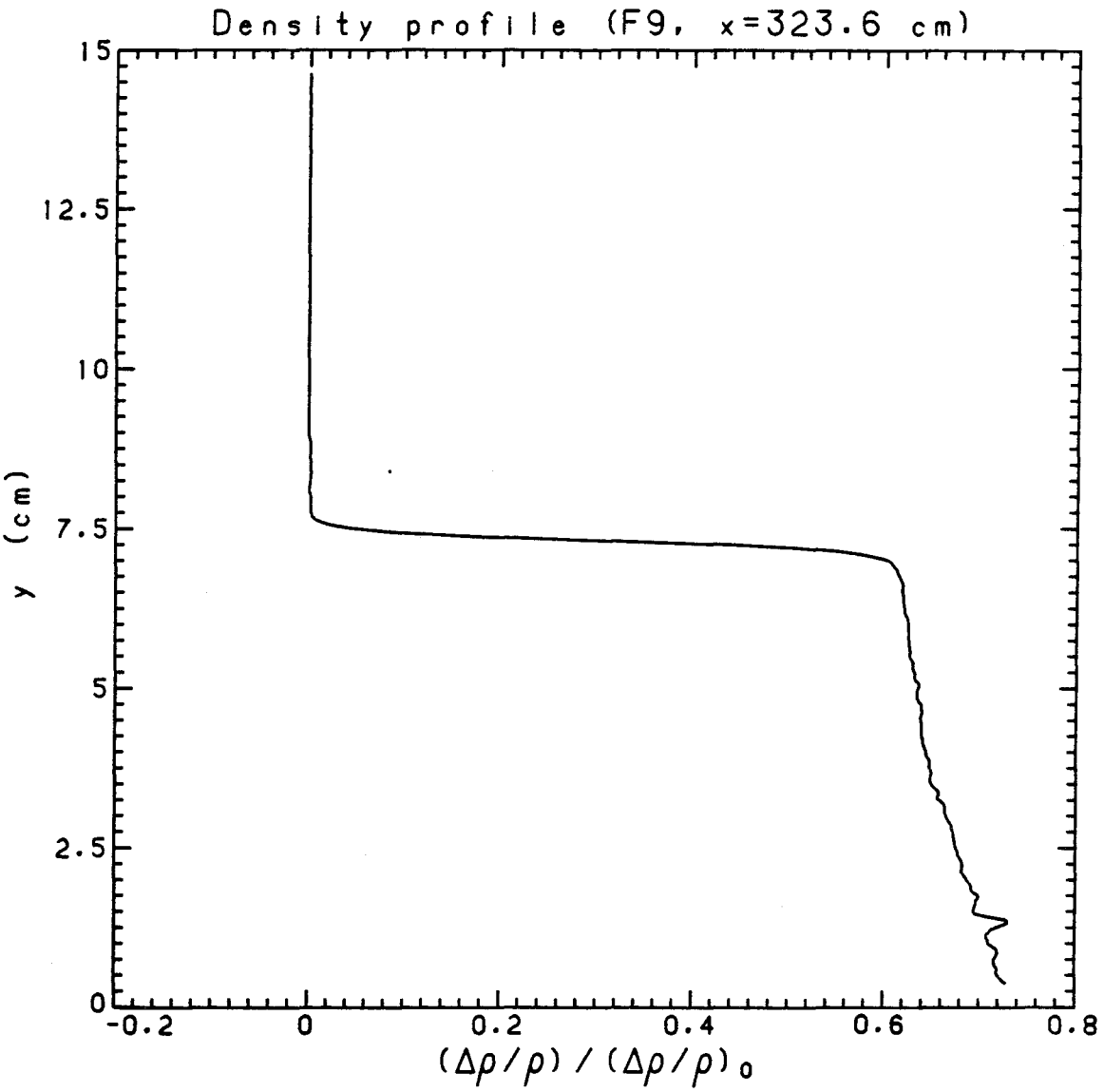

Figure 5.5: Average density profile.

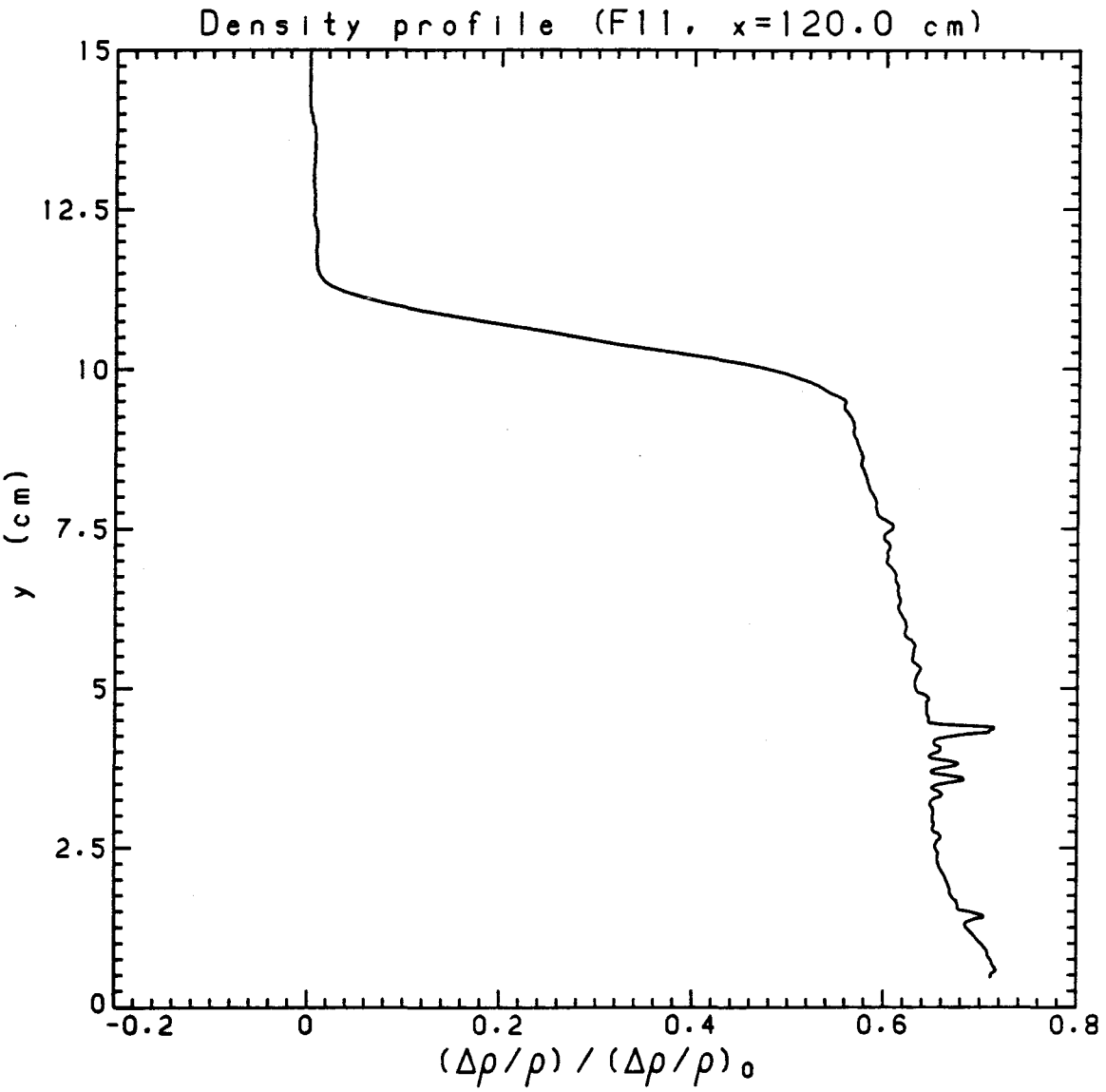

Figure 5.6: Average density profile.

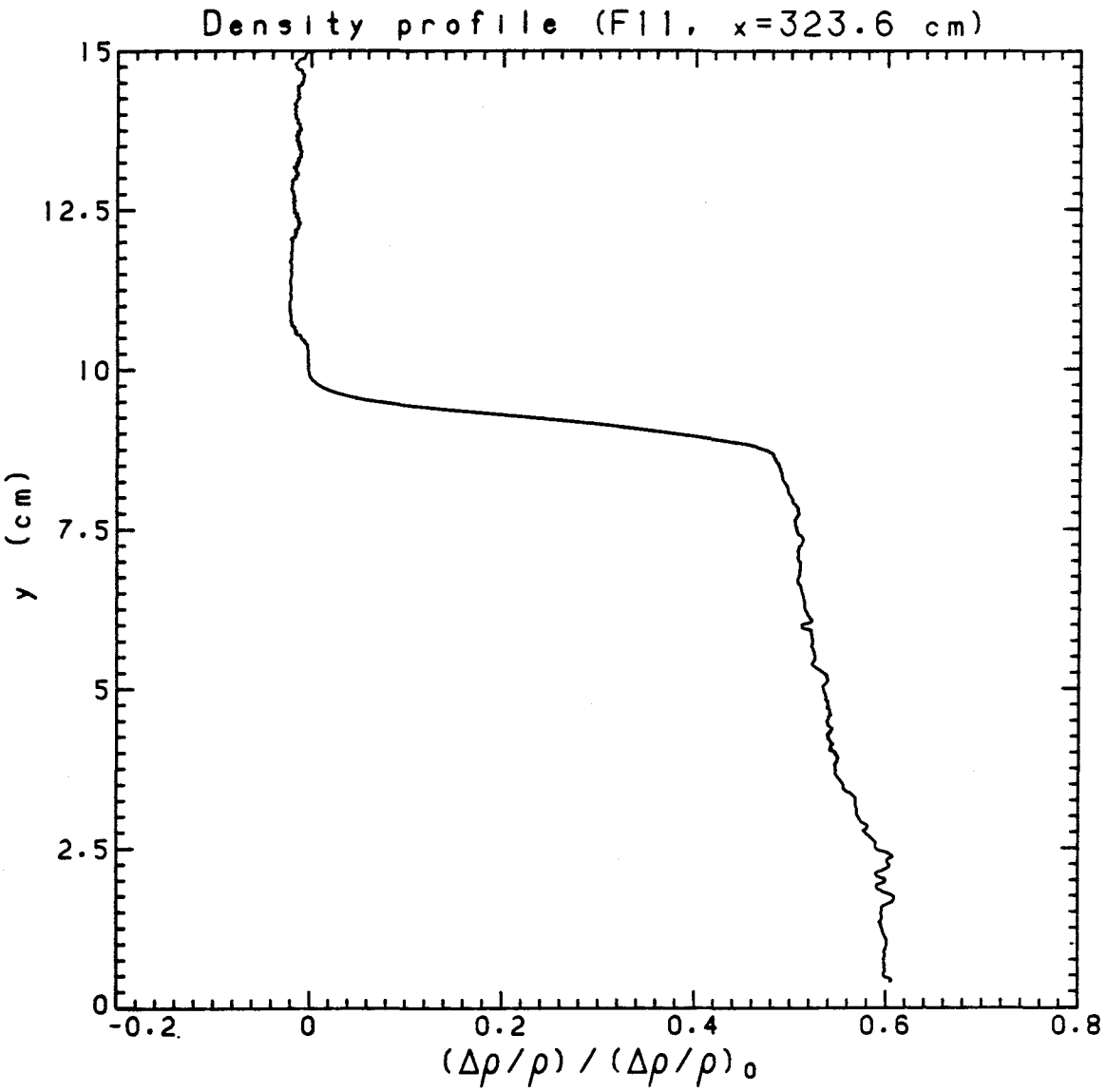

Figure 5.7: Average density profile.

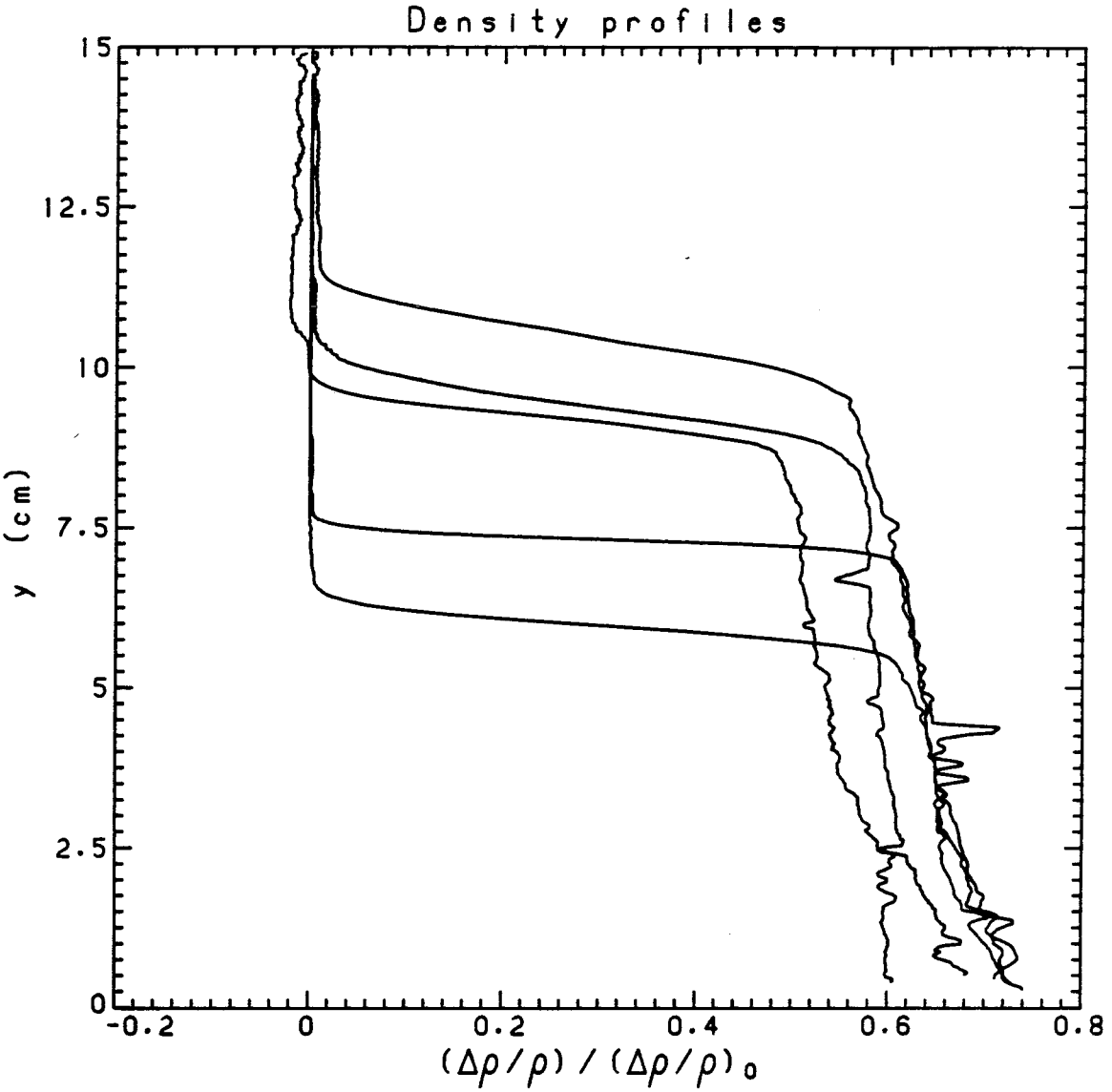

Figure 5.8: Average density profiles.

Experiment	$y_{50\%}$ (cm)	visual depth (cm)
F5, x= 55.9 cm	5.98	6.24
F9, x= 92.0 cm	9.40	9.23
F9, x=323.6 cm	7.31	7.61
F11, x=120.0 cm	10.50	11.10
F11, x=323.6 cm	9.21	9.21

Table 5.2: Comparison between depths of density interface and visual interface.

conditions in the blue-dye experiments; second, the accuracy with which the position of the visual interface was determined is limited (see Section 3.5).

The five normalized time-averaged density profiles are shown in Figure 5.9, where the normalizing parameters have been chosen to be $y_{50\%}$ and the density difference at $y = 0$, $(\Delta\rho/\rho)_{y=0}$. The latter was obtained by extrapolating the bottom part of the density profiles. It is remarkable how similar the five profiles are, if one considers that they have been recorded with very different flow conditions and at different locations along the channel. The downstream profiles (x = 323.6 cm) appear to have a sharper interface than the upstream profiles (x = $2\,L_j$). This is due to the fact that the internal wave amplitudes were at a maximum in the vicinity of the jump region.

It can also be observed that the average profiles are not very different from the uniform distribution assumed in the theoretical analysis, although a slight decrease in density from the bottom to the top of the lower layer is a characteristic feature

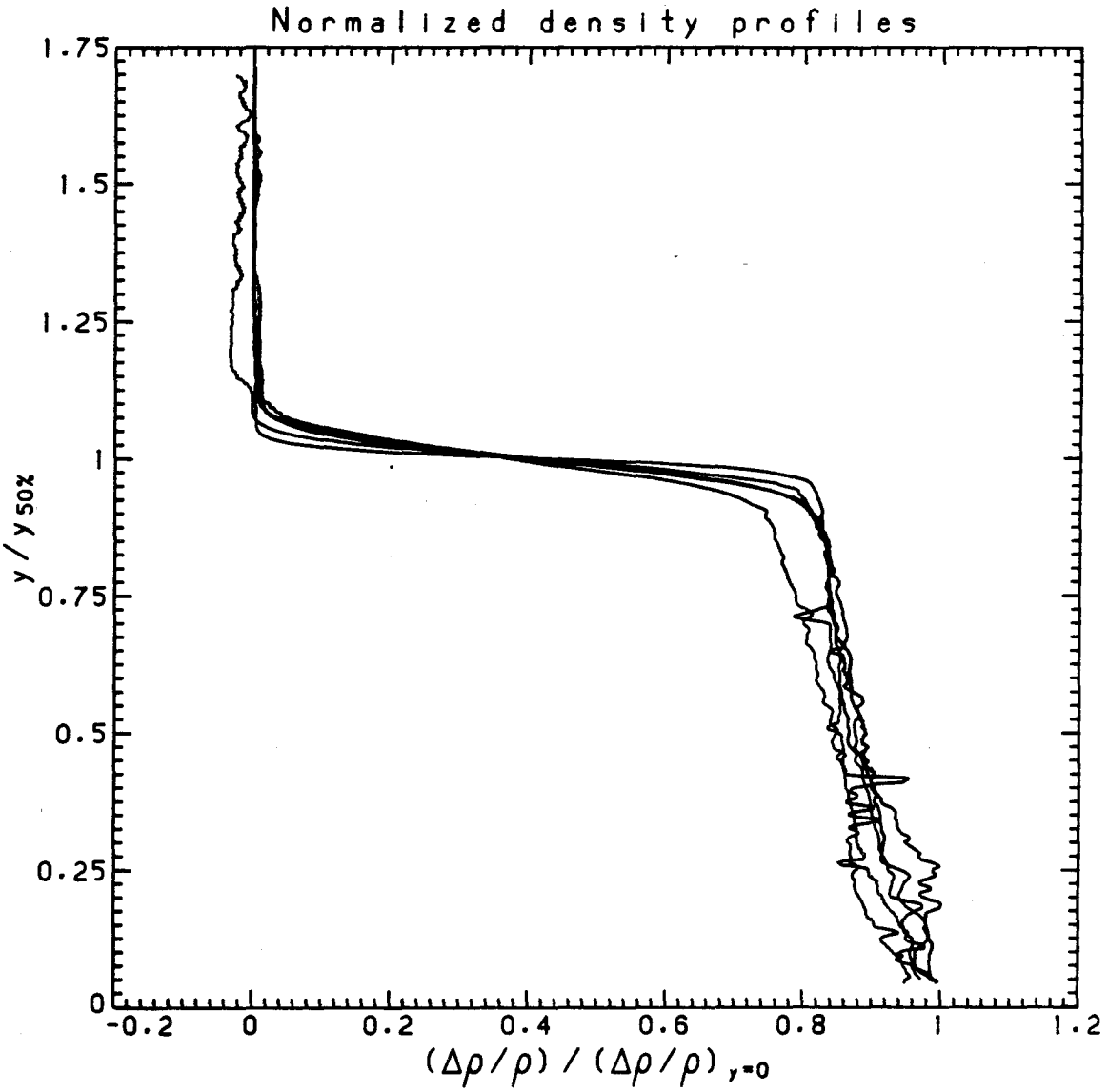

Figure 5.9: Normalized average density profiles.

of all the experiments. The uniformity of the density profiles is an indication of the presence of strong internal mixing within the salt water layer.

5.3 Velocity profiles

The complete horizontal velocity profile, from the channel bottom to the free surface, obtained in experiment 'F9, x=92.0 cm' is shown in Figure 5.10. The dashed line represents the position of the density interface, $y_{50\%}$, and it can be seen to be lower than the zero-velocity line, which is the depth where the velocity changes sign. The curve joining the experimental points is a cubic spline, drawn simply to improve the legibility of this and of the following figures.

The velocity profile obtained in experiment 'F9, x = 323.6 cm' is shown in Figure 5.11. The remaining three velocity profiles, namely those obtained in experiments 'F11, x = 120.0 cm', 'F11, x = 323.6 cm' and 'F5, x = 55.9 cm', are shown in Figures 5.12, 5.13 and 5.14, respectively. The change of sign of the horizontal velocity in the ambient fluid which took place in experiment 'F5, x = 55.9 cm' (Fig.5.14) was probably the result of a slight density stratification in the ambient fluid. The cause of this stratification is not clear, and its extent has not been measured. Therefore, although the dynamics of the lower layer may have been influenced only marginally by the presence of this undesired stratification, caution should be exercised in using the data obtained from this experiment.

The five velocity profiles exhibit a considerable departure from the uniformity which was assumed by the one-dimensional theory and the consequences of this non-uniformity will be quantified and discussed in Section 5.5.

If attention is focused on the more dynamically active lower layer, the five profiles appear as shown in Figure 5.15.

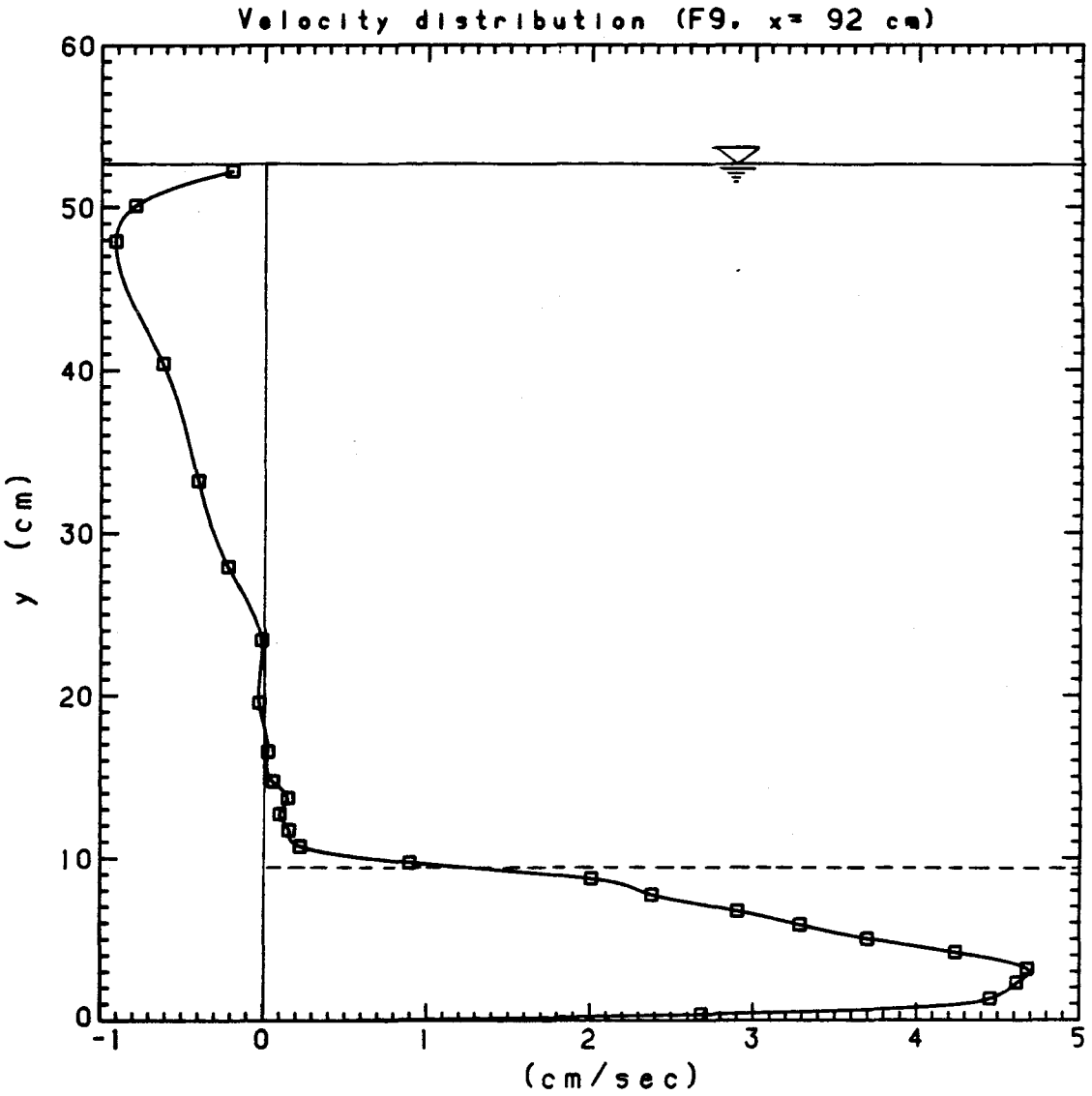

Figure 5.10: Horizontal velocity profile.

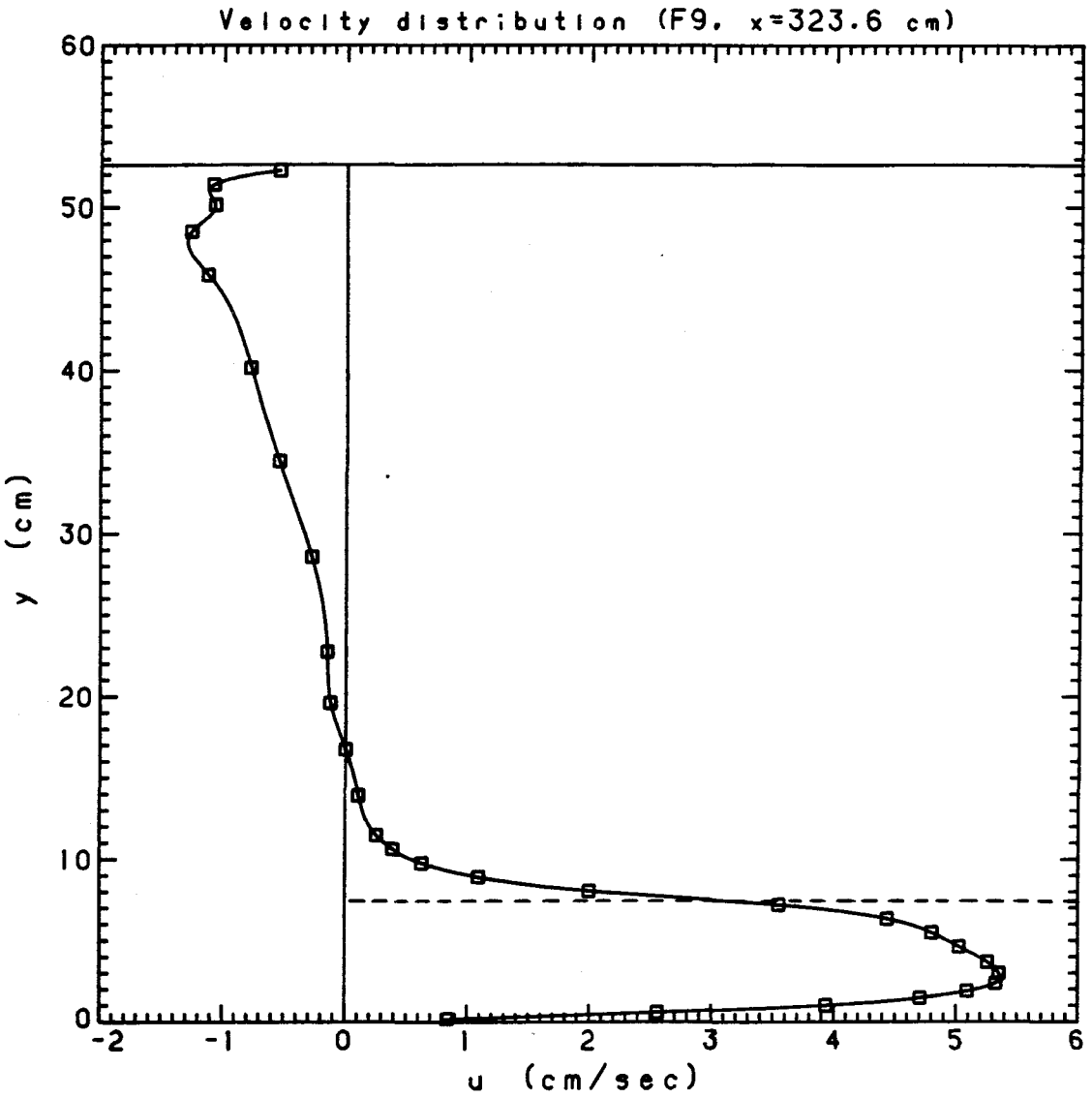

Figure 5.11: Horizontal velocity profile.

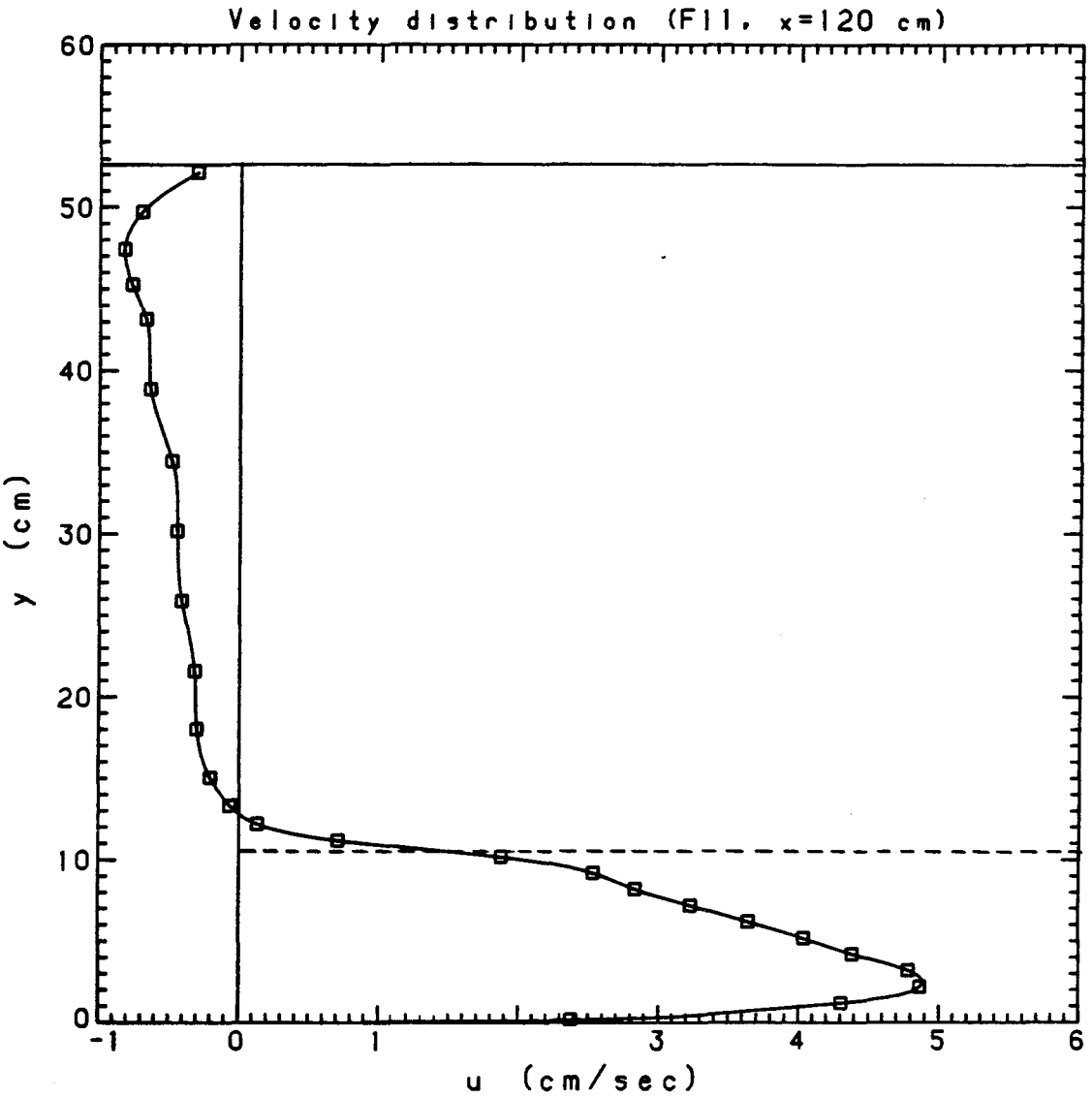

Figure 5.12: Horizontal velocity profile.

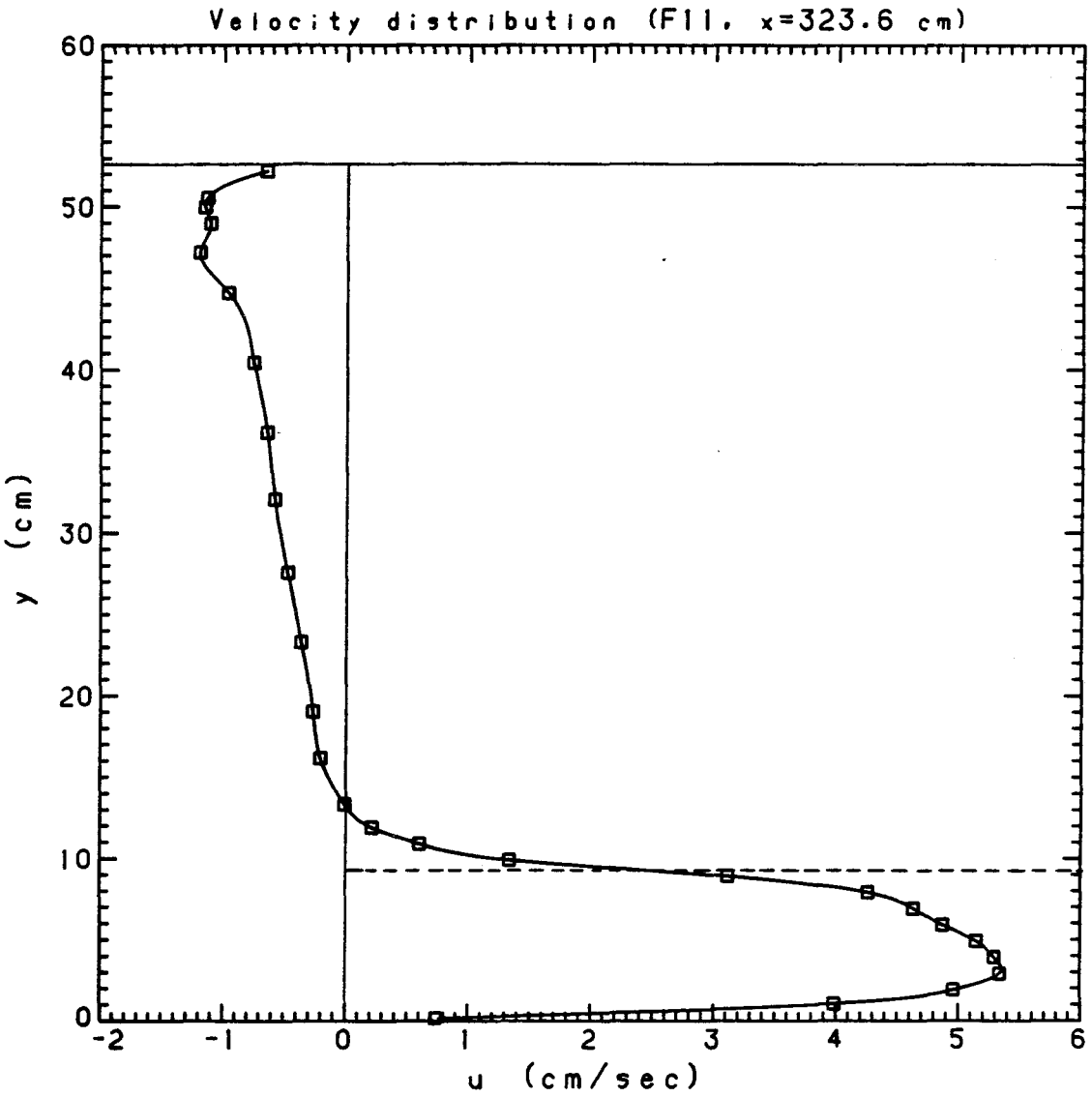

Figure 5.13: Horizontal velocity profile.

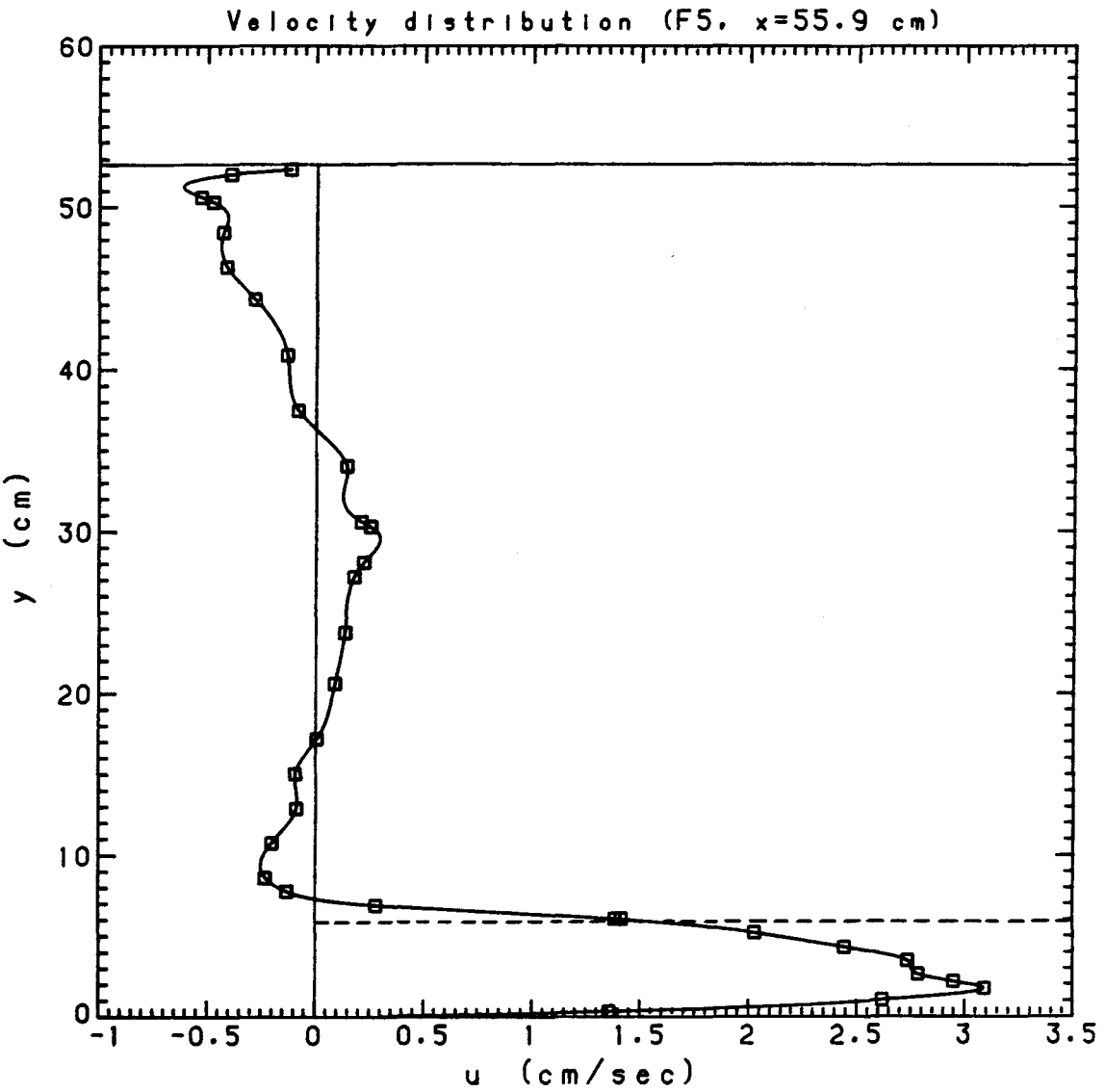

Figure 5.14: Horizontal velocity profile.

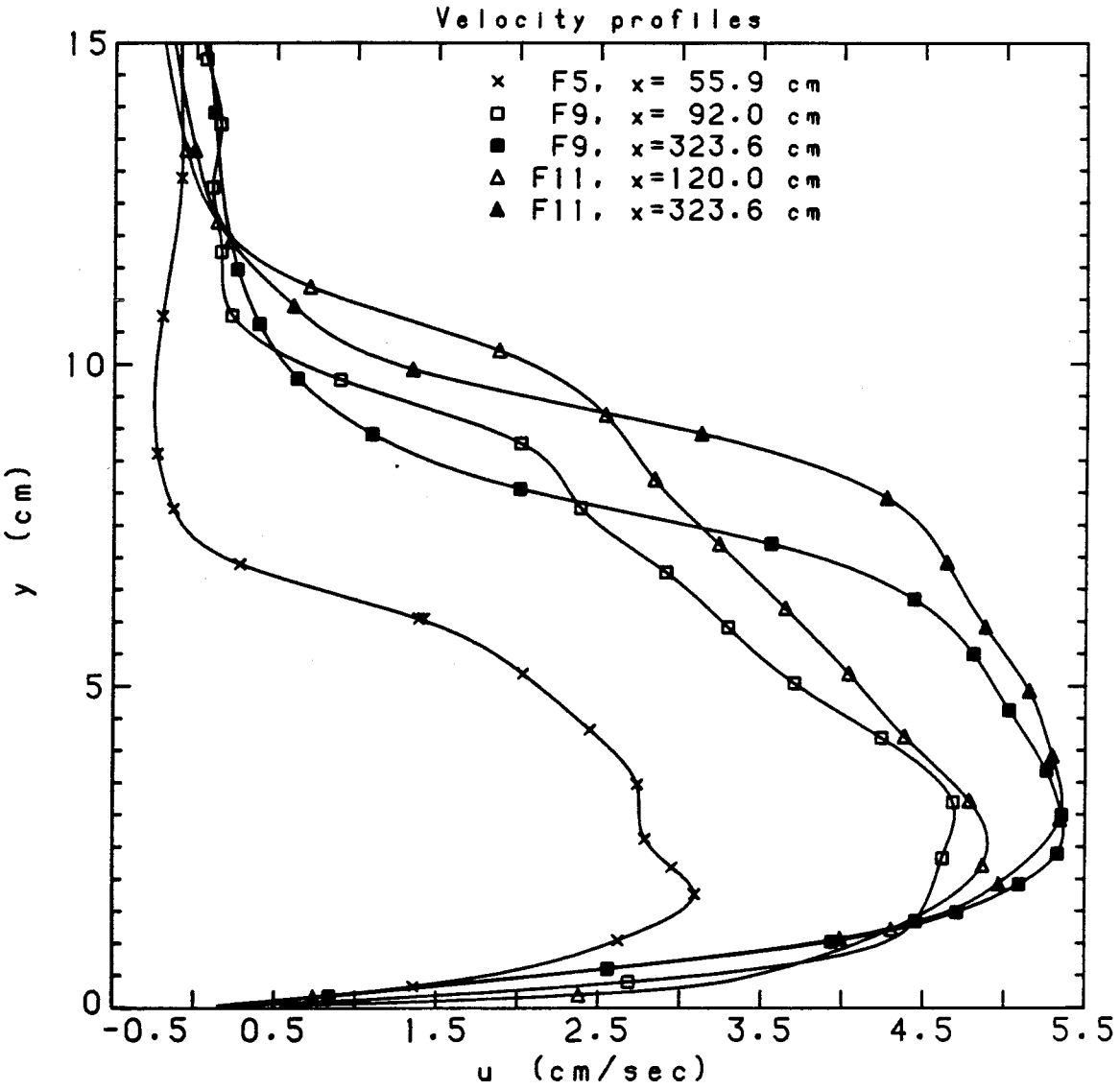

Figure 5.15: Velocity profiles in the lower layer.

Normalized velocity profiles are presented in Figure 5.16, where u/u_{max} is plotted against $y/y_{50\%}$. This normalization shows that the upstream profiles ('F9, x=92.0 cm' and 'F11, x=120.0 cm') are very different in shape from the downstream profiles ('F9, x=323.6 cm' and 'F11, x=323.6 cm'). In other words, the velocity profiles 'evolve' as the longitudinal position along the channel changes, and self-similarity arguments cannot be applied. This should hardly be surprising in a flow of this complexity. Other normalizations have been considered, and u/u_{max} has been plotted against y/y_0, y/y_{max}, and $y/y_{0.1}$, where

y_0 = depth of zero-velocity line, where u=0;

y_{max} = depth at which $u = u_{max}$;

$y_{0.1}$ = depth at which $u = 0.1\,u_{max}$.

These normalizations gave profiles which appeared even less self-similar than those presented in Figure 5.16.

The evolution of the velocity profiles is clearly visible in Figure 5.17, where the upstream and downstream profiles obtained under the same flow conditions (see Table 5.1) are compared. As the lower layer flows along the subcritical gradually-varied counterflow, the velocity profile becomes more 'rounded', while the time-averaged density interface becomes sharper and shallower. A role in this change of shape of the velocity profile is certainly played by the growth of the boundary layer, both at the bottom and at the walls of the experimental channel. This fact is addressed in more detail in the following sections.

5.4 Continuity checks

The density and velocity profiles presented in the two previous sections have been measured on the middle plane of the experimental flume. While it is reasonable

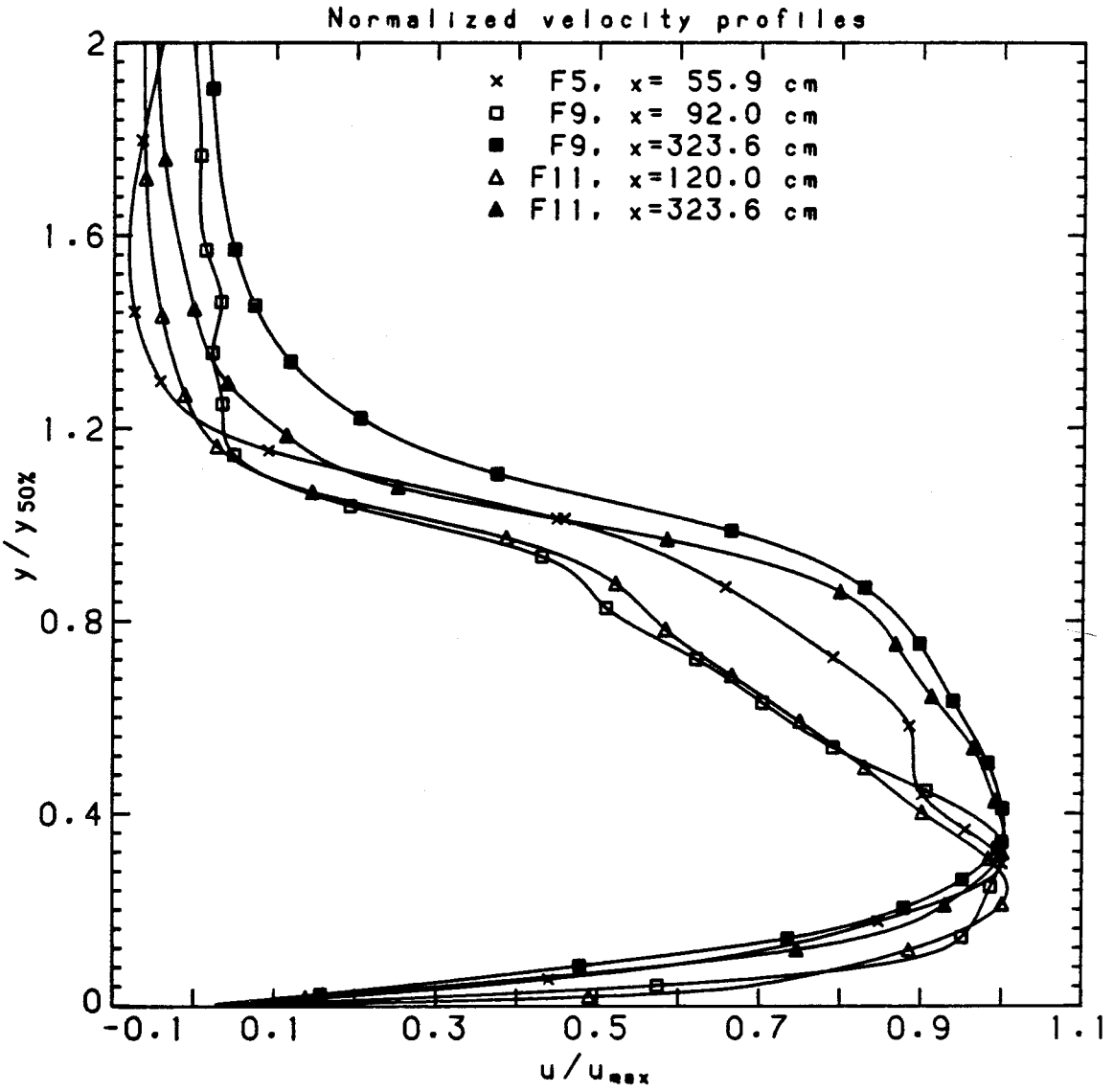

Figure 5.16: Normalized velocity profiles in the lower layer.

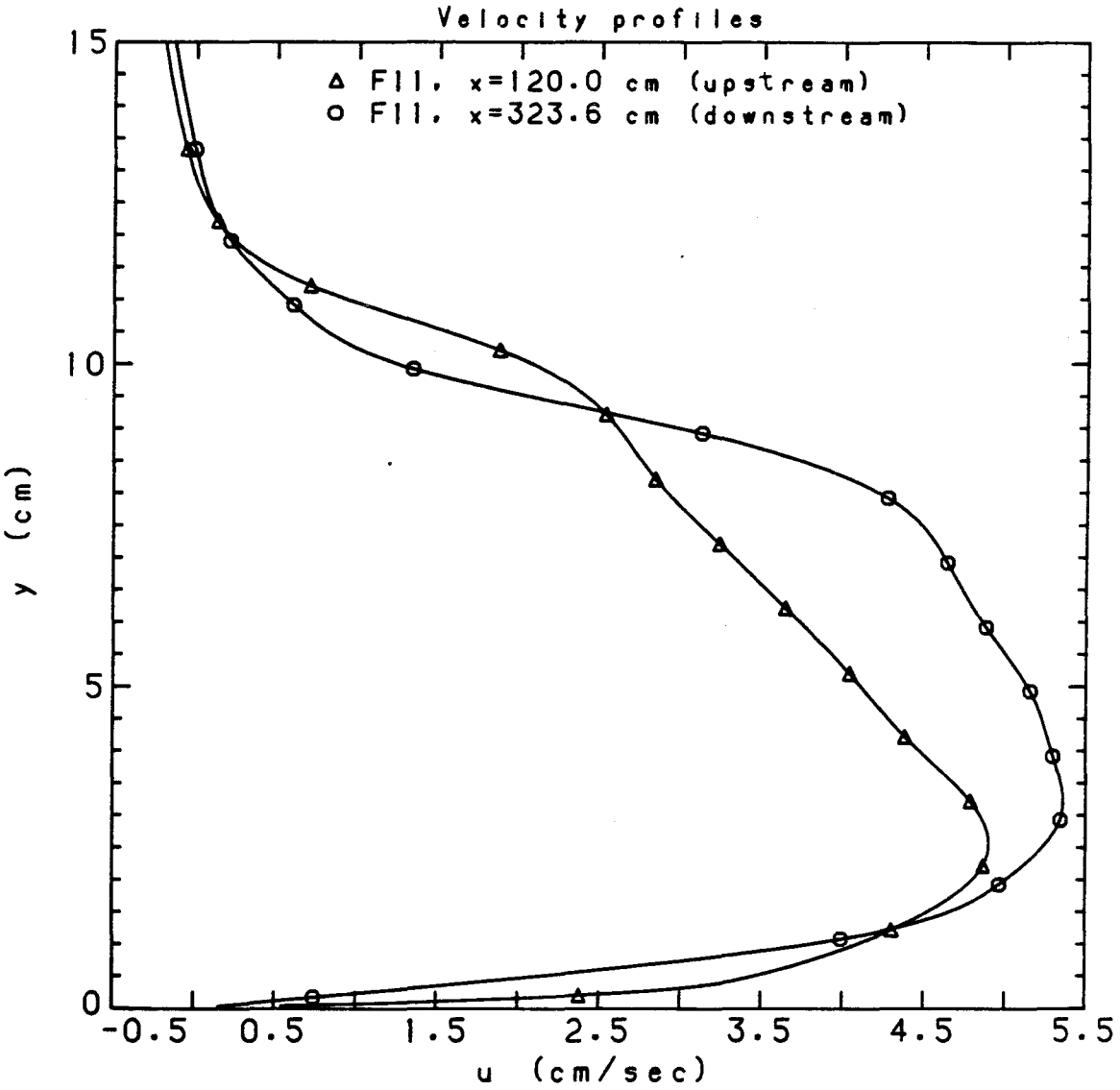

Figure 5.17: Evolution of velocity profiles along the channel.

to assume that the density distribution near the flume walls is not different from the distribution on the middle plane, the same cannot be said of the velocity distribution. In other words, the horizontal velocity is a function of z (see Figure 5.18), since a boundary layer will form near the walls. It is therefore necessary to account for this 'wall effect' if the measured profiles are to be used to compute flowrates, salt fluxes and momentum fluxes.

A characteristic velocity in the lower layer is defined as

$$U = \frac{q_1}{y_{50\%}} ,$$

where the flowrate in the lower layer, q_1, is defined as the product of the source flowrate, q_0, and the dilution S obtained from the blue-dye experiments under the same flow conditions.

The displacement thickness of the wall boundary layer at a distance x from the source is taken to be

$$\delta^* = 1.73 \frac{x}{\sqrt{Ux/\nu}} , \tag{5.1}$$

where ν is the kinematic viscosity of water (Batchelor, 1967).

The momentum thickness, on the other hand, is given by

$$\theta = 0.664 \frac{x}{\sqrt{Ux/\nu}} . \tag{5.2}$$

In the upper layer, where the fluid velocities are very small, a parabolic velocity distribution is hypothesized

$$u(z) = u_c [1 - (\frac{z}{b/2})^2] , \tag{5.3}$$

where u_c is the centerline velocity and b is the width of the flume.

The flowrate per unit width in the lower layer is then given by

$$q_l = \frac{1}{b} \int_{-\frac{b}{2}}^{\frac{b}{2}} \int_0^{y_0} u(y,z) dy dz \cong \frac{b - 2\delta^*}{b} \int_0^{y_0} u_c(y) dy , \tag{5.4}$$

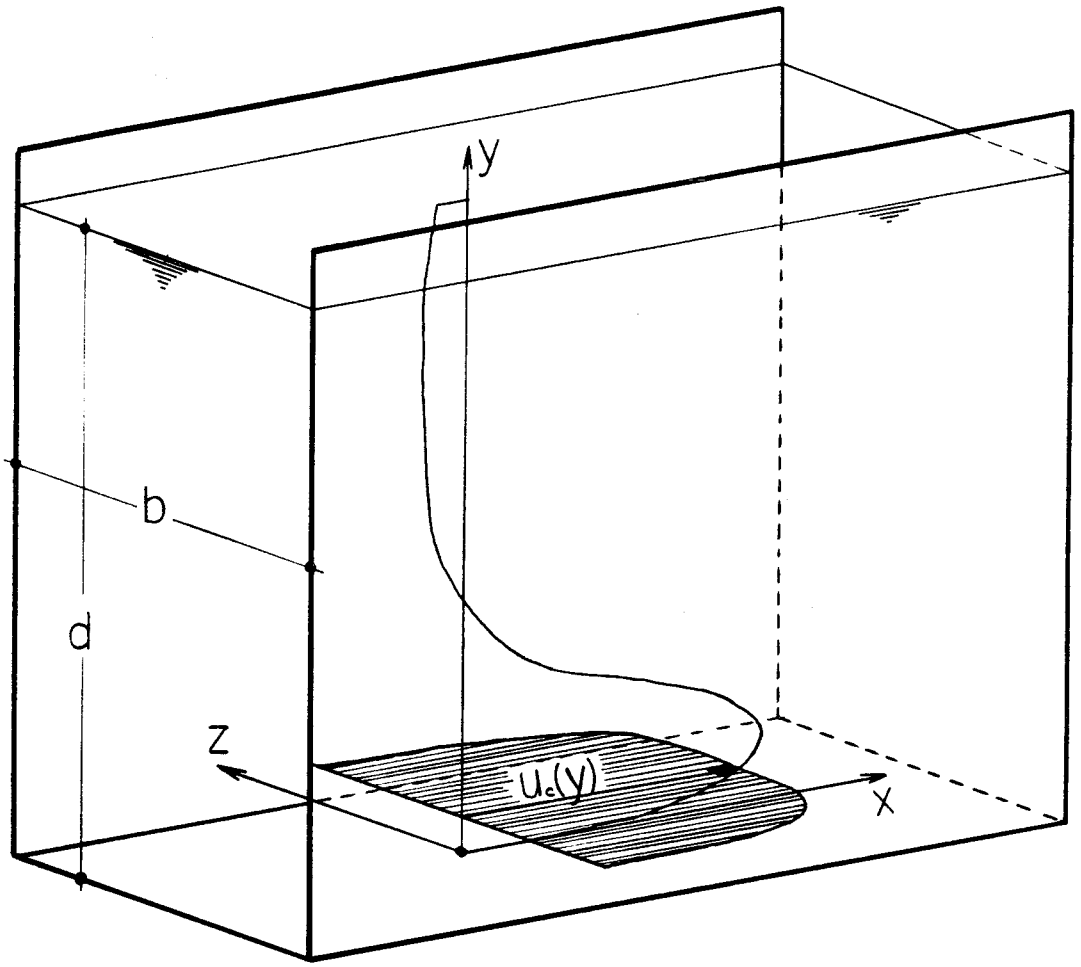

Figure 5.18: Sketch of velocity distribution $u(y, z)$.

Experiment	q_o (cm^2/s)	q_ℓ (cm^2/s)	q_u (cm^2/s)	q_{salt}/c_o (cm^2/s)	$\frac{q_o - q_\ell + q_u}{q_o}$ (%)	$\frac{q_o - q_{salt}/c_o}{q_o}$ (%)
F5, x= 55.9 cm	10.26	12.11	2.13	7.85	+2.7	+23.5
F9, x= 92.0 cm	16.79	27.40	9.72	15.80	-5.2	+5.9
F9, x=323.6 cm	16.73	25.94	13.73	14.64	+27.0	+12.5
F11, x=120.0 cm	18.80	31.50	12.68	19.33	-0.1	-2.8
F11, x=323.6 cm	18.93	30.00	15.87	15.23	+25.4	+19.5

Table 5.3: Flowrates and salt fluxes. 'Continuity checks'.

where the integral on the right hand side can be readily computed from the measured velocity distribution.

The flowrate per unit width in the upper layer is

$$q_u = \frac{1}{b}\int_{-\frac{b}{2}}^{\frac{b}{2}}\int_{y_0}^{d} u(y,z)dydz \cong \frac{2}{3}\int_{y_0}^{d} u_c(y)dy. \tag{5.5}$$

The salt flux per unit width, q_{salt}, can be obtained from

$$\frac{q_{salt}}{c_0} = \frac{1}{b}\int_{-\frac{b}{2}}^{\frac{b}{2}}\int_{0}^{d} u(y,z)\frac{c(y)}{c_0}dydz \cong \frac{b-2\delta^*}{b}\int_{0}^{d} u_c(y)\frac{c(y)}{c_0}dy, \tag{5.6}$$

where $c(y)$ is the salt concentration at depth y and c_0 is the salt concentration at the source. The integrals on the right hand side can, again, be easily computed using the measured velocity and density profiles. In a similar way, it is possible to compute momentum fluxes and hydrostatic pressure forces, as discussed in the next section.

Table 5.3 reports the flowrates and salt fluxes measured in the five laser-based experiments. Continuity of fluid flow requires that $(q_l - q_u)$ be equal to q_0, and continuity of salt flux requires that q_{salt}/c_0 be equal to q_0. These 'continuity checks' allow

an assesment of the accuracy of the experiments and of the 'wall effect' assumptions made. The relative errors in water and salt fluxes are defined and reported in the last two columns of Table 5.3. The accuracy is seen to be satisfactory, if it is remembered that many factors contributed to the reported errors:

- the displacement thickness has been computed using Equation 5.1, where a characteristic velocity, U, has been used instead of the actual velocity $u(y)$;
- a parabolic velocity profile (Eq. 5.3) has been assumed in the upper layer;
- there is a possible error associated with the flowmeter reading of the discharge flowrate q_0;
- errors in the LDV velocity measurements (Notice that very small errors in the velocities can cause large errors in the flowrates, since the errors are integrated over the entire ambient water depth. For example, a systematic underestimation of the velocity by only $\sim$0.08 cm/s in experiment 'F9, x = 323.6 cm' would by itself explain the entire continuity error found.);
- errors in the LIF density measurements;
- variability of the flume width b along the x and y directions (Fig. 5.18).

5.5 Flow force

5.5.1 Introductory considerations

The momentum principle applied to the entire channel depth between the source (section 0) and a cross-section just downstream of the jump (section 1) can be expressed as follows

$$FF_0 = FF_1 + \Delta FF_{01}, \tag{5.7}$$

where

FF_0 = flow force at section 0

FF_1 = flow force at section 1

ΔFF_{01} = flow force loss between sections 0 and 1.

The one-dimensional theory presented in Chapter 2 assumed uniform velocity and density profiles, and provided the results

$$FF_0 = \frac{q_0^2}{h_0} + \frac{1}{2} g_0' h_0^2 + g d \delta \tag{5.8}$$

$$FF_1 = \frac{q_1^2}{h_1} + \frac{(q_1 - q_0)^2}{d - h_1} + \frac{1}{2} g_1' h_1^2 \tag{5.9}$$

$$\Delta FF_{01} = 0 \tag{5.10}$$

as shown in Equation 2.7.

It will be recalled, however, that Equation 2.7 was found to be inaccurate for large values of the parameters H and $\mathbf{F_0}$. More specifically, the roots h_1 were too high, and this led to an overestimation of the dilution in the mixing channel when the upstream and downstream equations were combined to obtain hydraulic solutions. This section is devoted to developing new insight into this problem.

Attention will be focused, for the following discussion, on the flow conditions of two blue-dye experiments, F9 and F11, and of two laser-based experiments, 'F9, x = 92.0 cm' and 'F11, x = 120.0 cm'. Such flow conditions are within the range where the discrepancy between the one-dimensional theory and the blue-dye experimental results was observed.

The inaccuracy of the one-dimensional theory is evident if Equations 5.8 and 5.9 are used to compute flow forces under the conditions of experiments F9 and F11. This is shown in Table 5.4, where it can be seen that the flow force at section 1 is considerably lower than the flow force at section 0. If the velocity and density profiles

Experiment	FF_0 (cm^3/s^2)	FF_1 (cm^3/s^2)	$\frac{FF_0 - FF_1}{FF_0}$
F9	430.3	336.9	21.7%
F11	525.1	404.1	23.0%

Table 5.4: Flow force computed using Eqs. 5.8 and 5.9 (one-dimensional theory).

are allowed to be non-uniform, the flow force at section 1 can be expressed as

$$FF_1 = \frac{1}{b}\int_{-\frac{b}{2}}^{\frac{b}{2}}\int_0^{h_{1v}} u^2 dydz + \frac{1}{b}\int_{-\frac{b}{2}}^{\frac{b}{2}}\int_{h_{1v}}^{d} u^2 dydz + \int_0^d\int_y^d g' dydy \qquad (5.11)$$

(h_{1v} is the depth of the zero-velocity line at section 1) or, introducing the momentum thickness θ and assuming the upper layer to have the parabolic velocity distribution given by Equation 5.3,

$$FF_1 \cong \frac{b-2\theta}{b}\int_0^{h_{1v}} u_c^2 dy + \frac{8}{15}\int_{h_{1v}}^{d} u_c^2 dy + \int_0^d\int_y^d g' dydy. \qquad (5.12)$$

The data from the laser-based experiments 'F9, x=92.0 cm' and 'F11, x=120.0 cm' can be used to compute FF_0 using Equation 5.8 and FF_1 using Equation 5.12. The results are shown in Table 5.5. Two facts emerge from observation of Tables 5.4 and 5.5:

- if the assumptions of uniformity of velocity and density profiles are abandoned, the loss of flow force between sections 0 and 1 is not as large as it appeared to be

Experiment	FF_0 (cm^3/s^2)	FF_1 (cm^3/s^2)	$\frac{FF_0 - FF_1}{FF_0}$
F9,x= 92.0cm	412.8	357.6	13.4%
F11,x=120.0cm	517.2	424.6	17.9%

Table 5.5: Flow force computed using Equations 5.8 and 5.12.

when it was computed using the one-dimensional theory. This idea is clarified in Section 5.5.2, where the correction factors are computed;

- a considerable loss of flow force is still present between sections 0 and 1. In other words, Equation 5.10 needs to be reconsidered. This is done in Section 5.5.3, where the boundary shear along the jump region is estimated.

5.5.2 Correction factors

Let A be the momentum flux in the lower layer at section 1. Then

$$A = \frac{b - 2\theta}{b} \int_0^{h_{1v}} u_c^2 dy, \tag{5.13}$$

and if B is the momentum flux in the upper layer, then

$$B = \frac{8}{15} \int_{h_{1v}}^{d} u_c^2 dy, \tag{5.14}$$

and the hydrostatic pressure force is

$$C = \int_0^d \int_y^d g' dy dy. \tag{5.15}$$

With these definitions Equation 5.12 can then be rewritten as

$$FF_1 = A + B + C. \tag{5.16}$$

Consider now uniform velocity and density distributions with

depth of lower layer = $y_{50\%}$;

flowrate in lower layer = q_l;

flowrate in upper layer = q_u;

salt flux = q_{salt}.

The choice of $y_{50\%}$ as the depth of the lower layer in the assumed uniform distributions deserves some discussion. The one-dimensional theory assumes that the velocity changes sign at the density interface, i.e., that there is only one depth that characterizes the lower layer. In the actual profiles, on the other hand, there are two relevant depths: the interfacial depth, $y_{50\%}$, and the depth of the zero-velocity line, h_{1v}. Therefore, in defining uniform profiles 'equivalent' to the actual profiles, it is necessary to choose whether to use $y_{50\%}$ or h_{1v} as the depth of the lower layer. The interfacial depth $y_{50\%}$ is chosen in this study for two reasons. First, it is the interfacial depth that corresponds to the visual depth which was measured in the blue-dye experiments. Second, the error introduced in the momentum term A (Eq. 5.13) by assuming the uniform velocity to change sign at $y_{50\%}$ is much smaller than the error that would be introduced in the hydrostatic term C (Eq. 5.15) by assuming the uniform density to have the interface at h_{1v}. It should also be pointed out that had h_{1v} been chosen instead of $y_{50\%}$, the ideas developed in the following discussion would not have changed, and only the numerical values of the computed flow forces would have been different.

With the above mentioned uniform distributions, the flow force at section 1

would be

$$FF_1 = A' + B' + C', \tag{5.17}$$

where

$$A' = \frac{q_l^2}{y_{50\%}} \tag{5.18}$$

(momentum flux in lower layer),

$$B' = \frac{q_u^2}{d - y_{50\%}} \tag{5.19}$$

(momentum flux in upper layer),

$$C' = \frac{1}{2}\, g\, \frac{q_{salt}/c_0}{q_l} (\frac{\Delta\rho}{\rho})_0\, y_{50\%}^2 \tag{5.20}$$

(hydrostatic pressure force).

Now, if Equation 5.16 is written in the form

$$FF_1 = c_1 A' + c_2 B' + c_3 C', \tag{5.21}$$

the 'correction factors' c_1, c_2, and c_3 will be a measure of how non-uniform the velocity and density distributions are (obviously, if the actual distributions were uniform, c_1, c_2, and c_3 would all be equal to unity).

The correction factors for experiments 'F9, x=92.0 cm' and 'F11, x=120.0 cm' are computed in Table 5.6. The correction factor c_2 for the momentum flux in the upper layer is of little interest, since B is much smaller than A and C. The correction factor c_3, which is a measure of the non-uniformity of the density profiles, is seen to be close to 1. This is in agreement with the previous observation that the density profiles were nearly uniform. However, the correction factor c_1 in both experiments exceeded the value 1.4. This means that if a uniform distribution of velocity is assumed the momentum flux in the lower layer is underestimated by more than 40%.

Experiment	A	B	C	A′	B′	C′	c_1	c_2	c_3
F9, x= 92.0cm	112.8	5.1	239.7	79.9	2.2	234.9	1.412	2.33	1.02
F11, x=120.0cm	136.5	5.6	282.5	94.5	3.8	301.7	1.444	1.47	0.94

Table 5.6: Computation of correction factors (A, B, C, A', B', C' have units of cm^3/s^2).

Table 5.7 shows how the assumption of uniformity of profiles affects the value of the flowforce at section 1. The errors introduced by that assumption are seen to account approximately for the difference between the errors reported in Tables 5.4 and 5.5.

5.5.3 Boundary shear along the jump region

The goal of this section is to determine the order of magnitude of the boundary shear force on the flow between sections 0 and 1.

The bottom shear force along the supercritical entraining region is considered first. The velocity distribution in this region is assumed to be self-preserving (Wilkinson, 1970), and the influence of gravity is neglected, i.e., a non-buoyant wall-jet flow structure is hypothesized in the following computation. A parabolic velocity distri-

Experiment	A+B+C (cm^3/s^2)	A'+B'+C' (cm^3/s^2)	$\frac{(A+B+C)-(A'+B'+C')}{A+B+C}$
F9, x= 92.0cm	357.6	317.0	11.4%
F11, x=120.0cm	424.6	400.0	5.8%

Table 5.7: Errors in flow force due to the assumption of uniformity of velocity and density profiles.

bution of the form

$$\frac{u}{u_{max}} = \frac{y}{y_{max}}(2 - \frac{y}{y_{max}}), \tag{5.22}$$

is assumed to exist in the laminar layer between the channel bottom (y=0) and the depth y_{max} where $u = u_{max}$. The shear stress at the bottom can then be expressed as

$$\tau_b = \mu(\frac{du}{dy})_{y=0} = 2\mu\,\frac{u_{max}}{y_{max}}\,. \tag{5.23}$$

Experiments performed by Wilkinson (1970) in flows similar to those studied here showed that

$$y_{max}(x) \simeq 0.2\, y_{50\%}(x), \tag{5.24}$$

$$u_{max}(x) \simeq 1.6\, U(x) = 1.6\,\frac{q_l(x)}{y_{50\%}(x)}\,, \tag{5.25}$$

$$y_{50\%}(x) \simeq h_0 + 0.15\, x, \tag{5.26}$$

where $q_l(x)$ and $y_{50\%}(x)$ are the local flowrate and interfacial depth in the lower layer.

If it is further assumed that $q_l \sim x^{1/2}$, then

$$q_l(x) \simeq q_0 + [q_l(L_e) - q_0](\frac{x}{L_e})^{\frac{1}{2}} , \tag{5.27}$$

where L_e is the length of the entraining region, i.e., the distance between the source and the beginning of the roller region.

Combining Equations 5.23–5.27,

$$\tau_b \simeq 16\,\mu\,\frac{q_0 + [q_l(L_e) - q_0](x/L_e)^{\frac{1}{2}}}{(h_0 + 0.15\,x)^2} , \tag{5.28}$$

and the shear force per unit width along the entraining region, F_b, is obtained by integration

$$\frac{F_b}{\rho} \simeq \int_0^{L_e} 16\,\nu\,\frac{q_0 + [q_l(L_e) - q_0](x/L_e)^{\frac{1}{2}}}{(h_0 + 0.15\,x)^2}\,dx. \tag{5.29}$$

The values of the upstream parameters, h_0 and q_0, are known for experiments 'F9, x = 92.0 cm' and 'F11, x = 120.0 cm'; $q_l(L_e)$ can be taken to be equal to the measured flowrate at section 1, since negligible entrainment takes place in the roller and subcritical counterflow regions; L_e has been determined in the visual observations. Therefore Equation 5.29 can be integrated to obtain the values of F_b, as shown in Table 5.8.

Similar considerations, together with the experimental data, can be applied to estimate the shear forces F_w and F_s, where

F_w = force per unit width due to wall shear in the entraining region;

F_s = force per unit width due to bottom and wall shear in the roller and subcritical counterflow regions, i.e., between $x = L_e$ and $x = 2\,L_j$ (see Table 5.8).

The total estimated boundary shear force between sections 0 and 1, $F_t = F_b + F_w + F_s$, can be seen (Tables 5.8 and 5.5) to amount to $\sim$ 8.7% of the flow force at section 0, FF_0, in experiment 'F9, x=92.0 cm', and to $\sim$ 9.4% of FF_0 in experiment 'F11, x=120.0 cm'.

Experiment	L_e (cm)	F_b/ρ (cm^3/s^2)	F_w/ρ (cm^3/s^2)	F_s/ρ (cm^3/s^2)	F_t/ρ (cm^3/s^2)
F9, x= 92.0 cm	12	24.6	3.7	7.5	35.8
F11, x=120.0 cm	20	30.6	4.6	13.2	48.4

Table 5.8: Determination of boundary shear force between sections 0 and 1.

5.5.4 Conclusions on flow force considerations

The results of experiments 'F9, x=92.0 cm' and 'F11, x=120.0 cm' have been analyzed in detail in the previous sections in order to find an explanation for the inaccuracy of Equation 2.7 which was pointed out and discussed in Chapter 4. Equation 2.7, which states conservation of flow force across the jump region in a one-dimensional setting, has been shown to overpredict the flow force at section 1 by 21~23% (Table 5.4).

It has then been shown that an overprediction of 6~11% can be attributed to the simplifying assumption of uniformity of velocity and density profiles (Table 5.7), and an overprediction of ~9% was caused by the neglect of the boundary shear force along the jump region. This leaves a small fraction of the overprediction still unaccounted for. Three possible explanations are the following:

- experimental error. The computed values of flow force cannot be expected to be extremely precise, since the results of Section 5.4 showed that continuity errors of

up to almost 6% were present in experiments 'F9, x=92.0 cm' and 'F11, x=120.0 cm';

- approximations introduced in the determination of the boundary shear force;
- lowering of the free surface over the source region. It was already mentioned that the non-hydrostatic pressure distribution in the ambient fluid surmounting the entraining region might have resulted in an ambient water depth near the source region lower than the depth d that was present in the rest of the channel. This would have resulted in a flowforce at section 0, FF_0, lower than the values reported in Tables 5.4 and 5.5. No measurable lowering of the free surface was observed in experiments 'F9, x=92.0 cm' and 'F11, x=120.0 cm', but it should be realized that even an extremely small lowering could have a large impact on the flow force (for example, a lowering of only 0.01 mm would be sufficient to reduce FF_0 by $\sim$10%).

Chapter 6

Conclusions

6.1 Discussion

The main goal of this investigation was to gain new insight into the general problem of mixing in two-layer density-stratified flows, and more specifically to assess the importance and the nature of the role played by far-field controls and vertical confinement of the flow field. Many previous studies of mixing in stratified flows were found to ignore the effect of these factors, although some kind of downstream control always exists, and in many practical situations of interest to engineers and environmental scientists the flow system is vertically bounded.

The theoretical and experimental results developed in the previous chapters, which highlighted the interdependence of source parameters, far-field control, and ambient conditions (a summary of the main results can be found in Section 6.3) are now used to describe in detail the mechanics of a two-layer system. The example of a horizontal rectangular mixing channel is considered once again to address the key issues in a simpler way, but the ideas discussed below are sufficiently general to be applied to all problems involving conjugate flows in two-layer stratified systems.

For the sake of discussion it will be first assumed that a dense fluid is discharged from a rectangular slot located at the bottom of a deep channel in which *no* downstream control is present. This idealized condition, in which any downstream effect is

removed from the flow, is very unlikely to occur in any practical situation, but it can be envisioned from a theoretical standpoint by considering a channel with a sloping bottom, in which the slope is just sufficient to offset the boundary shear along the channel (this situation was actually approximated in the laboratory by Wright, 1986).

If the densimetric Froude number of the discharged flow is larger than about three (Chu and Baddour, 1984), the entraining region which follows the source section can be regarded as a horizontal buoyant wall jet. A large shear is applied across the density interface between the source and the ambient fluids, so that Kelvin-Helmholtz waves form, grow and overturn. These movements of the interface, which appear to be caused by the velocity fields of the eddies of the main turbulent motion, result in a folding and engulfing of the ambient fluid, with a net result of ambient fluid being entrained into the flowing layer (Townsend, 1970; Jirka, 1982).

Many investigations have been conducted on buoyant jets and, although a complete review is not intended here, some results are worth mentioning in this context. The problem of quantifying mixing across a density interface is a very difficult one, ultimately related to the structure of the turbulence. In a two-layer system, if there is a mean flow in at least one of the two layers, the shear stability of the interface, and not only the turbulence, is believed to be of primary importance. The main factors at play in the development of a horizontal buoyant jet are fundamentally three:

- turbulent energy is produced by the mean shear, which feeds the horizontal component of the turbulent velocity fluctuations; this energy is then redistributed among all three turbulent velocity components by the pressure fluctuations (Turner, 1973);

- energy is used to do work against buoyancy (this directly affects the vertical turbulent velocity fluctuations); the buoyancy-induced potential energy has a

profound impact on the turbulent kinetic energy, although the impact on the mean kinetic energy may be limited, since measurements in non-buoyant plane jets (e.g. see Rodi, 1975; Jirka, 1982) showed that the turbulent kinetic energy is an order of magnitude smaller than the mean flow energy. This implies (Jirka, 1982) that the buoyancy is expected to have an immediate impact on the turbulent structure, and therefore on the entrainment, while the influence on the mean motion is delayed in comparison;

- energy is lost to viscous dissipation (this affects all three components of the turbulent kinetic energy, since the strain field containing the viscous scales is not determined by the mean strain but by the turbulence, and this implies isotropy at small scales).

The development and the entraining characteristics of horizontal buoyant jets are therefore governed by the competition between the stabilizing effects of buoyancy and the destabilizing effect of shear, while viscous dissipation continuously drains energy from the system. This is equivalent to saying that if a flux Richardson number is defined as the ratio between the work done against buoyancy and the production of turbulent energy by the mean shear, then the interface between the two layers will become less and less unstable as this number increases from zero (non-buoyant case) to a critical value at which all entrainment is suppressed.

A recent review of the subject of interfacial stability was given by Christodoulou (1986). The stability has been traditionally expressed by means of the gradient Richardson number

$$\mathbf{R_i} = \frac{\partial g'/\partial y}{(\partial u/\partial y)^2} \,.$$

According to linear stability theory, its critical value is about 1/4 (Miles, 1961), above which infinitesimal perturbations are damped out and turbulence is not developed.

This criterion for stability is basically confirmed by recent experimental investigations (e.g., Rohr, Itsweire, Helland, and Van Atta, 1988).

Many investigations in layered systems, on the other hand, made use of a *bulk* Richardson number, $\mathbf{R_{i0}}$, defined in terms of total buoyancy difference, but the length and velocity scales employed to define $\mathbf{R_{i0}}$ were not unique and consequently many different critical values for $\mathbf{R_{i0}}$ have been established. Although there exist many, and sometimes contradictory, studies on the subject of horizontal buoyant jets, there is general agreement on the fundamental role played by some form of Richardson number. When this number is very low, typically at the jet source, the jet grows in thickness linearly, with a growth rate given by $dh/dx \simeq 0.068$ (where h is the depth of the lower layer, and x is the distance from the source), which is the same as the growth rate of a non-buoyant *wall* jet (Schwarz and Cosart, 1961), but considerably smaller than the growth rate of 0.1 for a free jet (Gutmark and Wygnansky, 1974). Chu and Baddour (1984) suggest that the small growth rate is caused by the suppression of the sinuous mode oscillations (which are more unstable than the varicous mode oscillations) by the solid boundary.

As one moves away from the source, the increasing influence of buoyancy, which is reflected in increasing values of the Richardson number, causes the entrainment rate across the interface to decrease, and consequently dh/dx continuously decreases. Several different laws for the dependence of the entrainment rate on the Richardson number have been proposed in the literature. For the purpose of this discussion, it will only be noted that all the investigations agree on the fact that decreasing entrainment rates are associated with increasing Richardson numbers.

In the hypothetical channel under consideration, in which the downstream control has been removed, the buoyant jet will eventually reach a 'neutrally stable state' (Chu and Baddour, 1984), corresponding to a situation in which the shear stress

that would be produced by the turbulence under non-buoyant conditions is entirely offset by the buoyant forces. Since in this neutrally stable state the turbulence is not able to receive energy from the mean shear, its decay, due to the continuous drain of turbulent kinetic energy by viscous dissipation, is believed to behave like the decay of the turbulence behind an ocillating grid (for a complete discussion on turbulence in zero-mean shear stratified flows, see Hannoun and List, 1988). The idea that for gradient Richardson numbers larger than critical the turbulence decays like grid-generated turbulence, and the influence of the mean shear on the dynamics of the flow is small, is supported by the experiments performed by Rohr, et al. (1988) in stably stratified shear flows. Additional support for this idea can be found in the observations made by Gartrell (1979) in two-layer 'temperature-stratified' flows; these observations showed that after the initial development of large two-dimensional vortex structures and their subsequent collapse (when the stratification was sufficiently strong), the turbulence farther downstream was dominated by large intermittent turbulent bursts, which were responsible for most of the mixing. This is very similar to what was observed in grid-generated turbulence by Hannoun and List (1988).

Integral-type predictive equations for horizontal buoyant jets have been constructed to describe the longitudinal development of the flow field. For example, Jirka (1982) proposed the equation

$$\beta = \beta_0[1 - \frac{\mathbf{R_{ih}}}{\sqrt{\mathbf{R_{ih}}^2 + 0.25^2}}](1 + \mathbf{R_{ih}})^{-1} , \qquad (6.1)$$

where

β = variable entrainment coefficient for buoyant jet,

β_0 = constant entrainment coefficient for non-buoyant jet,

$\mathbf{R_{ih}} = g_c' h / u_c^2$ = bulk Richardson number,

g_c' and u_c are the centerline values of the reduced gravity and of the horizontal

velocity. It will be discussed later when equations like Eq. 6.1 (see also Arita, Jirka, and Tamai, 1986) become useful.

The discussion is now extended to include the presence of a downstream control, but the channel is still considered to be very deep, so that no interaction exists between the dense layer and the free surface.

The controls investigated in this study, broad-crested weirs and a free overfall in a channel with non-negligible boundary shear, have been found to modify in a dramatic way the flow structure of the ideal 'uncontrolled channel' discussed above. The control establishes a critical flow at the downstream end of the channel, and generates a backwater effect, with the formation of a subcritical layer of dense fluid upstream of the control. The role played by buoyancy in this layer is fundamentally different from the role that buoyancy plays in the developing jet region previously discussed; while in the jet the main effect of buoyancy was an influence on the structure of turbulence, in the subcritical downstream layer buoyancy is the driving force of the mean flow. The subcriticality of the flow, intended in the sense of a densimetric Froude number lower than unity, ensures that negligible entrainment occurs across the interface in this region. Nevertheless, the subcritical layer established by the control has a profound impact on the mixing of the overall flow system (from the source to the control), since it governs the length of the entraining region. Experimental evidence shows that an abrupt transition between the supercritical entraining region and the subcritical downstream flow takes place when the local densimetric Froude number of the buoyant wall jet is conjugate to the densimetric Froude number of the downstream flow. This transition takes the form of a roller, characterized by a recirculation of dense fluid near the interface. The horizontal velocity of the dense fluid near the interface in this region is considerably lower than in the entraining region, so that the flow effectively becomes subcritical at the beginning of the roller, and

the interfacial shear within the roller region is insufficient to overcome the stabilizing effect of buoyancy. In other words, negligible entrainment of ambient fluid within the roller region occurs, because of the 'buffering' effect of the slow backwards flow of the dense fluid near the interface.

The visual observation of many such roller regions suggests the following speculation about their nature: the dense fluid forming the subcritical layer 'falls down the slope' of the buoyant jet interface by gravity (see Figure 6.1). As it descends, it encounters a jet which has a continuously increasing entrainment rate (moving towards the source). There is a point where the rate is so high that the whole descending dense fluid is entrained. Upstream of this point, which can be called the foot of the roller, *ambient fluid* is entrained, while downstream of it all the energy available for entrainment is used to entrain the gravity-driven descending dense fluid. This interpretation of the roller dynamics agrees with the observed steep slope of the interface in the roller region, and with the migration of the roller that is observed when the downstream control acts so as to change the depth of the subcritical downstream layer.

If the depth of the dense layer in the gradually-varied counterflow is increased, for example by raising a weir at the end of the channel, or by increasing the channel boundary friction, the excess hydrostatic pressure force driving the dense fluid down the slope is increased, so that a larger portion of the entraining region is used to reentrain recirculating dense fluid, and a shorter portion is available for entrainment of ambient fluid (Figure 6.2). The resulting reduced dilution of the source fluid across the mixing region is supported by the experimental results of this investigation.

Similarly, if the depth of the subcritical dense layer decreases as a result of a change in the downstream control, the roller migrates downstream, and both the extent of the entraining region and the dilution increase.

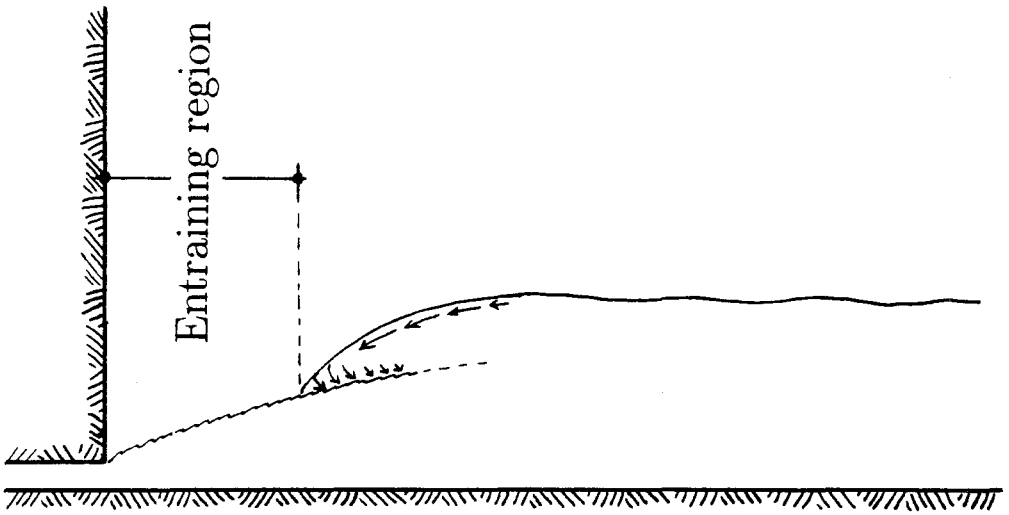

Figure 6.1: Mechanics of the roller.

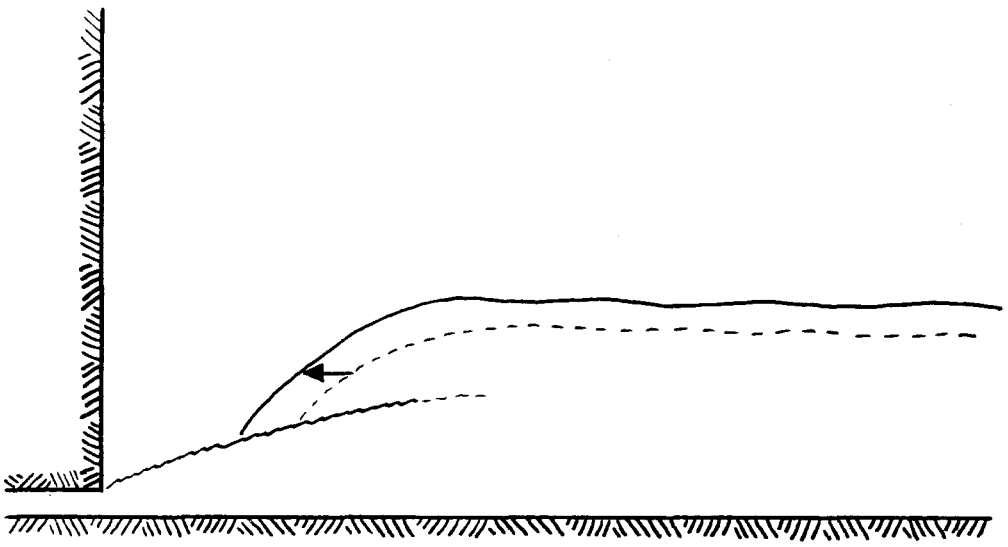

Figure 6.2: Migration of the roller.

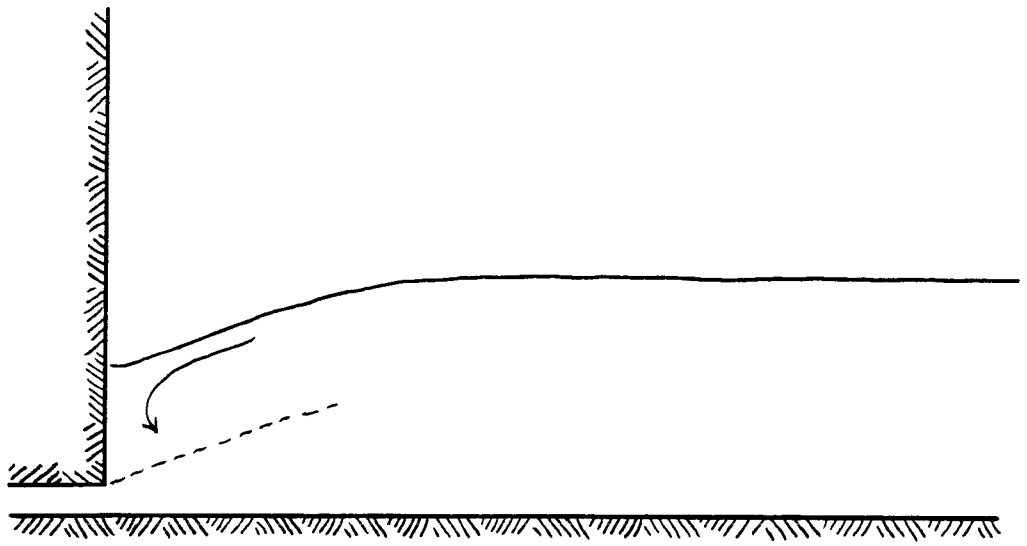

Figure 6.3: Flooded internal hydraulic jump.

If the discharge densimetric Froude number is small, i.e., if the buoyant jet has a small 'ability to entrain', and if the downstream control establishes a relatively deep subcritical layer, the dense fluid may descend all the way down to the source without being completely entrained (Figure 6.3). In this case a flooded internal hydraulic jump occurs, with a permanent cloud of dense fluid over the source completely eliminating the high-shear interface between the two layers, and with the entrainment of ambient fluid effectively blocked.

While this description of the mechanics of the roller region is rather speculative, there is no doubt about the fact that the downstream control strongly influences the overall flow in the channel, by governing the length of the entraining region. If the depth of the lower layer after the roller region is denoted by h_1 (see Figure 6.4), then the depth of the lower layer at the foot of the roller, h_j, is given by the Belanger-type equation

$$\frac{h_j}{h_1} = \frac{1}{2}[\sqrt{1 + 8\,\mathbf{F_1}^2} - 1], \tag{6.2}$$

where $\mathbf{F_1}$ is the densimetric Froude number at section 1. The applicability of this equation to two-layer systems derives from the fact that the entrainment of ambient fluid in the roller region is negligible, as previously pointed out. Theoretical arguments leading to Equation 6.2 have already been discussed in Section 2.4.3 (see also Equation 2.36), and experimental support was given by Rajaratnam and Subramanyan (1968, 1985, and 1986). The works of Rajaratnam and Subramanyan also provided experimental data on the longitudinal development of the roller region: their experiments showed that the longitudinal evolution of the roller region of denser wall jumps closely resembled the longitudinal evolution of open channel hydraulic jumps. More precisely, they determined an experimental curve $\zeta = \zeta(\xi)$, where

$$\zeta = \frac{h - h_j}{0.75(h_1 - h_j)}$$

$$\xi = \frac{x - x_j}{X} ,$$

and an experimental curve

$$\frac{X}{h_j} = \frac{X}{h_j}(\mathbf{F_j}) ,$$

where X is the length scale $(x - x_j)$ where $(h - h_j) = 0.75\,(h_1 - h_j)$, and $\mathbf{F_j}$ is the densimetric Froude number at section j (Figure 6.4). Situations in which these empirical results can become useful in this discussion will be pointed out in Section 6.2.

The upstream and the downstream flows have been considered separately in the previous discussion, in order the make the presentation clearer. However, it should not be forgotten that they are actually interdependent, since not only does the downstream control influence the upstream region (up to the foot of the roller), but also the entraining region influences the structure of the downstream flow, by governing the density and the flowrate which will exist after the mixing region. In other words, the overall flow in the channel can be successfully characterized only

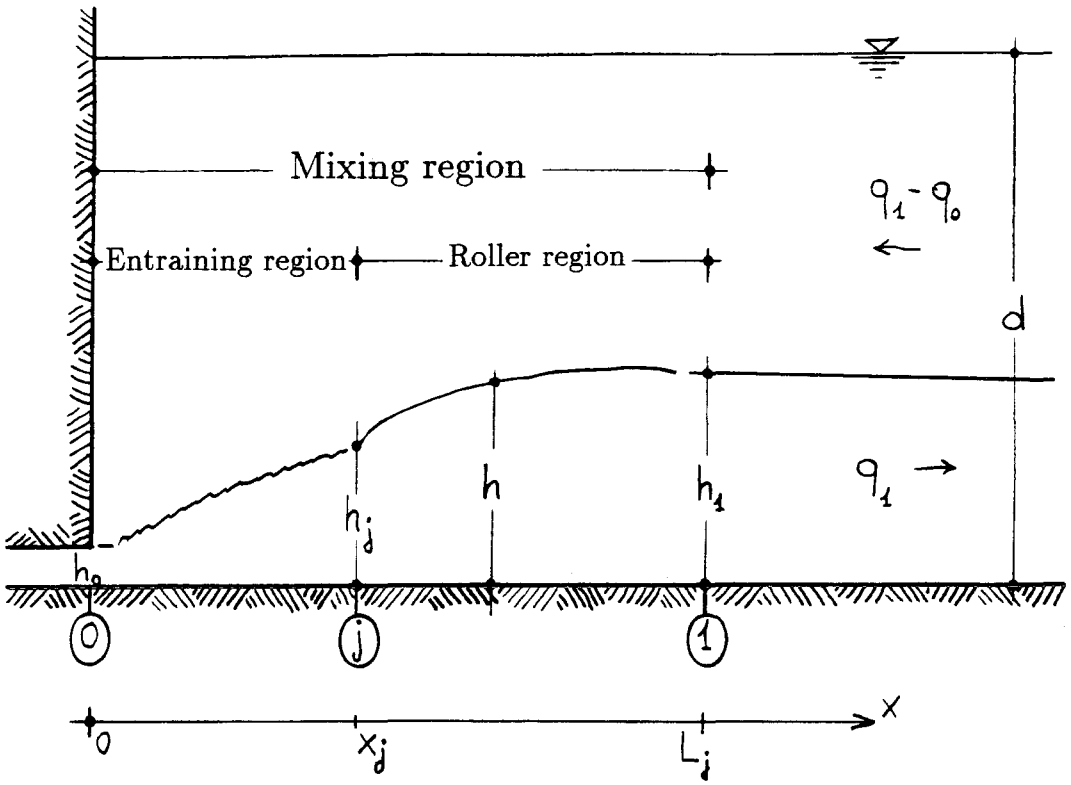

Figure 6.4: Sketch of the mixing region.

by an analysis that incorporates the interplay between upstream and downstream parameters, such as the analysis presented in Chapter 2.

Although this investigation is mainly concerned with horizontal channels, the effect of a slope in the channel bottom is worth mentioning at this point. If the slope is small, and more precisely if it is lower than the 'critical' slope at which the component of the buoyancy force down the slope equals the channel boundary friction, the downstream layer will remain subcritical and the flow in this layer will still be controlled from downstream. The only change in the flow produced by this small slope will be an increase in the dilution attained in the upstream mixing region, due to the fact that the downstream dense layer will be shallower, as if the friction along the channel had been reduced. Negligible entrainment would still occur, as for the horizontal channel, in the subcritical region, where the interface is stable.

On the other hand, if the slope is larger than the critical slope, the control from the downstream end of the channel is lost (Britter and Linden, 1980), and the downstream layer becomes supercritical. The experimental observations of Ellison and Turner (1959) showed that, because of the supercriticality of the flow, further entrainment of ambient fluid into the downstream dense layer takes place. The bulk Richardson number, which has reached a 'normal' value, determined by both the slope and the boundary friction, remains constant, but the entrainment does not cease, and the depth of the dense layer keeps on increasing (Turner, 1973). However, Wright (1986) suggested that further entrainment should not be regarded as an inevitable consequence of supercriticality, since rearrangement of the velocity and density profiles might promote interfacial stability even for densimetric Froude numbers somewhat larger than unity.

Attention is now directed towards the role played by the depth of the ambient fluid in the channel. In the previous discussion the ambient fluid has been considered to be stagnant. However, if the ambient depth d (see Figure 6.4) is limited, the entrainment flow $(q_1 - q_0)$ will generate a velocity field in the upper layer, with velocities of the order of $(q_1 - q_0)/(d - h_1)$. The effect of the counterflow on the structure of the two-layer system, therefore, becomes more and more important as d decreases, all other variables being fixed. As d decreases, while the densimetric Froude number of the lower layer is substantially fixed, the densimetric Froude number of the upper layer,

$$\mathbf{F_2} = \frac{q_1 - q_0}{[g_1'(d - h_1)^3]^{\frac{1}{2}}},$$

increases, so that the upper layer becomes more dynamically active. At first, the counterflow in the ambient fluid is believed to 'push' the roller region upstream (see Bewick, 1974), and this causes in general a reduction in the dilution in the mixing region for the reasons previously explained. If the depth of the ambient fluid is

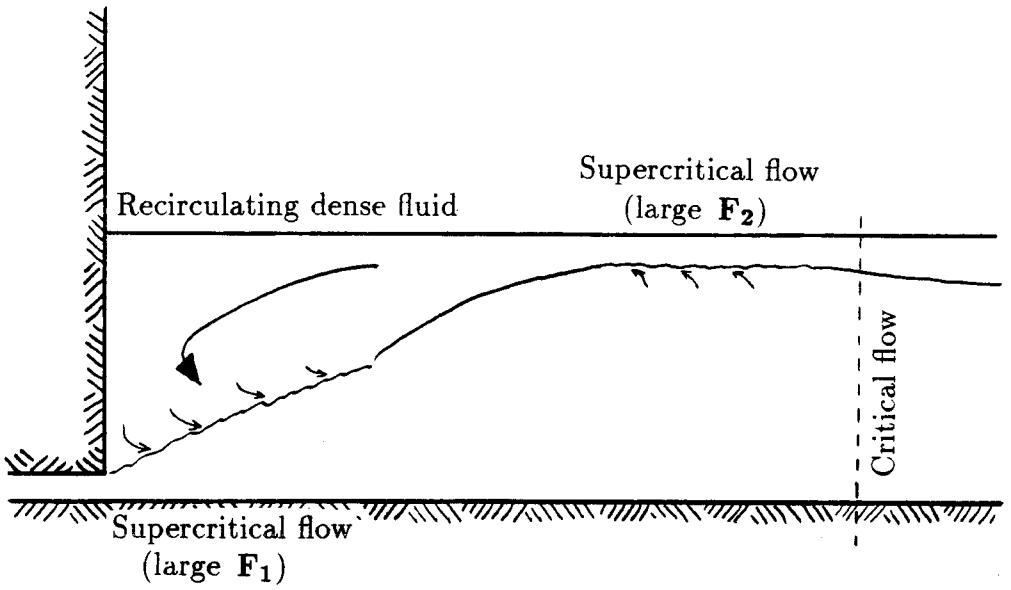

Figure 6.5: Upstream-controlled unstable flow.

further reduced, a point is reached at which the densimetric Froude number of the *upper* layer is so large that the two-layer system becomes supercritical ($\mathbf{F_1}^2 + \mathbf{F_2}^2 > 1$) just downstream of the roller region. This profoundly modifies the mechanics of the system, because now not only is the roller vigorously pushed towards the source, but also the shear between the two layers near the roller region is sufficient to cause instability of the interface, and the *upper* layer starts entraining dense fluid, as sketched in Figure 6.5. In this situation, which has been named an upstream-controlled unstable flow, a recirculation of dense fluid is generated. The dense fluid, entrained and mixed by the upper layer, is then reentrained by the lower layer near the source, with the net result of a decreased entrainment of ambient fluid in the mixing region.

After the attainment of this unstable flow structure, further decreases in the ambient depth (or, equivalently, increases in the discharge densimetric Froude number) have been experimentally shown to cause dramatic reductions in the entrainment

rate of ambient fluid. This is believed to be due to the fact that more and more of the energy available for entrainment in the discharge buoyant wall jet is used to entrain dense fluid carried over the source by the recirculating cell. The flow in the thin layer of fresh water was also observed to exhibit increasingly pronounced three-dimensional features, with the entrained salt water eddies, occasionally reaching the free surface, being located more often near the center of the channel than near the walls.

Both theoretical arguments and experimental evidence have shown that if the discharge densimetric Froude number is increased past a critical value, which depends on the depth of the ambient fluid, the upstream-controlled unstable flow eventually degenerates into another type of flow, which has been called a downstream-controlled unstable flow (see sketch in Figure 2.4). This occurs when the discharge densimetric Froude number is so large for the given ambient depth that all the ambient fluid near the source is swept downstream, so that the entire channel depth near the source is occupied by unmixed dense fluid. The mechanics of the transition from an upstream- to a downstream-controlled unstable flow is not fully clear, and it is believed to be strongly affected by the above-mentioned three-dimensional features, which greatly complicate the theoretical analysis of the flow. However, it was shown that downstream-controlled unstable flows afforded a negligible amount of entrainment of ambient fluid, so that they could be fully characterized only in terms of downstream variables. Knowledge of the downstream control and of the channel roughness and depth are sufficient to determine the entire interfacial profile, from the channel end to the point where the interface attains the free surface. A transition to an upstream-controlled unstable flow is believed to take place if the free surface is not attained within the length of the channel.

In summary, both the downstream control and the limited depth of the ambient fluid strongly interact with the discharge conditions and have a profound effect on

the mechanics of two-layer stratified systems. The downstream control plays a central role in determining the location of the roller region, and consequently the length of the entraining region, whereas the limited depth of the ambient fluid governs the stability of the system.

6.2 Application

Some criteria can be directly derived from the results of this investigation and applied both to the design of a mixing channel and to the resolution of the flow occurring in a mixing channel of prescribed characteristics.

If the discharge flowrate and the initial density difference between the discharge and the ambient fluids are given, as is often the case, the designer can act on one or more of the following parameters: channel length, depth, roughness, slope, downstream control and discharge inlet height. Obviously, the choice of the design parameters ultimately depends on an economic analysis, but the discussion is limited here to the technical aspects of the problem.

If the objective of the designer is to maximize dilution of the discharged fluid, it can be generally said that all the factors that tend to raise the depth of the lower layer in the subcritical downstream flow should be limited as much as possible. In other words, the downstream control should be low (e.g., a free overfall), the channel should be short and smooth, and possibly a sloping bottom should be used. Similarly, factors which increase the chances of the onset of unstable flows should be avoided: deep channels, in this respect, are to be preferred to shallower ones.

In order to regulate the discharge densimetric Froude number, the designer can choose the depth of the discharge inlet. This investigation has shown that an 'optimum' value of the discharge densimetric Froude number exists which maximizes

dilution for any prescribed set of all the other variables. Therefore the discharge inlet should be chosen so as to attain this value. The analytical tools to characterize this condition have been developed in the previous chapters, and are further discussed at the end of this section.

On the other hand, in some instances the goal of the designer, as previously pointed out, is to *minimize* dilution (e.g., in a cooling pond). This can be attained by creating the conditions for the occurrence of either a flooded jump or a downstream-controlled unstable flow, since the entrainment of ambient fluid has been shown to be negligible in both of these mixing modes. The occurrence of both these flow structures is facilitated by high downstream controls, long and rough channels, limited ambient water depths, and negative bottom slopes. Then, if a flooded jump is desired, the height of the discharge inlet should be large (low discharge densimetric Froude number), while if a downstream-controlled unstable flow is wanted, the height of the discharge inlet should be very small (very large discharge densimetric Froude number).

An iterative procedure is now outlined to show how the ideas developed in this investigation can be used to determine the characteristics of the flow in a mixing channel quite accurately. The geometry and the roughness of the channel, as well as the discharge parameters and the type of downstream control, are assumed to be known.

The first step consists in the determination of the mixing mode that will occur in the channel, and in the approximate resolution of the bulk flow; this can be done by using the one-dimensional theoretical model discussed in Chapter 2. It will be assumed, in the following discussion, that the occurring mixing mode is found to be a free internal hydraulic jump, and reference will be made to the sketch shown in Figure 6.4. Analysis of the bulk flow with the one-dimensional model provides approximate values of the flow parameters at section 1, i.e., the flowrate in the lower layer, q_1, and

in the upper layer, $q_1 - q_0$, the depth of the lower layer, h_1, and the density difference between the two layers, $\rho_1 - \rho_a$. The values are only approximate because of the limitations of the one-dimensional analysis, which have been discussed at length in Chapter 5, namely the assumptions of uniformity of velocity and density profiles, and of negligibility of flow force loss due to boundary shear between sections 0 and 1. It will also be recalled that only an approximate value of the length of the mixing region, L_j, was available before the solution of the system of equations representing the one-dimensional analysis, and that 'bulk' values of the friction factors were introduced for all the modeled flow conditions. Although not extremely accurate, the available values of the flow parameters at section 1 can now be used to study the mixing region in greater detail.

The depth of the lower layer at the foot of the roller, h_j, can be determined using Equation 6.2, and the development of the flow both in the mixing region and in the roller can be characterized by means of the results cited in the previous section; in particular, it is possible to obtain fairly accurate estimates of the length of the mixing region, and of the boundary shear force acting on the fluid along the mixing region. Since approximate values of the flow parameters in the subcritical gradually-varied counterflow are known, it is also possible, taking into cosideration the roughness of the material used for the channel boundaries, to obtain an accurate value of the boundary friction factors; even the assumption of constancy of these factors along the channel could now be released, since the entire interfacial profile along the subcritical region is known. Moreover, the knowledge of the local Reynolds and Froude numbers along the channel allows the determination of the interfacial friction factor, which, according to the investigations cited in Section 4.2.2, depends on such numbers or on a combination of them.

Finally, the one-dimensional model can now be applied again, with the new

values of the friction factors and of the length of the mixing region, and with Equation 2.7 replaced by

$$\frac{q_0^2}{h_0} + \frac{1}{2} g_0' h_0^2 + \frac{1}{2} \frac{(q_1 - q_0)^2}{(d - h_1)^2} d = c_1 \frac{q_1^2}{h_1} + \frac{(q_1 - q_0)^2}{d - h_1} + \frac{1}{2} g_1' h_1^2 + F \qquad (6.3)$$

where c_1 is the correction factor defined in Section 5.5.2, which accounts for the non-uniformity of the velocity profile after the jump, and was found to be of the order of 1.4 in this investigation, and F is the flow force per unit width lost across the mixing region because of bottom and wall shear resistance.

6.3 Summary and conclusions

The features of two-layer density-stratified flows were investigated, both theoretically and experimentally, by studying the flow in a horizontal mixing channel.

In order to highlight the interdependence of source parameters, far-field control and ambient conditions, experiments were performed over a wide range of all these factors. Visual observations were complemented by measurements employing high-resolution, laser-based techniques: a laser-induced fluorescence technique was used to obtain detailed density profiles, while laser-Doppler velocimetry allowed the determination of velocity distributions over the entire depth of the channel.

A one-dimensional theoretical analysis, based on the assumptions of uniformity of velocity and density profiles downstream of the mixing region, was discussed and extended, and its predictions were compared with the experimental results. This analysis, which applies to the general case of a mixing channel of finite depth and length, and includes the effects of friction along the boundaries of the channel, was carried out in three stages. First, the flow at the upstream end of the channel was considered, and a conservation of flow force in the total channel depth across the mixing region was hypothesized. Second, the gradually-varied counterflow, governed

by boundary shear and interfacial momentum transfer, as well as by the critical flow condition at the channel end, was studied by applying the momentum principle to both layers. Finally, the upstream and the downstream equations were combined to obtain hydraulic solutions, in a way that clearly established that the overall problem could only be solved if the importance of the interplay between source and control was recognized.

The basic conclusions from this study can be summarized as follows:

1. Four fundamentally different overall flow structures can take place in a mixing channel:

   - If a match between the flow force in the upstream supercritical flow and the flow force in the downstream subcritical flow occurs within the channel, the mixing mode named *free internal hydraulic jump* takes place. This is characterized by an entraining wall-jet-like region near the source, and a gradually-varied subcritical counterflow region in the downstream portion of the channel. The transition between these two regions takes the form of a roller similar to that observed in regular open channel flow.
   - If the flow force in the upstream flow is too low to match the flow force in the downstream flow, a *flooded internal hydraulic jump* occurs. The source region is drowned by the lower layer dense fluid, and the entrainment of ambient fluid is negligible.
   - If the flow force in the upstream flow exceeds the flow force attainable by the downstream flow, an instability occurs, with a recirculation cell of dense fluid forming near the source region. This mixing mode, named *upstream-controlled unstable flow*, is characterized by decreasing values of the dilution attained in the mixing region for increasing values of the discharge densi-

metric Froude number.

- If the discharge densimetric Froude number is very large, all the ambient fluid is swept downstream, and unmixed source fluid occupies the entire channel depth near the source. This flow structure, called *downstream-controlled unstable flow*, is characterized by the presence of a blocked wedge of fresh water, and is entirely governed by the far-field control and by friction.

2. The limited depth of the ambient fluid, and the resulting counterflow in the upper layer, can strongly influence the mechanics of the system and the dilution attained in the mixing region. For a prescribed ambient depth, an 'optimum' value of the discharge densimetric Froude number exists for which the dilution is a maximum. An increase in the ambient depth results in an increase in both the optimum Froude number and the maximum dilution attainable.

   The depth of the ambient fluid affects the dilution by playing a central role in determining the stability of the flow.

3. The downstream control influences the flow structure by governing the position of the roller region, thereby governing the length of the entraining region and the mixing achieved in the channel. The effect of the downstream control is so marked that any analysis not explicitly taking it into account is bound to be unsuccessful even in predicting the basic features of the flow.

4. The density profiles in the subcritical counterflow region were found to be very nearly uniform, both near the jump and close to the downstream end of the channel. The density interface, which was found to coincide with the visual interface when the lower layer was colored with dye, was stable but supported internal waves of various amplitudes and lengths; the largest amplitudes were

observed just downstream of the roller region.

5. The velocity profiles in the subcritical counterflow region showed considerable deviations from the top-hat distribution assumed in many investigations, and changed shape moving longitudinally along the channel. The zero-velocity line was found to be considerably farther from the channel bottom than the density interface.

6. The one-dimensional analysis successfully characterizes the overall flow in a mixing channel and properly predicts the role played by the downstream control and by the depth of the ambient fluid. However, it was found to be inaccurate under certain flow conditions, and more specifically it was found that the flow force at a cross-section just downstream of the jump region was overestimated by the analysis because of (i) the neglect of the cross-sectional variability of the velocity, (ii) the neglect of the boundary shear force exerted along the mixing region by the channel bottom and walls, and (iii) possibly other causes, such as the assumption of a hydrostatic pressure distribution in the ambient fluid over the source region, or the neglect of momentum transfer by interfacial waves.

7. An iterative procedure, which uses the one-dimensional model in conjunction with entrainment models for horizontal buoyant wall jets, can be used to remedy the inaccuracies discussed above. The first, approximate resolution of the bulk flow provides the information necessary to study the mixing region in detail. The characterization of the mixing region allows then an estimate of the flow force loss and of the length of this region. These, together with a correction factor that accounts for the non-uniformity of the velocity profile after the jump, can then be incorporated in the one-dimensional model.

8. The results of this investigation can be directly applied to the design of mixing channels. If the objective of the designer is to maximize mixing, the channel should be deep and short, have smooth boundaries and a low control at the downstream end, and possibly have a sloping bottom. For any prescribed set of all the other parameters, the height of the discharge inlet should be chosen so as to attain the optimum value of the discharge densimetric Froude number.

The domains of occurrence of the four different mixing modes in a channel of prescribed length, width and roughness can be represented as shown in Figures 6.6 and 6.7. It is interesting to observe that while in a relatively short channel (Figure 6.6) for any given dimensionless ambient depth, H, all four mixing modes can take place, depending on the discharge densimetric Froude number, $\mathbf{F_0}$, and therefore the transition from flooded to downstream-controlled conditions necessarily passes through the 'entraining modes' (free jump and upstream-controlled instability). In a longer channel (Figure 6.7) the possibility exists for a direct transition from flooded to downstream-controlled conditions (for $H < 23.3$ in the example shown in Fig. 6.7). In other words, if the ratio between the channel length and its depth is too large, a negligible dilution of the source fluid will occur under all discharge conditions.

It is also worth pointing out that the maximum dilution is attained within the free-jump domain. It is not clear why Baddour (1987) states that the optimum condition for dilution occurs at the boundary between free jumps and upstream-controlled unstable flows. Figure 6.7 clearly shows that for any given H the value of $\mathbf{F_0}$ which gives maximum dilution is lower than the value which causes flow instability. This fact is also supported by experimental evidence. (Careful inspection of the data in Table 4.1 proves this point. For example, consider the

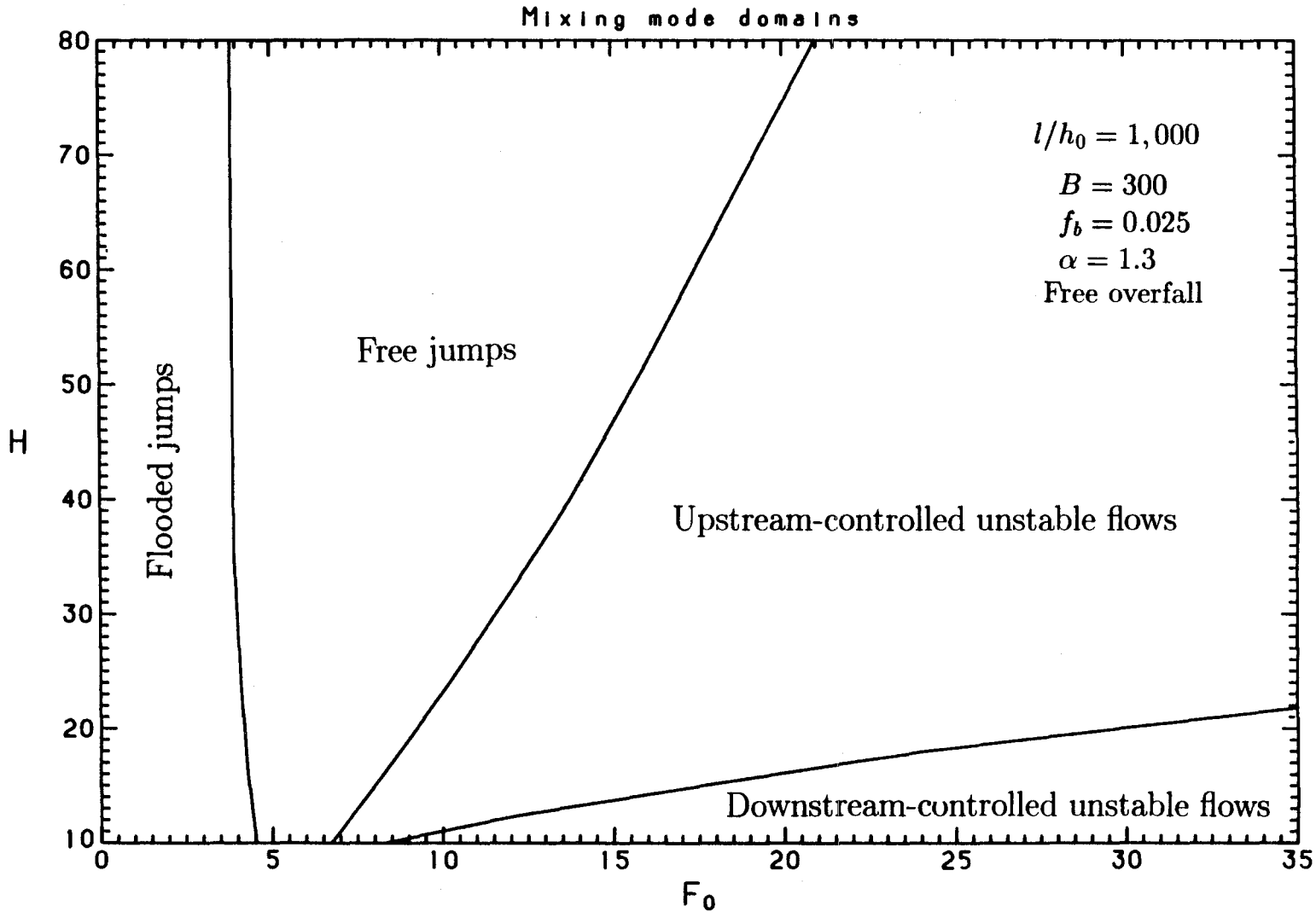

Figure 6.6: Domains of occurrence of mixing modes in a short channel.

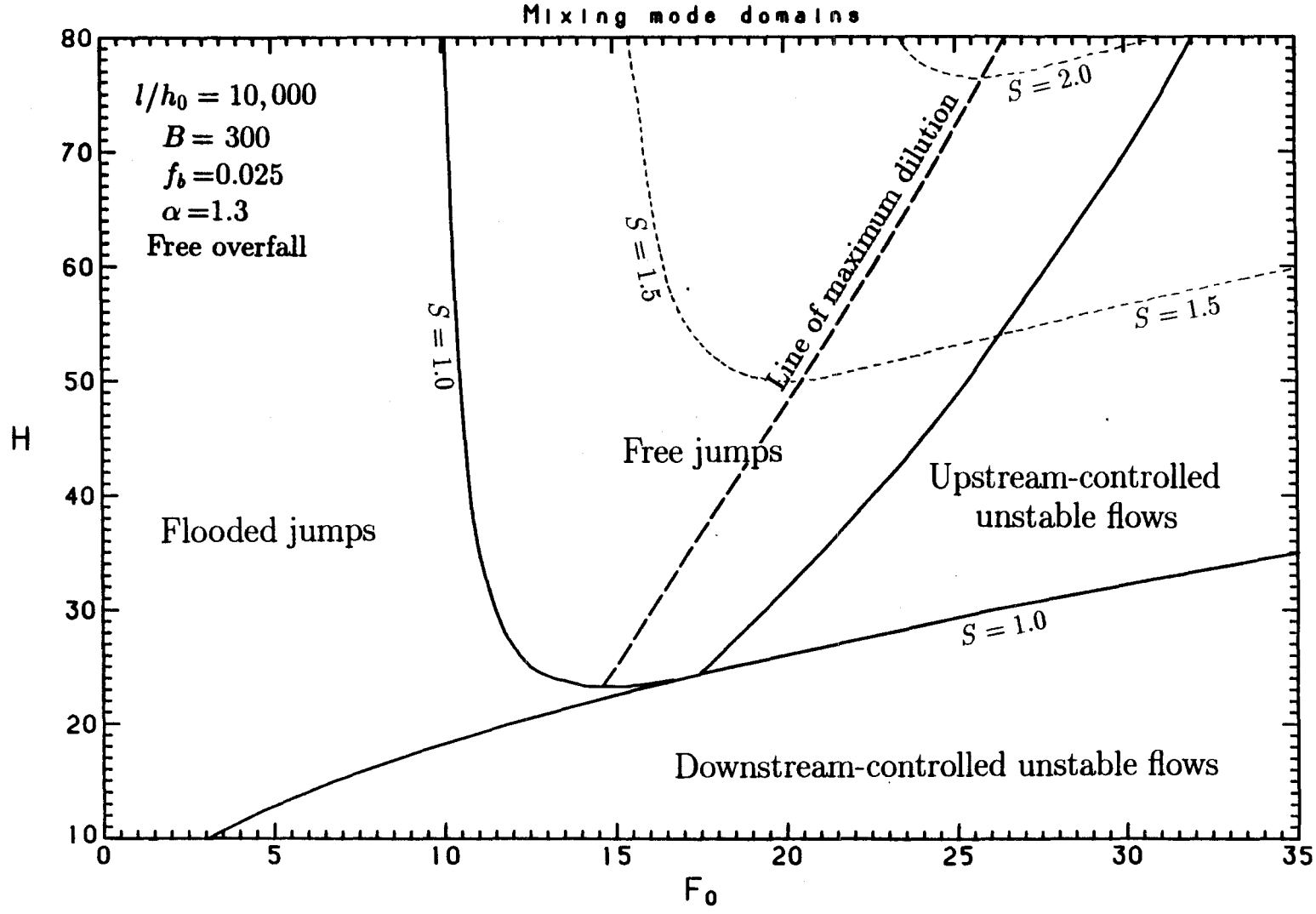

Figure 6.7: Domains of occurrence of mixing modes in a long channel.

data for the experiments with $H = 26.6$. Maximum dilution is attained near $\mathbf{F_0} = 10.5$, while the transition from free jumps to unstable flows takes place somewhere between $\mathbf{F_0} = 12.9$ and $\mathbf{F_0} = 13.7$).

Although only two examples are shown in Figures 6.6 and 6.7, the ideas developed in this study can be applied to obtain similar graphs by prescribing all the channel parameters except for two (H and $\mathbf{F_0}$ in the previous examples) and by representing the domains of the mixing modes in terms of the two variables chosen. Graphs like these can be of great help to the designer, since they efficiently summarize how the main features of the flow change when the factors under the control of the designer are varied.

6.4 Open questions

The following unresolved issues are believed to deserve the attention of future research on stratified conjugate flows:

1. The velocity profiles downstream of the jump have been shown to have a shape considerably different from the top-hat or Gaussian distributions often hypothesized in theoretical analyses of shear flows in stratified systems. It remains unexplained, though, what is causing the observed 'triangular' shape (Figures 5.10 and 5.12). It may be interesting, in this respect, to measure velocity profiles inside the entraining and roller regions, so as to observe how the evolution from the wall-jet-like to the after-jump distribution takes place. This is intimately related to the question of whether the shape of the velocity profile after the jump can or cannot be predicted only from the knowledge of the bulk characteristics of the conjugate states across the roller.

2. The free surface of the channel was assumed to have a constant depth, and this was justified by observing that the free surface Froude number (Equation 2.1) was very low in the flows under investigation. However, as the ambient depth decreases, or the discharge flowrate increases, the non-hydrostatic pressure distribution in the ambient fluid surmounting the source region, induced by the discharge jet, will eventually have an impact on the free surface.

   Extremely precise measurements of the position of the free surface along the channel could lead to the determination of the point at which the lowering of the free surface starts having a non-negligible impact on the flow force balance across the jump region.

3. The interpretation given in this study to the mechanics of the roller region, and to the transition from stable to unstable flows, with the onset of a recirculating cell of dense fluid (Section 6.1), was mostly based on intuition gained through visual observations. Experimental characterization of the velocity and density fields at these transitions would be useful to check the validity of this interpretation.

4. It is not clear what the mechanism generating the interfacial waves observed downstream of the jump is. A spectral analysis of these waves may lead to new insight into both the origin of these waves and their impact on the flow downstream of the mixing region.

5. Additional work should be done to characterize the shear at the stable interface between two layers of different velocity and density. The present understanding of interfacial friction does not allow an accurate determination of friction factors to be used in modeling shear at the interface, and although there is general agreement on what the parameters governing this shear are, known experimental data

are not very conclusive as yet, and a generally accepted functional relationship between these parameters and the shear is not available.

6. The integral-type equations that have been proposed for the study of the development and of the entraining characteristics of horizontal buoyant jets (e.g., Equation 6.1) are based on certain assumptions on the shapes of the velocity and density profiles. Neither these assumptions nor the predicted longitudinal development of the flow have received conclusive experimental support.

7. Suppose that a channel of prescribed length, width and roughness is given. If the channel is very deep for the considered range of source parameters, so that the dynamic effect of the counterflow in the ambient fluid is negligible, the depth of the lower layer after the jump, h_1, will in general depend on the source parameters (q_0, g_0', h_0) and on the downstream control (h_w). By dimensional analysis, the dependence of h_1 on the other variables can be expressed either as

$$\frac{h_1}{h_0} = \frac{h_1}{h_0}(\mathbf{F_0}, \frac{h_w}{h_0}), \tag{6.4}$$

or as

$$\frac{h_1}{l_s} = \frac{h_1}{l_s}(\mathbf{F_0}, \frac{h_w}{l_s}) \tag{6.5}$$

where

$$l_s = \sqrt{\frac{q_0^2}{g_0' h_0}} = h_0 \mathbf{F_0}. \tag{6.6}$$

(Equations 6.4 and 6.5 are only approximate, since the friction factors in the channel, as well as the length of the jump region, have an effect on h_1, and they change as the Reynolds and Froude numbers of the lower layer change.)

The normalization suggested by Equation 6.4 has been used in this investigation, i.e., dimensionless parameters have been defined using h_0 as the normalizing factor, e.g., $r_1 = h_1/h_0$, $r_w = h_w/h_0$ and $H = d/h_0$. However, it would have

also been possible to use a normalization based on the 'source length' l_s, as suggested by Equation 6.5, by defining the dimensionless variables $m_1 = h_1/l_s$, $m_w = h_w/l_s$ and $D = d/l_s$. All the equations developed in Chapter 2 could be expressed in terms of the new dimensionless variables. For example, Eq. 2.22 would be replaced by

$$(\frac{m_1^2}{2S} - 1)\,\mathbf{F_0}^2 + [\frac{(S-1)^2}{(D-m_1)^2}(\frac{D}{2} - m_1) + \frac{S^2}{m_1}]\,\mathbf{F_0} = \frac{1}{2}\,, \tag{6.7}$$

which is obtained normalizing the upstream equation, Eq. 2.7.

Although this idea is not pursued further at this point, there are indications that it might lead to an interesting reformulation of the one-dimensional model: Figures 6.8 and 6.9 show the same data presented in figures 4.11 and 4.25, respectively, but l_s is used in place of h_0 as the normalizing length. It can be seen that for large $\mathbf{F_0}$ (free jumps) h_1/l_s seems to become independent of $\mathbf{F_0}$ in the free overfall experiments (Figure 6.8). Furthermore, the new normalization makes the data of Figure 4.25 collapse on a single curve in Figure 6.9.

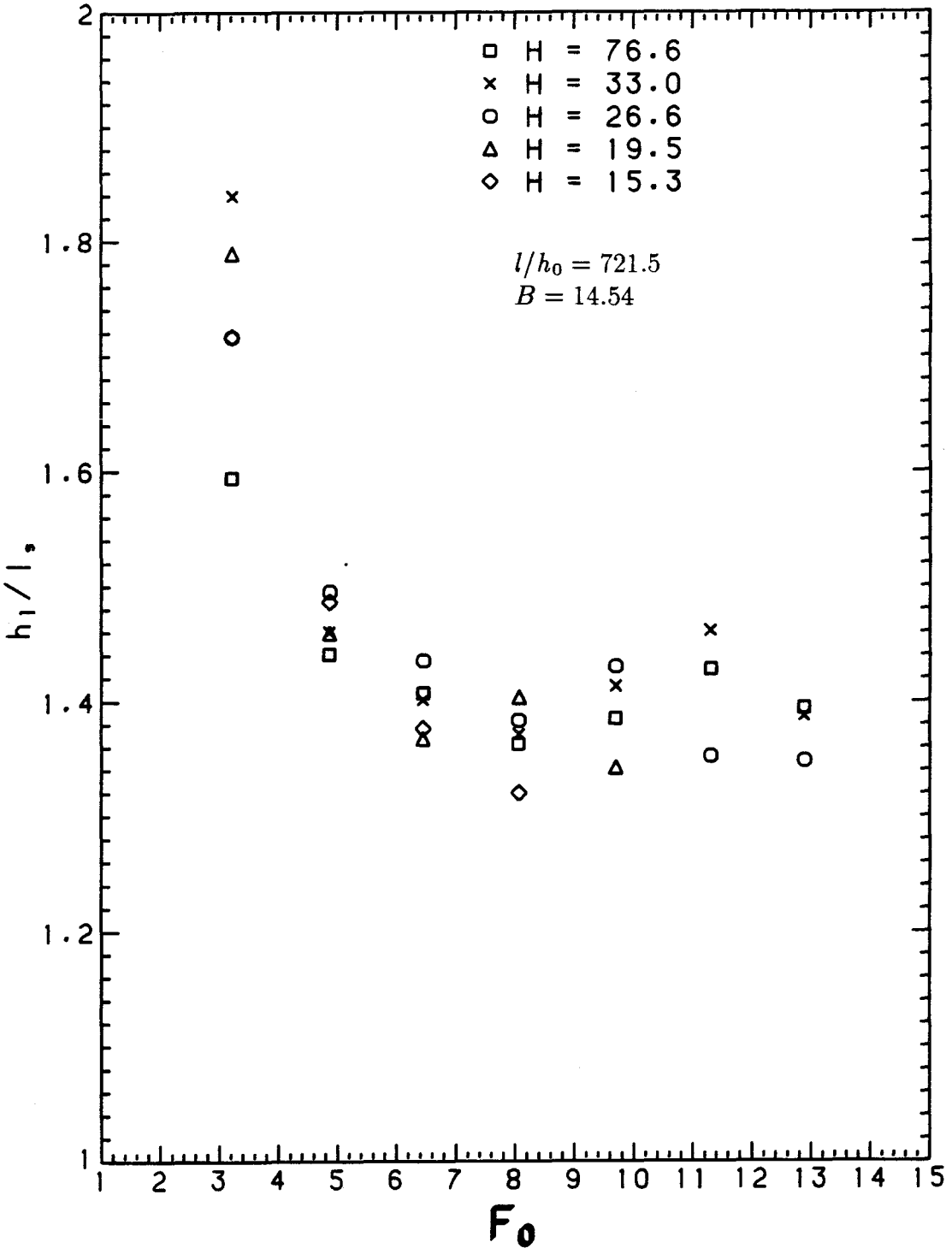

Figure 6.8: After-jump layer depth vs. Froude number.

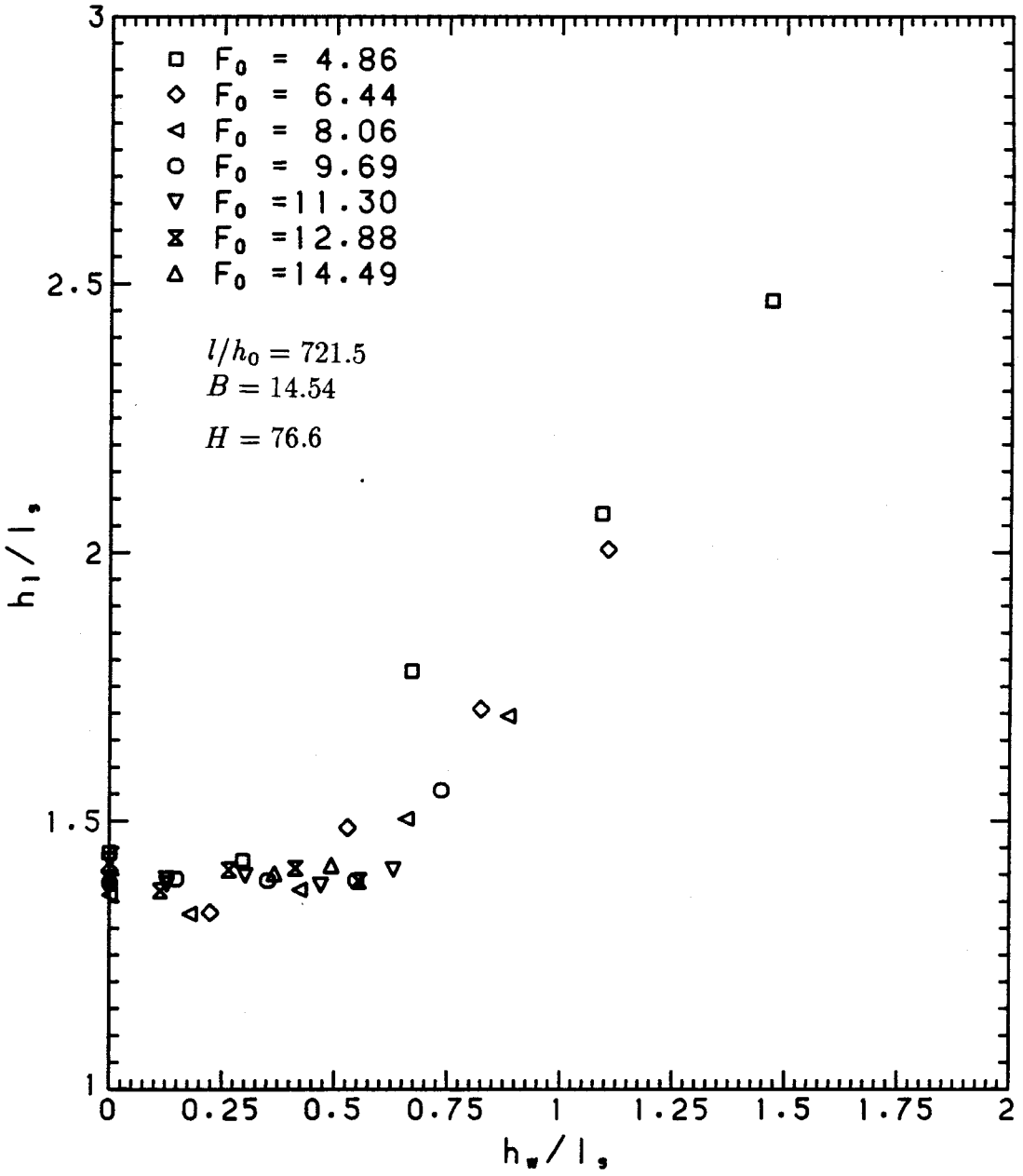

Figure 6.9: After-jump layer depth vs. weir height.

References

[1] Abraham, G. and Eysink, W.D. 1971. Magnitude of interfacial shear in exchange flow. *J. Hydraulic Research*, IAHR, **9** (2), 125–151.

[2] Arita, M. and Jirka, G.H. 1987. Two-layer model of saline wedge. I: Entrainment and interfacial friction. *J. Hydraulic Engineering*, **113** (10), 1229–1248.

[3] Arita, M., Jirka, G.H. and Tamai, N. 1986. Classification and mixing of two-dimensional buoyant surface discharges. *J. Hydraulic Research*, **24** (5), 333–345.

[4] Backhmeteff, B.A. and Matze, A.E. 1936. The hydraulic jump in terms of dynamic similarity. *Transactions*, ASCE, **101**, 630–647.

[5] Baddour, R.E. 1987. Hydraulics of shallow and stratified mixing channel. *J. Hydraulic Engineering*, **113** (5), 630–645.

[6] Baddour, R.E. and Abbink, H. 1983. Turbulent underflow in a short channel of limited depth. *J. Hydraulic Engineering*, **109** (5), 722–740.

[7] Ball, F.K. 1956. *Aust. Journal of Physics*, **9**, 373–386.

[8] Ball, F.K. 1957. *Tellus*, **9** (2), 201–208.

[9] Ball, F.K. 1959. *Antarctic Meteorology.* Pergamon Press, London.

[10] Batchelor, G.K. 1967. *An Introduction to Fluid Dynamics.* Cambridge University Press.

[11] Bewick, D.J. 1974. Entraining hydraulic jumps in two layer flows. Master of Engineering thesis. University of Canterbury, Christchurch, NZ.

[12] Britter, R.E. and Linden, P.F. 1980. The motion of the front of a gravity current traveling down an incline. *J. Fluid Mechanics*, **99**, 531–543.

[13] Christodoulou, G.C. 1986. Interfacial mixing in stratified flows. *J. Hydraulics Research*, **24** (2), 77–92.

[14] Chu, V.H. and Baddour, R.E. 1977. Surges, waves, and mixing in a two-layer density stratified flow. *Proceedings of XVIIth Congress*, IAHR, Baden-Baden, 303–310.

[15] Chu, V.H. and Baddour, R.E. 1984. Turbulent gravity stratified shear flows. *J. Fluid Mechanics*, **138**, 353–378.

[16] Clarke, R.H., Smith, R. and Reid, D.G. 1981. The morning glory of the Gulf of Carpentaria. *Mon. Weather Rev.*, **108**, 1726–1750.

[17] Dermissis, V. and Partheniades, E. 1984. Interfacial flow structure and significant shear stresses in arrested saline wedges. *Tech. Rep.*, Dept. Engr. Sci., U. Florida, Gainesville, Fla.

[18] Drain, L.E. 1980. *The laser-Doppler technique.* Wiley-Interscience, New York.

[19] Durst, F., Melling, A.H. and Whitelaw, J.H. 1976. Principles and practice of laser-Doppler anemometry. Academic Press, London.

[20] Ellison, T.H. and Turner, J.S. 1959. Turbulent entrainment in stratified flows. *J. Fluid Mechanics*, **6**, 423–448.

[21] Farmer, D.M. and Denton, R.A. 1985. Hydraulic control of flow over the sill in Observatory Inlet. (submitted to *J. Geophys. Res.*)

[22] Gartrell, G. 1978. A signal processor for a laser-Doppler velocimeter. *Tech. Memo. 78-5*, W.M. Keck Laboratory of Hydraulics and Water Resources, California Institute of Technology, Pasadena, California.

[23] Gartrell, G. 1979. Studies on the mixing in a density-stratified shear flow. *Report no. KH-R-39.* W.M. Keck Laboratory of Hydraulics and Water Resources, California Institute of Technology, Pasadena, California.

[24] Gutmark, E. and Wygnanski, I. 1976. The planar turbulent jet. *J. Fluid Mechanics*, **73**, 465–495.

[25] Hannoun, I.A. 1986. Use of the Reticon array camera. *Tech. Memo. 86-1*, W.M. Keck Laboratory of Hydraulics and Water Resources, California Institute of Technology, Pasadena, California.

[26] Hannoun, I.A. 1987. Turbulent mixing in stably-stratified fluids subjected to zero-mean shear. Ph.D. thesis. California Institute of Technology, Pasadena, California.

[27] Hannoun, I.A. and List, E.J. 1988. Turbulent mixing at a shear-free interface. *J. Fluid Mechanics*, **189**, 211–234.

[28] Harleman, D.R.F. 1960. Stratified flow. *Handbook of Fluid Dynamics*, V.L. Streeter, ed., sect. **26**, McGraw-Hill, New York.

[29] Hayakawa, N. 1970. Internal hydraulic jump in co-current stratified flow. *J. Engineering Mechanics Division*, **96** (EM5), 797–800.

[30] Jirka, G.H. 1982. Turbulent buoyant jets in shallow fluid layers. *Turbulent Buoyant Jets and Plumes*, W. Rodi, ed., Pergamon Press, New York. 69–119.

[31] Jirka, G.H. and Harleman, D.R.F. 1979. Stability and mixing of a vertical plane buoyant jet in confined depth. *J. Fluid Mechanics*, **94**, 275–304.

[32] Keulegan, G.H. 1981. Significant stresses of arrested saline wedges. *Miscellaneous Paper HL-81-5. Final Report,* U.S. Army Engr. Waterways Experiment Station.

[33] Koh, R.C.Y. 1971. Two-dimensional surface warm jet. *J. Hydraulics Division*, **97** (HY6), 819–836.

[34] Koochesfahani, M.M. 1984. Experiments on turbulent mixing and chemical reaction in a liquid mixing layer. Ph.D. thesis. California Institute of Technology, Pasadena, California.

[35] Lied, N.T. 1964. Stationary hydraulic jumps in a katabatic flow near Davis, Antarctica, 1961. *Aust. Met. Magazine*, **47**.

[36] Liu, H.T., Lin, J.T. and Robben, F.A. 1977. Application of a fluorescence technique to dye-concentration measurements in a turbulent jet. *Proc. Symp. on Flow in Open Channels and Closed Conduits.* NBS Special Publication **484**.

[37] Lofquist, K. 1960. Flow and stress near an interface between stratified liquids. *Phis. Fluids*, **3** (2), 158–175.

[38] Long, R.R. 1953. Some aspects of the flow of stratified fluids I. A theoretical investigation. *Tellus*, **5**, 42–58.

[39] Long, R.R. 1954. Some aspects of the flow of stratified fluids II. Experiments with a two-fluid system. *Tellus*, **6**, 97–115.

[40] Mehrotra, S.C. and Kelly, R.E. 1973. On the question of non-uniqueness of internal hydraulic jumps and drops in a two-fluid system. *Tellus*, **25**, 560–567.

[41] Miles, J.W. 1961. On the stability of heterogeneous shear flows. *J. Fluid Mechanics*, **68**, 577.

[42] Miller, D.R. and Comings, E.W. 1957. Static pressure distribution in the free turbulent jet. *J. Fluid Mechanics*, **3**, 1–16.

[43] Papanicolaou, P.N. 1984. Mass and momentum transport in a turbulent buoyant vertical axisymmetric jet. Ph.D. thesis. California Institute of Technology, Pasadena, California.

[44] Papantoniou, P.N. 1986. Observations in turbulent buoyant jets by use of laser-induced fluorescence. Ph.D. thesis. California Institute of Technology, Pasadena, California.

[45] Rajaratnam, N. and Subramanyan, S. 1968. Profile of the hydraulic jump. *J. Hydraulic Division*, **94** (HY3), 663–673.

[46] Rajaratnam, N. and Subramanyan, S. 1985. Plane buoyant surface jets and jumps. *J. Hydraulic Research*, **23**, 131–146.

[47] Rajaratnam, N. and Subramanyan, S. 1986. Plane turbulent denser wall jets and jumps. *J. Hydraulic Research*, **24**, 281–296.

[48] Reticon (1981). LC300A Camera Manual. EG&G Reticon.

[49] Righter, B.P. 1970. Density induced return currents in outlet channels. *J. Hydraulic Division*, **96** (2), 529–546.

[50] Rodi, W. 1975. A review of experimental data of uniform density free turbulent boundary layers. *Studies of Convection*, **1**. Academic Press.

[51] Rohr, J.J, Itsweire, E.C, Helland, K.N. and Van Atta, C.W. 1988. Growth and decay of turbulence in a stably stratified shear flow. *J. Fluid Mechanics*, **195**, 77–111.

[52] Rouse, H., Siao, T.T. and Nagaratnam, S. 1959. Turbulence characteristics of the hydraulic jump. *Transactions*, ASCE, 926–950.

[53] Schijf, J.B. and Schönfeld, J.C. 1953. Theoretical considerations on the motion of salt and fresh water. *Proc. Minnesota International Hydr. Convention*, IAHR & ASCE, 321–333.

[54] Schwarz, W.H. and Cosart, W.P. 1961. The two-dimensional turbulent wall jet. *J. Fluid Mechanics*, **10**, 481–495.

[55] Schweitzer, H. 1953. Attempts to explain the Föhn. *Archiv. Meteorologie, Geophisic, Hisclimatologie*, Series A, **5** (3), 350.

[56] Stefan, H. 1972. Dilution of buoyant, two-dimensional surface discharges. *J. Hydraulic Division*, **98** (Hy1), 71–86.

[57] Stefan, H. and Hayakawa, N. 1971. Surface discharge of heated water, Part II: the two-dimensional surface jet and the internal hydraulic jump. *Project Report 127*, St. Anthony Falls Hydraulics Laboratory. University of Minnesota.

[58] Stefan, H. and Hayakawa, N. 1972. Mixing induced by an internal hydraulic jump. *Water Resources Bull., Am. Water Res. Assn.*, **8** (3), 531–545.

[59] Townsend, A.A. 1970. Entrainment and the structure of turbulent flow. *J. Fluid Mechanics*, **41**, 13–46.

[60] Turner, J.S. 1973. *Buoyancy Effects in Fluids.* Cambridge University Press.

[61] Vanvari, M.R. and Chu, V.H. 1974. Two-dimensional surface jets of low Richardson number. *Fluid Mechanics Laboratory, Tech. Rep. 74-2.* McGill University.

[62] Wilkinson, D.L. 1970. Studies in density stratified flows. *Water Research Laboratory Report 118.* University of N.S.W..

[63] Wilkinson, D.L. and Wood, I.R. 1971. A rapidly varied flow phenomenon in a two-layer flow. *J. Fluid Mechanics*, **47**, 241-256.

[64] Wood, I.R. and Simpson, J.E. 1984. Jumps in layered miscible fluids. *J. Fluid Mechanics*, **140**, 329–342.

[65] Wright, S.J. 1986. Aspects of far-field control on buoyant jet mixing. Institut für Hydromechanik und Wasserwirtschaft. ETH, Zürich.

[66] Yih, C.S. and Guha, C.R. 1955. Hydraulic jump in a fluid system of two layers. *Tellus*, **7**, 358–366.